The Capacitive Resistivity Technique for Electrical Imaging of the Shallow Subsurface

by

Oliver Kuras

Dipl.-Phys. FGS

Thesis submitted to the University of Nottingham
for the degree of Doctor of Philosophy

December 2002

Caelum non animum mutant qui trans mare currunt.

Q. Horatius Flaccus (65–8 BC)

To my parents,

in memory of my grandparents

Sophie Kuras	*(1918–2000)*
Georg Kuras	*(1915–2001)*
Maria Scholz	*(1911–2001)*

Abstract

Capacitive resistivity (CR) is a novel geophysical technique for the non-intrusive characterisation of the shallow subsurface by electrical imaging. CR is capable of extending the scope of the conventional DC resistivity technique to the urban built environment and other settings where galvanic contact cannot be achieved or where high contact impedances result in poor data quality. Fundamentally, the CR technique is based upon the concept of capacitive coupling between sensors and the ground and a generalisation of the DC four-point array for measuring the resistivity of the subsurface at frequencies in the VLF range. This thesis provides a unified description of CR, including its physical principles, their theoretical formulation and practical implementation in geophysical instruments. In general, the transfer impedance across a capacitive array is a complex function of frequency and geometry. It is shown that a low induction number mode of operation exists where resistivity is proportional to the in-phase component of the transfer impedance. The quadrature component is generally sensitive to a combination of parameters including sensor elevation, dipole offset and ground resistivity. Under the low induction number regime, the electric field is quasi-stationary so that theoretical equivalence with the DC case is achieved and conventional DC interpretation schemes are applicable to CR data.

A comprehensive parameter study undertaken in this thesis investigates the applicability of the technique under the specific conditions typically encountered in environmental and engineering site investigation surveys. In those circumstances, practical CR measurements are shown to be limited to an optimal frequency window, typically between 1 kHz and 25 kHz. The condition of low induction numbers imposes further restrictions on the maximum dimensions of the sensor array and the minimum resistivity of the ground. However, a key finding of the parameter study is that even under the quasi-static regime, practical conditions may be such that substantial phase rotations may occur which are exclusively due to the capacitive nature of the technique. Modelling of sensor capacitances is used to demonstrate that the concept of point poles postulated in the quasi-static formulation of CR has a practical realisation in the form of plate-wire sensors.

Subsequently, the fundamental concepts of CR are validated experimentally in a series of elementary surveys where the fully complex transfer impedance (amplitude and phase) is measured with a newly developed prototype CR instrument. It is shown that for assessments of shallow subsurface conditions with typical survey parameters and standard geometries, the observed responses are typically in-phase. However, it is also demonstrated that practical circumstances exist under which significant phase rotations can be observed. In such cases, an estimation of apparent resistivity using the in-phase component only is more appropriate than the magnitude-based calculation performed by existing commercial instruments.

The nature of the CR technique facilitates the use of towed arrays that allow the dynamic collection of multi-offset apparent resistivity data without the disadvantages of galvanic coupling. This thesis examines the operational characteristics of towed CR arrays and compares data acquired with a range of instruments in a variety of different environments. It is shown that towed-array CR enables the collection of highly repeatable resistivity data at sampling intervals of the order of centimetres. Towing-induced noise is found to be much less problematic than previously found with DC towed-array techniques. It is also demonstrated that high-quality data can be obtained by towed-array CR on artificial surfaces such as tarmac or concrete. Consequently, the technique appears to be particularly suited for assessing the condition of engineered structures such as roads and pavements.

Finally, it is demonstrated how multi-offset towed-array CR can be employed for electrical tomographic imaging of the shallow subsurface. Conventional DC resistivity interpretation schemes based on quasi-2D, 2D and 3D inversion algorithms are shown to be applicable to such datasets, provided that some elementary rules are observed with regard to the design of towed-array surveys. Real-time interpretation during data acquisition is shown to be feasible with a continuous vertical electrical sounding (CVES) technique based on a Zohdy-type inversion. Examples of 2D and 3D surveys over shallow targets show the superior quality and resolution of CR datasets compared with conventional DC resistivity.

Affirmation

The research described in this thesis is my own work and has not been previously submitted for any other degree.

The following technical papers have been published based on this research:

Kuras, O., Ogilvy, R. D., Beamish, D., Meldrum, P. I. and Nathanail, C. P., Capacitive resistivity imaging with towed arrays: Paper accepted for presentation at the Symposium on the Application of Geophysics to Engineering and Environmental Problems (SAGEEP), San Antonio, Texas, 2003.

Kuras, O., Ogilvy, R. D., Beamish, D., Meldrum, P. I. and Nathanail, C. P., 2001, The capacitive resistivity technique: electrical imaging with towed arrays applied to shallow site investigations: Paper presented at the 7th Meeting of the Environmental and Engineering Geophysical Society - European Section (EEGS-ES), Birmingham, UK.

Beamish, D., Meldrum, P. I., **Kuras, O.** and Ogilvy, R. D., 2001, A new capacitively coupled resistivity system for the electrical impedance imaging of engineered structures: Paper presented at the 7th Meeting of the Environmental and Engineering Geophysical Society - European Section (EEGS-ES), Birmingham, UK.

Kuras, O., Ogilvy, R. D. and Nathanail, C. P., 2000, Capacitive measurement of subsurface resistivity: data processing for high-resolution surveys: Paper presented at the 6th Meeting of the Environmental and Engineering Geophysical Society - European Section (EEGS-ES), Bochum, Germany.

Oliver Kuras
Nottingham, UK
December 2002

Contents

Abstract iii

List of Figures xvii

List of Tables xviii

List of abbreviations xix

Glossary of notation xx

1 Introduction 1
- 1.1 Background and scope of research . . . 1
- 1.2 Aims and objectives . . . 2
- 1.3 Thesis structure . . . 3

2 Geophysics in environmental and engineering investigations 6
- 2.1 Environmental and engineering geophysics . . . 6
  - 2.1.1 Terminology . . . 6
  - 2.1.2 Relevant methods . . . 7
  - 2.1.3 Literature . . . 9
- 2.2 Site investigation and geophysics . . . 10
  - 2.2.1 Terminology . . . 10
  - 2.2.2 The value of geophysical information . . . 11
  - 2.2.3 Geophysics versus conventional techniques . . . 12
  - 2.2.4 Types of geophysical targets . . . 13
- 2.3 Fields of application in the UK . . . 15
  - 2.3.1 The contaminated land regime . . . 15
  - 2.3.2 Geohazards . . . 17
- 2.4 The relevance of resistivity methods . . . 18

3 Conventional resistivity methods 19
- 3.1 DC resistivity . . . 20
  - 3.1.1 Basic theory . . . 20
    - 3.1.1.1 Single current electrode at the surface . . . 21
    - 3.1.1.2 The four-electrode array . . . 21
    - 3.1.1.3 The concept of apparent resistivity . . . 23
    - 3.1.1.4 Reciprocity theorem . . . 24

3.1.2 Common array types 24
3.1.2.1 The Wenner array 24
3.1.2.2 The Schlumberger array 24
3.1.2.3 The dipole-dipole array 26
3.1.2.4 The pole-dipole and pole-pole arrays 27
3.1.3 Traditional field techniques and methods of interpretation 28
3.1.3.1 Vertical electric sounding 28
3.1.3.2 Resistivity profiling 28
3.1.3.3 Resistivity mapping 30
3.1.4 Electrical Resistivity Tomography (ERT) 30
3.1.4.1 Field techniques 30
3.1.4.2 Pseudosections and the absolute depth scale . . 32
3.1.4.3 Resistivity forward modelling 35
3.1.4.4 Resistivity inversion 35
3.1.5 Towed-array techniques 36
3.1.5.1 Automated electrode installation 36
3.1.5.2 Pulled-Array Continuous Electrical Profiling . . 37
3.1.6 Problems and disadvantages 38
3.1.6.1 Galvanic contact 38
3.1.6.2 Installation of electrodes 38
3.2 Ground conductivity 40
3.2.1 Basic theory 40
3.2.2 Operation at low induction numbers 42
3.3 Other techniques 45
3.3.1 Complex resistivity 45
3.3.2 Plane-wave EM 45
3.3.2.1 VLF 46
3.3.2.2 Radiomagnetotellurics 46
3.3.3 Magnetometric resistivity 47
3.4 Discussion 48

4 The capacitive resistivity (CR) technique 52
4.1 Historic origins 53
4.1.1 Early Russian research 53
4.1.2 The electrostatic approach 53
4.2 Fundamental concepts 54
4.2.1 The capacitive electrode 55
4.2.2 The capacitive four-electrode array 55
4.3 Capacitive sensors 56
4.3.1 The point electrode 57
4.3.2 The capacitive line antenna 57
4.3.3 The plate-wire combination 57
4.4 Existing instrumentation 58
4.4.1 Instruments based on line antennas 58
4.4.2 Instruments based on plate sensors 60
4.4.3 Borehole instruments 62
4.5 Early CR theory: the capacitive line antenna 62

4.5.1 The capacitive line antenna as a non-grounded dipole . . 62
4.5.2 The DC geometric factor 63
4.5.3 The equivalent grounded dipole 63
4.6 Electrostatic formalism and the complex transfer impedance . . . 65
4.6.1 The electrostatic quadrupole 65
4.6.1.1 Electrostatic charge near an air-earth interface . 65
4.6.1.2 The quadrupole concept 66
4.6.2 The quadrupole in quasi-static approximation 67
4.6.2.1 Variation of electric charge with time 67
4.6.2.2 The complex permittivity 67
4.6.2.3 The complex transfer impedance 68
4.6.2.4 Conditions for a quasi-static regime 68
4.6.3 The electrostatic geometric factor 69
4.6.4 Properties of the complex transfer impedance 72
4.6.4.1 Normalisation and generalised frequency 72
4.6.4.2 Variation with Ω 72
4.6.5 Solution of the reverse problem 77
4.6.5.1 The phase-sensitive apparent resistivity 77
4.6.5.2 Determination of α from a measured impedance 78
4.6.5.3 Relationship with conventional DC theory . . . 78
4.7 An electromagnetic formulation of CR 79
4.7.1 The elementary horizontal electric dipole 79
4.7.2 Finite dipoles 82
4.8 Discussion 83

5 A parameter study for practical CR measurements 86
5.1 Frequency of operation 87
5.1.1 The transfer impedance at low induction numbers 88
5.1.1.1 The upper frequency threshold 88
5.1.1.2 Functional dependence 88
5.1.2 The capacitive electrode as a reactive load 90
5.1.2.1 Complex impedance of the transmitter circuit . 91
5.1.2.2 The lower frequency threshold 91
5.1.3 The EM spectrum at radio frequencies 92
5.2 Array geometry 93
5.2.1 Dipole separation 93
5.2.1.1 Inline configuration 94
5.2.1.2 Equatorial configuration 94
5.2.2 Array elevation 97
5.2.2.1 Inline configuration 100
5.2.2.2 Equatorial configuration 100
5.3 Electrical properties 100
5.3.1 Resistivity 101
5.3.1.1 Inline configuration 101
5.3.1.2 Equatorial configuration 101
5.3.2 Relative permittivity 104
5.3.2.1 Inline configuration 104

5.3.2.2 Equatorial configuration . . . 104
5.4 Modelling of capacitive sensors . . . 107
5.4.1 The capacitance of elementary geometric structures . . . 107
5.4.1.1 Determination of capacitance . . . 108
5.4.1.2 Wire segment above a ground plane . . . 108
5.4.1.3 Finite-size plate above a ground plane . . . 109
5.4.2 Application to capacitive sensors . . . 109
5.4.2.1 The capacitive line antenna . . . 109
5.4.2.2 The plate-wire combination . . . 111
5.5 Discussion . . . 115

6 Experimental validation of CR concepts 118
6.1 The BGS prototype CRI system . . . 118
6.1.1 Measurement principle . . . 119
6.1.2 Specifications . . . 119
6.2 Properties of real capacitive sensors . . . 124
6.2.1 Effective sensor capacitance and elevation . . . 124
6.2.1.1 A practical measurement of capacitance . . . 124
6.2.1.2 Determining effective elevation . . . 125
6.2.2 Wideband reception properties . . . 126
6.2.2.1 Experimental setup . . . 126
6.2.2.2 Results and interpretation . . . 127
6.3 Spatial analysis of the complex transfer impedance . . . 130
6.3.1 Description of the test site . . . 131
6.3.1.1 Site geology . . . 131
6.3.1.2 Electrical properties . . . 131
6.3.2 Variation with distance: moveout surveys . . . 131
6.3.2.1 Equatorial configuration . . . 132
6.3.2.2 Inline configuration . . . 136
6.3.3 Comparison with DC resistivity . . . 139
6.3.3.1 Equatorial configuration . . . 139
6.3.3.2 Inline configuration . . . 142
6.3.4 Variation with azimuth: directional survey . . . 142
6.3.4.1 Parallel configuration . . . 144
6.3.4.2 Perpendicular configuration . . . 144
6.4 Discussion . . . 149

7 Dynamic measurements with towed CR arrays 152
7.1 Fundamental concepts . . . 153
7.1.1 Synchronous multi-channel acquisition . . . 153
7.1.2 Continuous spatial sampling . . . 153
7.1.3 The dipole-dipole geometry . . . 155
7.2 Operational characteristics of towed CR arrays . . . 160
7.2.1 OhmMapper™ . . . 160
7.2.1.1 Data quality . . . 162
7.2.1.2 Repeatability . . . 166
7.2.2 CORIM™ . . . 167

7.2.2.1 Data quality . . . 167
7.2.2.2 Repeatability . . . 175
7.2.3 BGS CRI system . . . 178
7.2.3.1 Data quality . . . 180
7.2.3.2 Repeatability . . . 186
7.2.3.3 Comparison with DC resistivity . . . 186
7.3 Basic processing of towed-array CR data . . . 190
7.3.1 Suppression of motion-induced noise . . . 190
7.3.1.1 Noise characterisation . . . 190
7.3.1.2 Despiking . . . 193
7.3.2 Correction of levelling errors . . . 196
7.3.2.1 Basic statistics and empirical levelling . . . 196
7.3.2.2 Micro-levelling by directional filtering . . . 200
7.4 Discussion . . . 203

8 Electrical imaging with multi-offset towed-array CR 205
8.1 Properties of multi-offset towed-array data . . . 205
8.1.1 Fixed-electrode versus towed-array acquisition . . . 205
8.1.2 Relation between array offsets and sampling interval . . . 208
8.2 Quasi-2D interpretation . . . 210
8.2.1 Continuous Vertical Electrical Sounding . . . 210
8.2.2 Zohdy's inversion . . . 212
8.2.3 Application to towed-array CR data . . . 215
8.2.4 Examples . . . 217
8.2.4.1 Synthetic data: shallow vertical contact . . . 217
8.2.4.2 Field data: river terraces at Chetwynd Barracks 221
8.3 2D interpretation . . . 223
8.3.1 2D iterative least-squares inversion . . . 223
8.3.2 Application to towed-array CR data . . . 225
8.3.3 Examples . . . 226
8.3.3.1 Synthetic data: shallow vertical contact . . . 226
8.3.3.2 Field data: river terraces at Chetwynd Barracks 229
8.3.4 MCD: an alternative to iterative inversion . . . 231
8.4 3D interpretation . . . 232
8.4.1 3D iterative least-squares inversion . . . 233
8.4.2 3D towed-array survey design and techniques . . . 233
8.4.3 Forward modelling of 3D structures . . . 236
8.4.4 Examples . . . 240
8.4.4.1 Synthetic data: the unit cube . . . 240
8.4.4.2 Field data: the EIGG geophysical test site . . . 245
8.5 Discussion . . . 255

9 Conclusions and further work 258

Acknowledgements 265

Bibliography 267

Appendix **278**

A Fundamentals of electromagnetic theory **279**
A.1 Maxwell's equations 279
A.2 Constitutive relations 280
A.3 Wave equations and the wavenumber 281
A.4 Diffusion or propagation? 281
A.5 Plane wave propagation 282
A.6 Complex electrical properties 282

B Electrical Capacitance Tomography **284**
B.1 Applications of ECT in Industrial Process Tomography 284
B.2 Basic principle 284
B.3 Image reconstruction 285
B.4 Applications 286

List of Figures

3.1 Equipotentials and current flow lines for two point sources of current at the surface of a homogeneous medium 22
3.2 The four-electrode array in DC resistivity 22
3.3 Electrode array types commonly used in DC resistivity 25
3.4 Configurations of the dipole-dipole array 27
3.5 VES curve obtained with a Schlumberger array and interpretation with two equivalent layered models 29
3.6 Constant separation traversing profiles obtained over a vertical contact using different array types 29
3.7 Example of an ERT survey using a Wenner array with a set of evenly spaced electrodes to collect multi-offset data 31
3.8 Example of electrodes arranged along a multicore cable for a 3D ERT survey on a regular grid 31
3.9 Results of a multi-offset 2D ERT survey displayed in the form of apparent resistivity profiles and a pseudosection 33
3.10 Classical method of plotting dipole-dipole data on a pseudosection 34
3.11 Comparison between a conventional DC resistivity profile and a continuous profile obtained with a towed array 37
3.12 Basic concept of a DC resistivity measurement with galvanic contact 39
3.13 Principle of the ground conductivity method 41
3.14 Configurations for the coil-coil EM sounding technique 41
3.15 The variation of electromagnetic skin depth with frequency. Parameter: resistivity. 43
3.16 Concept of the VLF technique for a conductor striking parallel to the propagation direction of the VLF signal 46
3.17 Schematic diagram of a field setup in radiomagnetotellurics . . . 47

4.1 Conceptual model of a capacitive electrode 55
4.2 Basic concept of a capacitive resistivity measurement 56
4.3 Conceptual model of a capacitive line antenna 57
4.4 Conceptual model of a plate-wire combination 58
4.5 Schematic setup and configurations of the RUSCAN system . . . 61
4.6 Schematic setup of the OhmMapper™ system 61
4.7 Schematic setup of the CORIM™ system 61
4.8 Inline dipole-dipole array composed of capacitive line antennas and equivalent grounded dipoles 64

4.9 Relation between a capacitive line antenna and its equivalent grounded dipole as a function of dipole separation for the inline dipole-dipole array 64
4.10 Electrostatic point charge near the interface between two permittive media 65
4.11 Geometry of an electrostatic quadrupole in the general case . . . 67
4.12 The symmetric equatorial and inline dipole-dipole configurations of the electrostatic quadrupole 70
4.13 Variation of the electrostatic geometric factor with elevation . . . 71
4.14 Variation of the normalised transfer impedance (in-phase and quadrature) with generalised frequency (parameter: geometric factor) 73
4.15 Variation of the normalised transfer impedance (magnitude and phase) with generalised frequency (parameter: geometric factor) 74
4.16 Variation of α with generalised frequency (in-phase and quadrature) 75
4.17 Horizontal electric dipole over a homogeneous conducting half-space 80

5.1 Variation of the complex potential with frequency for a unit square array (parameter: resistivity) 89
5.2 Electric circuit model for capacitive electrodes and ground 90
5.3 Variation of the complex potential with dipole separation in inline configuration (parameter: resistivity) 95
5.4 Variation of the complex potential with dipole separation in equatorial configuration (parameter: resistivity) 96
5.5 Variation of the complex potential with array elevation in inline configuration (parameter: resistivity) 98
5.6 Variation of the complex potential with array elevation in equatorial configuration (parameter: resistivity) 99
5.7 Variation of the complex potential with resistivity in inline configuration (parameter: dipole separation) 102
5.8 Variation of the complex potential with resistivity in equatorial configuration (parameter: dipole separation) 103
5.9 Variation of the complex potential with relative permittivity in inline configuration (parameter: dipole separation) 105
5.10 Variation of the complex potential with relative permittivity in equatorial configuration (parameter: dipole separation) 106
5.11 Cylindrical conductor above ground plane. 108
5.12 Finite-size rectangular plate above ground plane 109
5.13 Capacitance of a capacitive line antenna as a function of length . 110
5.14 Equivalent circuit model of a line antenna dipole close to the ground 110
5.15 Capacitance of a square finite-size plate above ground as a function of its width 112
5.16 Equivalent circuit model of a plate-wire combination close to the ground 112

5.17 Comparison between the capacitance of a standard plate and a unit line antenna as a function of elevation 114

6.1 Schematic setup of the BGS CRI prototype system 120
6.2 Static measurements with the BGS prototype CRI system in the field 122
6.3 Transmitter unit and current dipole of the BGS prototype CRI system 123
6.4 Potential dipole of the BGS prototype CRI system 123
6.5 Experimental setup for the measurement of effective sensor capacitance 124
6.6 Experimental setup for wideband recordings of the electric field using grounded and non-grounded dipoles. 127
6.7 Raw power spectra of the observed potential from plate sensors and stake electrodes with the CRI transmitter switched off . . . 128
6.8 Raw power spectra of the observed potential from plate sensors and stake electrodes with the CRI transmitter switched on 129
6.9 Moveout survey to determine the variation of the transfer impedance with distance 132
6.10 Complex transfer impedances for the moveout survey in equatorial configuration (model parameter: resistivity) 133
6.11 Complex transfer impedances for the moveout survey in equatorial configuration (model parameter: elevation) 134
6.12 Complex transfer impedances for the moveout survey in inline configuration (model parameter: resistivity) 137
6.13 Complex transfer impedances for the moveout survey in inline configuration (model parameter: elevation) 138
6.14 Direct comparison between CR and DC resistivity data: moveout survey in equatorial configuration 140
6.15 Direct comparison between CR and DC resistivity data: moveout survey in inline configuration 141
6.16 Directional survey to determine the azimuthal variation of the transfer impedance 143
6.17 Transfer impedances for the directional survey in parallel configuration (model parameter: resistivity) 145
6.18 Transfer impedances for the directional survey in parallel configuration (model parameter: elevation) 146
6.19 Transfer impedances for the directional survey in perpendicular configuration (model parameter: resistivity) 147
6.20 Transfer impedances for the directional survey in perpendicular configuration (model parameter: elevation) 148

7.1 Positional errors in apparent resistivity profiles arising from variations in towing speed during constant-frequency sampling 154
7.2 Configuration of a towed CR array with one transmitter and multiple receivers in dipole-dipole geometry 156

7.3 3D distribution of DC sensitivity for the inline dipole-dipole array in a homogeneous halfspace . . . 158
7.4 3D distribution of DC sensitivity for the equatorial dipole-dipole array in a homogeneous halfspace . . . 159
7.5 Components of the OhmMapper™ system . . . 161
7.6 The OhmMapper™ system in field operation . . . 161
7.7 OhmMapper™ apparent resistivity profile on grass (BGS test site) 163
7.8 OhmMapper™ apparent resistivity profile over an abandoned mineshaft (Minnie Pit, Silverdale) . . . 163
7.9 OhmMapper™ apparent resistivity profile on a dirt track (British Gas site, Aylestone Road, Leicester) . . . 164
7.10 OhmMapper™ apparent resistivity profile on a tarmac road (British Gas site, Aylestone Road, Leicester) . . . 164
7.11 OhmMapper™ repeatability test . . . 165
7.12 Correlation between repeated OhmMapper™ profiles . . . 165
7.13 Components of the CORIM™ system . . . 168
7.14 The CORIM™ system in field operation . . . 168
7.15 CORIM™ apparent resistivity profile on grass (BGS test site) . . 169
7.16 CORIM™ apparent resistivity profile on grass affected by towing noise (Chetwynd Barracks training site) . . . 170
7.17 CORIM™ apparent resistivity profile on grass/concrete over a void (EIGG test site) . . . 172
7.18 CORIM™ apparent resistivity profile on a tarmac road (BGS site) 173
7.19 CORIM™ apparent resistivity profile on reinforced concrete (Avenue coking plant, Chesterfield) . . . 174
7.20 CORIM™ repeatability test . . . 176
7.21 Detail of Rx 2 ($r = 2$ m) for the CORIM™ repeatability test . . . 177
7.22 Correlation between repeated CORIM™ profiles . . . 177
7.23 The BGS CRI system in field operation on a tarmac road 179
7.24 Geometry of the BGS CRI system in a towed-array setup 179
7.25 Geometry of the shallow concrete target at the BGS test site . . 180
7.26 CRI apparent resistivity profile on grass (BGS test site), Rx 1 . . 181
7.27 CRI apparent resistivity profile on grass (BGS test site), Rx 2 . . 182
7.28 Vertical layering of the sub-base of a road at the BGS site 183
7.29 CRI apparent resistivity profile on a tarmac road (BGS site), Rx 1 184
7.30 CRI apparent resistivity profile on a tarmac road (BGS site), Rx 2 185
7.31 CRI repeatability test . . . 187
7.32 Correlation between repeated CRI profiles . . . 188
7.33 Comparison between a CRI profile over the shallow concrete target and the corresponding DC resistivity traverse . . . 189
7.34 Evaluation of CR noise data: CORIM™ potentials measured without current injection (Tx off) . . . 191
7.35 Statistical distribution of CORIM noise data . . . 192
7.36 Predictive filtering of CR profile data contaminated by noise spikes 194
7.37 Comparison between conventional and predictive filtering of CR profile data . . . 195

7.38 Elementary line-based statistics for the towed-array CR survey at Chetwynd Barracks . . . 197
7.39 Histogram of apparent resistivities for the towed-array CR survey at Chetwynd Barracks . . . 197
7.40 Apparent resistivity map (raw data) obtained from a towed-array CR survey at Chetwynd Barracks . . . 198
7.41 Apparent resistivity map of the Chetwynd Barracks site after empirical levelling . . . 199
7.42 Decorrugated apparent resistivity map of the Chetwynd Barracks site after micro-levelling . . . 201

8.1 Distribution of datum points in the distance-pseudodepth plane as obtained with fixed-electrode and towed-array data acquisition 206
8.2 Lateral coincidence between datum points in the distance-pseudo-depth plane for a towed CR array . . . 209
8.3 Compilation of overlapping measurements for the construction of a VES curve from multi-offset towed-array CR data . . . 211
8.4 The principle of Zohdy's inversion algorithm . . . 213
8.5 Example of Zohdy's inversion applied to a VES curve derived from CR data . . . 216
8.6 Cross-section through the resistivity model of a shallow vertical contact . . . 217
8.7 Quasi-2D interpretation of synthetic towed-array CR data with CORIM™ geometry . . . 218
8.8 Quasi-2D interpretation of synthetic towed-array CR data with added Gaussian noise . . . 219
8.9 Quasi-2D interpretation of towed-array CR field data acquired with the CORIM™ system . . . 222
8.10 Example of model discretisation for the 2D inversion of towed-array CR data. . . . 226
8.11 2D inversion of synthetic towed-array CR data (CORIM™ geometry) for a shallow vertical contact . . . 227
8.12 Example of model discretisation for the 2D inversion of CORIM™ field data . . . 229
8.13 2D inversion of CORIM™ field data, Chetwynd Barracks . . . 230
8.14 One-pass 2D inversion of PACES data by multichannel deconvolution . . . 232
8.15 Example of parallel survey lines covering a regular grid of electrode/sampling positions . . . 234
8.16 3D towed-array CR survey on parallel lines representing a regular grid of electrode positions and sampling locations . . . 234
8.17 Continuous survey path for a bi-directional 3D towed-array CR survey using Real-Time Kinematic Differential GPS positioning . 235
8.18 Model of a unit cube embedded in a homogeneous halfspace . . . 237
8.19 Model response from a resistive unit cube for a towed CR array with CORIM™ geometry . . . 238

8.20 Model response from a conductive unit cube for a towed CR array with CORIM™ geometry 239
8.21 Horizontal depth sections of the 3D resistivity model for the resistive unit cube 241
8.22 Vertical cross-sections of the 3D resistivity model for the resistive unit cube 242
8.23 Horizontal depth sections of the 3D resistivity model for the resistive unit cube with 5% Gaussian noise 243
8.24 Vertical cross-sections of the 3D resistivity model for the resistive unit cube with 5% Gaussian noise 244
8.25 The EIGG geophysical test site at Southmeads Road, Leicester . 246
8.26 The CORIM™ system in field operation on the EIGG test site . . 247
8.27 Example of an apparent resistivity profile recorded at Area 8 of the EIGG test site 248
8.28 3D resistivity model of Area 8 of the EIGG test site: horizontal depth sections, layers 1–4 249
8.29 3D resistivity model of Area 8 of the EIGG test site: horizontal depth sections, layers 5–7 250
8.30 3D resistivity model of Area 8 of the EIGG test site: vertical cross-sections ($y = 14.5\,\mathrm{m} \ldots 18.25\,\mathrm{m}$) 251
8.31 3D resistivity model of Area 8 of the EIGG test site: vertical cross-sections ($y = 18.25\,\mathrm{m} \ldots 22.0\,\mathrm{m}$) 252
8.32 3D resistivity model of Area 8 of the EIGG test site: vertical cross-sections ($y = 22.0\,\mathrm{m} \ldots 25.75\,\mathrm{m}$) 253
8.33 3D tomogram of Area 8 of the EIGG test site, showing the resistivity iso-surface for $\rho = 28\,\Omega\mathrm{m}$ 254

B.1 The principle of ECT sensors 285
B.2 Schematic representation of the sequential sampling of ECT electrodes 285

List of Tables

2.1 Summary information on the most commonly used surface and airborne geophysical methods 8
2.2 Types of geophysical targets in environmental and engineering site investigations 14

3.1 Resistivity and non-resistivity electrical methods in environmental and engineering geophysics 19
3.2 Effective (median) depths for relevant array types 34
3.3 Commercial conductivity meters and their frequencies of operation 44

4.1 Specifications of existing CR instruments 59
4.2 Numerical values of K for a range of array parameters 70
4.3 Range of possible values for the generalised frequency Ω 76

5.1 The electromagnetic spectrum at radio frequencies 92
5.2 Spectrum of man-made VLF transmissions relevant to CR 93

7.1 Dimensions of the CORIM™ system and effective depths of investigation 168
7.2 Dimensions of the BGS CRI system and effective depths of investigation 178

8.1 Spacings at which CORIM™ VES curves were resampled to match the six-point forward filter 216
8.2 Approximate ground lithology at Chilwell Barracks at the bottom of the slope 221
8.3 Suitable layer parameters for inversion of CORIM™ data using RES2DINV 228
8.4 Number of iterations and RMS error values for the inversion of synthetic CORIM™ data over a shallow vertical contact 228

List of abbreviations

AC	Alternating current
CR	Capacitive Resistivity
CRI	Capacitive Resistivity Imaging
CST	Constant Separation Traversing
CVES	Continuous Vertical Electrical Sounding
DC	Direct current
DIC	Depth of investigation characteristic
ECT	Electrical Capacitance Tomography
EM	Electromagnetic
ERT	Electrical Resistivity Tomography
GPR	Ground-Penetrating Radar
GPS	Gobal Positioning System
HCPL	Horizontal coplanar loops
HED	Horizontal electric dipole
HMD	Horizontal magnetic dipole
IP	Induced Polarisation
MCD	Multichannel Deconvolution
MERIT	Magneto-Electrical Resistivity Imaging Tool
MMR	Magnetometric Resistivity
MT	Magnetotellurics
NAPL	Non-aqueous phase liquid
NDIC	Normalised depth of investigation characteristic
PA-CEP	Pulled-Array Continuous Electrical Profiling
RMS	Root-Mean-Square
SIP	Spectral Induced Polarisation
SP	Self-Potential
VCAL	Vertical coaxial loops
VCPL	Vertical coplanar loops
VED	Vertical electric dipole
VES	Vertical Electrical Sounding
VLF	Very low frequency
VLSI	Very large-scale integration
VMD	Vertical magnetic dipole

Glossary of notation

Symbol	Description	Unit
B	Induction number	
$\mathbf{B}$	Magnetic induction	[Wb/m^2]
C	Capacitance	[F]
$\mathbf{D}$	Dielectric displacement	[Cb/m^2]
$\mathbf{E}$	Electric field	[V/m]
$\mathbf{F}$	Smoothing matrix	
$\mathbf{H}$	Magnetic field intensity	[A/m^2]
I	Electric current	[A]
$\mathbf{I}$	Identity matrix	
$\mathbf{J}$	Jacobian matrix	
J_n	Bessel function of 1st kind, order n	
K	Geometric factor	[m]
L	Scale length	[m]
Q	Electrostatic charge	[Cb]
R	Resistance	[Ω]
V	Electric potential	[V]
X	Reactance	[Ω]
Y_n	Bessel function of 2nd kind, order n	
Z	Electric impedance	[Ω]
a	Array "a"-spacing	[m]
d	Elevation; distance	[m]
f	Frequency	[s^{-1}]
$\mathbf{f}$	Model response vector	
$\mathbf{g}$	Discrepancy vector	
h	Elevation	[m]
i	Imaginary unit	
$\mathbf{j}$	Electric current density	[A/m^2]
k	Wave number	[m^{-1}]
n	Array "n"-factor	
l	Dipole length	[m]
$\mathbf{q}$	Model parameter vector	
r	Dipole separation; distance	[m]
s	Coil spacing; distance	[m]
Δs	Sampling distance	[m]
t	Time	[s]

Symbol	Description	Unit
x	Cartesian coordinate; position	[m]
y	Cartesian coordinate; position	[m]
$\mathbf{y}$	Observed data vector	
z	Depth; elevation	[m]
Ω	Generalised frequency	
Π	Helmholtz potential	
Φ	DC sensitivity	[A/m]
α	Dielectric factor	
δ	Skin depth	[m]
ε	Dielectric permittivity	[F/m]
ε_0	Permittivity of free space	[F/m]
ε_r	Relative permittivity	
η	Electric charge density	[Cb/m^3]
λ	Eigenparameter of the Bessel functions, damping factor	
μ	Magnetic permeability	[H/m]
μ_0	Magnetic permeability of free space	[H/m]
φ	Phase angle	
ϕ	Azimuth	
ρ	Electrical resistivity	[Ωm]
ρ_a	Apparent resistivity	[Ωm]
σ	Electrical conductivity	[S/m]
ω	Angular velocity	[s^{-1}]
∇	Nabla operator	

Chapter 1

Introduction

1.1 Background and scope of research

The non-intrusive characterisation of the shallow subsurface is nowadays routinely carried out on the basis of geophysical observations. Geophysical methods have been successfully applied to a wide range of problems in the environmental, engineering and groundwater sectors over many years. Among the many methods available, investigation of the electrical properties of the ground has proven to be highly effective in a variety of contexts. Electrical resistivity, in particular, is a versatile physical parameter because of its diagnostic qualities. The traditional methodology of measuring resistivity is based on passing a direct current into the ground between a pair of galvanic probes, with the resulting potential being observed at a distance by means of a second pair of probes. Historically, the interpretation of DC resistivity data was often geared towards geological structures and initially limited to simplistic 1D or 2D earth models. However, the development of advanced field procedures and sophisticated interpretation schemes in recent years have made "electrical imaging" possible, i.e. the generation of tomographic images of the subsurface from multiple resistivity measurements. With its ability to assess complex structures in the subsurface, this methodology has become an invaluable tool for environmental and engineering site investigations.

Evermore geophysical surveys in the UK and other countries are carried out on sites in the urban built environment, for example on derelict or contaminated land, industrial sites, collieries, gas works or landfills. The nature of such sites and their associated infrastructure implies that conventional DC resistivity is not always applicable and a need has arisen for electrical techniques better adapted to such conditions. The problems encountered are twofold. On the one hand, many sites in the built environment are highly engineered and comprise large sealed areas such as pavements, roads and runways with artificial surfaces such as tarmac or concrete. Their presence rules out the use of conventional DC resistivity because the mechanical installation of electrodes would be difficult if not impossible. Even in cases where probes can be deployed, resistivity measurements are often inaccurate due to the high contact impedances caused

by resistive surface materials such as concrete or tarmac. On the other hand, environmental and engineering site investigations are often faced with a complex subsurface where the spatial distribution of electrical properties may be highly irregular. As a consequence, dense spatial sampling and efficient procedures for data acquisition, processing and interpretation are required. While processing and interpretation techniques for DC resistivity data have become increasingly sophisticated in recent years, data acquisition has remained comparatively cumbersome since electrodes must still be manually implanted and moved between their respective positions.

1.2 Aims and objectives

This thesis investigates a novel geophysical technique which has the potential to overcome the problems described and may complement DC resistivity in environments where the need for galvanic coupling currently inhibits the application of electrical imaging methodologies. The "capacitive resistivity" technique (CR) is a specific realisation of a general electromagnetic (EM) measurement based on capacitive coupling between sensors and the ground. It is associated with a low induction number mode of operation and quasi-stationary fields.
Although the concept of CR is not entirely new and its origins can be traced back as far as the 1970s, it is only now that the technique is beginning to be more comprehensively understood; however its full potential in the context of environmental and engineering site investigations has yet to be recognised. As a general aim, this thesis seeks to instigate this process by presenting a full appraisal of all aspects of the technique. The context in which this assessment is undertaken is the potential use of CR for geophysical site investigations in the built environment. The scope of the thesis and main research objectives are:

1. to investigate the fundamental concepts of the CR technique and prove their practical validity by experiment,
2. to provide a unified description of CR, including its physical principles, their theoretical formulation and practical implementation in geophysical instruments,
3. to determine a valid range of system design parameters for practical CR measurements and to study the effect of variations in these parameters on the results,
4. to examine the operational characteristics of CR instruments for dynamic measurements with towed arrays,
5. to establish suitable procedures for the acquisition, processing and interpretation of CR data in 2D and 3D surveys, and
6. to evaluate the use of high resolution multi-offset towed-array datasets for electrical resistivity tomography (ERT).

These objectives are reflected in the following thesis structure.

1.3 Thesis structure

Chapter 2 of this thesis is intended to "set the stage" for the technical content by illustrating the context in which the research was carried out. Firstly, background information on geophysical methodologies in environmental and engineering site investigations is provided. The non-specialist reader is introduced to terminology, relevant methods and their applications. Secondly, the role of geophysical surveying in the site investigation process is addressed. It is shown that all stages of a typical site investigation may benefit from the application of geophysical methods. A comparison between geophysical and conventional (intrusive) techniques shows their advantages, disadvantages and limitations. Typical geophysical targets encountered during site investigations are discussed. The UK's contaminated land regime and geohazards are then cited as examples for fields of application in which the application of geophysical methods can add value to environmental and engineering site investigations. Finally, the particular relevance of electrical methods is discussed.

Chapter 3 reviews conventional methods allowing the measurement of electrical resistivity. DC resistivity as the most widely used technique is based on stationary flow of electric current. Its basic theory, field techniques, data processing and interpretation schemes are described. A thorough understanding of DC resistivity is essential because the CR measurement can be regarded as a generalisation of the DC method. Many aspects of the two methodologies are similar and under certain conditions, well-known DC interpretation schemes may be directly applied to CR data. Resistivity methods based on electromagnetic induction are introduced subsequently, including the ground conductivity technique which is based on inductive coupling between pairs of coils. It typically operates at low induction numbers, making it a close relative of the CR technique. Other techniques include plane-wave EM (VLF, MT) and magnetometric resistivity. Finally, conventional resistivity methods are compared and critically discussed.

The capacitive resistivity (CR) technique is introduced in Chapter 4. Firstly, the history of CR and previous research are reviewed. The fundamental concepts of the technique such as the capacitive electrode, the capacitive four-point array and different sensor types are discussed. Existing CR instruments are classified and a comprehensive list of such systems is provided. Early CR theory based on the use of capacitive line antennas is subsequently presented. The quasi-static formalism based on Grard's (1990a) concept of the electrostatic quadrupole is the relevant theoretical framework for this thesis. A detailed derivation and structured discussion of the complex transfer impedance is presented. The formulation is valid for point poles and low induction numbers. Subsequently, a new phase-sensitive expression for apparent resistivity is developed. If conditions are such that the quasi-static approximation does not apply to a CR measurement, a full EM formulation of CR is more appropriate. For this purpose, the generic forward problem of a horizontal electric dipole above a layered earth is solved.

Chapter 5 comprises a systematic parameter study in which the practicality of CR measurements under quasi-static conditions is examined. The quasi-static formalism is used to calculate a predicted system response. Firstly, the variation with frequency is considered, keeping in mind that both transfer impedance and sensor capacitance are functions of frequency. Potential interference from ambient EM signals must also be taken into account, hence the conditions for operation of CR instruments in the UK are examined. Secondly, the functional dependence of the transfer impedance of array separation, sensor elevation and subsurface resistivity is studied. Thirdly, capacitance modelling is used to assess the influence of sensor design, and the implications for the two generic sensor types are discussed.

In Chapter 6, a series of basic experiments is described which were undertaken to validate the fundamental concepts of CR. Parallel to this thesis, the British Geological Survey has developed a prototype CR instrument, which is introduced in the first part of the chapter. The BGS CRI system employs modern signal detection technology to measure the fully complex transfer impedance on multiple channels synchronously. The instrument was designed to test the concept of "capacitive resistivity imaging". Subsequently, the properties of real capacitive sensors are determined. Practical capacitance measurements are undertaken and the wideband reception properties of plate-wire sensors are assessed. The remaining part of the chapter describes elementary surveys for the spatial analysis of the complex transfer impedance. These experiments are used to verify the predictions of the quasi-static formalism.

A key characteristic of the CR technique is that it facilitates a dynamic mode of operation. Chapter 7 examines the use of towed arrays for CR measurements. Such measurements yield a novel type of geophysical data with distinctive attributes. In the first part of the chapter, the fundamental concepts of towed-array acquisition are discussed. Subsequently, the operational characteristics of towed CR arrays are studied. The performance of existing commercial instruments is compared with that of the BGS CRI system. Finally, basic processing techniques for towed-array CR data are investigated. Key topics are the suppression of motion-induced noise and the correction of levelling errors.

Chapter 8 examines how high-resolution multi-offset towed-array CR can be used for electrical imaging. The introductory part of the chapter discusses the properties of multi-offset towed-array data and the basic requirements to enable "capacitive resistivity imaging". Subsequently, procedures for the interpretation of datasets with increasing complexity are outlined. The schemes discussed include quasi-2D interpretation using continuous vertical electrical soundings in combination with a fast 1D inversion technique, and 2D and 3D interpretation by means of iterative least-squares resistivity inversion. All variants are illustrated by examples comprising synthetic as well as field datasets.

Chapter 9 summarises the conclusions drawn from this research and outlines further work which may arise from the findings of this thesis.

Chapter 2

Geophysics in environmental and engineering investigations

2.1 Environmental and engineering geophysics

In recent years, the use of geophysical methods for environmental and engineering applications has gained a wider acceptance than ever before. At the same time, the diversity of techniques, the use of varying terminology to describe the same method and the varying degrees of proficiency required for the interpretation of different types of geophysical data is likely to cause confusion amongst an increasingly non-specialist user community. It is therefore deemed beneficial to define the terminology and introduce basic concepts and methods of environmental and engineering geophysics in the context of site investigations.

2.1.1 Terminology

Over the last three decades, increasing demand within the environmental and engineering sectors for new, non-intrusive site investigation techniques to complement intrusive methods has led to the evolution of environmental and engineering geophysics as relevant sub-disciplines of applied geophysics (e.g. Reynolds, 1997). Both subjects study the the shallow subsurface as the part of the earth that is or has been directly impacted by or has impacts on human activities. Although both sub-disciplines have a lot in common, their individual objectives are quite distinct. "Engineering geophysics" is described by Sheriff (1991) as

> *"the application of geophysical methods to the investigation of subsurface materials and structures which are likely to have (significant) engineering implications."*

Typical applications in engineering geophysics are for example the detection of buried objects, services and cavities, assessments of the integrity of engineered structures such as roads, bridges, foundations, walls and dams or the stability of slopes. "Environmental geophysics" emerged during the late 1980s and early 1990s, along with increased public concern about the environment and the

process of tightening environmental legislation in many countries. The term has been defined by Sheriff as

> *"the application of geophysical methods to the investigation of near-surface physico-chemical phenomena which are likely to have (significant) implications for the management of the local environment."*

Typical applications of environmental geophysics are for example the detection and mapping of contaminants and pathways for their migration, landfill leachate or pollution plumes, particularly in the context of derelict and contaminated land investigations.
In practice there are situations where considerable overlap exists between the two subjects, i.e. the investigation of a specific site may comprise engineering as well as environmental aspects. Moreover, many geophysical methods have been successfully employed in the context of both sub-disciplines. As this thesis is concerned with the development of a generic geophysical technique, one of the aims is to find out its potential applications in different contexts.

2.1.2 Relevant methods

Geophysical methods can be broadly grouped into three categories: surface, airborne and downhole methods. Only airborne and surface geophysical techniques can be regarded as non-destructive in the sense of the discussion in the following section. Although downhole techniques have developed rapidly over recent years, particularly due to the success of tomographic imaging methods, they involve boreholes and are therefore intrusive. Table 2.1 shows the most commonly used surface and airborne geophysical methods, along with their capabilities regarding the potential detection of typical environmental targets, their typical penetration depths and relative cost. All geophysical measurements rely on specific physical properties of the earth and before any geophysical surveying is considered, it is highly important to identify the appropriate physical, chemical or geotechnical parameters which are deemed to provide the most relevant information about a particular problem on a site under investigation. One should also bear in mind that it is often contrasts due to spatial variation in those parameters that geophysical methods are sensitive to.

Electric and electromagnetic. Electric and electromagnetic methods make use of electromagnetic energy in various parts of the spectrum and include a wide range of techniques which have proven to be extremely useful for environmental and engineering applications. The relevant physical parameters are electrical resistivity (or conductivity) and dielectric permittivity. Resistivity is a fundamental and diagnostic property that can be determined with a range of alternative techniques. It is linked with geotechnical parameters such as porosity, permeability or moisture content and hydrological parameters such as hydraulic conductivity and can therefore be used to indirectly determine those properties.

Technique	Can detect:				Penetration depth [m][a]	Cost[b]
	Soils/ geology	Leachate	Buried wastes	NAPLs		
Surface electrical and electromagnetic methods						
Self-potential	yes	yes (C)	yes	no	S ?	L
DC resistivity*	yes	yes (C)	yes	possibly	S 60 km	L-M
Induced Polarisation	yes	yes (C)	yes	possibly	S km	L-M
Complex resistivity	yes	yes (C)	yes	yes	S km	M-H
Electromagnetic induction*	yes	yes (C)	yes	possibly	S 60/C 15	L-M
Transient electromagnetics	yes	yes (C)	yes	no	S 150	M-H
Metal detectors	no	no	yes	no	C/S 0-3	L
VLF-resistivity	yes	yes (C)	yes	no	C/S 20-60	M-H
Magnetotellurics	yes	yes (C)	no	no	S 1000+	M-H
Ground penetrating radar*	yes	yes (C)	yes	yes	C 1-25 (100s)	M
Surface seismic and acoustic methods						
Seismic refraction*	yes	yes	no	no	S 1-30	L-M
Shallow seismic reflection	yes	no	no	no	S 10-30	M-H
Continuous seismic profiling	yes	no	no	no	C 1-100	L-M
Seismic shear/surface waves	yes	no	no	no	S 2 10s-100s	M-H
Surface potential field methods						
Magnetometry*	no	no	yes (F)	no	C/S 0-20[c]	L-M
Gravity	yes	yes	no	no	S 100s+	H
Other surface geophysical methods						
Radiometry	no	no	yes (N)	no	C/S n/s	L
Airborne geophysics						
Airborne electromagnetics	yes	yes (C)	yes	possibly	0-100	M
Aeromagnetics	yes	no	yes	no	10s-100s	M

* = most commonly used methods at contaminated sites
(C) = detectable if contaminant(s) change electrical properties of ground water; (F) = ferrous metals only; (N) = nuclear
[a]: S = station measurement; C = continuous measurement. Depths are for typical shallow applications. n/s = near surface.
[b]: Ratings are very approximate. L = low; M = moderate; H = high.
[c]: For ferrous metal detection; greater depths possible for larger masses of metal.

Table 2.1: Summary information on the most commonly used surface and airborne geophysical methods (After U.S. Environmental Protection Agency, 1993).

Seismic and acoustic. Seismic and acoustic methods make use of acoustic energy and are particularly useful in engineering applications. They can be divided into refraction and reflection methods. While refraction seismics has historically been the preferred choice in shallow site investigations, there has been a major shift since the 1980s towards using high-resolution seismic reflection surveying for this purpose. The physical properties relevant to seismic methods are the elastic wave velocities and related parameters such as elastic moduli and density. Seismic attenuation can give information about petrophysical properties. Shear and surface wave techniques are also commonly used for geotechnical assessments.

Potential field. Potential field methods make use of the Earth's magnetic and gravitational fields and are used both for mapping and locating purposes. Magnetic methods are based on measurements of the flux density of the geomagnetic field, which is affected by the magnetic susceptibility of geological or man-made materials. Gravity methods are based on measurements of acceleration due to gravity, which is affected by density variations in the subsurface. On a site investigation scale, high-resolution microgravity surveys are usually required.

2.1.3 Literature

The portfolio of geophysical techniques is vast and a detailed discussion of geophysical methodology is clearly beyond the scope of this thesis, except where it is directly relevant to the research conducted. The reader is referred to the extensive literature on applied geophysics in general and environmental and engineering geophysics in particular. A large number of textbooks on applied geophysics is available, for example Dobrin and Savit (1988), Telford et al. (1990) or Parasnis (1997). A number of textbooks describe geophysical techniques specifically in the context of engineering and environmental applications, for example the books by Ward (1990), Vogelsang (1995) and Reynolds (1997). Government institutions, professional associations and other public bodies have published their own documentation on the use of geophysics for environmental and engineering applications. A very comprehensive guidance document on the use of geophysical techniques at "contaminated sites" has been published by the U.S. Environmental Protection Agency (1993). It contains an extensive bibliography on individual techniques and case histories. The book by McCann et al. (1997), published by the Geological Society of London, contains a spectrum of applications and case studies in engineering geophysics. The Construction Industry Research and Information Association (CIRIA) has published comprehensive guidance about the role of geophysics in engineering investigations (McDowell, 2002). This document represents a revised and updated version of an earlier report by the Geological Society Engineering Group Working Party (Anon, 1988).

2.2 Site investigation and geophysics

2.2.1 Terminology

The concepts of sustainability and risk prevention play an increasingly important role in the decision-making process of many modern societies today. One of the practical consequences of such political change is an increased demand for accurate and reliable site investigations, for example as part of the redevelopment of contaminated and derelict land or the detection of geohazards (cf. Section 2.3). However, the importance of site investigations is not restricted to remedial action alone. The construction, maintenance and monitoring of facilities that constitute the infrastructure of today's industrialised countries (e.g. roads, buildings, plants, dams, landfills etc.) creates a constant need for increasingly detailed non-destructive investigations of highly engineered sites and structures from the very early stages of planning throughout the entire lifespan of these installations.
The term "site investigation" has a specific meaning in the context of environmental and engineering assessments. It summarises the procedures undertaken to assess a site with regard to

- its suitability for a particular purpose (e.g. the construction of civil engineering and building works),
- any risk that may be associated with the site (e.g. due to pollution or other hazards) or
- the structural integrity of the site (e.g. roads, dams, landfills).

Full-scale site investigations are subject to a certain degree of standardisation as government departments and professional bodies have published specifications and guidance documents. A code of practice has been established by the British Standard BS 5930 (Anon, 1999), which was written from the point of view of civil engineering, but is widely accepted also in other areas. A separate, more specific document covers site investigations of contaminated land (Anon, 2001). It should be appreciated that a site investigation does not just comprise the collection of data, but also wider aspects such as the development, testing and refinement of conceptual models, the assessment and management of risk, and the management of health and safety aspects. Site investigations are commonly undertaken in a phased approach:

- Phase 1: Desk study, site reconnaissance, walk-over surveys
- Phase 2: Detailed investigation
- Phase 3: Review, follow-up investigations, verification, appraisal of performances, monitoring

The majority of the fieldwork is typically carried out during Phase 2 of the investigation.

2.2.2 The value of geophysical information

Tighter economic constraints require environmental and engineering site investigations to be carried out more efficiently and cost-effectively in order to achieve cost benefits. While the risk due to the uncertainty in ground conditions can be somewhat reduced by the adoption of modern management methodologies, there is a clear recognition in the geotechnical industry that overall economy in large engineering projects can only be realised if thorough high quality site investigations are carried out (Everton, 1998). Inadequate site investigation can lead to significant delays and escalating cost. The scale of this problem in the UK was demonstrated by Littlejohn (1991) using several examples from the construction industry. Littlejohn emphasized the importance of a well-planned, comprehensive site investigation process.

The application of geophysical methods to environmental and engineering site investigations has enormous potential for improving both the quality and the efficiency of the process. Geophysical surveys can produce useful information at all times throughout the life cycle of a site investigation. Geophysics is an ideal reconnaissance tool and the greatest savings in time and cost due to the use of geophysical methods are often achieved in the early stages of a site investigation (Reynolds, 1998; Soudain, 1998). Many geophysical techniques are suitable for use in a walk-over survey (Phase 1). One of the most important applications of geophysical methods is to provide initial datasets with comprehensive areal coverage to locate anomalies ("hotspots"), to define sampling locations or to guide the siting of boreholes or trial pits for detailed intrusive investigation (Phase 2). Repeated geophysical surveys or time-lapse experiments can be extremely useful to verify the objectives of a site investigation, for example that remedial action has succeeded, or for the purposes of long-term monitoring (Phase 3).

Evidence of the growing importance of geophysics in site investigations can be seen in the discussion related to the recent revision of BS 5930 (Anon, 1999, 2000) and other guidelines (Anon, 1988; McDowell, 2002). Soudain (1998) acknowledged that geophysics in site investigation has "undergone somewhat of a revolution, with new methods that are more applicable to shallow investigations on land". Reynolds (1998) stresses the "effectiveness of using properly designed geophysical surveys as part of a comprehensive site investigation strategy" and concludes that "geophysical methods, where appropriate, should complement direct methods of investigation". Walter (2001), quoting Watson, observes that more and more civil, structural, geotechnical and environmental engineers are beginning to recognise the value of geophysics. The author points out that, contrary to the perception of geophysical investigation being expensive, if it is applied on a potentially contaminated site it could help prevent problems which may be expensive to solve later on.

2.2.3 Geophysics versus conventional techniques

Conventional site investigation techniques are well established and commonly based on direct investigation by intrusive sampling. Intrusive sampling is typically undertaken by means of boreholes, probes, trial pits, penetrometer tests or water and gas sampling. In effect, direct methodologies can only provide spot measurements or one-dimensional data such as borehole logs (Barr et al., 2002). However, the interpretation of site investigation data is often used as a basis for the assessment of risk or may have implications on matters of statutory liability, hence areal coverage and spatial resolution are vital factors for a meaningful site investigation. The inherent level of uncertainty associated with the use of spot measurements is undesirable and can only be reduced by increasing the number of samples taken.
In contrast to the direct approach, geophysical techniques are indirect and non-invasive. The benefits of geophysical investigation are the following:

- The ground is sampled volumetrically, even if measurements are taken at discrete stations. Provided they are detectable, anomalies in the physical properties of the subsurface (e.g. due to pollutants, structural weaknesses etc.) are therefore less likely to be missed by a geophysical survey than by drilling.
- A geophysical survey provides rapid areal coverage and high spatial resolution.
- 2D and 3D datasets, which are now commonplace, can give detailed information about a site even if the subsurface is highly complex.
- Geophysical investigation can provide quantitative data on mass characteristics in-situ. Geotechnical and hydrological parameters can be derived from geophysical data at much higher resolutions than could be achieved by direct sampling.
- Geophysical techniques are environmentally benign due to their non-invasive (and hence non-destructive) nature.
- In contrast to intrusive methods, the application of geophysical techniques does not disturb, exacerbate or remobilise buried contaminants.
- Geophysical methodology facilitates repeat measurements over time to monitor amounts and rates of change (e.g. time-lapse imaging). 4D surveys have become state-of-the-art in environmental and engineering geophysics.
- Geophysical investigation tends to reduce the Health & Safety risk to field operatives by reducing their potential exposure to contaminants during intrusive investigation.

However, the application of geophysical methods should not be regarded as universal remedy to any site investigation problem. The use of geophysics

in site investigations is not always perceived as a success and there is still a certain amount of distrust of geophysics amongst the potential user community. The reasons for this distrust include excessively high expectations, the lack of technical appreciation with regard to geophysical methodology and the lack of adequate calibration of indirect measurements (Rankin quoted by West, 1997). Failure of geophysics can be due to the inappropriate selection of techniques, unfavourable geological conditions or excessive levels of cultural noise.

2.2.4 Types of geophysical targets

A particular challenge to geophysical methodology is the wide variety of materials encountered in environmental and engineering investigations. Geophysical methods tend to work well on undisturbed geology (i.e. on greenfield sites). Yet the very nature of environmental and engineering investigations implies the use on brownfield (i.e. previously developed) sites or engineered structures. Thus, a far greater range of materials may be geophysical targets. These materials include made ground, solid objects, waste products and liquids other than groundwater. Table 2.2 lists some of the relevant types of targets together with their associated physico-chemical parameters and possible geophysical methods for their investigation (cf. Reynolds, 1998). This list is non-exhaustive and the suggested choice of method is only indicative.

Made ground often comprises reworked geological materials whose physical properties will be different to those of the virgin formation. However, man-made materials such as waste or demolition rubble are also frequently used as backfill. Solids can range from building materials such as concrete and asphalt (including foundations) to buried objects such as tanks, pipes, cables or drums. Subsurface voids and cavities (natural or engineered) are also common targets. A wide range of waste products may be encountered on landfills or other brownfield sites, including residue from industrial processes (e.g. ash, slag, tar) and other domestic or industrial waste. Many environmental assessments are concerned with liquids other than groundwater, such as leachates, hydrocarbons, and NAPLs[1] (e.g. solvents). Typical examples are the detection of leaks and spillages from storage tanks or leachate migration from landfills.

This enormous variety of potential targets underlines the importance of selecting the appropriate geophysical method (or suite of methods) for a given site and task. The choice often depends on the amount of existing knowledge about the site. Geophysics can be usefully employed as a reconnaissance tool, particularly if information about the site history is sketchy and previous uses are unknown. It is then important to appreciate that the application of one particular method may not be able to reveal all possible targets and thus may not cover all aspects of a particular site investigation. Geophysical methods often have the greatest impact when employed in combination with each other.

It is also important to consider not only the spatial distribution and extent of a particular target, but also the changes that may occur as a function of time, as for example by migration or attenuation of contaminants.

[1] Non-Aqueous Phase Liquids

Material type	Physico-chemical parameter	Geophysical methods
Made ground:		
Construction rubble, bricks etc.	Moisture content	Ground conductivity, resistivity
Railway ballast	Resistivity, susceptibility	Resistivity, magnetometry
Solid objects:		
Asphalt, tarmac, concrete	Moisture content, resistivity, permittivity	Resistivity, GPR
Foundations (reinforced concrete)	Conductivity, susceptibility	Ground conductivity, magnetometry
Pipes (metallic)	Conductivity, susceptibility	Ground conductivity, magnetometry
Pipes (asbestos cement, PVC)	Resistivity	Resistivity, ground conductivity
Steel drums	Conductivity, susceptibility	Ground conductivity, magnetometry
Voids and cavities:		
Air- or gas-filled voids	Mass deficit, resistivity, reflectivity	Gravity, resistivity, GPR
Waste products:		
Ash, clinker, slag, tar	Conductivity, susceptibility	Ground conductivity, magnetometry
Landfill wastes	Conductivity, susceptibility	Ground conductivity, magnetometry
Sewage	Conductivity, resistivity	Ground conductivity, resistivity
Liquids:		
Leachates	Conductivity, resistivity	Ground conductivity, resistivity, GPR
Hydrocarbons	Resistivity, permittivity	Ground conductivity, resistivity, GPR, SIP
LNAPLs	Resistivity, permittivity	Ground conductivity, resistivity, GPR, SIP
DNAPLs	Resistivity, permittivity	Ground conductivity, resistivity, GPR, SIP

Table 2.2: Types of geophysical targets in environmental and engineering site investigations (After Reynolds, 1998).

2.3 Fields of application in the UK

In this section, two relevant fields of application in the UK are discussed where geophysics can usefully contribute to the conduct and outcome of environmental and engineering site investigations. It is demonstrated that for the chosen examples the main impetus for the execution of a site investigation is of political, regulatory or economical nature. The number of potential cases and associated cost is such that they are likely to have a significant impact on the UK's economy.

2.3.1 The contaminated land regime

Environmental and engineering site investigations in the UK and worldwide are carried out for a variety of reasons. While many such investigations are commissioned out of individual necessity, a growing number are enforced by statutory requirements. The conception and execution of a site investigation can be part of a site appraisal governed by a regulatory framework on a national or indeed supra-national (e.g. European Union) level. An example for such a scenario in the UK is the contaminated land regime.

The UK has a substantial inherited legacy of land which has been contaminated in the past, for example by previous industrial, mining and waste disposal activities. Expert estimates of the extent of the problem range between 50,000 and 100,000 potentially contaminated sites across the UK, with the extent of land ranging between 100,000 and 200,000 ha (POST, 1993; Environment Agency, 2002). With effect from 1 April 2000, a new statutory regime for the identification and remediation of contaminated land has entered into force in England (DETR, 2000). For this purpose, Part IIA of the Environmental Protection Act 1990 (DoE, 1990) has come into operation. Part IIA was inserted into the 1990 Act by section 57 of the Environment Act 1995 (DoE, 1995).

The UK Government's approach to the remediation of contaminated land is based upon the principles of risk assessment and a "suitable for use" philosophy, which focuses on the risks to human health or the wider environment caused by land contamination. This is reflected in the statutory definition of contaminated land in section 57 of the 1995 Act, which includes the notion of "significant harm" and the "significant possibility" of such harm being caused (DoE, 1995). The "suitable for use" approach recognises that the risks presented by a given level of contamination will vary greatly according to the present or intended use of the land and a wide range of other factors, including the underlying geology of a site. Under the contaminated land regime, risks are therefore assessed on a site-by-site basis and land classification may change with the land use without a change in the substances (Nathanail, 1999). The primary regulatory role under Part IIA rests with local authorities who have a duty to inspect their areas for the purpose of identifying contaminated land and who are required to act in accordance with statutory guidance issued by the Secretary of State in determining what is "significant" in the context of the above definition. The statutory guidance uses the concept of a "pollutant linkage" which defines a relationship between the three elements "contaminant",

"pathway" and "receptor" (DETR, 2000). A piece of land is not regarded as contaminated land in the context of the regime, unless all three elements are identified and the linkage is defined. Under the provisions concerning liabilities, financial responsibility for remediation will largely follow the "polluter pays" principle (DETR, 2000). In the first instance, the person(s) who caused or knowingly permitted the contamination will be the appropriate person(s) to undertake the remediation and bear the costs, however responsibility may be passed on to the current owner or occupier of the land. The scale of the problem in the UK indicates that such procedures could have an enormous financial impact, not only on individuals but also on the economy as a whole.

In cases where an inspection of a piece of land by the local authority concludes that it is likely that a contaminant is actually present and that, given the current use of the land, a receptor is present or likely to be present, a full-scale site investigation may be authorised. A contaminated land site investigation is an integral part of the site-specific risk assessment and should only collect data required for this purpose to support the decision-making process. It would normally be driven by and seek to confirm a conceptual model of the site including the contaminant-pathway-receptor relationship. The significance of a conceptual model is also recognised in the British Standard BS 10175:2001 (Anon, 2001), which defines a code of practice for site investigations of potentially contaminated land. Although intrusive methods are the traditional mainstay of contaminated land site investigations due to frequent necessity of geochemical sampling, there is great potential for the efficiency and effectiveness of the process being improved by the application of geophysical techniques.

The first and foremost argument in favour of geophysics in the contaminated land context is that the nature of geophysical data is favourable to the risk-based philosophy. Site investigation results have a critical influence on risk management decisions hence reliability of interpretations is crucial. Geophysics can provide site-wide quantitative volumetric data with total coverage and at much higher resolution than intrusive techniques which can only provide spot measurements. Methods of interpolating between sparse borehole and trial pit data are notoriously unreliable (Reynolds, 1998). At the same time, the amount of information gathered during a site investigation should be enough to reduce unacceptable uncertainty in the conceptual model (Nathanail, 2001). Geophysics can be a cost-effective tool to help achieve this level of reliability. It can be used at all stages of the risk assessment, including initial walk-over surveys (Phase 1), full-scale site investigations (Phase 2) or long-term monitoring (Phase 3). Depending on the nature of the conceptual model, geophysics may be usefully applied to all three elements of the contaminant-pathway-receptor linkage: it can be used to establish the location, extent and possibly the nature of the contamination and to identify, map out and characterise potential migration pathways and environmental receptors (e.g. aquifers) in the subsurface. The advantages of geophysics listed under section 2.2.3 apply equally in a contaminated land context. A particularly important advantage is that the non-invasive character of surface geophysics prevents buried contamination being disturbed, exacerbated or remobilised. One of the dangers of using intrusive methods is that migration pathways for pollutants might be created by the site

investigation itself (e.g. drilling through otherwise low permeability geology). Due to the novelty of the regime and bearing in mind its statutory nature and potential legal implications, published case histories on the use of geophysics in contaminated land site investigations under the new regulations are virtually non-existent as yet. However, there is a vast number of case histories in the UK and abroad where geophysics has been successfully employed in circumstances and on sites which would now fall under the contaminated land regime in the UK. Many such case histories are listed in a guidance document by the U.S. Environmental Protection Agency (1993).

2.3.2 Geohazards

Geohazards are another important field of application in which a growing number of site investigations are conducted in the UK. Geohazards are geological or hydrological processes that pose a threat to people and their property, damage the environment, or cause excessive cost and disruption. They are a consequence of an adverse combination of ground conditions, often brought about by human activity, which result in a dangerous condition or failure. They may be natural or manmade and include regional-scale events such as earthquakes and volcanic eruptions and local-scale events such as landslides, subsidence and cavity collapses (e.g. sinkholes, mineshafts). Ice-rich ground is a significant geohazard in regions where climatic conditions result in the existence of permafrost (cf. Section 4.1.1).

The presence of mining-related cavities or weak zones in the rock mass is perhaps the most common geohazard in the UK. The UK has a long history of mining activities dating back more than 3000 years and many areas that have been undermined at some time in the past are now located in urban environments (Culshaw et al., 2000). The presence of abandoned mineshafts, bell pits or shallow workings and adits beneath a site can cause major problems for new developments or existing occupants of a site due to the risk of subsidence or collapse. In the UK, many coal workings developed prior to 1873 were never recorded, as it was not a legal requirement until after this date. Even workings abandoned after this date are very poorly recorded and it is not usually possible to establish their position with any confidence (Bishop et al., 1997). Natural cavities such as sinkholes, caverns and dissolution features occuring in karstic environments can cause similar problems.

An essential component of any site investigation in areas with a potential risk of encountering cavities should be the detection of these features. Traditional methods to locate shallow mine workings are based on intrusive investigation. Trial pits are dug or boreholes are drilled in a regular pattern to determine the spatial extent of the cavities (Healy and Head, 1984). This approach is clearly prohibitive if the size of the cavities is small compared to the size of the search area because small grid spacings are required to avoid missing a target. Geophysical methods are attractive as an alternative means to detect cavities such as abandoned shallow mine workings (Cripps et al., 1988). The cavity represents an anomaly in physical parameters such as density, resistivity or susceptibility, thus making it detectable by means of geophysical measurements.

2.4 The relevance of resistivity methods

Amongst the geophysical portfolio, electrical methods in general and resistivity methods in particular play an important role in environmental and engineering site investigations. The versatility of resistivity as a diagnostic parameter makes resistivity methods applicable to a large variety of problems. Non-contacting techniques such as ground conductivity (cf. Section 3.2) are extremely popular for reconnaissance purposes, for example to map out resistivity over large areas of a site and to locate anomalous areas. Galvanic techniques such as DC resistivity (cf. Section 3.1) are more laborious, but the stationary current flow bears some advantages, for example better depth discrimination.

A significant breakthrough for resistivity methods was the development of electrical resistivity tomography (ERT), which made resistivity imaging possible, i.e. the creation of 2D or 3D images of the subsurface (cf. Section 3.1.4). This technique is now being used extensively for site investigations in the environmental and engineering sectors. One of the standard applications is the detection and mapping of contaminants and associated pathways. Such investigations are typically carried out on contaminated and derelict land and the results may be highly relevant for risk assessments under the contaminated land regime (cf. Section 2.3.1). For example, ERT was used by Ogilvy et al. (1999, 2002) to image the leachate distribution in landfills. Chambers et al. (1999) used ERT to characterise buried waste deposits in 3D on a site which is likely to be classified as contaminated land under the new regime.

Resistivity methods have also been successfully employed in a geohazards context, particularly for cavity detection (cf. Section 2.3.2). ERT is suitable for this purpose as empty (air-filled) cavities have a higher resistivity than undisturbed ground, whereas flooded (water-filled) cavities would result in lower values. Ogilvy et al. (2001) have demonstrated that shallow mineshafts can be expected to be detectable with 3D ERT.

One of the objectives of this thesis is to demonstrate that the capacitive resistivity technique is capable of extending the applicability of ERT to areas where DC resistivity has so far been difficult if not impossible to use. ERT can rarely be employed for contaminated land or geohazard investigations in the urban built environment, where artificial surfaces prevent the use of the DC resistivity technique. It will be shown in the following chapters how CR can overcome this disadvantage of conventional ERT.

Chapter 3

Conventional resistivity methods

Throughout the history of geophysics, the application of electrical and electromagnetic methods has revealed a tremendous amount of information about the physical properties of the subsurface on a global, regional and local scale. These methods have proven to be equally powerful at a range of depths from hundreds of kilometres to the near-surface (say 0–10 m). The shallow end of this depth scale is of interest in environmental and engineering site investigations. A wide range of electrical methods is available, a subset of which is sensitive to electrical resistivity, a fundamental and diagnostic physical property (Table 3.1).
Electrical or electromagnetic methods that allow the direct or indirect measurement of resistivity are referred to as "resistivity methods". Two of the most frequently employed resistivity methods in site investigations are DC resistivity and the ground conductivity technique or coil-coil EM. DC resistivity uses stationary electric currents and is based on galvanic coupling, while ground conductivity is an electromagnetic method that operates in the frequency domain. They are the closest relatives of the capacitive resistivity technique and are described in detail hereafter. Some resistivity methods such as VLF and radiomagnetotellurics utilise remote source signals. Other methods such as transient EM or the magnetometric resistivity technique are rarely used for environmental and engineering site investigations, but are of theoretical interest.

Resistivity methods	Non-resistivity methods
DC resistivity	Self Potential (SP)
Complex resistivity (SIP)	Induced Polarisation (IP)
Ground conductivity and other FDEM	Ground Penetrating Radar (GPR)
Very-low-frequency methods (VLF)	
Radiomagnetotellurics (RMT)	
Transient EM (TEM)	
Magnetometric Resistivity (MMR)	

Table 3.1: Resistivity and non-resistivity electrical methods in environmental and engineering geophysics.

The remaining group of electrical methods (referred to as "non-resistivity methods") comprises techniques which are concerned with effects of electric polarisation (SP, IP). Another important electromagnetic method is ground penetrating radar (GPR). GPR is based upon wave propagation and operates at much higher frequencies than the other methods. It is therefore mainly sensitive to dielectric properties, since resistivity variations merely cause wave attenuation. Although non-resistivity methods are not discussed here, they are equally important in environmental and engineering site investigations (cf. Section 2.1.2).

3.1 DC resistivity

The direct current (DC) resistivity method is the traditional way of measuring the resistivity of the subsurface. It has been in use for nearly a century and is an extremely well established technique. It has strong theoretical foundations, is applicable in many situations and can provide robust datasets for which sophisticated interpretation techniques are available. The technique employs an artificial source of direct or pseudo-direct electric current injected into the ground via galvanic contact through point electrodes, thus creating stationary current flow in the earth. By measuring potentials at the surface in the vicinity of this current flow it is then possible to determine the effective resistivity of the subsurface for a given electrode geometry. From such measurements a spatial distribution of intrinsic resistivity can be derived, which represents a physical model of the subsurface. This section reviews the physical and mathematical basis of the technique together with its use for electrical imaging and discusses practical problems and disadvantages.

3.1.1 Basic theory

The full theory of DC resistivity is set out in geophysical textbooks such as Parasnis (1997), Reynolds (1997), Telford et al. (1990) or Dobrin and Savit (1988). The fundamental assumption is that of a stationary and continuous electric current flow in a homogenous and isotropic conductive medium. The electric field E can thus be regarded as the gradient of a scalar potential,

$$\mathbf{E} = -\nabla V, \tag{3.1}$$

since $\nabla \times \mathbf{E} = 0$ for $\dot{\mathbf{B}} = 0$ (A.3). This is a far-reaching assumption because it excludes any variation of the field with time. Using Ohm's Law (A.8) one has

$$\mathbf{j} = -\sigma \nabla V. \tag{3.2}$$

Continuous current flow in regions of finite conductivity does not allow for the accumulation of free charge, hence $\dot{\eta} = 0$, so that the continuity equation (A.5) yields $\nabla \cdot \mathbf{j} = 0$. Therefore

$$\nabla\sigma \cdot \nabla V + \sigma \nabla^2 V = 0, \tag{3.3}$$

which in regions with constant σ ($\nabla\sigma = 0$) reduces to Laplace's equation

$$\nabla^2 V = 0. \tag{3.4}$$

Potentials which satisfy this differential equation are possible solutions of the geoelectrical problem.

3.1.1.1 Single current electrode at the surface

Ideally the electric current is delivered by a single point electrode located at the surface of a homogeneous isotropic medium. The point at which current is returned is assumed to be at infinity so that its influence can be neglected for the time being. Because of spherical symmetry in the Earth, it is convenient to consider Laplace's equation in spherical coordinates as the potential will be a function of the radial distance r from the electrode only:

$$\nabla^2 V = \frac{\partial^2 V}{\partial r^2} + \frac{2}{r}\frac{\partial V}{\partial r} = 0. \tag{3.5}$$

The boundary condition at the surface arises from the fact that air is non-conductive ($\sigma = 0$) so that $E_z = \partial V/\partial z = 0$ is required at $z = 0$. The solution is then of the form

$$V(r) = -\frac{A}{r} + B \tag{3.6}$$

where A and B are constant with respect to r. Although the potential gauge is arbitrary it is reasonable to demand $V = 0$ for $r \to \infty$ so that $B = 0$. The total current crossing a hemispherical surface in the subsurface is given by

$$I = 2\pi r^2 \mathbf{j} = -2\pi r^2 \sigma \frac{\partial V}{\partial r} = -2\pi\sigma A = -2\pi \frac{1}{\rho} A \tag{3.7}$$

so that

$$A = -\frac{I\rho}{2\pi} \tag{3.8}$$

and hence with (3.6)

$$V(r) = \frac{I\rho}{2\pi r}. \tag{3.9}$$

This means hemispherical symmetry in the subsurface, i.e. the potential is constant at a given radial distance from the electrode. In other words, equipotential surfaces are hemispheres around the point of current injection.

3.1.1.2 The four-electrode array

In practice, two electrodes are required in order to pass an electric current into the ground. The current electrodes are commonly referred to as C_1 and C_2 or, historically, A and B. Since the distance between the current electrodes is necessarily finite, the potential at any surface point nearby will be affected by both. As before, the potential due to C_1 observed at a potential electrode P_1 is

$$V_1 = \frac{I\rho}{2\pi r_{11}}. \tag{3.10}$$

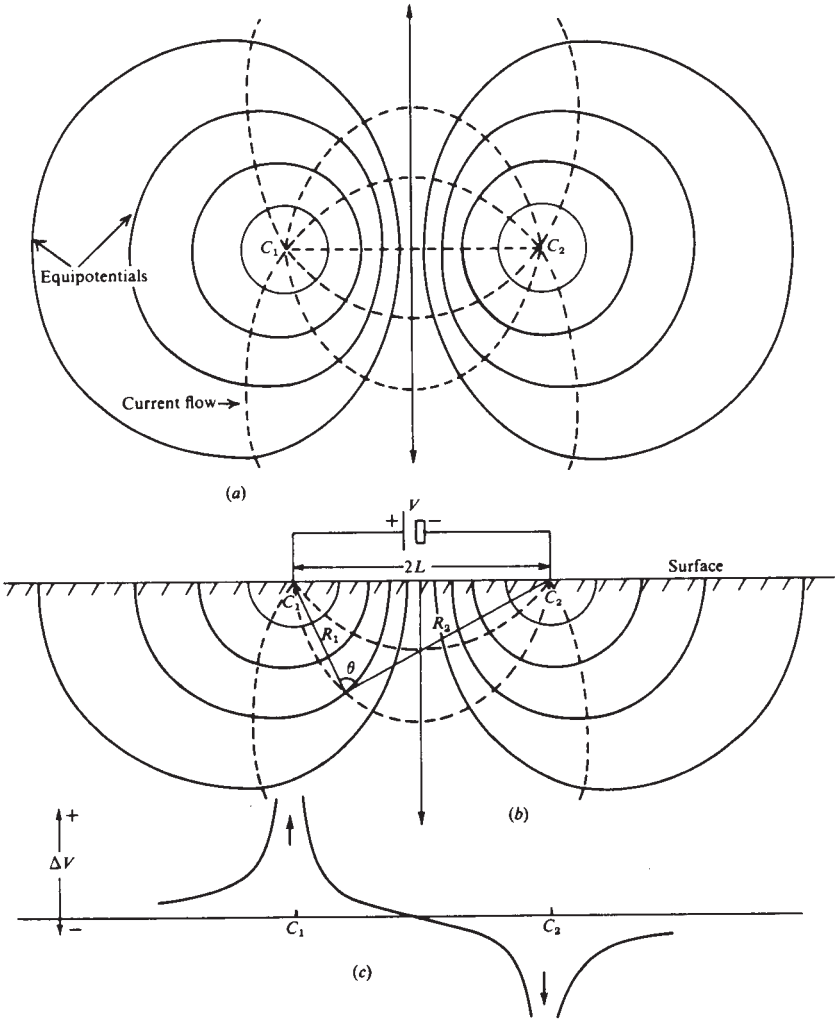

Figure 3.1: Equipotentials and current flow lines for two point sources of current at the surface of a homogeneous medium (Telford et al., 1990).

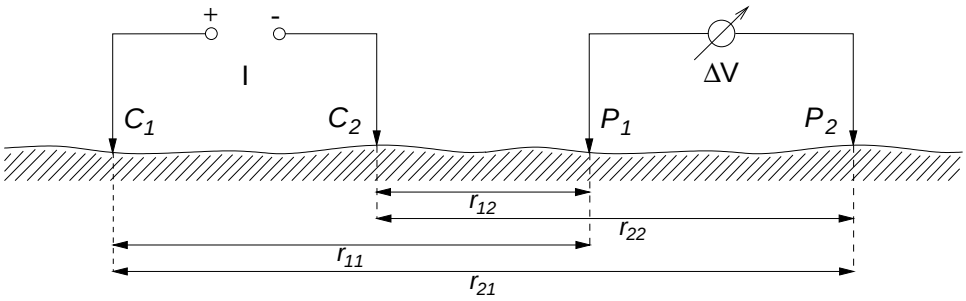

Figure 3.2: The four-electrode array consisting of two current and two potential electrodes.

The current at C_2 is of equal size but opposite in direction, hence the potential due to C_2 observed at P_1 must be

$$V_2 = -\frac{I\rho}{2\pi r_{12}}. \tag{3.11}$$

In total, the superposition of both potentials is observed at P_1:

$$V = V_1 + V_2 = \frac{I\rho}{2\pi}\left(\frac{1}{r_{11}} - \frac{1}{r_{12}}\right). \tag{3.12}$$

The lines of constant potential (equipotentials) together with the current flow lines are shown in Figure 3.1. It is worth noting that (3.12) is the potential of a dipole with finite extent, sometimes referred to as a *bipole*. If the distances r_{11} and r_{12} are large compared with the separation C_1C_2, (3.12) is an approximation for the potential created by an ideal point dipole.

Similar to the current dipole, two electrodes are required to measure a potential difference between two points on the surface, referred to as P_1 and P_2 or, historically, M and N. This concept of a four-electrode array is shown in Figure 3.2. The potential difference (or voltage) observed between P_1 and P_2 is then given by the superposition of the individual potentials:

$$\Delta V = \frac{I\rho}{2\pi}\left[\left(\frac{1}{r_{11}} - \frac{1}{r_{12}}\right) - \left(\frac{1}{r_{21}} - \frac{1}{r_{22}}\right)\right]. \tag{3.13}$$

It should be noted that ΔV is essentially a function of three parameters: halfspace resistivity, injected current and the geometry of the electrode spread.

3.1.1.3 The concept of apparent resistivity

In practice, the potential difference ΔV can be measured for an array of known geometry and a known injection current. A resistivity can then be obtained by solving (3.13) for ρ. For a homogeneous isotropic subsurface ("homogeneous halfspace") this resistivity is equal to the bulk resistivity of the halfspace and hence constant for any injection current and electrode geometry:

$$\rho = \frac{\Delta V}{I} \cdot K \tag{3.14}$$

where the term

$$K = \frac{2\pi}{\left[\frac{1}{r_{11}} + \frac{1}{r_{22}} - \frac{1}{r_{12}} - \frac{1}{r_{21}}\right]} \tag{3.15}$$

denotes the *geometric factor*. On inhomogeneous ground, different values for ρ are obtained if the array is moved or the electrode geometry is changed. The measured quantity is therefore referred to as the *apparent resistivity* ρ_a, indicating that it reflects the properties of a theoretical model (a homogeneous halfspace) which may not exist in practice.

3.1.1.4 Reciprocity theorem

From the above discussion it can be seen that in the case of a homogeneous halfspace it is irrelevant whether the electrode pair (A, B) acts as the current source and (M, N) as the potential dipole or vice versa — the expression for the geometric factor remains unchanged and hence the same current passing through the current electrodes will produce the same potential in both cases. It can be shown that the same is true for the more general case of an inhomogeneous earth with an arbitrary resistivity distribution, provided the resistivity at any point is independent of the current density. This is the proposition of the so-called reciprocity theorem (Parasnis, 1988). As a consequence, the apparent resistivity obtained with any of the array types discussed below remains the same if current and potential dipoles are interchanged and the current is kept the same, no matter how complicated the resistivity distribution in the subsurface. Reciprocity is particularly important for survey design, because it means that measured resistivities are independent of the array orientation.

3.1.2 Common array types

Various array types are in common use with DC resistivity, each of which has specific advantages and disadvantages. These are mainly concerned with ease of use in the field, but also with the spatial resolution of subsurface inhomogeneities. The quality of results is also affected by the choice of geometry because signal-to-noise properties vary between array types. Furthermore, the results of a measurement can be degraded by mutual inductive coupling between cables. The intensity of this effect is also a function of array type.

3.1.2.1 The Wenner array

In the Wenner array the four electrodes are collinear, with the potential electrodes being located *between* the current electrodes (Figure 3.3a). The separation a between adjacent electrodes is constant, so that the geometric factor of the Wenner array becomes

$$K_{\mathrm{We}} = 2\pi a \tag{3.16}$$

In spite of the simple geometry, this arrangement is often quite inconvenient for fieldwork because all four electrodes have to be moved to vary the depth of investigation.

3.1.2.2 The Schlumberger array

In the Schlumberger (or gradient) array, the potential electrodes are also located symmetrically between the current electrodes, however the current electrodes are placed much further apart ($AB \gg MN$, Figure 3.3b). At an arbitrary point P on the line $AMNB$ at a distance x from the centre of the array one obtains

$$U = \Delta V = \frac{I\rho}{2\pi}\left(\frac{1}{S+x} - \frac{1}{S-x}\right) \tag{3.17a}$$

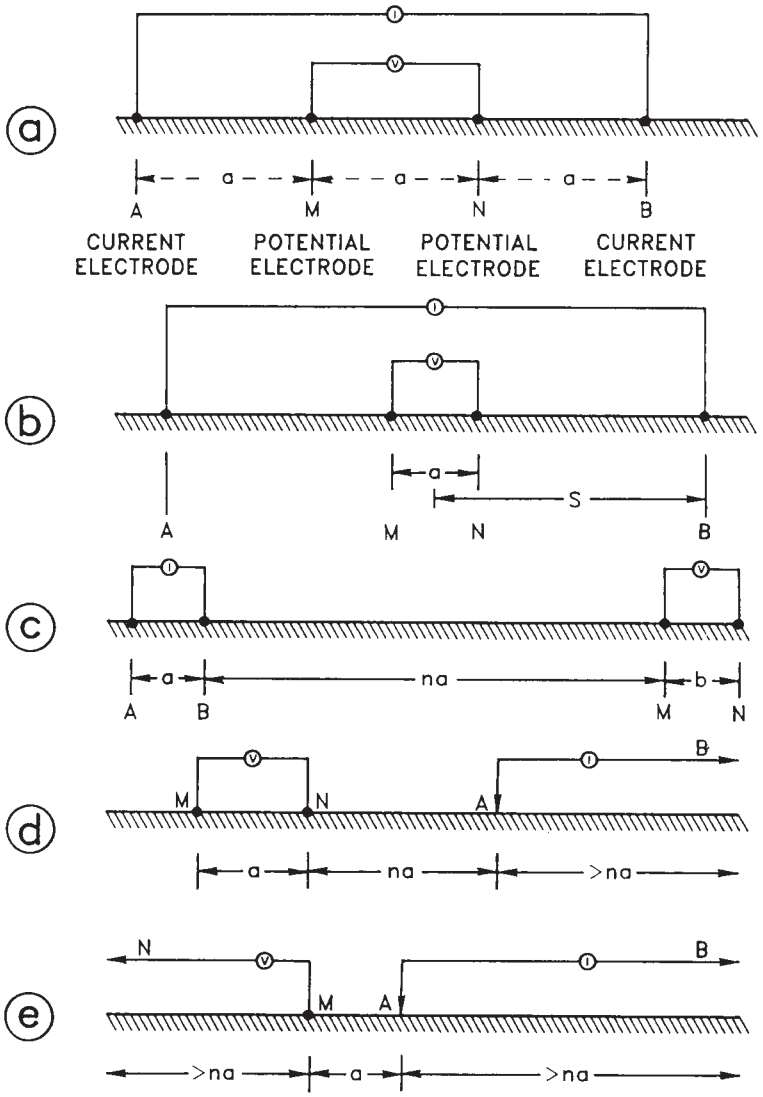

Figure 3.3: Electrode array types commonly use in DC resistivity (Dobrin and Savit, 1988). (a) Wenner array; (b) Schlumberger array; (c) dipole-dipole array; (d) pole-dipole array; (e) pole-pole array. Parameters a and n (a- and n-spacings) are often used in conjunction with regular grids of electrodes.

$$\frac{dU}{dx} = -\frac{I\rho}{2\pi}\left(\frac{1}{(S+x)^2} - \frac{1}{(S-x)^2}\right) \tag{3.17b}$$

where S is the half-length of the array. At the centre ($x = 0$) one has therefore

$$\frac{dU}{dx} = -\frac{I\rho}{\pi S^2} \tag{3.18}$$

and the apparent resistivity becomes

$$\rho_a = \frac{\pi S^2}{I}\left(-\frac{dU}{dx}\right) \tag{3.19}$$

hence the name gradient array. If MN is sufficiently small, then $(-dU/dx) = U/a$ and therefore one obtains for the geometric factor

$$K_{\mathrm{Sb}} = \frac{\pi S^2}{a} \tag{3.20}$$

The Schlumberger array is typically used for vertical electric sounding surveys for which the electrode spacing is expanded by simply increasing the distance of the current electrodes.

3.1.2.3 The dipole-dipole array

The class of geometries where current and potential dipoles are separated from each other is called a dipole-dipole array[1]. The dipole-dipole array is of particular significance to this research because in practice the capacitive resistivity technique is limited to the use of dipole-dipole geometries. Specific terminology has become established for a number of dipole-dipole configurations (Figure 3.4). The inline (also known as axial or polar) and equatorial configurations of the dipole-dipole array will be used in this thesis.

The inline dipole-dipole array (Figure 3.3c, 3.4 top left) consists of two dipoles whose axes are on the same line. The separations AB and MN (i.e. the dipole lengths) are typically equal ($AB = MN = a$). In DC resistivity, the distance between the two dipoles is often defined as the distance BM which is normally expressed in terms of a multiple n of the separation a. The "n-factor" is often an integer. The geometric factor of the inline dipole-dipole array, expressed by n and a, is

$$K_{\mathrm{DDin}} = \pi n(n+1)(n+2)a \tag{3.21}$$

In the general case however, it is more convenient to define the distance between the two dipoles as the distance r between their respective midpoints. In order to distinguish between the two conventions, the symbol l will be used for the dipole

[1]Strictly speaking, the term dipole-dipole array only applies if the distance between the two dipoles is much greater than the dipole lengths. For consistency however, all configurations of the type $ABMN$ (or where M and N are otherwise outside A and B) are referred to as dipole-dipole in this thesis.

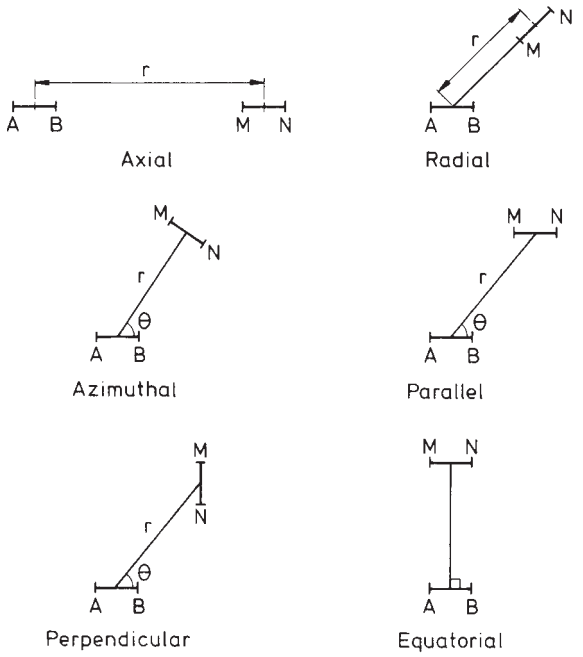

Figure 3.4: Configurations of the dipole-dipole array (Parasnis, 1997).

lengths in the latter case. A dipole-dipole array can then be fully described by either the pair $(a,\ n)$ or $(l,\ r)$. The alternative geometric factor of the inline dipole-dipole array is then

$$K_{\mathrm{DDin}} = \frac{2\pi}{\frac{2}{r} - \frac{1}{r-l} - \frac{1}{r+l}} = \pi r \left(1 - \frac{r^2}{l^2}\right) \tag{3.22}$$

The equatorial dipole-dipole array (Figure 3.4 bottom right) consists of dipoles which are parallel but not collinear and where the four electrodes form a rectangle. Its geometric factor is

$$K_{\mathrm{DDeq}} = \frac{\pi}{\frac{1}{r} - \frac{1}{\sqrt{l^2+r^2}}} \tag{3.23}$$

assuming a symmetric array. A special case of the equatorial dipole-dipole array is the square array for which $r = l$ (Habberjam, 1979).

3.1.2.4 The pole-dipole and pole-pole arrays

If one of the current electrodes is removed to a great distance from the measurement area, the remaining current electrode can be regarded as a single current pole. This arrangement is referred to as a pole-dipole (or three-point) array (Figure 3.3d). Its geometric factor is

$$K_{\mathrm{PD}} = 2\pi an(n+1) \tag{3.24}$$

If, in addition, one of the potential electrodes is also removed to a great distance, the remaining potential electrode can be regarded as a single potential pole and the array is referred to as a pole-pole array (Figure 3.3e). Here, the geometric factor is

$$K_{\mathrm{PP}} = 2\pi a \tag{3.25}$$

3.1.3 Traditional field techniques and methods of interpretation

The interpretation of DC resistivity data depends upon the field technique employed during a survey. Traditionally, three basic procedures have been used in connection with four-point arrays. *Vertical electric sounding* (VES) is employed if variations of resistivity with depth are of interest, while *resistivity profiling* or *resistivity mapping* are used to study lateral contrasts or localised anomalies. However, the information obtained is a function either of depth or lateral distance only.

3.1.3.1 Vertical electric sounding

The procedure here is to use an expanding spread of electrodes around a fixed centre. For Schlumberger and Wenner geometries, the separation between current electrodes is increased so that a larger fraction of the total electric current flows at larger depths (Telford et al., 1990). For dipole-dipole configurations, the potential is measured outside the current dipole and greater depths of investigation are achieved by increasing the inter-dipole spacing. In a dipole-dipole sounding, the dipole separation is increased, usually in conjunction with an increase in dipole lengths. The more accurate statement is therefore that, in general, the maximum depth from which information is obtained, is governed by the distance between the current source and potential probes (Parasnis, 1997). The result of a VES survey is a curve of apparent resistivity as a function of depth. It can be interpreted by 1D layered earth models, however these are inherently non-unique (Figure 3.5). The technique is useful in determining thickness of overburden, depth, structure and resistivity of flat-lying sedimentary beds or depth to water-bearing layers.

3.1.3.2 Resistivity profiling

This procedure involves the lateral movement of an electrode array of fixed size, i.e. with a constant electrode separation. It is also known as *constant separation traversing* (CST). If progression is along a single line, the result is a profile of apparent resistivity with distance. Values are usually plotted against the position of the array midpoint on the profile. Lateral variations in apparent resistivity indicate anomalous areas along the profile. CST is particularly useful to determine the location of sharp electrical contrasts such as vertical faults or other geological boundaries (Figure 3.6). CST is the fundamental mode of operation for towed-array resistivity techniques because these techniques require the use of fixed-size arrays and data must be acquired along linear profiles (cf. Section 3.1.5).

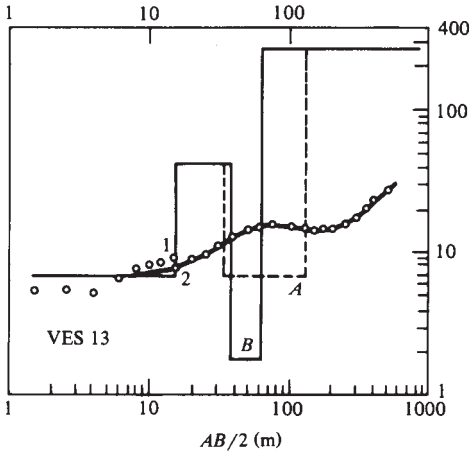

Figure 3.5: VES curve (apparent resistivity ρ_a vs. pseudodepth $AB/2$) obtained with a Schlumberger array and interpretation with two equivalent layered models A and B. (Telford et al., 1990).

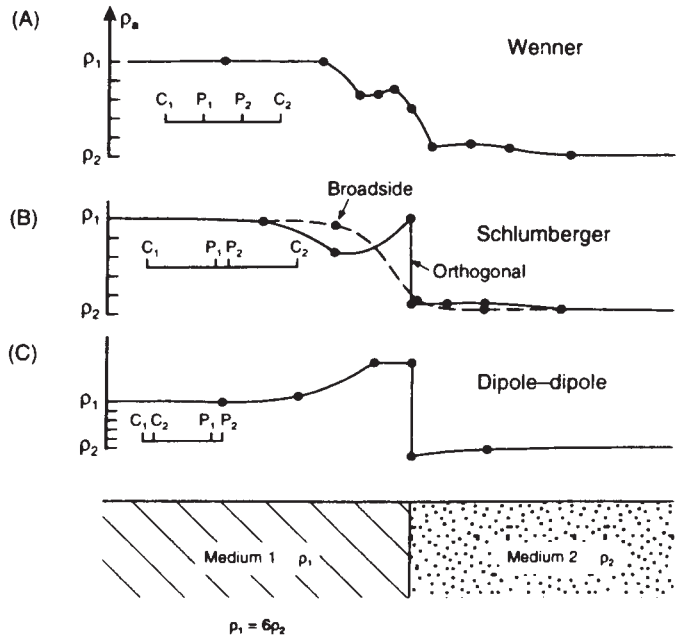

Figure 3.6: Constant separation traversing profiles (apparent resistivity vs. distance) obtained over a vertical contact using different array types. (A) Wenner array; (B) Schlumberger array; (C) dipole-dipole array (Reynolds, 1997).

3.1.3.3 Resistivity mapping

This procedure is a logical extension of resistivity profiling to a sequence of parallel lines. When one traverse is finished, the array is moved to the next parallel line and so forth until the area of investigation is covered. The apparent resistivity values are then plotted on a map which is typically displayed in the form of gridded contours. A typical application of high-resolution resistivity mapping is field archaeology, where fixed-array surveys are commonly used as a reconnaissance tool (e.g. Walker, 2000).

3.1.4 Electrical Resistivity Tomography (ERT)

A great limitation of these basic field procedures is that their quantitative interpretation is restricted to simple geological structures such as a 1D layered earth (e.g. sedimentary beds) or lateral contrasts such as vertical boundaries (e.g. faults or dykes). The type and geometry of the anomaly must be known for the apparent resistivity to be diagnostic. Although these basic techniques have turned out to be extremely useful in some geological applications, they are insufficient in areas of complex geology and mostly inapplicable in a site investigation context where the subsurface is often highly heterogeneous and includes localised anomalous features. Here, two-dimensional (2D) or three-dimensional (3D) earth models must be considered, according to the degree of complexity. However, interpretation of the associated apparent resistivity datasets is then no longer trivial and more sophisticated techniques had to be developed for this purpose.
The construction of two-dimensional and three-dimensional images of the subsurface from resistivity data has become commonly known as electrical resistivity tomography (ERT). Sometimes the term "resistivity imaging" is used synonymously. It is worth noting that imaging techniques can reflect different degrees of realism. In a looser sense of the term "imaging", basic visualisation techniques such as pseudosections based on *apparent* resistivity data (cf. Section 3.1.4.2) provide simple images which contain spatial information but are not representative of the true distribution of intrinsic resistivity. Imaging in a stricter sense involves the creation of 2D or 3D models of "true" resistivity which can be regarded as "realistic" representations of the subsurface by virtue of its electrical properties. The procedure of deriving a true resistivity model from apparent resistivity field data is known as "resistivity inversion" (cf. Section 3.1.4.4).

3.1.4.1 Field techniques

Electrical resistivity tomography surveys are nowadays conducted with multiplexed computer-controlled systems using a large number of electrodes connected to multicore cables at regular spacings (Barker, 1981; Griffiths and Turnbull, 1985; Griffiths et al., 1990). Single lines or 2D grids (sequences of parallel lines) of electrodes are installed at the beginning of the survey and one or several multicore cables are connected to the electrodes. Data acquisition is then entirely automatic with a computer-controlled switching unit collecting data

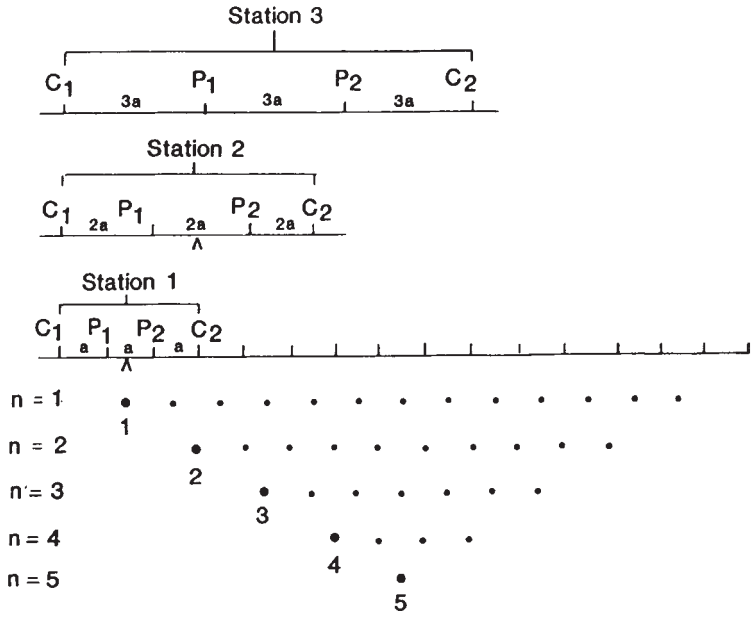

Figure 3.7: Example of an ERT survey using a Wenner array with a set of evenly spaced electrodes to collect multi-offset data (Reynolds, 1997).

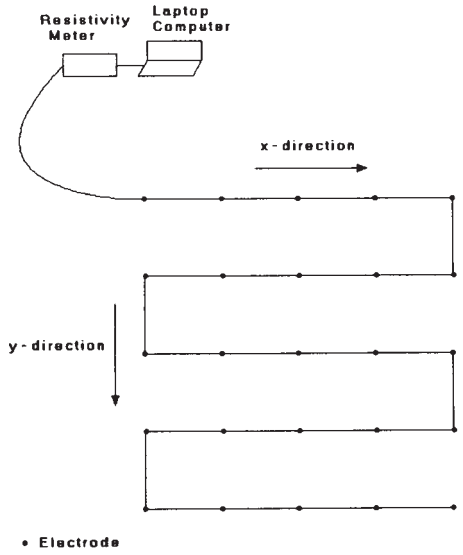

Figure 3.8: Example of electrodes arranged along a multicore cable for a 3D ERT survey on a regular grid (Loke and Barker, 1996a).

from a predefined sequence of electrode arrays with varying geometries (Figure 3.7). Early resistivity imaging was purely two-dimensional and the associated field technique comprised the installation of a single line along the profile to be investigated (Griffiths and Barker, 1993; Dahlin, 1993). Prior to the development of genuine 2D inversion algorithms, interpretation of such datasets was limited. One simple interpretation technique is to create quasi-2D resistivity sections by extracting closely spaced VES from the 2D data, a procedure known as continuous vertical electric sounding (CVES) (Dahlin, 1993, 1996).
It was only after the advent of increasingly sophisticated modelling and inversion algorithms that 3D imaging became technically feasible. Practical field techniques in conjunction with user-friendly interpretation were described by Loke and Barker (1996a). The initial suggestion involved the deployment of one multicore cable in snake-lines across a regular grid of electrodes (Figure 3.8). However, such a procedure is only viable for small grids of the order of 10×10 electrodes. For larger (or more detailed) 3D surveys, data are usually acquired along a sequence of parallel lines which involves the installation of multiple cables or the use of roll-along techniques (Dahlin and Bernstone, 1997) in order to increase efficiency.

3.1.4.2 Pseudosections and the absolute depth scale

If resistivity data are acquired using multiple array separations on the same profile, the resulting dataset contains information about both lateral and vertical variations of resistivity. The usual form of display is then to plot apparent resistivities on a section of profile distance versus depth. This is referred to as a *pseudosection* since it is indicative of variations with distance and depth, but does not necessarily correspond to the true distribution of resistivity in the form of a cross-section. Pseudosections are often displayed as a contour map (Figure 3.9) or a coloured image.
With the true resistivity-depth function unknown, depth information contained in apparent resistivity data can only be represented by a *pseudodepth*. This theoretical depth is a function of the array geometry. For the dipole-dipole array, the classical way to assign pseudodepths to apparent resistivity readings is a geometric procedure, whereby each measured value is placed at the intersection of two 45-degree lines through the centres of the dipoles (Figure 3.10). Each n-spacing then corresponds to a horizontal line in the pseudosection, representing a nominal depth of investigation. Similar procedures exist for other array types as well. The drawback of the geometric approach is that results obtained with different dipole lengths cannot be combined into one single pseudosection. Edwards (1977) therefore introduced the concept of "effective depth", in which a median depth of investigation can be calculated for each electrode array as a function of array geometry. For dipole-dipole arrays, the median depth is expressed in terms of the a-factor and the overall length of the array L. The apparent resisistivity value is then plotted at this median depth in the pseudosection.
Edwards' definition is based on the "depth of investigation characteristic" (DIC) which had been introduced by Roy and Apparao (1971) for arrays over a homo-

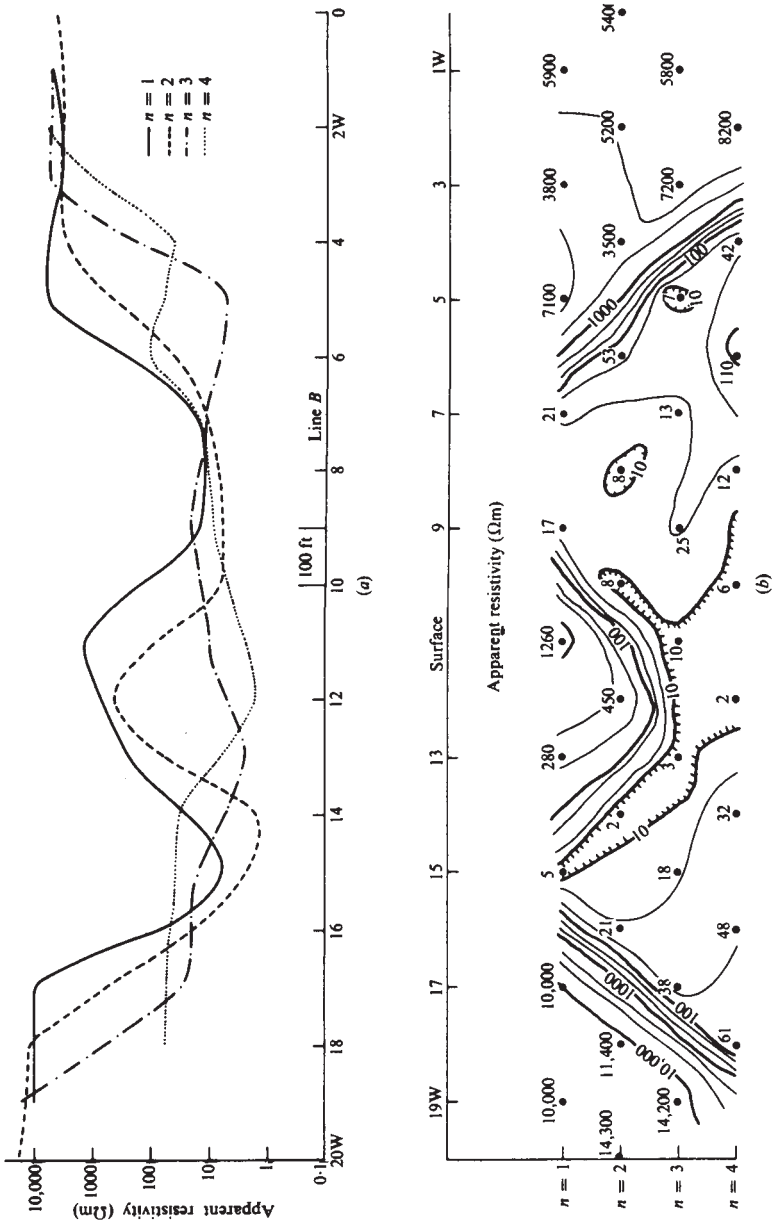

Figure 3.9: Results of a multi-offset 2D ERT survey displayed in the form of apparent resistivity profiles (top) and a pseudosection (bottom) (Telford et al., 1990).

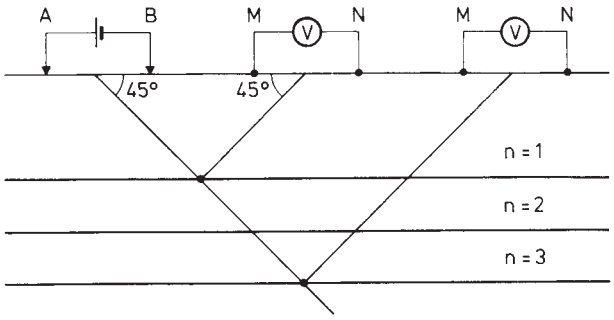

Figure 3.10: Classical method of plotting dipole-dipole data on a pseudosection (Parasnis, 1997).

	n	z_e/a	z_e/L
Inline Dipole-dipole	0.222	0.139	0.063
	0.5	0.253	0.101
	1	0.416	0.139
	2	0.697	0.174
	3	0.962	0.192
	4	1.220	0.203
	5	1.476	0.211
	6	1.730	0.216
	7	1.983	0.220
	8	2.236	0.224
	20	5.250	0.239
	∞	—	0.250
Equatorial dipole-dipole	1	0.451	0.319
	2	0.809	0.362
	3	1.180	0.373
	4	1.556	0.377
	10	3.840	0.383
	∞	—	0.384
Wenner α	—	0.519	0.173
Schlumberger ($a \to 0$)	—	—	0.192

Table 3.2: Effective (median) depths for relevant array types (after Edwards, 1977).

geneous earth to define an absolute depth scale for resistivity surveys. The DIC examines the contribution of each elementary volume of earth to the total signal ($\Delta V/I$) at the surface. Integrating this contribution over a thin horizontal layer and normalising so that the total signal equals unity, Roy and Apparao constructed "normalised depth of investigation characteristic" (NDIC) curves for different arrays. These show that the maximum signal contribution arises from a layer at a well-defined depth. Edwards adapted Roy and Apparao's original definition of this "effective depth" to represent a depth at which exactly 50% of the total signal originates from above and 50% from below. His median depth z_{med} is defined as (Edwards, 1977)

$$\int_0^{z_{\text{med}}} \text{NDIC}\, dz = \frac{1}{2}. \tag{3.26}$$

The median depth has today widely replaced geometric definitions of pseudo-depth. It can be used as a measure for the nominal depth of investigation of a particular array. This quantitative approach can be extremely useful for survey design considerations or the automatic creation of starting models in inversion algorithms (Loke, 1999). Table 3.2 shows numerical values of effective depths for some relevant array types.

3.1.4.3 Resistivity forward modelling

For a given subsurface resistivity distribution, the objective of forward modelling is to calculate the apparent resistivity that would be measured by a survey over that structure. This procedure is an essential stage of any automated resistivity interpretation algorithm.
A solution of the forward problem involves solving the Laplace equation (3.4) numerically for arbitrary resistivity distributions. The most versatile implementations of resistivity forward modelling algorithms are based upon the finite difference (FD) method (Mufti, 1978; Dey and Morrison, 1979) or the finite element (FE) method (Coggon, 1971). A certain class of models, namely localised bodies in otherwise layered media, lends itself to solutions based upon integral equations (Das and Parasnis, 1987). Although the associated algorithm is fast, the method is not suitable for modelling semi-infinite features. A method using alpha centres was suggested by Petrick et al. (1981).

3.1.4.4 Resistivity inversion

A resistivity inversion is the mathematical process required to derive a model of the true spatial distribution of intrinsic resistivity in the region of interest from an apparent resistivity dataset. Early algorithms were limited to certain model geometries or comparisons with precalculated model responses (Pelton et al., 1978a; Tripp et al., 1984; Smith and Vozoff, 1984). Modern inversion techniques can deal with arbitrary resistivity distributions, are fully automated and frequently use non-linear optimisation methods to iteratively improve simple starting models in an attempt to achieve a "best fit" between model and measured data. As a consequence of the increased availability of computing

power outside of mainframe environments in recent years, resistivity inversions are now routinely carried out on desktop PCs, even for large 2D and medium-size 3D datasets (Loke and Barker, 1996a).
One of the most popular general geophysical inversion techniques is the Gauss-Newton least-squares inversion (Lines and Treitel, 1984) due to its robustness and variety of applications. One particular incarnation of this method, known as Occam's inversion[2], demands smoothness of the model as a general constraint (Constable et al., 1987; deGroot-Hedlin and Constable, 1990). It is widely used in conjunction with electrical and electromagnetic techniques because smooth models tend to reflect the resolving power of these techniques best. Loke and Barker (1996b) have developed a fast and particularly versatile implementation of the smoothness-constrained least-squares inversion. A quasi-Newton method is used to estimate the Jacobian matrix of partial derivatives during each iteration, resulting in a dramatic reduction of processor time and memory requirements. Both their 2D and 3D algorithms have proven to be robust under many circumstances and have been successfully applied to complex datasets obtained during environmental and engineering site investigations (Ogilvy et al., 2002, 1999; Chambers et al., 1999).
Other algorithms for DC resistivity inversion have been described by Smith and Vozoff (1984), Li and Oldenburg (1994), Ellis and Oldenburg (1994b), Dabas et al. (1994) and Zhang et al. (1995). A detailed overview of relevant DC resistivity inversion techniques was given by Tsourlos (1995).

3.1.5 Towed-array techniques

Many near-surface applications including environmental and engineering site investigations, hydrology, pedology and archaeology require high-density information about physical parameters of the subsurface. The conventional acquisition of high-resolution DC resistivity data however is cumbersome, slow and often impractical on large survey areas. As a consequence, much effort has gone into developing mobile techniques using towed arrays in order to improve the efficiency of conventional DC resistivity surveys.

3.1.5.1 Automated electrode installation

Data acquisition rates can be increased by simply automating the electrode installation process. A system which uses electrodes that are mounted on a trailer and lowered pneumatically ("Mobile Electrode Group") was described by Südekum (2000). Survey progress however is still stepwise with this technique. Panissod et al. (1998) have reviewed towed-array techniques employed in recent years by the University of Paris VI. The authors describe how DC resistivity can be measured almost continuously with a towed device ("RATEAU"). In its simplest form, stake electrodes were replaced by metallic wheels with spikes. A remarkable development was the idea to use high-pressure liquid jets of conducting fluid as electrodes, thus providing galvanic contact to the

[2] "*It is vain to do with more what can be done with fewer*" (William of Occam, early 14th century). A simple solution is preferable to one which is unnecessarily complicated.

ground (Hesse et al., 1986). Both techniques seemed to provide good quality data and apparent resistivity profiles were shown to contain much more detail than manually acquired datasets (Figure 3.11). These techniques were reported to have been successfully applied to archaeological and pedological[3] surveys. Prototype instruments initially comprised only a single four-electrode square array but were later extended to optimised multiple arrays (Panissod et al., 1997a), allowing the simultaneous recording of resistivity information from multiple array separations at once ("multidepth maps").

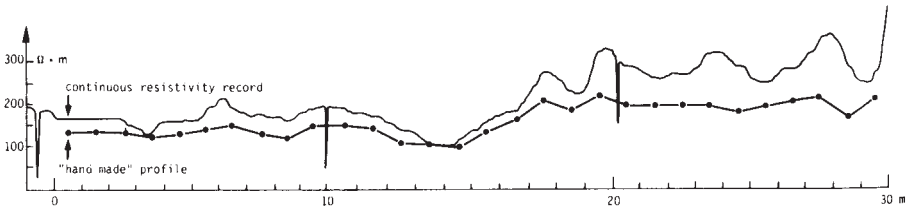

Figure 3.11: Comparison between a conventional DC resistivity profile and a continuous profile obtained with a towed array. The continuous profile resolves lateral changes in resistivity much better, but is affected by motion noise in the form of single outliers (Hesse et al., 1986).

3.1.5.2 Pulled-Array Continuous Electrical Profiling

A more straightforward approach was pursued by Sørensen (1996) with the Pulled-Array Continuous Electrical Profiling technique (PA-CEP). In the instrumental design used by Sørensen, heavy cylindrical steel tubes acting as electrodes are mounted on a towed cable and pulled by a small off-road vehicle. Galvanic contact is achieved directly through the metallic electrode sliding across the ground surface. The main difficulty with this technique is to maintain a constant injection current as galvanic contact varies greatly during the measurement. Towing-induced noise voltages at the potential electrodes were found to cause considerable problems and appropriate data processing techniques had to be developed to retrieve reliable resistivity estimates from the raw data. As a consequence, PA-CEP relies on heavy oversampling along the survey profile. A sampling frequency of 80 Hz is employed which roughly equates to a sampling interval of 1 cm for the raw data. Robust statistical processing yields resistivity estimates at intervals of the order of 1 m (Munkholm, 1996). PA-CEP has been used extensively in Danmark for hydrogeological mapping and aquifer characterisation.

[3]pedology = science that quantifies the factors and processes of soil formation

3.1.6 Problems and disadvantages

3.1.6.1 Galvanic contact

A practical DC resistivity measurement requires galvanic contact with the ground. In theory, this contact is implicitly assumed to be of good quality. If this is not the case in practice, serious restrictions may result for the applicability of the technique. Indeed, a frequently encountered problem in DC resistivity is serious degradation of data quality which occurs when electrodes are being installed on highly resistive surfaces such as dry sands, gravels, rubble, ice, frozen soils or building materials. The term "poor galvanic contact" is used in these circumstances to describe a situation in which the resistive part of the contact impedance between the electrodes and the surface material becomes so large that it affects (or even prevents) current injection or potential measurement. The resistivity of the material immediately surrounding the electrode dominates the size of the contact resistance (Lile et al., 1997), so that highly resistive surface materials are particularly problematic. Figure 3.12 shows an equivalent electrical circuit model for a four-electrode array. Contact impedances can be thought of as additional impedances in series with the ground impedance Z_{Earth} in both the current and the potential circuits (Wait, 1995). It is usually found that $Z_{\text{C1}}, Z_{\text{C2}}, Z_{\text{P1}}, Z_{\text{P2}} \gg Z_{\text{Earth}}$. In the case of the current circuit, the injected current for a given transmitter output power is therefore mainly limited by contact impedances. In return, signal levels measured at the potential circuit are controlled by the amount of current that is injected into the ground. With regard to the potential circuit, high contact impedances are equally detrimental. To this end, high contact impedances can invalidate a potential measurement if the input impedance of the voltmeter is insufficiently low (cf. Figure 3.12 right). Zonge and Hughes (1986) have found that dipolar electric field measurements (as employed in DC resistivity) can be biased by up to 50 percent due to the effects of electrode contact resistance. Poor galvanic contact is also often associated with (undesired) capacitive or IP effects at the electrodes, because practical instruments usually employ switched DC or slowly varying AC current with frequencies of the order of several Hz rather than true DC current for the impedance measurement. Possible solutions that may improve galvanic contact comprise (Reynolds, 1997)

- wetting of electrodes with conductive fluid (e.g. water, saline solution, addition of bentonite);
- the use of multiple electrodes connected to the end of the current-carrying wire.

3.1.6.2 Installation of electrodes

A more practical problem with DC resistivity is that steel electrodes must be manually implanted in the survey area before measurements can commence. Strictly speaking, the technique must be regarded as intrusive, even if the electrodes require only minimal surface penetration. Not only is this procedure extremely cumbersome for large-scale surveys, but installation of electrodes may

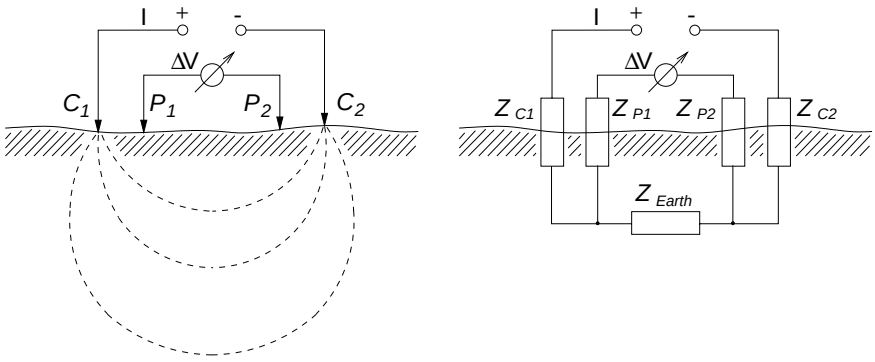

Figure 3.12: Basic concept of a DC resistivity measurement with galvanic contact. Left: a DC four-electrode array. Right: equivalent electrical circuit model showing the ground impedance Z_{Earth} and the contact impedances Z_{C1}, Z_{C2} (current electrodes) and Z_{P1}, Z_{P2} (potential electrodes).

be impossible altogether. Metal stake electrodes are particularly unsuitable for installation on hard ground or artificial surfaces such as roads, pavements and other engineered structures. Practical work-arounds include

- drilling small-diameter holes prior to installation;
- using electrodes with larger contact area (e.g. disc electrodes) which do not penetrate the surface in conjunction with the use of conductive substances to enhance galvanic contact (e.g. mud, bentonite, saline solutions etc.)
- using non-polarisable electrodes which provide contact via an electrolytic solution and a porous membrane.

However, the successful mechanical installation of electrodes is no guarantee for a good quality electrical measurement. Mechanically hard surfaces are often associated with highly resistive materials, causing high contact impedances.

3.2 Ground conductivity

Electromagnetic induction is an alternative means of exploring subsurface resistivity variations. EM methods represent a more general approach to the measurement of electrical properties since time-varying electromagnetic fields include static currents as a special case at zero frequency. A wide variety of instrumentation is available, ranging from small handheld instruments to airborne survey systems. EM methods can be either time-domain (TEM), where transient signals are used and measurements are made as a function of time, or frequency-domain (FEM), where signals employed are either monochromatic or multi-frequency. Near-field methods (the ground conductivity technique) and far-field or plane-wave methods (VLF, RMT) are available. In the context of this thesis, near-field frequency-domain techniques are directly relevant.
As in the case of DC resistivity, EM field techniques may be subdivided into depth-sounding techniques to examine the variation of conductivity with depth and horizontal profiling or mapping techniques to record lateral changes in conductivity. However, quantitative interpretation of EM data is more complicated than DC resistivity data due to the use of time-varying fields. While 1D and 2D interpretation schemes are readily available, EM methods are still rarely employed for 3D imaging applications. 3D EM is particularly difficult in strongly heterogeneous environments, due to the increased risk of ambiguity. The computational expense for 3D EM modelling and inversion is high, yet recent progress in this field, fueled by applications in the exploration sector, has been promising (e.g. Lesselier and Habashy, 2000). Such progress may also lead to increased use of EM imaging in the environmental and engineering sector.

The classical ground conductivity technique is immensely popular in environmental and engineering applications. The basic theory of operation and fundamental characteristics are discussed hereafter. The technique is based on the mutual inductive coupling of two coils in the presence of the conductive ground. Under certain conditions the system response is directly proportional to the subsurface conductivity, i.e. practical instruments can be calibrated to display a resistivity reading directly. It should be noted at this stage that the condition of "*low induction numbers*" is equally relevant in the context of the capacitive resistivity technique.

3.2.1 Basic theory

The theory of the ground conductivity technique is well-established (Keller and Frischknecht, 1966; McNeill, 1980; Wait, 1982; Ward and Hohmann, 1988). A transmitter coil, driven by an alternating current at an audio-range frequency, creates a time-varying primary magnetic field $\mathbf{H_p}$. The presence of the conducting earth within this primary field causes the induction of eddy currents in the subsurface which in turn generate a secondary magnetic field $\mathbf{H_s}$ in their vicinity (Figure 3.13). The superposition of both fields induces a voltage in a receiver coil located a short distance away from the transmitter.
Transmitter and receiver coils essentially represent elementary magnetic dipoles.

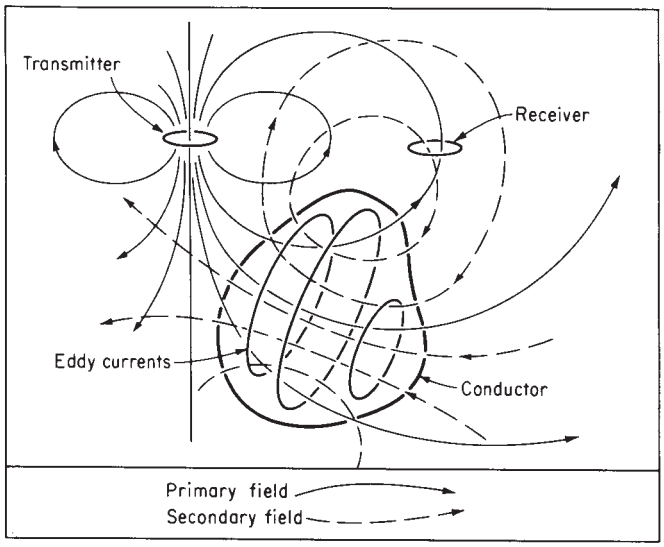

Figure 3.13: Principle of the ground conductivity method. The primary field induces eddy currents in a conductor which in turn generate a secondary magnetic field. The superposition of both is measured (Grant and West, 1965).

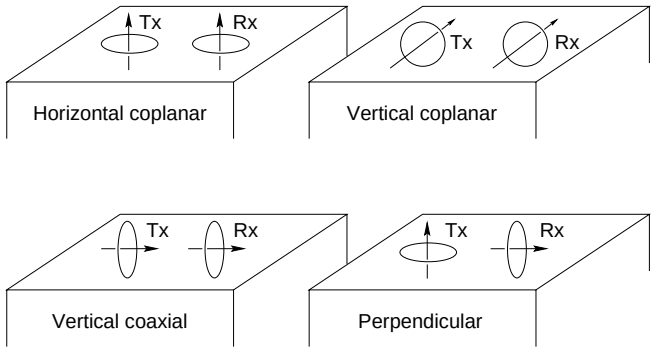

Figure 3.14: Configurations for the coil-coil EM sounding technique. Horizontal coils are associated with vertical magnetic dipoles and vice versa.

Their relative orientation determines the degree of mutual coupling. Four elementary configurations are commonly used for the two-loop technique: horizontal coplanar loops (HCPL) representing vertical magnetic dipoles (VMD), Vertical coplanar loops (VCPL) representing horizontal magnetic dipoles (HMD) in parallel orientation, vertical coaxial loops (VCAL) representing horizontal magnetic dipoles in in-line configuration and a perpendicular orientation of transmitter and receiver loops (Fig. 3.14).
The coupling between the coils can be described in a quantitative manner by means of the transfer (or mutual) impedance $Z = U/I$, where V is the voltage induced in the receiver coil as a result of the current I generating the primary magnetic field. In free space the transfer impedance is given by (Keller and Frischknecht, 1966)

$$Z_0^{CP} = \frac{i\mu_0\omega n_1 n_2 A_1 A_2}{4\pi r^3} \tag{3.27}$$

$$Z_0^{CA} = -\frac{i\mu_0\omega n_1 n_2 A_1 A_2}{2\pi r^3} \tag{3.28}$$

for coplanar and coaxial coils, respectively. Here n_1, n_2 are the numbers of turns on the coils and A_1, A_2 are the effective cross-sectional areas. In free space, the induced voltage is therefore a simple function of the magnetic dipole moments of transmitter and receiver coils and their separation. The presence of a conductor affects this interdependence by virtue of the secondary magnetic field. The degree of coupling is then often expressed as the ratio between mutual impedance Z in the presence of the conductor and the free space mutual impedance Z_0. The resulting functions are the so-called mutual coupling ratios which are complicated expressions of electrical parameters and coil geometry. Wait (1955) has shown that over a homogeneous earth with finite conductivity and under neglection of displacement currents the coupling ratios for HCPL, VCPL and VCAL are given by

$$\left(\frac{Z}{Z_0}\right)_{HCPL} = \frac{2}{(ks)^2}\left\{9 - \left[9 + 9ks + 4(ks)^2 + (ks)^3\right] e^{-ks}\right\} \tag{3.29a}$$

$$\left(\frac{Z}{Z_0}\right)_{VCPL} = 2 - \frac{2}{(ks)^2}\left\{3 + \left[3 + 3ks + (ks)^2\right] e^{-ks}\right\} \tag{3.29b}$$

$$\left(\frac{Z}{Z_0}\right)_{VCAL} = 2 - 12\left\{\frac{1}{(ks)^2} + \left[12 + 12ks + 5(ks)^2 + (ks)^3\right] e^{-ks}\right\} \tag{3.29c}$$

where $k = \sqrt{i\omega\mu_0\sigma}$ is the wavenumber (or propagation constant), and s denotes the intercoil spacing.

3.2.2 Operation at low induction numbers

Under certain conditions, known in electromagnetic geophysics as the "low induction number regime", the expressions for the mutual coupling ratios can be greatly simplified. The induction number B is a means of describing the nature of the electromagnetic induction as a function of geometry and electrical properties. B is defined as the ratio between a characteristic scale length L and the

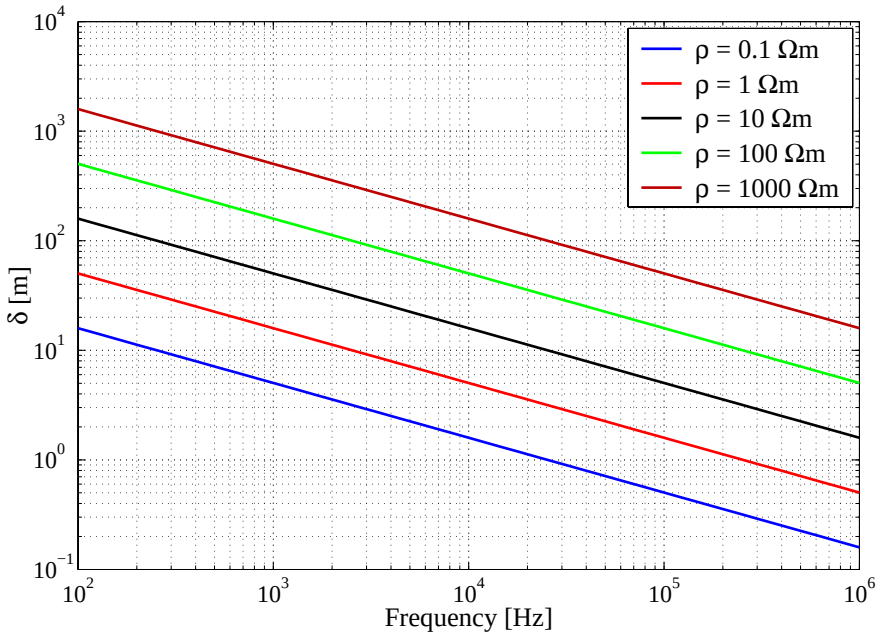

Figure 3.15: The variation of electromagnetic skin depth with frequency. Parameter: resistivity.

electromagnetic skin depth δ (A.23) (McNeill, 1980)[4]:

$$B = \frac{L}{\delta} = L\sqrt{\frac{\omega\mu_0\sigma}{2}} \tag{3.30}$$

The skin depth is the characteristic length of the diffusion process, describing the distance at which a plane electromagnetic wave entering a conductor has decreased to $1/e$ of its original amplitude. Figure 3.15 shows the variation of skin depth across a range of frequencies with different resistivities as a parameter. It is evident that skin depth increases with resistivity and decreases with frequency. The induction number can thus be regarded as a measure which relates the geometry of the experiment to the spatial extent of the electromagnetic induction by which it is governed.

In the case of the ground conductivity technique, the characteristic scale length is the intercoil spacing, i.e. $L = s$. The induction number can therefore be expressed as

$$B = \frac{ks}{\sqrt{2i}} \tag{3.31}$$

Examination of this term shows that three different cases can now be distinguished:

[4]Sometimes the induction number is defined as the square of expression (3.30), dropping the constant factor 1/2: $B' = L^2\omega\mu_0\sigma$.

$|B| \ll 1$ or $ks \ll 1$. The induction number is much smaller than one or, what is equivalent, s is much smaller than both the skin depth and the wave length $\lambda = k^{-1}$ in the medium. This is known as the low induction number regime.

$|B| \approx 1$ or $ks \approx 1$. The induction number is approximately equal to one. This implies that s is of the order of both the skin depth and the wavelength in the medium.

$|B| \gg 1$ or $ks \gg 1$. The induction number is much greater than one or s is much greater than both skin depth and wavelength.

In the case of low induction numbers ($ks \ll 1$) the coupling ratios (3.29a) and (3.29b) reduce to the simple form

$$\left(\frac{Z}{Z_0}\right)_{HCPL} \approx \left(\frac{Z}{Z_0}\right)_{VCPL} \approx \frac{iB^2}{2} = \frac{i\omega\mu_0\sigma s^2}{4} \tag{3.32}$$

i.e. the instrument response is directly proportional to conductivity and almost purely imaginary, which means that the secondary magnetic field is in quadrature with the primary magnetic field. Hence the apparent conductivity derived from a two-loop measurement may be defined as (McNeill, 1980)

$$\sigma_a = \frac{4}{\omega\mu_0 s^2} \operatorname{Im}\left(\frac{Z}{Z_0}\right) \tag{3.33}$$

It remains to be discussed how the condition of low induction numbers can be achieved. For most near-surface applications the maximum probable conductivity can be estimated and sensor separations are chosen according to the desired depth of investigation. Once a particular geometry has been adopted so that s is fixed, the skin depth must be much greater than s, which can only be achieved by decreasing the frequency of operation. From $ks \ll 1$ one obtains

$$f \ll \frac{1}{\pi\mu_0\sigma s^2} \tag{3.34}$$

Instrument	Frequency [kHz]
DUALEM-2/-4	9.0
Geonics EM 31	9.8
Geonics EM 34-3	0.4, 1.6, 6.4
Geonics EM 38	14.6
Geophex GEM-2	0.3 ... 24.0
GF Instruments CM-031	9.765
GSSI GEM-300	0.325 ... 19.975
Iris Instruments Promis 4	0.11 ... 28.16
Iris Instruments Promis 10	0.11 ... 56.32

Table 3.3: Commercial conductivity meters and their frequencies of operation.

The frequency of operation must be chosen such that (3.34) is satisfied. As an example, for a maximum conductivity of $\sigma = 0.1\ \mathrm{Sm}^{-1}$ ($\rho = 10\ \Omega\mathrm{m}$) and an intercoil spacing of $s = 10$ m, the right-hand side of (3.34) equals 25.3 kHz. Most commercial ground conductivity meters operate at frequencies below 20 kHz (Table 3.3).

3.3 Other techniques

3.3.1 Complex resistivity

The complex resistivity method makes use of the observation that the electrical resistivity of rocks is complex and frequency-dependent within a typical frequency range between 1 μHz and 1 kHz (e.g. Olhoeft, 1980, 1985b). This effect is associated with the induced electrical polarisation of a porous rock mass due to the application of electric fields. With this method, multifrequency resistance data are collected in terms of amplitude and phase, conventionally using galvanically coupled electrodes. The method is also referred to as spectral induced polarisation (SIP).
The main mechanisms of induced polarisation are metallic and membrane polarisation. The latter is particularly associated with the presence of clay minerals. Consequently, complex resistivity was initially applied to the characterisation of metallic ore bodies (Pelton et al., 1978b) and has also been used to determine hydraulic properties of sedimentary rocks (Börner and Schön, 1991). There has been evidence to suggest that an additional mechanism affecting complex resistivity measurements are clay-organic reactions (Olhoeft, 1985a) and that complex resistivity may be able to detect and discriminate between organic contaminants in the form of NAPLs (e.g. Olhoeft, 1985b; Börner et al., 1993). Unless metallic polarisation is involved, observed phase angles in complex resistivity measurements are typically very small, being of the order of tens of milliradians.

3.3.2 Plane-wave EM

Electromagnetic methods based on local sources such as the ground conductivity technique operate in the near-field or intermediate regions of the source (Section 3.2). For strong distant sources such as radio transmitters, measurements in the far-field region of the source are possible. At large distances from the source the local electromagnetic field may be considered uniform within a small survey area and equivalent to that of a plane wave. The VLF and RMT techniques make use of the carrier waves of powerful radio transmitters. Both techniques are frequently employed for near-surface investigations in the environmental and engineering sector. The VLF technique is particularly relevant in the context of this thesis because it operates in the same frequency range as the capacitive resistivity technique and VLF signals must be regarded as a potential disturbance to CR measurements (cf. Section 5.1.3).

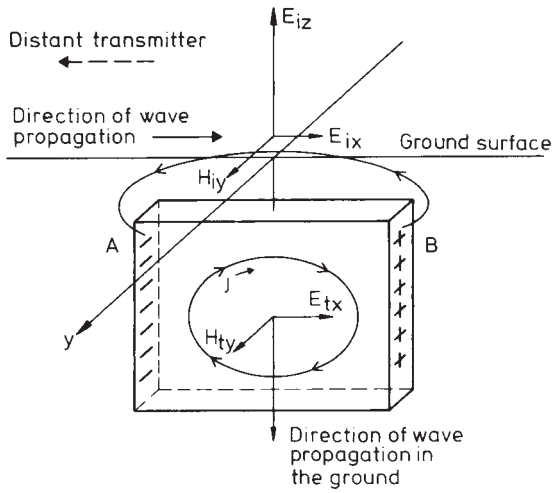

Figure 3.16: Concept of the VLF technique for a conductor striking parallel to the propagation direction of the VLF signal (Parasnis, 1997).

3.3.2.1 VLF

The VLF (Very-Low-Frequency) technique is typically applied to 2D problems (Parasnis, 1997). VLF stations transmit in the frequency band 10–30 kHz[5]. At the survey location, both the electric and the magnetic field at the known transmitter frequency may be observed. As the analysis is dependent on the direction of geological strike, the transmitter must be chosen such that it is roughly either in strike direction ("E polarisation", Figure 3.16) or perpendicular to it ("H polarisation"). Measurements in E polarisation are more common since the H polarisation is not associated with an induced magnetic field. The VLF technique can be used for conductor detection (H field tilt) or for the estimation of apparent resistivity (via the wave impedance E_x/H_y). This is known as VLF-R.

3.3.2.2 Radiomagnetotellurics

Radiomagnetotellurics is an extension of the VLF technique to a higher frequency band up to 1 MHz (Tezkan, 1999). The principle of this method is shown schematically in Figure 3.17. The magnetic field is measured with a coil and compared to the electric field measured typically between a pair of grounded electrodes. From the ratio of amplitudes of the horizontal electric and magnetic field components apparent resistivity values are derived using the

[5]In radio technology, these frequencies are considered "very low", however they are comparatively high in the context of applied geophysics

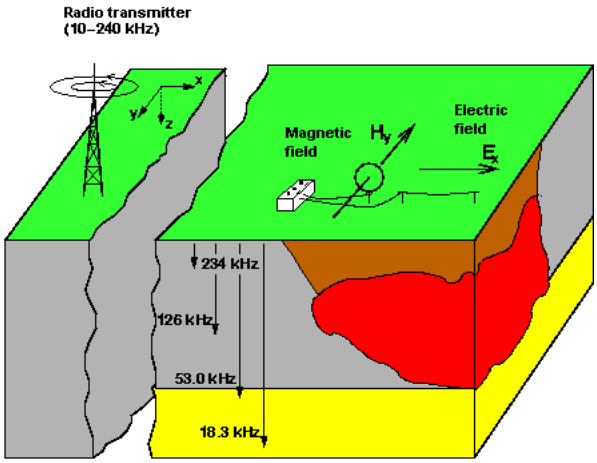

Figure 3.17: Schematic diagram of a field setup in radiomagnetotellurics (Tezkan, 1999).

classical relation of magnetotellurics (Cagniard, 1953):

$$\rho_a^{xy} = \frac{1}{\omega\mu_0}\left|\frac{E_x}{H_y}\right|^2 \tag{3.35}$$

$$\varphi^{xy} = \arctan\left[\frac{\mathrm{Im}(E_x/H_y)}{\mathrm{Re}(E_x/H_y)}\right] \tag{3.36}$$

As opposed to traditional MT however, phase measurements between electric and magnetic field components are precise because the transmitter operates at a single, well-defined frequency. Due to the extended frequency range of RMT and the large number of available transmitters, data can be interpreted quantitatively by resistivity models from which depth information can be derived.

3.3.3 Magnetometric resistivity

A relatively unknown electrical method that uses low-frequency galvanic currents analogous to DC resistivity is referred to as the Magnetometric Resistivity (MMR) method (Edwards, 1974; Edwards et al., 1978). It is based on the measurement of low-level magnetic fields associated with non-inductive current flow in the earth at frequencies between 1 and 5 Hz. It bears some resemblance to DC resistivity in so far as a pair of galvanic current electrodes is used to create quasi-stationary (pseudo-DC) current flow, however the potential electrodes are replaced by a highly sensitive component magnetometer measuring the low-frequency magnetic field due to this current. The horizontal component perpendicular to the current dipole is typically recorded. The presence of an inhomogeneity in the resistivity distribution causes perturbation of the current and hence the magnetic field. The resulting "MMR anomaly" is defined as the difference between the measured value of the horizontal component of the magnetic field and the "normal" value expected over a uniform earth. Magnetic fields due to EM induction are negligible due to the low frequencies used.

MMR does not yield absolute values of resistivity, yet it is directly sensitive to the resistivity distribution in the subsurface. The close relation with DC resistivity facilitates an integration of the two techniques. Kulessa et al. (2000) have recently described a method known as the Magneto-Electrical Resistivity Imaging Tool (MERIT), which provides a framework for the joint inversion of electrical and MMR data. According to the authors, MERIT is intended to be applied to the high-resolution imaging of subsurface pollution.

3.4 Discussion

The principle aim of all resistivity methods is to determine the spatial resistivity distribution in the subsurface. In the context of environmental and engineering assessments, one of the main applications is the detection, mapping and imaging of complex structures or contamination in the shallow subsurface. Resistivity methods are non-unique, but inherently stable and hence comparatively reliable. The "reduction of scale" associated with the application of these methods to shallow site investigations rather than regional geological studies gives rise to specific challenges:

- The near-surface resistivity distribution tends to be more complex than at depth. While large-scale studies often justify the assumption of layered earth models or simple two-dimensional structures, a site investigation is usually concerned with the examination of localised three-dimensional targets.
- The presence of man-made infrastructure as encountered on sites in the built environment can restrict the applicability of geophysical techniques. Engineered surfaces, reinforcements, services, power lines and similar features present a particular hindrance to the successful application of electrical methods.
- Inhomogeneities which could affect the detection of subsurface structures are often located at or near the surface (e.g. made ground, rubble etc.), potentially masking the target under investigation.
- Due to the presence of man-made materials, the electrical properties encountered in a site investigation may vary across a larger range of values. Hence the electrical contrast between an actual target structure and its host environment may be lower than for other, unrelated anomalies.
- Ground truth is much more readily obtainable for near-surface investigations and results from geophysical surveys may be challenged by evidence obtained from intrusive investigations.

Besides resistivity methods, other geophysical methods also have tomographic imaging capabilities. These include other electrical methods such as ground penetrating radar, self potential or induced polarisation. Seismic methods and potential field methods (gravity, magnetics) are equally suitable for tomographic imaging. However, these methods are all sensitive to different physical

parameters (dielectric permittivity, polarisability, acoustic impedance, density, magnetisation). The popularity of resistivity imaging is due to the fact that resistivity is a multi-purpose parameter linked to a variety of relevant physical and chemical properties and processes. Resistivity is an ideal parameter for general reconnaissance since it is one of the most dynamic physical properties in nature and can vary across many orders of magnitude.
Among the resistivity methods discussed, DC resistivity represents perhaps the most obvious methodology to obtain resistivity information from the shallow subsurface. It is reliable and inexpensive. The active injection of electric current (i.e. the use of a local source) gives rise to the inherent stability of the DC resistivity measurement. However, despite its many merits, the technique is not always advantageous. Its measurement principle, which requires galvanic contact to the ground, severely restricts the applicability of DC resistivity to surveys in the built environment. The ground conductivity technique is perhaps the second most important resistivity method in the environmental and engineering context. Its measurement principle is based on EM induction which implies certain advantages, but also disadvantages over conventional DC resistivity (McNeill, 1980). A critical comparison of the two approaches is presented in the following.

Galvanic vs. inductive coupling. Poor galvanic contact in DC resistivity (cf. Section 3.1.6.1) can severely affect data quality and at the worst prohibit the application of the method altogether. The only known remedy is to measure the contact resistances of individual electrodes and, if necessary, attempt to improve galvanic contact. This can be a painstaking process during large-scale surveys. Poor galvanic contact is the main impediment for routine application of DC resistivity surveys in the built environment. Problems of such kind are not encountered with the ground conductivity method since coupling is inductive and currents are induced magnetically. The method can therefore be employed also on resistive surfaces. Inductive conductivity measurements can be carried out fairly rapidly since no fixed installations (electrodes, cables, etc.) are required. Most ground conductivity instruments are highly portable and can therefore be used also in difficult terrain.

Dynamic range. The presence of extremely high or low resistivities affects the dynamic range of the DC resistivity and ground conductivity techniques differently. Electromagnetic methods have a limited dynamic range compared with DC resistivity. In areas of high resistivity/low conductivity it is difficult to magnetically induce a sufficient amount of current in the ground to generate detectable magnetic fields at the receiver coil (McNeill, 1980). While contact impedances may be a problem, it is generally easier to inject current galvanically into resistive ground. For very low resistivities/high conductivities the low induction number approximation may no longer hold and the inductive response becomes a nonlinear function of conductivity. In contrast, there is no theoretical limit below which DC resistivity does not work. However, the rapid signal decay in conductive environments may lead to limitations in array separation.

Vertical sounding capability. In theory, information about the vertical resistivity distribution can be obtained with inductive techniques by varying the intercoil spacing. This is analogous to the variation of electrode separation in DC resistivity. In practice however, the rapid fall-off of the magnetic field generated by the transmitter coil means that considerable effort is required to produce sufficiently large signals at larger coil separations, given a fixed coil size (McNeill, 1980). This problem is somewhat less significant in DC resistivity since current and potential dipoles can easily be increased in size to make up for smaller signals.

Near-surface inhomogeneities. For the ground conductivity technique, local inhomogeneities in conductivity close to the transmitter or receiver coils have only small effects on the measured response. This is in contrast to DC resistivity, where inhomogeneities near the potential electrodes can cause significant errors. Such a phenomenon is well-known from magnetotellurics where it is referred to as "static shift", however an equivalent effect exists in DC resistivity (Spitzer, 2001).

Electromagnetic effects. The presence of metallic objects (e.g. fences, power lines, cables, services, steel reinforcements, cars etc.) in the vicinity of inductive sensors may cause strong electromagnetic coupling which can result in erroneous readings or even sustained system saturation. This is a severe impediment for the use of the ground conductivity method in the urban built environment where such objects are omnipresent. Electromagnetic coupling is less problematic in DC resistivity as stationary currents are inherently unable to induce time-varying electromagnetic fields.

System calibration. For the ground conductivity technique, apparent resistivities are derived from the system response function which is defined relative to the response in free space. Ideally, conductivity meters would therefore have to be suspended far away from any conductive medium in order to set the instrument zero. In practice however, high resistivity environments are chosen for calibration where resistivities have been determined using conventional DC resistivity. Absolute values of resistivity obtained from inductive measurements are therefore always subject to potential bias due to loss of calibration. In contrast, DC resistivity is an absolute measurement which does not require such calibration.

Survey economics. Large-scale DC resistivity surveys are extremely fieldwork intensive, especially if high-resolution information is desired, because they require a large amount of individual electrode positions. Besides the installation of electrodes, the actual measurement is also time consuming because the higher the desired resolution, the more different array geometries are required. Although this problem has been addressed by the development of multichannel resistivity meters and intelligent field techniques, DC resistivity is still not very frequently used for large-scale surveys.

In contrast, the ground conductivity technique employs portable sensors which allow a single reading to be taken at a time, hence the inherent advantage of the non-galvanic measurement is lost due to the fact that measurements are performed sequentially. This is of particular disadvantage if depth information is required and multiple readings at different separations are to be taken at the same location.

It is evident that none of the resistivity methods discussed is ideally suited for high-resolution imaging in environmental and engineering site investigations. The greatest impediment with DC resistivity is that galvanic contact is required which rules out routine application on artificial surfaces and makes the technique cumbersome. The applicability of EM techniques is mainly restricted by undesired coupling effects and limited imaging capability. Other techniques such as complex resistivity and MMR are still emerging and it remains unclear whether these techniques will become routinely applicable to site investigations. In conclusion, there is a need for a technique that extends the simplicity, high-resolution imaging capability and proven track record of DC resistivity to surveys in the built environment, while at the same time increasing the efficiency of data acquisition.

Chapter 4

The capacitive resistivity (CR) technique

All electrical and electromagnetic methods require some form of coupling between a sensor and the ground. The coupling mechanism can have predominantly galvanic, inductive or capacitive character, depending on the nature of the source field, and the frequencies and type of sensors employed (coils, electrodes etc.). In the DC technique, resistivity is measured with static or low-frequency electric fields giving rise to a direct or pseudo-direct current. Galvanic contact is required between electrodes and the ground to enable current flow. For higher frequencies however, EM coupling is more advantageous. From an electromagnetic point of view, resistivity is more generally described by the complex permittivity which accounts for conduction currents by virtue of a resistivity component as well as for displacement currents by means of a dielectric component. The DC technique can be regarded as the zero- or low-frequency implementation of electromagnetic principles for the investigation of the resistivity component. At very high frequencies, EM techniques give rise to wave propagation and assessments of the dielectric component (e.g. GPR). In an intermediate frequency interval in the audio range, a low induction number, quasi-static mode of operation exists. This mode of operation is well known for magnetic sources used in the ground conductivity technique (Section 3.2).
The capacitive resistivity (CR) technique exploits the fact that, for electric sources, the quasi-static mode allows for capacitive coupling between sensors and the ground by virtue of the time-varying electric source field. This chapter introduces the CR technique to the reader. After a review of the historical development of CR and existing literature, the fundamental concepts of the technique are discussed. A classification of the basic types of capacitive sensors is given and existing CR instruments are reviewed. After discussing an early approach to CR theory based on the use of capacitive line antennas, the electrostatic formalism is established as the preferred theoretical model for a capacitive resistivity measurement under quasi-static conditions. Based on this formalism, a new phase-sensitive expression for apparent resistivity is developed. The final section discusses open questions about CR which are addressed in the later chapters of this thesis.

4.1 Historic origins

4.1.1 Early Russian research

Capacitive measurements of resistivity apparently originated in Russia where researchers in the 1970s successfully employed capacitive line-antennas as sensors for electric and electromagnetic profiling. (Timofeev, 1973, 1974, unpublished, and 1978). Prototype instrumentation was developed and the technique appears to have been in routine use in the Soviet Union at the time. Its development may have been a consequence of the need for an electrical technique applicable to surveys on frozen ground. The importance of this application is not to be underestimated, bearing in mind that about one fifth of the Earth's land surface is underlain by permafrost. Permafrost is permanently frozen subsoil that maintains a temperature below 0 ℃ permanently for two years or longer. It may contain moisture in the form of water or ice. Where the ice volume exceeds the pore volume that the ground would naturally have when unfrozen, the permafrost contains excess ice and is termed ice-rich. Ice-rich ground is a geotechnical engineering hazard (cf. Section 2.3.2) and is often subject to detailed mapping investigations in periglacial regions. It is associated with extremely high resistivities ($> 10^4\,\Omega$m) which makes electrical techniques suitable for its detection. However, DC resistivity is impractical for this application as most fieldwork has to be carried out during winter time when the top soil is frozen. It is only then that those regions are accessible with vehicles and heavy equipment. On frozen ground however, galvanic contact is almost impossible to achieve. Ground conductivity mapping is not always an alternative since inductive techniques operate at their limits in a high resistivity environment such as the permafrost. The capacitive technique however was found to overcome these problems.
As part of the Russia-Canada Northern Scientific Exchange Programme, the technology was exported to North America and joint research was carried out by Russian scientists and the Geological Survey of Canada in the 1980s, which comprised extensive field studies (Burns et al., 1993). These efforts eventually led to the development of an early Canadian capacitively-coupled resistivity system using line antennas (Timofeev et al., 1994; Douma et al., 1994) which was later commercialised.

4.1.2 The electrostatic approach

Grard (1990a) clearly had a different application in mind when he first proposed a system to measure the complex permittivity of the ground by virtue of the properties of a quadrupolar array. In his paper, an earlier concept of Storey et al. (1969) to measure space plasma properties was adapted to the investigation of planetary surfaces, a potential application being the use in unmanned planetary rovers. Two poles of a quadrupolar array carry electrostatic charges of opposite sign each of which create an electrostatic potential in the surrounding space. The difference in potential can then be measured at the two remaining poles of the array, its magnitude being linked directly to the permittivity of the medium. The key proposition was that this relation remains valid

for time-varying charges, as long as quasi-static conditions are maintained. In a second paper (1990b), Grard applies the same principle to sensors mounted on so-called penetrators, i.e. devices that invade the surface material during a planetary landing mission and carry out in-situ measurements.

Shortly afterwards, Grard and Tabbagh (1991) highlighted the implications of this new concept for near-surface geophysical investigations. They examined the parameters required to apply Grard's concept to resistivity surveying and suggested that the technique could even yield dielectric information in highly resistive environments. Additionally, they indicated the possibility of using mobile sensor arrays and presented a first instrument prototype together with results from early surveys in Garchy[1]. However, although the capacitive nature of the technique was acknowledged, some of the implications of this discovery had yet to be fully examined.

4.2 Fundamental concepts

Resistivity measurements based on capacitive coupling have been described from rather diverse viewpoints in the literature. Aspects related to the use of a particular type of instrument or sensor have somewhat disguised the concept of CR as a very specific realisation of a general electromagnetic measurement. CR is associated with a unique mode of operation that has the following characteristics:

1. An oscillating non-grounded electric dipole is used as a controlled source to create electric current flow in the ground.

2. Moderate frequencies in the audio range are employed.

3. The measurement operates in a quasi-static mode under the condition of low induction numbers.

4. The coupling mechanism between sensors and the ground is predominantly capacitive, i.e. coupling is mainly provided by the electric field and inductive effects are negligible. The sensors are referred to as *capacitive electrodes*. Their properties are crucial to the spatial extent of the coupling.

5. Under quasi-static conditions the capacitive measurement of resistivity is essentially equivalent to the DC method. The resistivities obtained can be used in conventional DC interpretation schemes.

Given the variety of approaches, a common terminology contributes to the understanding and propagation of a method. Therefore, the term "capacitive resistivity (CR) technique" has been conceived to describe measurements that

[1]Testing facilities for applied geophysical techniques are maintained by the Centre National de la Recherche Scientifique (CNRS) at the Centre de Recherches Géophysiques, Garchy, Pouilly sur Loire, France. This location is otherwise well-known for hosting a long-term comparative study of conventional electrodes for electric field monitoring (Perrier et al., 1997).

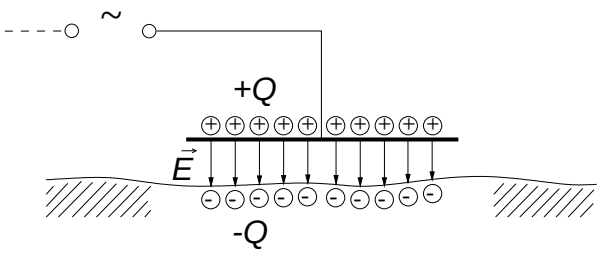

Figure 4.1: Conceptual model of a capacitive electrode: a charged conductor in the proximity of the ground surface.

follow the concepts outlined above. The term will be used in this thesis to stress the capacitive nature of the measurement.

4.2.1 The capacitive electrode

Any insulated conductor can accumulate electric charge while creating an electric potential with regard to its environment. An accumulation of electric charge on one conductor induces a charge of opposite sign on neighbouring conductors, giving rise to a difference in electric potential. The ratio $C = Q/U$ between accumulated charge Q and the resulting potential difference $U = \Delta V$ is constant and defined as the *capacitance* of the arrangement. The charge distributions create an electric field which provides coupling and contains the energy stored in the arrangement due to the separation of charge.
This physical concept is the underlying principle of CR. A conductor in close proximity to the surface of the conductive Earth can be regarded as a *capacitive electrode* since it has a finite capacitance against ground and can therefore act as a pathway for electric current. When charged by an electrical generator, an electric field is established between the conductor and the ground surface. The conceptual model of such a capacitive electrode is shown in Figure 4.1. Shima et al. (1996) have shown that metallic objects such as plates, suspended horizontally above the ground while being kept insulated from the surface, are practical implementations of capacitive electrodes. The authors present an analogous electric circuit model where the capacitive electrode is represented by a simple capacitance in series with the ground resistance. However, this analogy is only conceptual and does not capture all aspects of the measurement.

4.2.2 The capacitive four-electrode array

The concept of capacitive electrodes can be applied to the four-electrode array used in conventional DC resistivity (cf. Section 3.1.1). Figure 4.2 shows a four-electrode capacitive array together with a simplified equivalent electric circuit model in which the contact resistances representing galvanic electrodes have been replaced by capacitances. As in the DC technique, the measurement circuit is divided into two parts: a transmitter circuit is used to energise the ground while the receiver part measures a potential. In transmitter mode, an electric current must be actively injected across the electrodes which pose a reactive

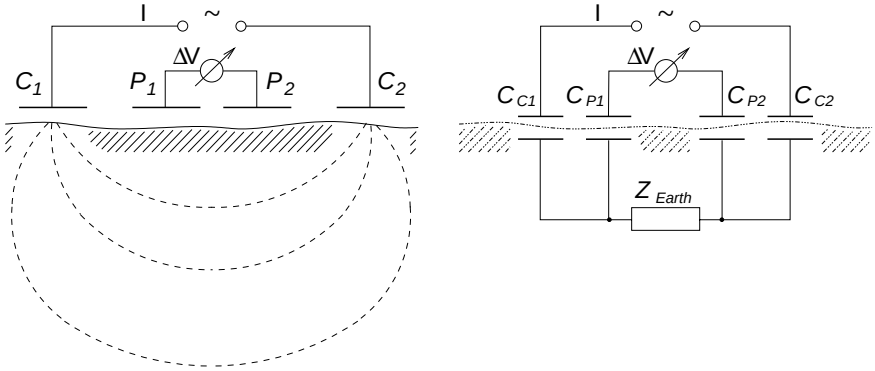

Figure 4.2: Basic concept of a capacitive resistivity measurement. Left: the four-electrode capacitive array. Right: simplified equivalent electric circuit model.

load to the generator. In receiver mode, capacitive electrodes are required to passively monitor the local electric field created by the source. In circuit terms, the potential measurement is coupled to the complex load that represents the ground via the capacitance of the receiver electrodes (Figure 4.2).

4.3 Capacitive sensors

Thus far the actual nature and extent of the capacitive coupling mechanism has not yet been described. In DC resistivity theory, electrical contact between the measuring device and the ground surface is restricted to point poles. In practice however, galvanic contact is established across those parts of the electrode surface which are buried in the ground and in physical contact with the soil. Despite this obvious discrepancy, the point electrode is found to be a sufficiently accurate approximation in most cases.
In the capacitive case, the objective must be to obtain a similar simplification as it is not immediately obvious which parts of the electrode surface actively participate in the coupling process. Capacitive electrodes never exist as localised, electrically isolated objects. Connecting wires and circuitry also have a capacitance against ground which will inevitably contribute to overall coupling. It may therefore be appropriate to replace the potentially misleading term "*capacitive electrode*" by the more general term "*capacitive sensor*". A capacitive sensor comprises all parts of the measuring device that significantly contribute to the electrical coupling and thus may have an influence on the result of a measurement. The design of capacitive sensors has an influence on the spatial extent of electric coupling and the lateral resolution of a measurement. Understanding sensor design is therefore crucial for the understanding of the CR technique. Different types of capacitive sensors are conceivable and the following classification seems appropriate.

4.3.1 The point electrode

This sensor type represents the theoretical situation in which capacitive coupling is restricted to a single point at the surface. Such "ideal" sensors correspond to the concept of point electrodes in DC resistivity, where current injection into the ground and potential measurement are restricted to single points. Point electrodes are equally important in capacitive resistivity. The electrostatic formalism (Section 4.6) as the preferred theoretical formulation of CR describes the characteristics of an idealised four-electrode capacitive array ("electrostatic quadrupole") based on the assumption of point poles. As in DC resistivity, a practical realisation of a point electrode is a conductor whose dimensions are small compared to the size of the four-electrode array and where coupling is confined to the surface of this conductor.

4.3.2 The capacitive line antenna

The opposite extreme of a point electrode is a linear antenna where capacitive coupling occurs over a certain distance. In this case no single point on the sensor is priviledged in terms of electrical contact. A segment of insulated wire or cable in close proximity to the surface can act as a "capacitive line antenna". The capacitance of such an antenna is evenly distributed across its length. Its conceptual model is shown in Figure 4.3. Historically, capacitive line antennas were the first sensors to be used for CR measurements (cf. Section 4.1.1). A theoretical description based on point poles is inherently inappropriate for line antennas and customised theory is required. A simple approach is described in Section 4.5.

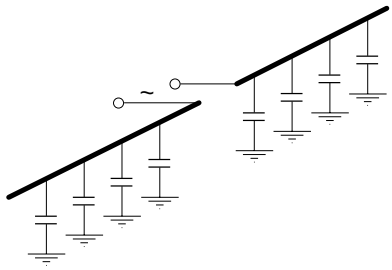

Figure 4.3: Conceptual model of a capacitive line antenna.

4.3.3 The plate-wire combination

Any practical realisation of the concept of a localised capacitive electrode as described in Section 4.2.1 is necessarily an object with a considerable surface area, for example a thin metal plate. The potential conflict with the requirements of a point electrode is obvious. Moreover, if such a plate is used as a capacitive electrode, it will be connected to the current source or potential measurement device by wire segments which themselves may contribute to the coupling, provided they have a significant capacitance against ground. In this thesis, such

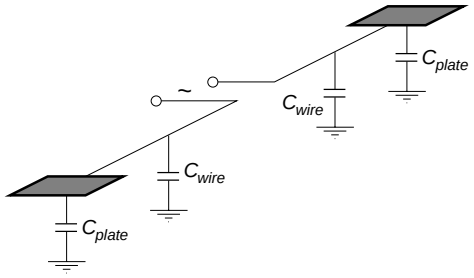

Figure 4.4: Conceptual model of a plate-wire combination.

an arrangement is referred to as a "plate-wire combination", whose conceptual model assumes a measurable capacitance for plates *and* wires (Figure 4.4). It can be regarded as a hybrid between a point electrode and a line antenna. The aim of using plate-wire combinations as capacitive sensors is to have a sensor for which the majority of the capacitive coupling is confined to the area of the plate, thus making the influence of the wire negligible. If the plate dimensions are small compared to the array dimensions, the point pole approximation may hold. It will be shown in Chapter 5 of this thesis that this is indeed possible, so that the plate-wire combination can be regarded as a practical realisation of the point pole concept.

4.4 Existing instrumentation

Although the CR technique has been in use for quite some time, it still remains widely unknown within the geophysical community, perhaps partly due to the inconsistent terminology used in the past. Only a small number of CR instruments has been developed over the years, some of which are research prototypes and therefore unavailable to the public. Among the few commercial CR instruments, two systems (OhmMapper™, CORIM™) have entered the market only very recently. All commercial systems have one property in common: their operation is based on the assumption of injected current and measured potential being in-phase. This can be a severe restriction, as no provision is made for circumstances where this assumption is invalid.
Different types of CR instruments can vary greatly in their specifications, which directly reflects the diversity of theoretical descriptions and intended applications. The distinguishing factors of all instruments are the frequency of operation, the type of capacitive sensors used and whether or not the instrument design allows the measurement of the CR phase. A comprehensive list of existing instruments and their specifications is given in Table 4.1.

4.4.1 Instruments based on line antennas

Historically, the early CR instruments such as the Russian VHCEP system employed line antennas in the form of cables laid out on the surface (Timofeev, unpublished). Such antennas consisted of flexible electric wire or cable

1	*Description:*	**VCHEP**
	Manufacturer:	VSEGINGEO, Russia
	Reference:	Timofeev (unpublished)
	Type:	Research
	Sensors:	Cables
	Frequency:	2 . . . 32 kHz
2	*Description:*	**RUSCAN**
	Manufacturer:	Androtex Ltd., Canada
	Reference:	Douma et al. (1994)
	Type:	Commercial
	Sensors:	Cables
	Frequency:	4, 8, 16, 32 kHz
3	*Description:*	**Active electrode EM/resistivity system**
	Manufacturer:	ERA, Russia
	Reference:	www.wplus.net/pp/era
	Type:	Commercial
	Sensors:	Cables
	Frequency:	4.88 Hz, 625 Hz
4	*Description:*	**Electrostatic Quadrupole**
	Manufacturer:	Université Paris VI, France
	Reference:	Grard and Tabbagh (1991)
	Type:	Research
	Sensors:	Plates, wheels
	Frequency:	44 . . . 128 kHz
5	*Description:*	**Multichannel capacitive electrode system**
	Manufacturer:	OYO Corp., Japan
	Reference:	Shima et al. (1995)
	Type:	Research
	Sensors:	Plates
	Frequency:	1Hz . . . 1.1 kHz
6	*Description:*	**OhmMapper™**
	Manufacturer:	Geometrics, USA
	Reference:	www.geometrics.com
	Type:	Commercial
	Sensors:	Cables
	Frequency:	16.5 kHz
7	*Description:*	**CORIM™**
	Manufacturer:	IRIS Instruments, France
	Reference:	www.iris-instruments.com
	Type:	Commercial
	Sensors:	Plates
	Frequency:	12 kHz
8	*Description:*	**Capacitively coupled borehole system**
	Manufacturer:	Geological Survey of Canada
	Reference:	—
	Type:	Research
	Sensors:	?
	Frequency:	?
9	*Description:*	**Borehole resistivity tool with capacitive sensors**
	Manufacturer:	Laboratoire Central des Ponts et Chaussées, France
	Reference:	Cottineau et al. (2000)
	Type:	Research
	Sensors:	Cylinders
	Frequency:	25 kHz
10	*Description:*	**CRI system**
	Manufacturer:	British Geological Survey, UK
	Reference:	This thesis
	Type:	Research
	Sensors:	Plates
	Frequency:	14.2 kHz, 10 . . . 50 kHz possible
	Special feature:	Measures fully complex transfer impedance

Table 4.1: Specifications of existing CR instruments.

in a dielectric sheath. The same is true for all instruments which were derived from the original Russian design, such as the RUSCAN system by Canadian manufacturers Androtex Ltd., or the recently introduced OhmMapper™ by Geometrics Inc. (USA). The VHCEP system was reportedly operated across a frequency range from as low as 2 kHz up to 32 kHz, while its commercial successors employ fixed frequencies of 4, 8, 16 or 32 kHz (RUSCAN) or 16.5 kHz (OhmMapper™).
Other Russian reports have also described resistivity measurements with non-grounded dipoles (Sapozhnikov, unpublished) but their relation with Timofeev's research is unclear. Timofeev et al. (1994) have pointed out that transmitter and receiver type and geometry can be varied depending upon the application. In particular, it was reported that the signal feeding point could either be located at the centre of the antenna (symmetric arrangement) or at the end point (asymmetric arrangement), in which case a ground reference is required and the system acts as a monopole (Figure 4.5). Based on extensive experience with permafrost mapping, the authors regard the collinear dipole-dipole configuration as the most efficient array since it can be pulled along the ground by a single operator.
The OhmMapper™ as modern successor of the original system reflects this concept. A dipole-dipole array consisting of transmitter and receiver sections linked by a piece of rope is pulled along the ground either by a person or attached to a vehicle. The line antennas consist of robust coaxial cables which can be exchanged for longer or shorter sections to vary the overall dipole lengths. Remarkably, all instruments based on line antennas have originally been designed with only one single receiver channel. In principle however, multi-receiver instruments can operate in the same fashion but with increased efficiency, particularly in towed array mode. The latest OhmMapper™ version employs a second receiver in a collinear arrangement, making simultaneous measurements on two channels possible.

4.4.2 Instruments based on plate sensors

It was not until the early 1990s that CR systems emerged in which localised capacitive sensors were employed. Based on the work of Grard (1990a), who devised the concept of an electrostatic quadrupole, a range of prototype CR systems were developed by the group of Prof. Alain Tabbagh at the Université Paris VI in France. The earliest model was used to prove the validity of the electrostatic concept and employed metal chains contained in plastic bags as capacitive sensors (Grard and Tabbagh, 1991). Later models used capacitive plates (Panissod et al., 1997b) and sensors were also mounted inside the wheels of towed trailers for road applications (Panissod et al., 1998).
Other systems have been developed and tested which employ capacitive plates as sensors and where the effect of capacitive coupling at the plates was explicitly recognised. However, the wider implications of the use of high frequency signals appear to have been largely disregarded. One such system was developed by Shima et al. (1995, 1996) who also indicated the possible application to multichannel imaging. The recently introduced CORIM™ system by French

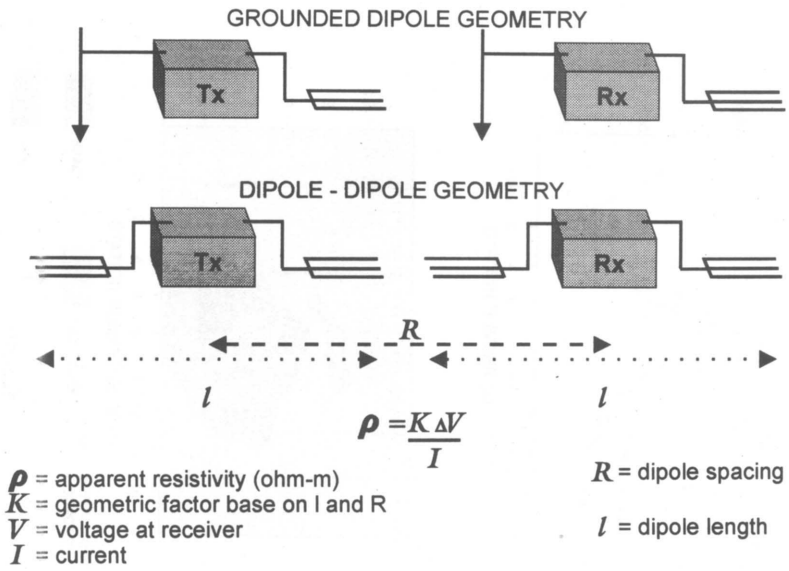

Figure 4.5: Schematic setup and configurations of the RUSCAN system (Timofeev et al., 1994).

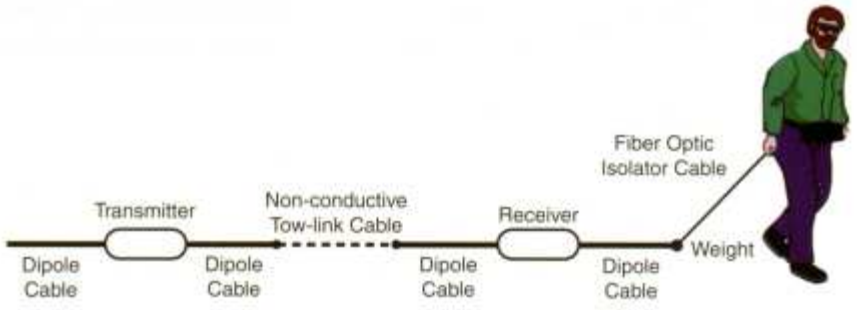

Figure 4.6: Schematic setup of the OhmMapper™ system (www.geometrics.com).

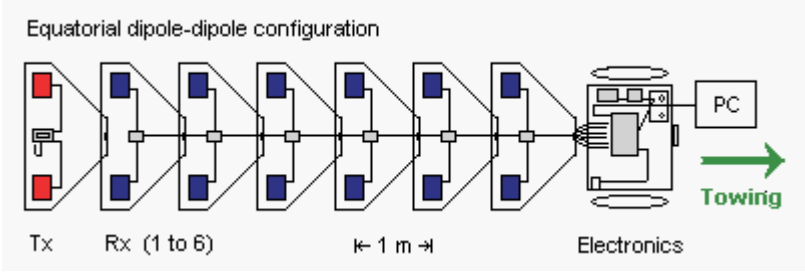

Figure 4.7: Schematic setup of the CORIM™ system (www.iris-instruments.com).

manufacturers IRIS Instruments is such a multichannel system based on plate sensors. It employs one transmitter and six receiver channels lined up at 1 m separations in an equatorial configuration (Figure 4.7).

4.4.3 Borehole instruments

The CR technique can also be employed for borehole applications. Dry boreholes with plastic casing, which would otherwise preclude the use of electrical techniques, seem particularly suited for a capacitive measurement. A prototype resistivity tool based on cylindrical capacitive electrodes has been developed by the Laboratoire Central des Ponts et Chaussées, a French organisation involved in civil engineering and transport research (Cottineau et al., 2000). A similar instrument is thought to be under development at the Geological Survey of Canada.

4.5 Early CR theory: the capacitive line antenna

From a very early stage of development, adequate theoretical description of the CR technique appears to have somehow lagged behind its practical application. In the original Russian research, capacitive line antennas were successfully employed to inject current and perform measurements of the electric potential. In order to interpret these measurements with regard to the resistivity of the subsurface, a corresponding theory had to be developed. DC resistivity theory was adapted for this purpose, taking into account that electrical coupling is no longer restricted to point electrodes. A brief overview of this early incarnation of CR theory is given in the following.

4.5.1 The capacitive line antenna as a non-grounded dipole

The DC resistivity technique uses grounded dipoles for which the current intensity along the transmitting line (i.e. the connecting wire) and the potential along the receiving line are generally assumed to be constant. The reason is that the conducting wire can be regarded as an equipotential for static or slowly varying fields. This remains true even for grounded wires with high contact resistances. The assumption however breaks down for the use of high-frequency fields, as observed by Timofeev (unpublished) during VLF surveys using grounded dipoles. The following empirical result was obtained from these experiments: on a given segment of line antenna close to the surface, the current was found to decay linearly with distance,

$$I(x) = \hat{I}(1 - \frac{x}{L}) \tag{4.1}$$

where $\hat{I}$ is the input current intensity, L the length of the antenna segment and x the distance along the segment. This behaviour was observed for frequencies in the audio range where corresponding wavelengths are much larger than antenna dimensions. Although no explanation for this result was given by the author, it can be understood by examining an equivalent electrical circuit of a linear conductor in close proximity to the ground. Details are discussed in Chapter 5.

4.5.2 The DC geometric factor

Based on this current distribution, a geometric factor K can be calculated by discretising the line antenna into a series of four-point arrays, each associated with a corresponding portion of the total current. Timofeev (unpublished) has shown that for the inline dipole-dipole array this geometric factor is given by the integral

$$\frac{1}{K} = \frac{\Delta V}{\rho I} = \frac{1}{\pi} \int_0^{L_T} \int_0^{L_R} \frac{I(x_1)}{\hat{I}} \cdot \frac{I(x_2)}{\hat{I}} \cdot \frac{1}{(r - x_1 + x_2)^3} \, dx_1 dx_2 \tag{4.2}$$

where L_T and L_R are the lengths of the transmitter and receiver antennas, respectively, r is the separation between them and x_1 and x_2 are distance coordinates along the transmitter and receiver antennas, respectively. This expression can be written as

$$K^{\mathrm{LA}} = \frac{\pi L_T}{\ln\left(\left(\frac{B^2}{B^2-1}\right)^{2B}\left(\frac{B^2+2B}{(B+1)^2}\right)^{2+B}\left(\frac{B^2-2B}{(B-1)^2}\right)^{B-2}\right)} \tag{4.3}$$

where

$$B = 2 \cdot \frac{r + \frac{1}{2}L_T + \frac{1}{2}L_R}{L_T}. \tag{4.4}$$

This method, together with the injected current and the potential measured at the feeding point of the antenna, can be used to calculate an apparent resistivity of the subsurface as observed with the capacitive line antenna. However, it has to be kept in mind that the entire length of the antenna contributes to the measurement, both in terms of current injection and potential measurement. This has important consequences for the interpretation of resistivity data obtained with capacitive line antennas.

4.5.3 The equivalent grounded dipole

Suppose capacitive line antennas are employed to form a dipole-dipole array and apparent resistivity measurements are conducted on a homogeneous subsurface. Then a dipole-dipole array of conventional grounded dipoles exists which would measure the same transfer impedance as the line antenna array. As the apparent resistivity on a homogeneous subsurface is independent of array geometry, the geometric factor K^{DC} of such an equivalent grounded dipole must satisfy the condition $K^{\mathrm{DC}} = K^{\mathrm{LA}}$. However, for equal separations r the length of the equivalent grounded dipoles l_{DC} is then obviously different from the length of the line antenna dipoles l_{LA} (Figure 4.8).
This is important if interpretation schemes (e.g. modelling and inversion algorithms) developed for DC resistivity (and grounded dipoles) are considered for use with data obtained from capacitive line antennas. In order to calculate the length of the equivalent grounded dipole l_{DC} explicitly, Timofeev's geometric factor (4.3) must equal the geometric factor of the conventional inline dipole-dipole array (3.22). An algebraic solution is unlikely to exist since (4.3)

would have to be solved for L. The results of a numerical comparison are shown in Figure 4.9. Assuming a symmetric array ($L_T = L_R$), the condition $K^{\mathrm{DC}} - K^{\mathrm{LA}} = 0$ as a function of L was solved for a range of dipole separations r. The ratio $l_{\mathrm{DC}}/l_{\mathrm{LA}}$ has been plotted against dipole separation r. This ratio is always smaller than one, i.e. the line antenna is always longer than its equivalent grounded dipole. For large separations, the equivalent grounded dipole is approximately half the length of the line antenna ($l_{\mathrm{DC}}/l_{\mathrm{LA}} \approx 0.5$). For $r > 4l$ the deviation from this value is smaller than 1%. At short separations however, the equivalent DC dipole can be significantly longer. For $r < 1.5l$, which is not an unusual configuration for line antenna instruments, the deviation is already greater than 7%.

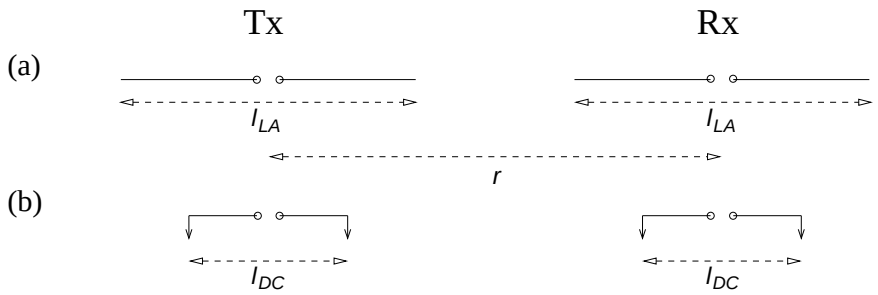

Figure 4.8: Inline dipole-dipole array composed of (a) capacitive line antennas and (b) equivalent grounded dipoles.

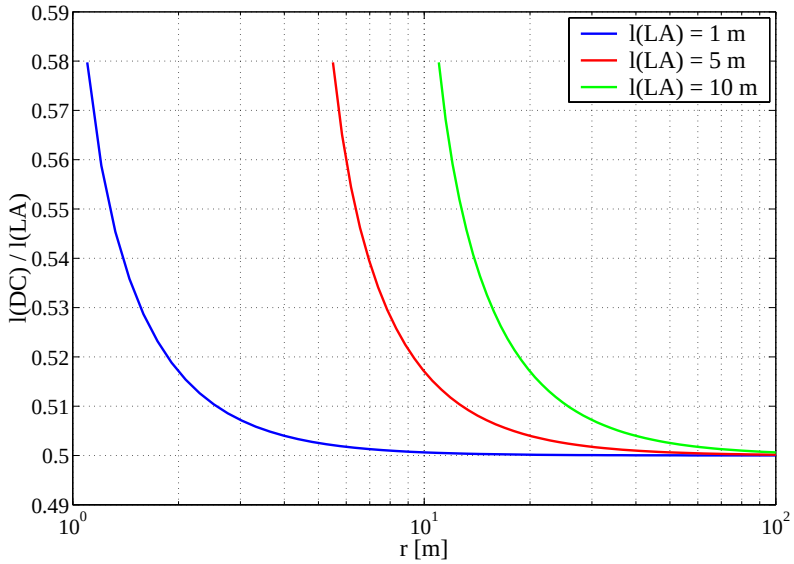

Figure 4.9: Relation between a capacitive line antenna and its equivalent grounded dipole as a function of dipole separation for the inline dipole-dipole array.

4.6 Electrostatic formalism and the complex transfer impedance

When localised capacitive sensors were first used in the early 1990s, a new theoretical framework was required to describe their specific properties. The concept of an "electrostatic quadrupole", introduced by Grard (1990a), was the key idea for a simple generic description of the capacitive resistivity technique. Electrodes are represented by point poles, hence the description is not limited to a particular sensor design. This section discusses details of this concept and redevelops Grard's formalism with unified and updated notation. This framework will be referred to as the "electrostatic formalism" in the following. It provides the necessary tools for the interpretation of resistivity measurements obtained with capacitive arrays based on localised sensors such as the plate-wire combination.

4.6.1 The electrostatic quadrupole

4.6.1.1 Electrostatic charge near an air-earth interface

Grard (1990a) considers electrostatic point charges near a planar interface between two homogeneous and isotropic halfspaces representing electrically different media. A charge located in the vicinity of the interface will create an electrostatic potential in its surroundings, which is a function of the dielectric properties of both media. The electrostatic potential can be readily calculated

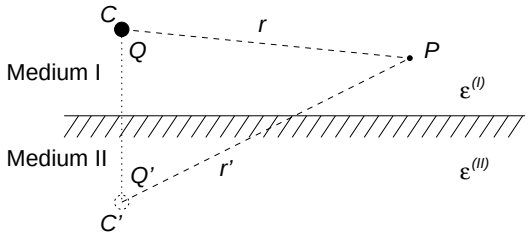

Figure 4.10: Electrostatic point charge Q near the interface between two media with dielectric permittivities $\varepsilon^{(\mathrm{I})}$ and $\varepsilon^{(\mathrm{II})}$. The image charge Q' is located at the opposite side of the interface.

using the theory of images. Suppose a charge Q is located at C and its image charge $Q' = -Q$ at C' (Figure 4.10), then the potential at a point P is given by

$$V(P) = \frac{Q}{4\pi\varepsilon^{(\mathrm{I})}} \left(\frac{1}{r} - \alpha \frac{1}{r'} \right) \tag{4.5}$$

where r corresponds to the distance $\overline{CP}$ and r' to the distance $\overline{C'P}$. Compared with the free space expression, (4.5) represents a superposition of two potentials, with an additional contribution originating from the image charge. The real

factor α contains the dielectric permittivities of the two media:

$$\alpha = \frac{\varepsilon^{(\mathrm{II})} - \varepsilon^{(\mathrm{I})}}{\varepsilon^{(\mathrm{II})} + \varepsilon^{(\mathrm{I})}} \tag{4.6}$$

In the case of an air-earth interface, these are given by

$$\varepsilon^{(\mathrm{I})} = \varepsilon_0 \tag{4.7}$$
$$\varepsilon^{(\mathrm{II})} = \varepsilon_0 \varepsilon_r \tag{4.8}$$

For *static* charges, α is therefore fully determined by the relative permittivity (dielectric constant) of the subsurface:

$$\alpha = \frac{\varepsilon_r - 1}{\varepsilon_r + 1} \tag{4.9}$$

4.6.1.2 The quadrupole concept

It is now straightforward to extend this result to a situation with four poles. In practice, an electric current source has two poles which carry opposite electric charges at any moment in time. Equally, potentials can only be measured in respect to a reference potential. This leads to the concept of an *electrostatic quadrupole* where two poles C_1, C_2 carrying charges $+Q$ and $-Q$, respectively, act as a current source, while the potential difference $\Delta V = V_1 - V_2$ is measured between the two other poles P_1, P_2 (Figure 4.11). The potential difference is given by (Grard, 1990a)

$$\Delta V = \frac{Q}{4\pi\varepsilon_0}\left(\frac{1}{r_{11}} + \frac{1}{r_{22}} - \frac{1}{r_{12}} - \frac{1}{r_{21}} - \alpha\left(\frac{1}{r'_{11}} + \frac{1}{r'_{22}} - \frac{1}{r'_{12}} - \frac{1}{r'_{21}}\right)\right) \tag{4.10}$$

This expression can be simplified by introducing the electrostatic geometric factor

$$K^{\mathrm{ES}} = \frac{\frac{1}{r'_{11}} + \frac{1}{r'_{22}} - \frac{1}{r'_{12}} - \frac{1}{r'_{21}}}{\frac{1}{r_{11}} + \frac{1}{r_{22}} - \frac{1}{r_{12}} - \frac{1}{r_{21}}} \tag{4.11}$$

which contains the distances between all poles, including the virtual poles carrying image charges. It is also useful to recognise that

$$C_0 = \frac{4\pi\varepsilon_0}{\frac{1}{r_{11}} + \frac{1}{r_{22}} - \frac{1}{r_{12}} - \frac{1}{r_{21}}} \tag{4.12}$$

has the dimensions of a capacitance and can be regarded as a mutual capacitance of the configuration in free space, although this is purely formal. The potential difference can hence be expressed as

$$\Delta V = \frac{Q}{C_0}\left(1 - K\alpha\right). \tag{4.13}$$

For a given pair of static charges in the vicinity of a homogeneous earth, the voltage across any two neighbouring points can thus be calculated if all four positions and the dielectric properties are known.

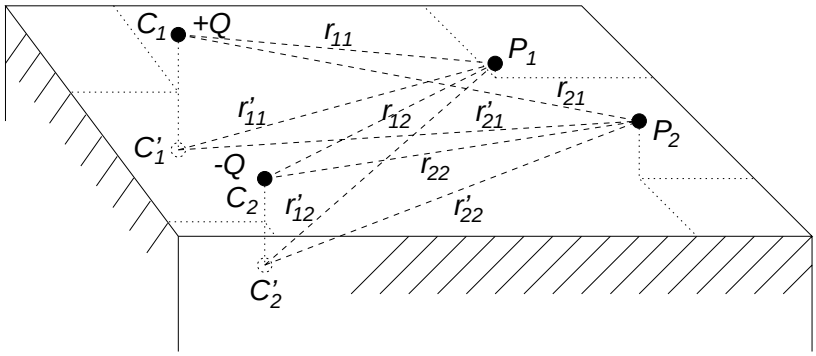

Figure 4.11: Geometry of an electrostatic quadrupole in the general case. Point charges $+Q$ and $-Q$ are situated at C_1 and C_2 near the interface between two permittive media. Image charges are located at C_1' and C_2' on the other side of the interface and the difference in electrostatic potential is measured between P_1 and P_2.

4.6.2 The quadrupole in quasi-static approximation

4.6.2.1 Variation of electric charge with time

The formulation used so far has been purely electrostatic, i.e. the results are strictly valid only for charges that are constant in time. However, for charges varying slowly with time, $Q = Q(t)$, it can be shown that the formulation (4.13) still applies under certain conditions. Suppose an alternating current $I = I(t)$ is injected across C_1 and C_2, then instantaneous charges $Q_1 = -Q_2$ with a magnitude of $|Q_1| = |Q_2| = Q$ will be observed at these poles. These charges can be expressed as the time integral of the injected current and with $I = \dot{Q}$ one obtains for harmonic currents

$$Q(t) = \int_{t_0}^{t} I(\tilde{t}) d\tilde{t} = \frac{1}{i\omega} I(t) + \text{const.} \tag{4.14}$$

The integration constant represents an arbitrary static charge at time t_0 which plays no role in the time-varying process and can be assumed to be zero. The formerly static expression for the potential difference now becomes time-dependent:

$$\Delta V(t) = \frac{I(t)}{i\omega C_0} (1 - K\alpha) . \tag{4.15}$$

4.6.2.2 The complex permittivity

At the same time as charge, current and potential become a function of time, the dielectric permittivities in (4.6) must now be regarded as being fully complex. As the injection of current across C_1 and C_2 implies electric current flow in the subsurface, the resistivity of the subsurface must be taken into account. The general form of the complex permittivity is (cf. Equation A.9, Appendix)

$$\varepsilon = \varepsilon_0 \varepsilon_r - i \frac{1}{\rho \omega} \tag{4.16}$$

In the case of the air-earth interface, the relevant permittivites are

$$\varepsilon^{(\mathrm{I})} = \varepsilon_0 \tag{4.17a}$$

$$\varepsilon^{(\mathrm{II})} = \varepsilon_0\varepsilon_r - i\frac{1}{\rho\omega} \tag{4.17b}$$

Accordingly, α is now also a complex number:

$$\alpha = \frac{\rho\omega\varepsilon_0(\varepsilon_r - 1) - i}{\rho\omega\varepsilon_0(\varepsilon_r + 1) - i} \tag{4.18}$$

It contains the electrical properties of both media together with the frequency and is therefore representative of the electrical behaviour of the arrangement.

4.6.2.3 The complex transfer impedance

The transfer impedance

$$Z = \frac{\Delta V}{I} \tag{4.19}$$

between the current dipole and the potential dipole can be regarded as the characteristic response function of the quadrupole arrangement. In (4.15), it is useful to identify

$$Z_0 = \frac{1}{i\omega C_0} \tag{4.20}$$

as the transfer impedance of the quadrupole in free space ($\alpha = 0$). The result is a simple complex relation for the transfer impedance:

$$Z = Z_0(1 - K\alpha) \tag{4.21}$$

The deviation from the free space value Z_0 is given by the product of the geometric factor K and the complex factor α, representing the electrical properties of the system.

4.6.2.4 Conditions for a quasi-static regime

The above results were derived from electrostatic equations by inserting a time-varying charge function associated with the injected current. This procedure ignores the electrodynamic framework of Maxwell's equations, according to which the time-varying current is associated with an electromagnetic field (cf. Appendix A.1). It is therefore crucial to establish a condition under which electromagnetic effects can be neglected. Grard and Tabbagh (1991) argue that the *quasi-static approximation* applies and (4.15) remains valid if the wavelengths $\lambda^{(\mathrm{I})}$, $\lambda^{(\mathrm{II})}$ of an electromagnetic wave of angular frequency ω in media of permittivities $\varepsilon^{(\mathrm{I})}$, $\varepsilon^{(\mathrm{II})}$ are much greater than the characteristic distances r and r' in the respective medium. In electromagnetic terms, this corresponds to the well-known conditions of a low induction number regime, i.e. the characteristic distances used must be small compared with the electromagnetic skin depth (cf.

Section 3.2.2). Based on experience with applying the electrostatic technique to long-offset resistivity soundings, Benderitter et al. (1994) have proposed the condition

$$\frac{\mu\omega L^2}{\rho} < 1, \tag{4.22}$$

where L is a characteristic dimension of the electrostatic array. If this condition is violated, (4.15) and (4.21) are no longer valid as the quasi-static approximation breaks down and inductive effects become relevant.

4.6.3 The electrostatic geometric factor

In order to understand the influence of geometry on the properties of the electrostatic quadrupole, it is useful to study the properties of the electrostatic geometric factor. For a number of reasons discussed at a later stage, dipole-dipole geometries are favourable for practical realisations of the electrostatic quadrupole. Two complementary configurations of a dipole-dipole array are the inline (also known as axial) and equatorial geometries (cf. Section 3.1.2.3), which will be considered here. Without loss of generality, only symmetric arrays will be discussed, i.e. current and potential dipoles are of equal size and elevation above the ground surface is identical for all poles. In the case of a symmetric equatorial array (Figure 4.12 top, cf. Figure 3.4), the electrostatic geometric factor (4.11) becomes

$$K_{\mathrm{eq}} = \frac{\frac{1}{\sqrt{r^2+4h^2}} - \frac{1}{\sqrt{r^2+l^2+4h^2}}}{\frac{1}{r} - \frac{1}{\sqrt{r^2+l^2}}} \tag{4.23}$$

where l denotes the length of current and potential dipoles, r their separation and h the elevation of all poles above the surface. In similar fashion, the geometric factor of a symmetric inline dipole-dipole array (Figure 4.12 bottom) is given by

$$K_{\mathrm{in}} = \frac{\frac{2}{\sqrt{r^2+4h^2}} - \frac{1}{\sqrt{(r+l)^2+4h^2}} - \frac{1}{\sqrt{(r-l)^2+4h^2}}}{\frac{2}{r} - \frac{1}{r+l} - \frac{1}{r-l}} \tag{4.24}$$

For a given practical array with fixed dipole lengths and fixed dipole separation, the geometric factor remains a function of the elevation h above ground. This is in contrast to DC resistivity where the geometric factor is fixed. Figure 4.13 shows the variation of K with h for both equatorial and inline geometries. The limiting cases are

$$K \longrightarrow 1 \quad \text{for} \quad h \longrightarrow 0 \tag{4.25}$$

$$K \longrightarrow 0 \quad \text{for} \quad h \longrightarrow \infty. \tag{4.26}$$

Numerical values of K for a range of array parameters are given in Table 4.2. It is evident that for realistic arrays with $r > l$ and elevations $h < 0.1$ m the geometric factor K is always > 0.999 (i.e. $K \approx 1$).

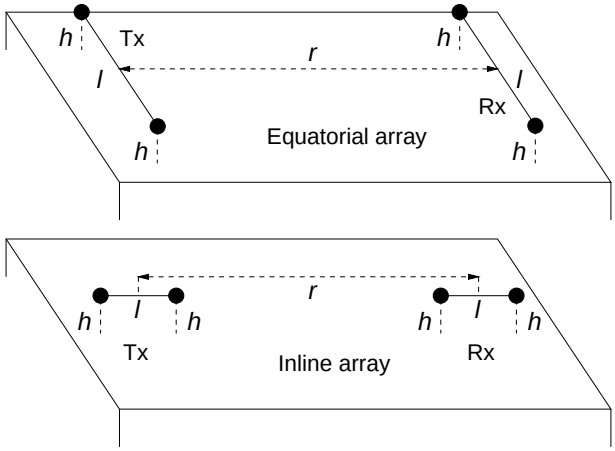

Figure 4.12: The symmetric equatorial (top) and inline (bottom) dipole-dipole configurations of the electrostatic quadrupole.

l [m]	r [m]	h [m]	K_{in}	K_{eq}
1	2	0.001	0.9999952778	0.9999986528
1	5	0.001	0.9999994894	0.9999997646
1	10	0.001	0.9999998782	0.9999999403
1	2	0.01	0.9995279472	0.9998652938
1	5	0.01	0.9999489461	0.9999764635
1	10	0.01	0.9999878175	0.9999940298
1	2	0.1	0.9544156143	0.9866781496
1	5	0.1	0.9949111436	0.9976509134
1	10	0.1	0.9987826698	0.9994032697
2	5	0.001	0.9999993712	0.9999997768
2	10	0.001	0.9999998724	0.9999999412
2	5	0.01	0.9999371275	0.9999776761
2	10	0.01	0.9999872362	0.9999941158
2	5	0.1	0.9937401944	0.9977717170
2	10	0.1	0.9987246570	0.9994118646

Table 4.2: Numerical values of K for inline and equatorial array geometries and a range of array parameters.

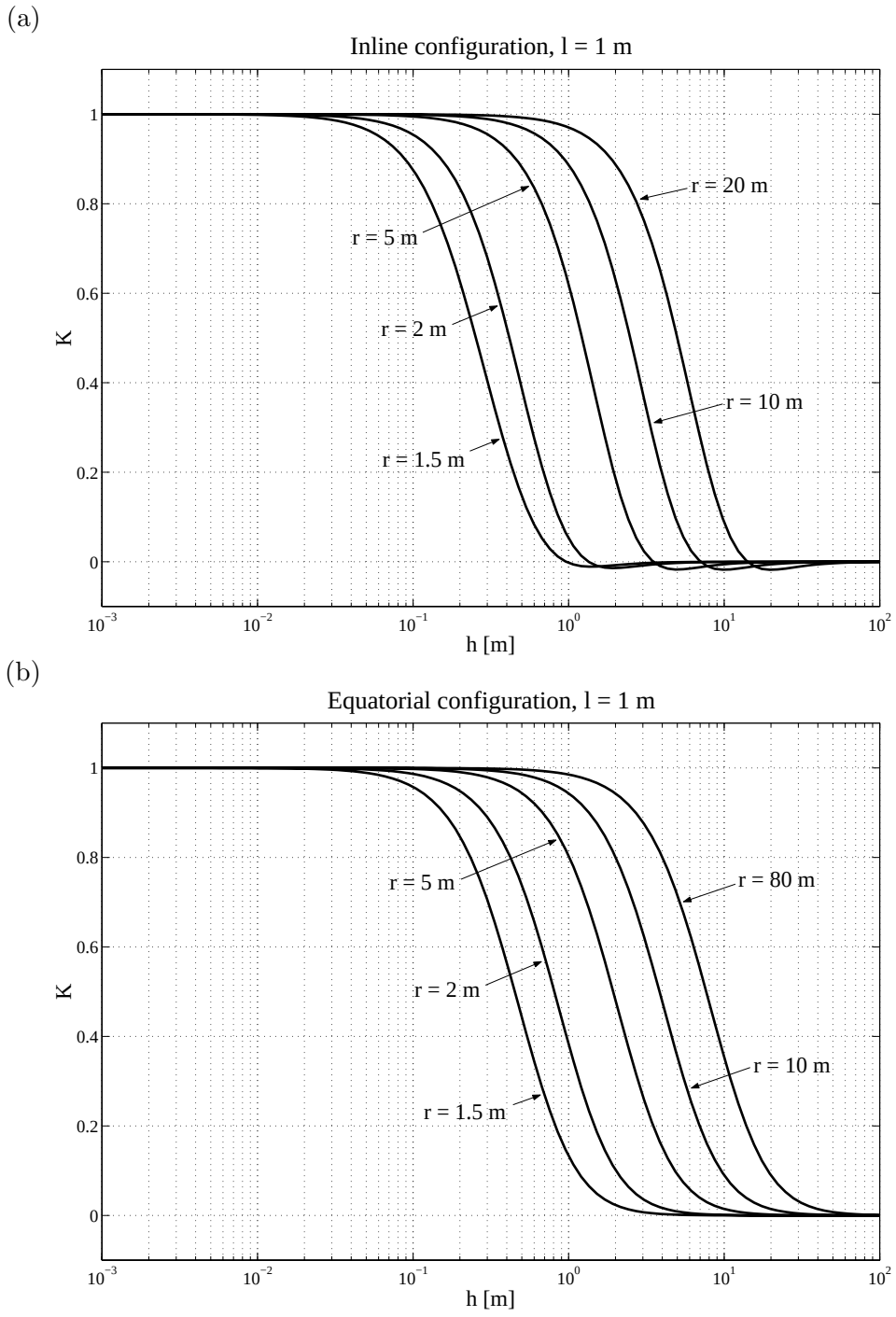

Figure 4.13: Variation of the electrostatic geometric factor with elevation h. (a) inline dipole configuration, (b) equatorial dipole configuration. Tx and Rx dipoles are 1 m long and all poles have the same elevation above ground.

4.6.4 Properties of the complex transfer impedance

4.6.4.1 Normalisation and generalised frequency

For a better understanding of the general properties of the quadrupole in quasi-static approximation, it is necessary to examine the behaviour of the complex transfer impedance over a wide range of frequencies. For this purpose, it appears convenient to consider the expression

$$\frac{Z}{|Z_0|} = -i(1 - K\alpha) \tag{4.27}$$

which represents a normalisation of (4.21) by the modulus of the free space value, i.e. phase relations and signs are retained. A generalised frequency can be introduced that contains subsurface properties in addition to the angular frequency (Grard, 1990a):

$$\Omega = \rho\omega\varepsilon_0(\varepsilon_r + 1) \tag{4.28}$$

Thus, (4.18) can be rewritten as

$$\alpha = \frac{\Omega\frac{\varepsilon_r - 1}{\varepsilon_r + 1} - i}{\Omega - i} = \frac{\Omega^2\frac{\varepsilon_r - 1}{\varepsilon_r + 1} + 1 - i\frac{2\Omega}{\varepsilon_r + 1}}{\Omega^2 + 1} \tag{4.29}$$

and the normalised transfer impedance (4.27) becomes

$$\frac{Z}{|Z_0|} = \frac{\frac{2K\Omega}{\varepsilon_r + 1} - i\left(\Omega^2\left(1 - K\frac{\varepsilon_r - 1}{\varepsilon_r + 1}\right) + 1 - K\right)}{\Omega^2 + 1} \tag{4.30}$$

4.6.4.2 Variation with Ω

The variation of Equation (4.30) with generalised frequency over six decades is shown in Figures 4.14 (in-phase and quadrature) and 4.15 (magnitude and phase) for a range of values for the electrostatic geometric factor K. Figure 4.16 shows the variation of the factor α for the same frequency range and for a range of values for ε_r. Three different regions with respect to Ω can be identified from the graphs:

$\Omega \approx 1$. The normalised transfer impedance is found to be highly sensitive around $\Omega = 1$, which corresponds to the situation in which the dielectric term $\varepsilon_0\varepsilon_r$ and the resistivity term $(\rho\omega)^{-1}$ of the complex permittivity (4.16) are of the same order of magnitude. In electromagnetic terms, $\Omega = 1$ represents the transition from a conductive to a dielectric regime. At $\Omega = 1$ the in-phase component has a maximum, reaching about 50% of the free space value Z_0 for $K \approx 1$ (Figure 4.14 top), and both magnitude and phase of $Z/|Z_0|$ have steep gradients for relevant K (Figure 4.15).

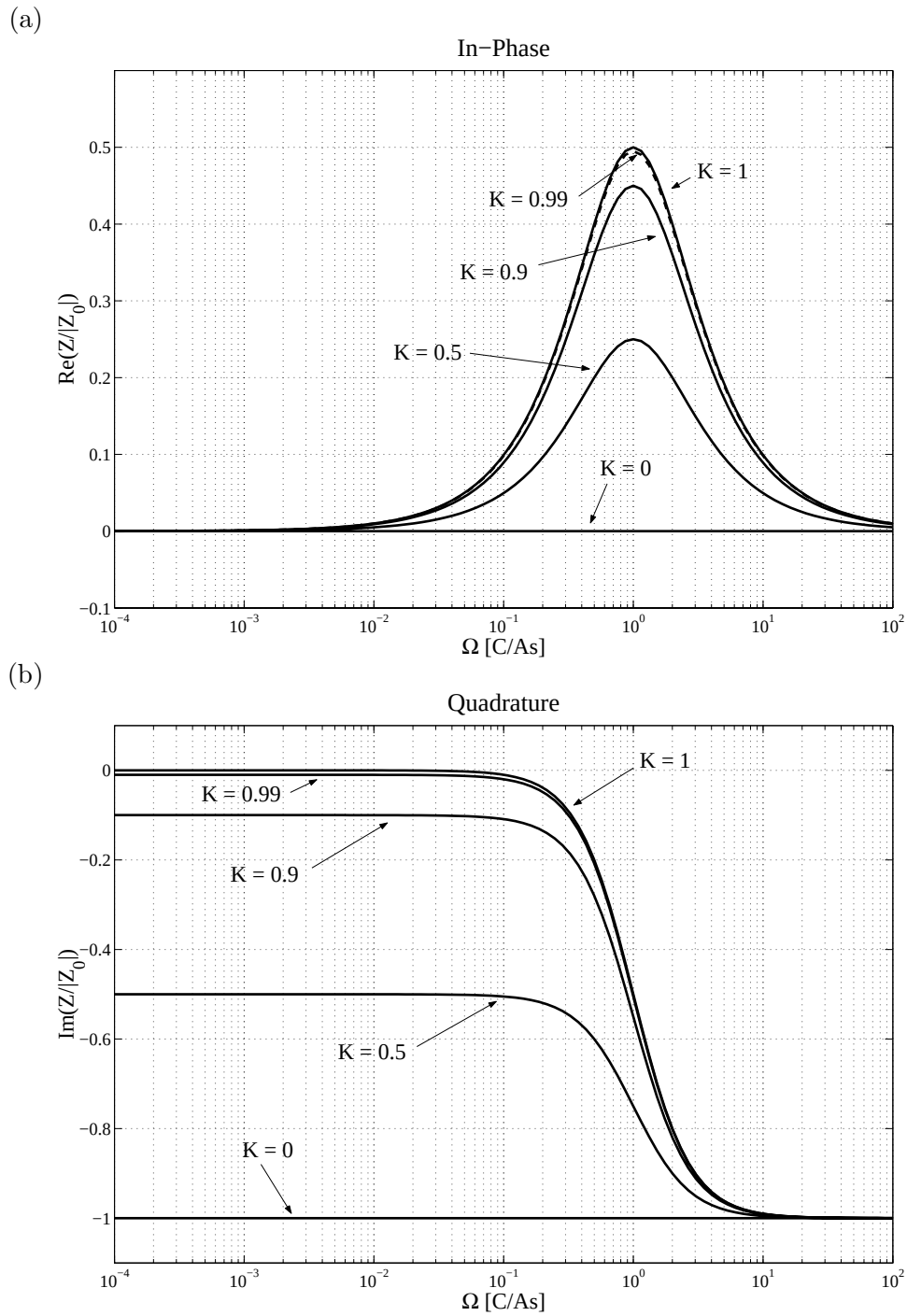

Figure 4.14: Variation of the normalised transfer impedance $Z/|Z_0|$ with generalised frequency Ω (parameter: geometric factor K). (a) in-phase, (b) quadrature.

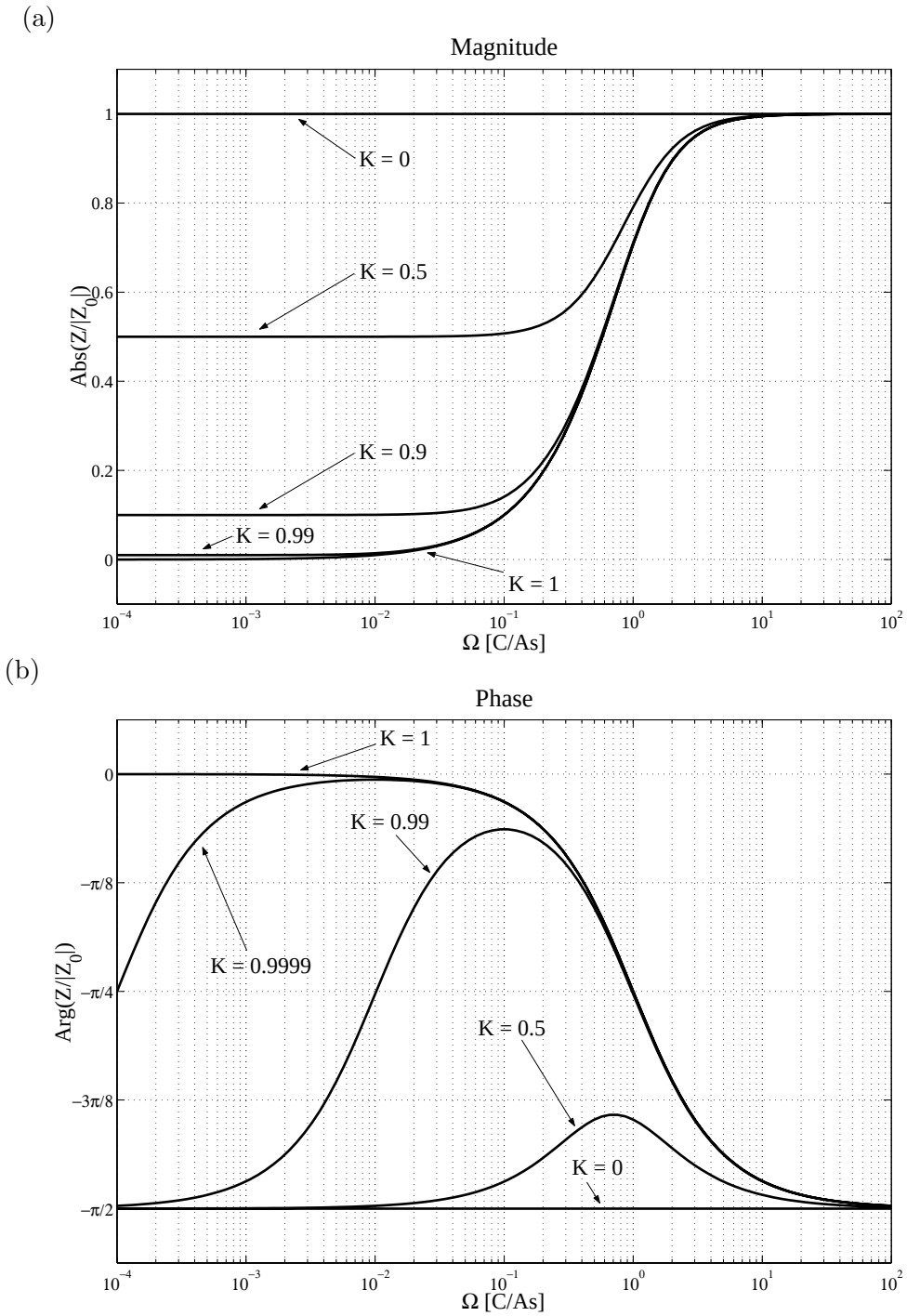

Figure 4.15: Variation of the normalised transfer impedance $Z/|Z_0|$ with generalised frequency Ω (parameter: geometric factor K). (a) magnitude, (b) phase.

(a)

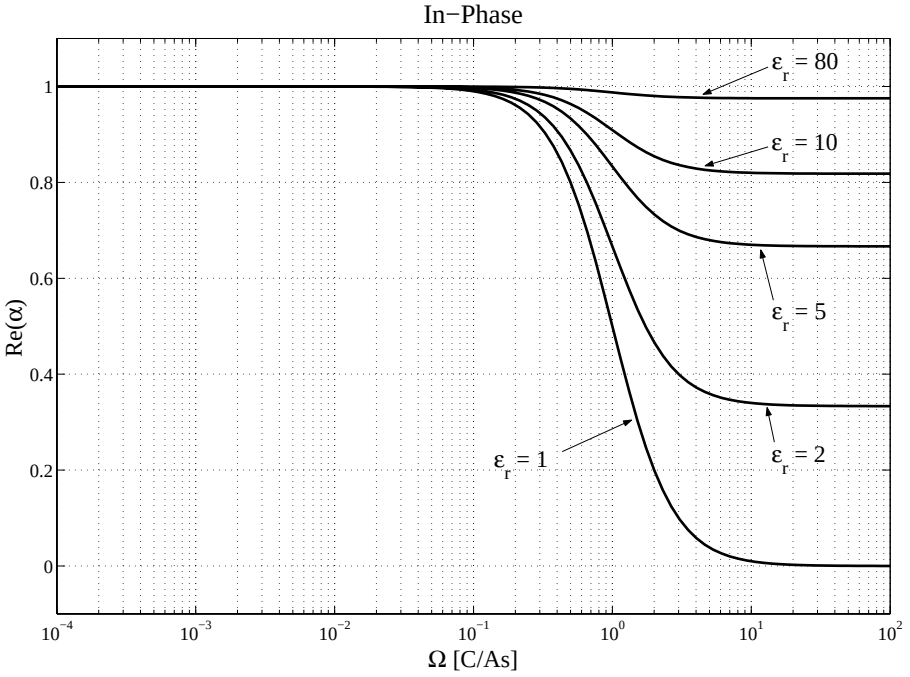

(b)

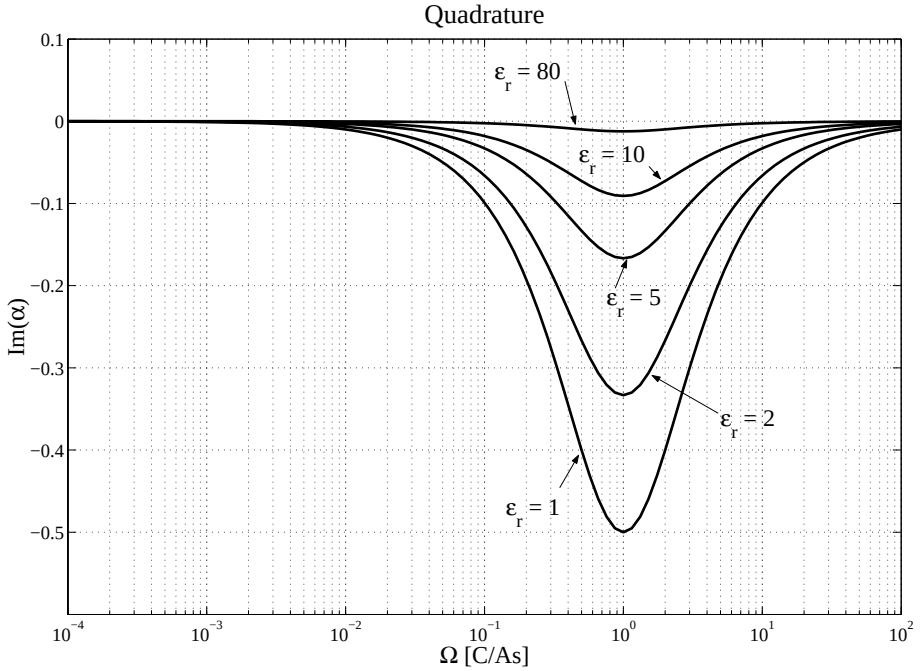

Figure 4.16: Variation of α with generalised frequency Ω. (a) in-phase, (b) quadrature.

$\Omega \ll 1$. This region corresponds to a conductive regime, i.e. the resistivity term $(\rho\omega)^{-1}$ dominates the dielectric term $\varepsilon_0\varepsilon_r$. Under these circumstances one observes that $\mathrm{Re}\,\alpha \approx 1$ (Figure 4.16, cf. Equation 4.29). The magnitude of $Z/|Z_0|$ tends towards a constant value which strongly depends on K (Figure 4.15 top). $K = 1$ represents the situation where poles are situated on the interface, which corresponds to the DC arrangement (cf. Section 4.6.5.3) but is unrealistic for capacitive operation of the quadrupole. For $K \approx 1$ the magnitude of $Z/|Z_0|$ in this region is of the order of a few percent of Z_0. Smaller values of K are not encountered in practice. Meanwhile, the phase angle varies considerably in this region and strongly depends on K (Figure 4.15 bottom). It generally tends towards $-\pi/2$ for $K \neq 1$ and very small Ω, however for $1 > K > 0.99$ and a broad range of Ω ($10^{-3} < \Omega < 10^{-1}$ for $K = 0.9999$), Z tends to have very small phases, i.e. the measured potential is nearly in-phase with the injected current. However, significant phase variations are possible in this region, for example due to changes in K.

$\Omega \gg 1$. This region corresponds to a dielectric regime where the dielectric term $\varepsilon_0\varepsilon_r$ dominates the resistivity term $(\rho\omega)^{-1}$. This is expressed in the sensitivity of the in-phase component of α towards relative permittivity (Figure 4.16 top). For $\Omega \gg 1$ the magnitude of the normalised transfer impedance tends towards one, i.e. Z assumes its free space value under the dielectric regime. The phase becomes $-\pi/2$, as one would expect from Z_0 being imaginary and negative.

	Low	Typical	High
ρ [Ωm]	1	50	100000
f [kHz]	1	15	100
ε_r	1	3	80
Ω [C/As]	$1.1 \cdot 10^{-7}$	$1.7 \cdot 10^{-4}$	45.1

Table 4.3: Range of possible values for the generalised frequency Ω.

Since Ω is a generalised frequency, it is necessary to explore the influence of the incorporated parameters. These are resistivity, dielectric constant and (true) frequency of operation. Table 4.3 shows the range of these parameters likely to be employed in field surveys, together with the resulting range of values for Ω. Resistivities of the order of 1 Ωm can be considered low, although even lower values are possible in extreme cases. The smallest possible dielectric constant is $\varepsilon_r = 1$ and the lowest frequencies likely to be used are of the order of 1 kHz (a more detailed discussion will follow in Chapter 5). In contrast, resistivities of $\rho = 10^6$ Ωm, frequencies of 100 kHz and $\varepsilon_r = 80$ would be considered high values. Typical values for all three parameters would be expected to be well inside of these limits. The resulting values for Ω indicate that the generalised frequency can easily vary across many orders of magnitude, but is most likely to be much smaller than one. Realistically, the electrostatic quadrupole will therefore operate under a conductive regime ($\Omega \ll 1$).

4.6.5 Solution of the reverse problem

The electrostatic formalism models the quadrupole response in the form of a transfer impedance, based upon knowledge of the electrical properties of the subsurface and geometric parameters. A practical field technique must solve the reverse problem, i.e. the electrical properties of the subsurface must be derived from a measurement of the transfer impedance. Surprisingly, this particular aspect of the CR technique has so far remained unmentioned in the open literature and is therefore discussed here in detail for the first time.

4.6.5.1 The phase-sensitive apparent resistivity

The general solution of the reverse problem must provide an expression for resistivity as a function of magnitude and phase (or in-phase and quadrature components) of the observed transfer impedance. Using the results of Section 4.6.2, the factor α is found to be a convenient starting point for the following calculation. The complex equation (4.18) can be split into real and imaginary parts:

$$\mathrm{Re}\,\alpha = \frac{\rho^2\omega^2\varepsilon_0^2(\varepsilon_r^2-1)+1}{\rho^2\omega^2\varepsilon_0^2(\varepsilon_r+1)^2+1} \tag{4.31a}$$

$$\mathrm{Im}\,\alpha = \frac{-2\rho\omega\varepsilon_0}{\rho^2\omega^2\varepsilon_0^2(\varepsilon_r+1)^2+1} \tag{4.31b}$$

Solving (4.31a) and (4.31b) for ρ and ε_r, one obtains

$$\rho^2 = \frac{1-\mathrm{Re}\,\alpha}{\omega^2\varepsilon_0^2((\varepsilon_r+1)^2\mathrm{Re}\,\alpha-\varepsilon_r^2+1)} \tag{4.32a}$$

$$\varepsilon_r = \sqrt{-\frac{2\rho\omega\varepsilon_0+\mathrm{Im}\,\alpha}{\rho^2\omega^2\varepsilon_0^2\mathrm{Im}\,\alpha}} - 1 \tag{4.32b}$$

Mutual insertion eliminates the interdependence and a relation for resistivity is obtained which is a function of α only:

$$\rho = -\frac{1}{2\omega\varepsilon_0}\left(\frac{(1-\mathrm{Re}\,\alpha)^2}{\mathrm{Im}\,\alpha}+\mathrm{Im}\,\alpha\right) \tag{4.33}$$

In similar fashion, an expression for relative permittivity can be found:

$$\varepsilon_r = \frac{2|1-\mathrm{Re}\,\alpha|}{(1-\mathrm{Re}\,\alpha)^2+(\mathrm{Im}\,\alpha)^2} - 1 \tag{4.34}$$

This is an important result because it shows that the quasi-static formulation of the complex transfer impedance formally contains independent information about both ρ and ε_r. However, reliable estimates of ε_r will be difficult to obtain due to the lack of sensitivity of low-frequency methods towards dielectric properties. This physical principle is reflected in the lack of sensitivity of α towards ε_r for $\Omega \ll 1$ (cf. Figure 4.16).

4.6.5.2 Determination of α from a measured impedance

The reverse problem is now reduced to the determination of α from a practical impedance measurement. The transfer impedance Z can be expressed by the current $I(t) = \hat{I}e^{i\omega t}$ injected across the current dipole (C_1, C_2) and the voltage $U(t) = \hat{U}e^{i\omega t}e^{i\varphi}$ across the potential dipole (P_1, P_2) where φ is the phase shift between the two signals:

$$Z = \frac{U}{I} = \frac{\hat{U}e^{i\varphi}}{\hat{I}} = \frac{\hat{U}(\cos\varphi + i\sin\varphi)}{\hat{I}} \tag{4.35}$$

In a practical measurement, $\hat{U}$, $\hat{I}$ and φ must be determined. $\hat{U}$ and $\hat{I}$ can be either true amplitudes or RMS values, as long as both are of the same type. Reordering Equation (4.21) for α yields

$$\alpha = \frac{1}{K}\left(1 - \frac{Z}{Z_0}\right) \tag{4.36}$$

and after insertion

$$\alpha = \frac{1}{K}(1 - i\omega C_0 \hat{Z}(\cos\varphi + i\sin\varphi)) \tag{4.37}$$

After separating α into in-phase and quadrature components, the measured apparent resistivity (4.33) finally becomes

$$\rho_a = -\frac{1}{2\omega\varepsilon_0}\left(\frac{(1 - \mathrm{Re}\,\alpha)^2}{\mathrm{Im}\,\alpha} + \mathrm{Im}\,\alpha\right) \tag{4.38}$$

$$\mathrm{Re}\,\alpha = \frac{1}{K}(1 + \omega C_0 \hat{Z}\sin\varphi) = \frac{1}{K}(1 + \omega C_0 \mathrm{Im}\,Z) \tag{4.39}$$

$$\mathrm{Im}\,\alpha = -\frac{1}{K}\cdot\omega C_0 \hat{Z}\cos\varphi = -\frac{1}{K}\cdot\omega C_0 \mathrm{Re}\,Z \tag{4.40}$$

and a unique solution is found for the reverse problem. These three equations represent a new formulation of apparent resistivity as derived from capacitive measurement under quasi-static conditions. It is evident that $\rho_a = \rho_a(\hat{Z}, \varphi)$, i.e. ρ_a is now a function of magnitude and phase of the measured transfer impedance.

4.6.5.3 Relationship with conventional DC theory

The nature of the relationship between a quadrupole under quasi-static conditions and a conventional DC measurement remains to be examined. In Section 4.6.4.2 it was observed that $\mathrm{Re}\,\alpha \approx 1$ if the quadrupole is operated in the conductive regime ($\Omega \ll 1$). Under these circumstances, and if the quadrupole is close to the surface ($K^{\mathrm{ES}} \approx 1$), the quadrature component of Z vanishes (cf. Equation 4.39) and the response can be expected to be in-phase. As a consequence, Equation (4.38) reduces to

$$\rho_a \approx -\frac{\mathrm{Im}\,\alpha}{2\omega\varepsilon_0} \approx \frac{C_0}{2\varepsilon_0}\mathrm{Re}\,Z \tag{4.41}$$

and together with the definition of C_0 (4.12) one obtains

$$\rho_a \approx \frac{\mathrm{Re}\, U}{\hat{I}} \cdot K^{\mathrm{DC}} \tag{4.42}$$

i.e. the phase-sensitive apparent resistivity (4.38) reduces to the classical DC expression for the in-phase component of the transfer impedance. The electrostatic formalism can therefore be regarded as a generalisation of conventional DC theory (Tabbagh et al., 1993).
Also, it can now be seen why an estimation of relative permittivity ε_r is difficult for $\Omega \ll 1$. As a consequence of $\mathrm{Re}\,\alpha \approx 1$, (4.34) is numerically unstable due to the term $(1 - \mathrm{Re}\,\alpha)$ that appears in the denominator of (4.34).

4.7 An electromagnetic formulation of CR

It has been shown that a capacitive four-electrode array can be treated as a quasi-static quadrupole, provided that induction numbers are low. This condition cannot always be satisfied, particularly for conductive environments, large array separations or higher frequencies. Inductive effects can then no longer be neglected and must be accounted for by a full EM treatment of the problem. This section introduces the necessary theory, thus completing the range of theoretical descriptions for the CR technique. Only the mathematical formalism is described here; numerical solutions are considered beyond the scope of the thesis.

4.7.1 The elementary horizontal electric dipole

Tabbagh et al. (1993) have suggested that the source field in the CR technique can be approximated by that of a finite electric dipole in the vicinity of a conducting halfspace. The EM field of a finite electric dipole above earth can be derived from the generic solution to the boundary-value problem of an elementary Hertzian dipole which has been treated extensively in classical antenna theory. In two early papers, Sommerfeld (1909, 1926) examined the influence of a conductive earth on EM radiation from dipole antennas. Both electric and magnetic sources, located at the surface in horizontal and vertical configuration, were considered. Wait (1969) has given a more recent formulation of the same problem, extending the solution to the case of a dipole source at an elevation above the surface. Both authors have assumed the subsurface to be a homogeneous halfspace, but an extension to a 1D layered earth model is straightforward (Tabbagh and Panissod, 2000). An alternative treatment of the same general problem using a decompositon of the field into TE and TM modes can be found in Ward and Hohmann (1988).

Consider a homogeneous conductive halfspace of relative permittivity ε_r, conductivity σ and magnetic permeability μ_0. Initially, the source is assumed to be an elementary horizontal electric dipole (HED) situated at z_0 above the boundary $z = 0$ (Figure 4.17). It is regarded as an infinitesimal current element in x-direction of length dl with a harmonic current of time factor $e^{-i\omega t}$. The EM

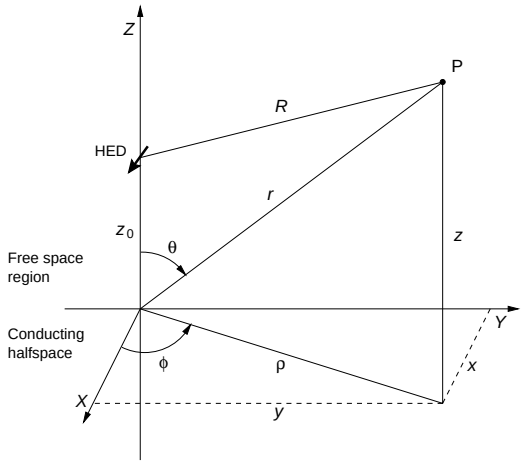

Figure 4.17: Horizontal electric dipole over a homogeneous conducting halfspace.

field is described by a Hertz potential vector $\mathbf{\Pi} = (\Pi_x, \Pi_y, \Pi_z)$ which satisfies the homogeneous Helmholtz equation

$$(\nabla^2 - k^2)\mathbf{\Pi} = 0 \tag{4.43}$$

componentwise except at the source. The wave number k is given by

$$k^2 = \begin{cases} k_0^2 = -\mu_0\varepsilon_0\omega^2 & z > 0 \\ k_1^2 = i\omega\mu_0\sigma - \mu_0\varepsilon_0\varepsilon_r\omega^2 & z < 0 \end{cases} \tag{4.44}$$

Solutions for Π_i must consist of linear superpositions of eigenfunctions. With reference to a cylindrical coordinate system (ρ, ϕ, z) these have the form

$$\begin{matrix} \cos n\phi \, J_n(\lambda\rho) \\ \sin n\phi \, Y_n(\lambda\rho) \end{matrix} \; e^{\pm\sqrt{\lambda^2+k^2}z} \tag{4.45}$$

where λ denotes the eigenparameter. J_n and Y_n are Bessel functions of the first and second kind, respectively, and of order n. The solutions are periodic in ϕ, hence n must be an integer. Moreover, the solutions containing Y_n must be rejected since fields should be finite at $\rho = 0$ except at the source. For the HED, eigenfunctions for $n = 0$ and those for $n = 1$ which are even about $\phi = 0$ are required. These have the form

$$J_0(\lambda\rho)e^{\pm\sqrt{\lambda^2+k^2}z} \qquad \text{and} \qquad \cos\phi \, J_1(\lambda\rho)e^{\pm\sqrt{\lambda^2+k^2}z}, \tag{4.46}$$

respectively. Once a solution is found, the electromagnetic field $\mathbf{E}$, $\mathbf{H}$ may be obtained from

$$\mathbf{E} = \boldsymbol{\nabla}(\boldsymbol{\nabla}\mathbf{\Pi}) - k^2\mathbf{\Pi} \tag{4.47}$$

$$\mathbf{H} = \frac{k^2}{i\omega\mu_0}(\boldsymbol{\nabla} \times \mathbf{\Pi}). \tag{4.48}$$

The source term $\mathbf{\Pi^p} = (\Pi_x^p, 0, 0)$ is an elementary dipole in x-direction:

$$\Pi_x^p = C \cdot \frac{e^{-k_0 R}}{R} = C \int_0^\infty \frac{\lambda}{u_0} J_0(\lambda\rho)\, e^{-u_0|z-z_0|}\, d\lambda \tag{4.49}$$

where $C = Idl/4\pi i\omega\varepsilon_0$, $u_0^2 = \lambda^2 + k_0^2$, $R^2 = (z-z_0)^2 + \rho^2$ and $\rho^2 = x^2 + y^2$ as in Figure 4.17. The integral representation of the source term is favourable for this problem as it contains the elementary solutions of the wave equation. In the presence of the conducting halfspace, it is convenient to split the Hertz vector in the free space region into a primary part representing the source field and a secondary part due to the contribution from the subsurface:

$$\mathbf{\Pi} = \begin{cases} \mathbf{\Pi^p} + \mathbf{\Pi_0^s} & z > 0 \\ \mathbf{\Pi_1^s} & z < 0 \end{cases} \tag{4.50}$$

Boundary conditions require the continuity of the tangential components E_x, E_y and H_x, H_y at the surface. It turns out that these conditions cannot be met assuming that the Hertz vector had an x-component only, $\mathbf{\Pi} = (\Pi_x, 0, 0)$. It must have both x- and z-components. Thus

$$\mathbf{\Pi} = (\Pi_x, 0, \Pi_z) = \begin{cases} (\Pi_{0x}, 0, \Pi_{0z}) = (\Pi_x^p + \Pi_{0x}^s, 0, \Pi_{0z}^s) & z > 0 \\ (\Pi_{1x}, 0, \Pi_{1z}) = (\Pi_{1x}^s, 0, \Pi_{1z}^s) & z < 0 \end{cases} \tag{4.51}$$

The secondary excitation is due to the influence of the subsurface and can be arranged in the same form as the source term. For the horizontal component one can write

$$\Pi_{0x}^s = C \int_0^\infty \tfrac{\lambda}{u_0} f_0(\lambda)\, J_0(\lambda\rho)\, e^{-u_0(z+z_0)}\, d\lambda \tag{4.52a}$$

$$\Pi_{1x}^s = C \int_0^\infty \tfrac{\lambda}{u_1} f_1(\lambda)\, J_0(\lambda\rho)\, e^{+u_1 z}\, d\lambda \tag{4.52b}$$

where $u_1^2 = \lambda^2 + k_1^2$ and the coefficients f_0 and f_1 of the kernel are unknown functions of λ. Accordingly, the vertical component is of the form

$$\Pi_{0z}^s = C\cos\varphi \int_0^\infty \tfrac{\lambda}{u_0} g_0(\lambda)\, J_1(\lambda\rho)\, e^{-u_0 z} d\lambda \tag{4.53a}$$

$$\Pi_{1z}^s = C\cos\varphi \int_0^\infty \tfrac{\lambda}{u_1} g_1(\lambda)\, J_1(\lambda\rho)\, e^{+u_1 z} d\lambda. \tag{4.53b}$$

where g_0 and g_1 are unknown functions of λ. From (4.47), (4.48) and (4.51), the EM field components are then given by

$$E_x = \tfrac{\partial}{\partial x}\left(\tfrac{\partial \Pi_x}{\partial x} + \tfrac{\partial \Pi_z}{\partial z}\right) - k^2\Pi_x \qquad H_x = \tfrac{k^2}{i\omega\mu_0}\tfrac{\partial \Pi_z}{\partial y} \tag{4.54a}$$

$$E_y = \tfrac{\partial}{\partial y}\left(\tfrac{\partial \Pi_x}{\partial x} + \tfrac{\partial \Pi_z}{\partial z}\right) \qquad H_y = \tfrac{k^2}{i\omega\mu_0}\left(\tfrac{\partial \Pi_x}{\partial z} - \tfrac{\partial \Pi_z}{\partial x}\right) \tag{4.54b}$$

$$E_z = \tfrac{\partial}{\partial z}\left(\tfrac{\partial \Pi_x}{\partial x} + \tfrac{\partial \Pi_z}{\partial z}\right) - k^2\Pi_z \qquad H_z = \tfrac{-k^2}{i\omega\mu_0}\tfrac{\partial \Pi_x}{\partial y} \tag{4.54c}$$

Four relations are obtained from the boundary conditions:

$$H_x: \qquad k_0^2\,\Pi_{0z}|_{z=0} = k_1^2\,\Pi_{1z}|_{z=0} \tag{4.55a}$$

$$H_y: \qquad k_0^2\,\frac{\partial\Pi_{0x}}{\partial z}\Big|_{z=0} = k_1^2\,\frac{\partial\Pi_{1x}}{\partial z}\Big|_{z=0} \tag{4.55b}$$

$$E_y: \qquad \frac{\partial\Pi_{0x}}{\partial x}\Big|_{z=0} + \frac{\partial\Pi_{0z}}{\partial z}\Big|_{z=0} = \frac{\partial\Pi_{1x}}{\partial x}\Big|_{z=0} + \frac{\partial\Pi_{1z}}{\partial z}\Big|_{z=0} \tag{4.55c}$$

$$E_x: \qquad k_0^2\,\Pi_{0x}|_{z=0} = k_1^2\,\Pi_{1x}|_{z=0} \tag{4.55d}$$

For the horizontal component Π_x, insertion of (4.49) and (4.52) yields

$$f_0 = \frac{u_0 - u_1}{u_0 + u_1} \qquad\qquad f_1 = \frac{k_0^2}{k_1^2} e^{-u_0 z_0}(1 - f_0) \tag{4.56}$$

while for the vertical component Π_z, one obtains

$$g_0 = 2\lambda u_0 e^{-u_0 z_0} \frac{u_0 - u_1}{k_1^2 u_0 + k_0^2 u_1} \qquad\qquad g_1 = \frac{k_0^2}{k_1^2}\frac{u_1}{u_0} g_0 \tag{4.57}$$

by insertion of (4.53). Hence the full solution is found and the total Hertz potential in air ($z > 0$) of the HED becomes

$$\Pi_{0x} = C \int_0^\infty J_0(\lambda\rho) \left[e^{-u_0|z-z_0|} + \frac{u_0 - u_1}{u_0 + u_1}\, e^{-u_0(z+z_0)} \right] \frac{\lambda}{u_0}\, d\lambda \tag{4.58a}$$

$$\Pi_{0z} = 2C\cos\varphi \int_0^\infty J_1(\lambda\rho)\, \frac{u_0 - u_1}{k_1^2 u_0 + k_0^2 u_1}\, e^{-u_0(z+z_0)} \lambda^2 d\lambda. \tag{4.58b}$$

The explicit form of the potential in the ground ($z < 0$) has no further relevance and is therefore omitted.

4.7.2 Finite dipoles

A CR array constitutes a transmitter dipole and a receiver dipole of finite length. Their typical dimensions and separations are such that the finite size must be taken into account for practical calculations. This can be accomplished by the superposition of elementary EM dipoles. The electromagnetic field created by two localised injection poles C_1 and C_2, connected via the transmitter by current-carrying wire is equivalent to the field created by the superposition of infinitesimal dipoles along a line connecting C_1 and C_2. Hence the electric field at any given point in the vicinity of the transmitter dipole is obtained by integration between C_1 and C_2 over the contributions of these elementary dipoles to the field. According to the previous results (cf. Equations 4.47 and 4.51), the final expressions of the horizontal components of the electric field of the elementary dipole in air are

$$E_{0x} = \frac{\partial}{\partial x}\left(\frac{\partial}{\partial x}\Pi_{0x} + \frac{\partial}{\partial z}\Pi_{0z} \right) - k_0^2 \Pi_{0x} \tag{4.59a}$$

$$E_{0y} = \frac{\partial}{\partial y}\left(\frac{\partial}{\partial x}\Pi_{0x} + \frac{\partial}{\partial z}\Pi_{0z} \right) \tag{4.59b}$$

This is the contribution of an infinitesimal dipole with the dipole moment $Id\mathbf{l}$. The total electric field created by the finite dipole C_1C_2, assuming a constant current everywhere, is then given by

$$E_x^{\text{tot}} = \int_{C_1}^{C_2} E_{0x} dx \qquad\qquad E_y^{\text{tot}} = \int_{C_1}^{C_2} E_{0y} dy \tag{4.60}$$

The measurement of the potential difference between the two receiving poles P_1 and P_2 corresponds to an integration over the electric field obtained at each point on the line connecting P_1 with P_2:

$$\Delta V = V(P_2) - V(P_1) = \int_{P_1}^{P_2} \mathbf{E}^{\text{tot}} \cdot d\mathbf{l} = \int_{P_1}^{P_2} E_x^{\text{tot}} dx + E_y^{\text{tot}} dy \tag{4.61}$$

The received voltage is found and hence the electromagnetic forward calculation of the finite electric dipole is complete.

4.8 Discussion

Capacitive resistivity is a unique method that exploits a niche position between conventional DC resistivity and electromagnetic methods. In this chapter, the fundamental concepts of a CR measurement and the various approaches to CR theory have been discussed in an attempt to provide a unified description of the technique.

The concept of point poles. The first important step was to recognise the impact of the sensor type on the nature of the capacitive measurement. The two fundamental sensor types with complementary character are linear sensors and point poles. While linear sensors have a practical equivalent in the form of line antennas, capacitive point sensors only exist in theory. Line antennas are attractive because they provide a simple means of capacitive coupling, the degree of which can be adapted by changing the length of the antenna. However, the fact that coupling occurs over the whole length of the antenna makes interpretation more difficult, not least as a result of spatial averaging. Point poles are much better suited to the understanding of CR as a generalisation of conventional DC resistivity, because the concept of a four-point array is directly transferable, together with existing DC interpretation schemes including forward modelling and inversion algorithms. Plate-wire combinations have been suggested as a practical realisation of point poles, however this assumption has yet to be confirmed experimentally.

Electrostatic formalism. The electrostatic formalism was presented as a formulation of CR theory based upon the use of point poles under quasi-static conditions. Under a quasi-static regime, inductive effects are negligible and the transfer impedance can be expressed algebraically as a complex function of the electrical properties, frequency and geometry. The criterion for the prevalence of quasi-static conditions is that induction numbers are low, which are governed

by the frequency of operation. However, the use of low frequencies alone cannot guarantee quasi-static conditions. Two other independent parameters control the electromagnetic regime: ground resistivity and a characteristic scale length of the measurement. In order to achieve quasi-static conditions, the subsurface should not be too conductive and all geometric dimensions (i.e. array separation, depth of investigation) should be small compared with the wavelength of the electrical field in the medium. While frequency and geometry are fixed in a practical system and within the control of the designer, the resistivity is initially unknown. A balance between all three parameters must be found in each individual case; for conductive environments and/or large arrays a careful judgement has to be made as to whether the quasi-static formulation is justified. At higher frequencies, the electrostatic quadrupole lends itself to assessments of dielectric properties as the complex response contains independent information about resistivity and relative permittivity. In practice however, estimates of ε_r are only likely to be stable in highly resistive ($> 1000\,\Omega$m) environments, using small arrays ($L \approx 1\,$m) and high frequencies ($> 100\,$kHz) (Tabbagh et al., 1993).

Relevance of the CR phase. The feasibility of capacitively coupled resistivity measurements has been known for some time and a number of commercial and research-type instruments are available. Market evaluation has shown that existing CR instruments operate on the basis of the assumption of an in-phase response, hence measurement of the magnitude of the CR transfer impedance is accepted as sufficient. However, although there is evidence to suggest that such practice may often be justified (cf. Section 4.6.4.2), it must be stressed that quasi-static conditions are merely a requirement for the electrostatic formalism to apply, but not commensurate for the CR response to be in-phase. Even under quasi-static conditions, the electrostatic formalism provides for circumstances in which the quadrature component is non-negligible.
It is important to recognise that the occurrence of a CR phase rotation is entirely due to the capacitive coupling mechanism and the geometry of the sensor array, but does not result from a subsurface material property. CR phases are therefore distinct from phase rotations measured by induced polarisation or complex resistivity methods. The phase shifts observed by those methods are associated with electrical polarisation within the medium. The difference is that resistivity itself must then be regarded as a complex frequency-dependent property, while CR assumes resistivity to be real and constant. Moreover, the largest effects due to electrical polarisation are typically observed at much lower frequencies (e.g. 1 μHz – 1 kHz, c.f. Section 3.3.1)
In order to derive an accurate resistivity estimate from a CR measurement, magnitude and phase of the fully complex response must be considered. A phase-sensitive formulation of apparent resistivity for the general case of complex Z has been developed in this thesis. It can be regarded as the "exact" expression, although its practical significance is limited. Under quasi-static conditions the phase-sensitive expression was shown to reduce to the classical DC formula for the in-phase component of the transfer impedance, i.e. apparent resistivity is simply proportional to $\mathrm{Re}\,Z$.

Analogy with ground conductivity. The observation that an accurate determination of resistivity by CR requires a measurement of the in-phase component of the transfer impedance is a fundamental analogy with the ground conductivity technique. There, a conductivity estimate can be obtained from the component of the transfer impedance that is in quadrature with the primary current (cf. Section 3.2.2). In CR, such a measurement implies the establishment of a phase reference between transmitter and receiver unit and can be realised by synchronous detection (Benderitter et al., 1994). However, none of the existing CR instruments is thought to be measuring the fully complex transfer impedance, that is both in-phase *and* quadrature components, and experimental data of such kind are unavailable in the literature. Consequently, the development of a CR instrument capable of such measurements is highly desirable.

Beyond the quasi-static regime. Under conditions where the approximation $\Omega \ll 1$ is no longer valid, inductive effects become relevant and the electrostatic quadrupole gives way to an EM quadrupole (Benderitter et al., 1994). It should be noted that the technique is then no longer predominantly capacitive, but must be regarded as a hybrid between a DC four-point measurement and EM induction methods. For the sake of completeness of CR theory, the electromagnetic formulation of the technique has been presented. It is based on the solution of the problem of a horizontal electric dipole above ground which can be used to calculate the complete electromagnetic field observed at the potential dipole. This approach has previously been used to interpret CR measurements obtained at higher induction numbers, such as long-offset capacitive soundings in conductive environments (Benderitter et al., 1994; Tabbagh and Panissod, 2000).

Open questions. In order to investigate the conditions for quasi-static operation of CR in the context of environmental and engineering site investigations, a detailed parametric study must be undertaken. A wide frequency range is conceivable for instrument design and the application of CR to site investigations may result in a wide range of values for subsurface electrical properties. At the same time, tomographic imaging surveys require the use of a range of different array separations and geometries. Several questions arise that will be addressed in Chapters 5 and 6: What are the exact constraints required to ensure operation under quasi-static conditions? Analysis of the complex transfer impedance has shown that significant phase rotations may occur even under quasi-static conditions. What are the exact circumstances in which these phase shifts are observed? Can the theoretical predictions be confirmed by quantitative experiments?

Chapter 5

A parameter study for practical CR measurements

The means by which the theoretical concepts of the capacitive resistivity technique can be translated into a practical measurement will now be examined. By studying the predicted system response function, it is shown that a realistic set of system design parameters exists that allows practical operation of CR instruments under quasi-static conditions. This kind of systematic parameter study is not available in the literature.
The parameter study is based upon evaluation of the electrostatic formalism. Rather than studying the transfer impedance itself, it is useful to treat the injection current as a separate parameter and to examine the electric potential observed with a given array configuration. The results can then be regarded as voltage levels that must be detectable by a practical CR instrument for successful operation in a particular situation. The complex electric potential can be thought of as a function of multiple variables:

$$U = U(f, I, r, l, \rho) \tag{5.1}$$

Its explicit form, derived from (4.21) and separated into in-phase and quadrature components, is the following:

$$\operatorname{Re} U = \frac{1}{C_0} \cdot \frac{2\varepsilon_0 I K^{\mathrm{ES}} \rho}{\rho^2 \omega^2 \varepsilon_0^2 (\varepsilon_r + 1)^2 + 1} \tag{5.2a}$$

$$\operatorname{Im} U = \frac{I}{\omega C_0} \left(K^{\mathrm{ES}} \cdot \frac{\rho^2 \omega^2 \varepsilon_0^2 (\varepsilon_r^2 - 1) + 1}{\rho^2 \omega^2 \varepsilon_0^2 (\varepsilon_r + 1)^2 + 1} - 1 \right) \tag{5.2b}$$

The most obvious and perhaps most critical design parameter is the frequency of operation (cf. Benderitter et al., 1994). Not only does the frequency govern the nature of the electromagnetic regime, but it also controls the character of capacitive coupling at the sensors. Both theoretical aspects (the low induction number criterion) and practical restrictions (impedance of the injection circuit, presence of competing signals in the desired frequency range) must be considered for a realistic choice of frequency. Other parameters affecting the transfer impedance, such as array geometry and resistivity, are examined subsequently.

Sets of "master curves" have been calculated so that fundamental characteristics can be studied and the sensitivity to parameter variations assessed. The dynamic range associated with a practical instrument and the detection of small signals at large array separations are relevant issues in this context.
Finally, practical realisations of capacitive sensors are studied with regard to their compliance with the point-pole concept associated with the electrostatic formalism. Capacitance modelling of elementary structures is used to determine the geometric distribution of capacitance for relevant sensor types.

5.1 Frequency of operation

Frequency of operation is the fundamental parameter that determines both the electromagnetic regime in which the instrument operates and the concepts of its electronic design. Bearing in mind the findings of Chapter 4, the criteria for the choice of frequency are:

1. The character of the system response is governed by the complex permittivity of the ground in which the resistivity component dominates only at low frequencies. At higher frequencies, the sensitivity towards the dielectric term increases.

2. Induction numbers must be low so that the quasi-static approximation applies (cf. Section 4.6.2) and inductive effects remain negligible. This condition can only be satisfied by using low frequencies.

3. The CR transmitter must inject an electric current across sensors representing a predominantly capacitive complex load (cf. Section 4.2.2). Capacitive reactance decreases with increasing frequency, hence higher frequencies result in higher currents for a given transmitter output power. The total impedance must be such that a minimum amount of current can be injected.

4. Potential interference from external signal sources must be minimised. Ideally, the received signal is exclusively due to the field generated by the CR transmitter. Interference with competing signals in the same frequency band must be avoided.

5. The electronic design of the CR instrument should facilitate modular concepts and the use of standard components. As high frequency designs require a higher degree of complexity (e.g. shielding), the use of low frequencies (kHz) is preferable.

It is evident that any practical choice of frequency must necessarily be a tradeoff between these partially contradicting criteria.

5.1.1 The transfer impedance at low induction numbers

5.1.1.1 The upper frequency threshold

The basic conditions for operation at low induction numbers have been discussed in the context of the ground conductivity method and the use of magnetic dipoles (Section 3.2). The same conditions apply in the case of the CR technique. The characteristic scale length L for an electric array is the separation r between the current and potential dipoles. The CR equivalent of the upper frequency threshold (3.34) is therefore

$$f \ll f_L = \frac{\rho}{\pi \mu_0 r^2} \tag{5.3}$$

The limiting frequency f_L decreases with distance as $1/r^2$ and grows porportionally with resistivity. As far as distance is concerned, array separations of $r \leq 10\,\mathrm{m}$ are a reasonable assumption for near-surface applications of CR, particularly with towed arrays. A lower resistivity limit of $\rho \geq 10\,\Omega\mathrm{m}$ might apply to most resistivity surveys conducted in the built environment, although lower values may be encountered in some circumstances. For these values one obtains a critical frequency of $f_L \approx 25\mathrm{kHz}$. The corresponding wavelength $\lambda_0 = 2\pi/|k_0|$ of an electromagnetic wave in vacuum is approximately $1.2 \cdot 10^3$ m. In a $10\,\Omega\mathrm{m}$ medium the wavelength reduces to approximately 45 m. For the quasi-static approximation to apply, practical CR systems should therefore operate at frequencies well below this critical limit of 25kHz so that the low induction number criterion is satisfied. It should be noted that the same condition can also be met for larger separations in more resistive environments or vice versa. However, using larger distances in a conductive environment would require lower frequencies to uphold quasi-static conditions.

5.1.1.2 Functional dependence

The quasi-static transfer impedance remains a function of frequency (cf. Section 4.6.4). As a general example, the properties of a unit square array ($l =$ 1 m, $r = 1$ m, cf. Figure 4.12 top) at a small elevation ($h = 1$ mm) are examined hereafter. Figure 5.1 shows the variation of the complex potential with frequency observed with this array over a homogeneous conducting halfspace. Curves have been plotted for five different resistivities in the range between $10^{-1}\,\Omega$m and $10^3\,\Omega$m. All calculations are based upon Equation (4.21), assuming a typical injection current of 10 mA. Other authors have reported the use of similar currents (Tabbagh et al., 1993; Benderitter et al., 1994) and commercial CR instruments (OhmMapper™, CORIM™) operate in the same range.
The frequencies considered here range from two orders of magnitude below to two orders above the critical frequency f_L, i.e. from 10^2 Hz to 10^6 Hz. The predicted magnitude of the observed potential at constant current is shown in Figure 5.1a, together with the values for an equivalent DC array. The CR magnitude is found to be proportional to resistivity only above a frequency-dependent limit. This is in contrast to the DC case, where the relation is frequency-independent. In the CR case, the magnitude curves show asymptotic

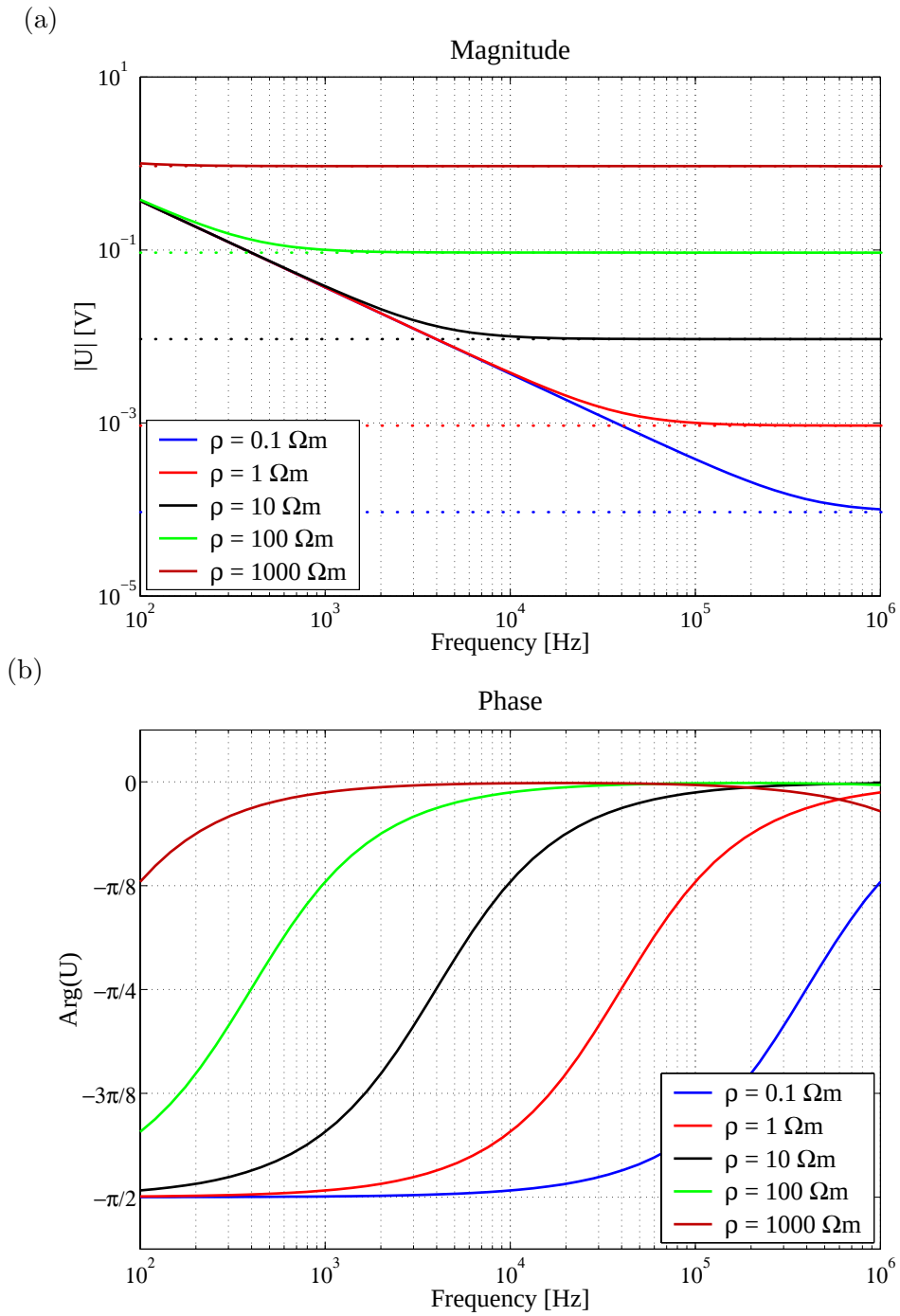

Figure 5.1: Variation of the complex potential with frequency for a unit square array ($l = 1\,\mathrm{m}$, $r = 1\,\mathrm{m}$). Parameter: resistivity. Array elevation $h = 10^{-3}\,\mathrm{m}$, relative permittivity $\varepsilon_r = 1$, injected current $I = 10\,\mathrm{mA}$. (a) magnitude, (b) phase. Values for an equivalent DC array are shown as dotted lines.

behaviour towards low frequencies due to the growing influence of the quadrature component. The limiting curve is the one with the lowest resistivity. With decreasing frequency, the transfer impedance (and hence the potential) approaches its free-space value in quadrature. This loss in sensitivity towards subsurface properties is resistivity-dependent. While in resistive environments the magnitudes are constant over the entire range of frequencies considered, this is not the case in a conductive environment, where the onset of asymptotic behaviour occurs at much higher frequencies. Absolute values of the CR potential are dependent on geometry, but for the unit square array magnitudes on the limiting curve increase from around 0.1 mV at 10^6 Hz up to 100s of mV at 10^2 Hz. Smaller values would be observed for larger dipole separations.
The phase curves show that, for the relevant frequency range, high frequencies produce an in-phase response ($\varphi = 0$) while low frequencies are associated with a response in quadrature ($\varphi = -\pi/2$). The point of transition between the two limits (e.g. $\varphi = -\pi/4$) is a function of resistivity. The frequency at which it is reached corresponds to the onset of asymptotic behaviour in the magnitude. At frequencies greater than 10^4 Hz, the response is largely in-phase for resistivities greater than 10 Ωm. Below that, the influence of the quadrature component is significant. It should be noted that, for frequencies much higher than the range of the diagram, the properties of the responses may only be formal due to the breakdown of the quasi-static approximation at high frequencies.

5.1.2 The capacitive electrode as a reactive load

So far, electric current has merely been treated as an independent parameter with constant magnitude, disregarding any issues related to current generation. In reality, the injected current is also a function of frequency because the capacitive sensors represent a reactive load within the injection circuit. A simple electric circuit model can be used to estimate the current in the transmitter output circuit for a given frequency (Shima et al., 1995). Conversely, the same model can be used to examine the frequency-dependence of the load at the transmitter output.

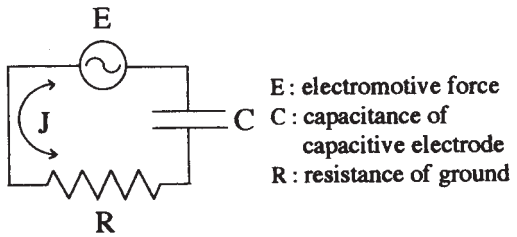

Figure 5.2: Electric circuit model for capacitive electrodes and ground (Shima et al., 1995).

5.1.2.1 Complex impedance of the transmitter circuit

The transmitter circuit may be modelled as the ground resistance in series with the capacitance of the sensors, driven by the electromotive force of the generator (Figure 5.2). The load represents a complex impedance of

$$Z(\omega) = R + X_C = R + \frac{1}{i\omega C} \tag{5.4}$$

where R is some representative value for ground resistance, X_C the reactive component of the impedance and C the effective sensor capacitance. It is worth noting that R represents the *ground resistance* in series with the transmitter circuit, as opposed to the *transfer resistance* typically measured in DC resistivity which is calculated from the voltage measured at the receiver and the transmitter current. Here, the voltage U_{Tx} generated by the transmitter (or E in the notation of Shima et al.) is relevant. Its application at the terminals will result in a current flow

$$I = \frac{U_{\mathrm{Tx}}}{Z(\omega)} \tag{5.5}$$

A practical aim both in DC resistivity and CR is to create high electric dipole moments at the transmitter so that the observed signal strength at the receiver is above detection level at a given array separation. Hence a minimum magnitude of electric current is required. From experience with DC resistivity, currents of the order of 10 mA can be considered appropriate for this purpose. A portable, battery-powered transmitter can be expected to generate a typical output power of the order of 10 W, hence voltages of 10^3 V must be available from the generator in order to generate a 10 mA current. The maximum impedance the transmitter would then be able to cope with while maintaining a constant current would be of the order of $10^5\ \Omega$.

5.1.2.2 The lower frequency threshold

Realistic values for the sensor capacitance are crucial for a meaningful estimation of the total impedance. Shima et al. (1995) have used the parallel-plate approximation to estimate sensor capacitance. This may suffice for an approximate calculation, however a more detailed analysis is required if the influence of sensor properties is of interest. Such an analysis will be carried out in Section 5.4. The parallel-plate formula states

$$C = \varepsilon_r \varepsilon_0 \frac{A}{d} \tag{5.6}$$

where A is the area of the plates and d their separation. The factor A/d can be assumed to be of the order of 10^2 m so that capacitances in free space ($\varepsilon_r = 1$) are expected to be of the order of $C = 100 \cdot \varepsilon_0$ m ≈ 1 nF.
It is then safe to assume that the ohmic ground resistance is negligible against the reactive part of the impedance, so that the total impedance becomes

$$Z(\omega) \approx \frac{1}{i\omega C} \tag{5.7}$$

This assumption has been verified by practical measurements (Section 5.4). Hence, in order to keep the impedance below a desired threshold, the frequency must satisfy

$$f \geq f_L = \frac{I}{2\pi CU} \tag{5.8}$$

For the above values, i.e. a typical capacitance of 1 nF and an impedance limit of $10^5\ \Omega$, one obtains a lower frequency threshold of $f_L = 1.6$ kHz.

5.1.3 The EM spectrum at radio frequencies

An important practical aspect in determining a suitable frequency of operation is the potential interference of ambient natural or man-made electromagnetic noise with the CR transmitter signal. According to the results of the previous sections, the CR technique will operate in the VLF band of the EM spectrum (Table 5.1). This frequency band contains a variety of signals of natural origin, for example "sferics" caused by atmospheric disturbances such as lightning discharges (Ward, 1967b). Natural signals are difficult to account for as they represent bursts of energy whose spectrum may contain a whole range of frequencies. On the other hand, natural signals only occur sporadically and can normally be identified and suppressed by repeat measurements. Man-made signals may be more problematic. In the VLF range, these include transmissions for long-range communication or navigational purposes. A well-known subset of these transmissions is associated with a network of military transmitters for submarine communications. They are located all over the world and produce high-power, fixed-frequency signals at frequencies between 15 and 30 kHz which are easily detectable with geophysical instrumentation and give rise to the "VLF" technique (cf. Section 3.3.2). One of these transmitters is situated in Rugby, UK (52° 22′ N, 1° 1′ W), and operates at distinct frequencies of 16.0 kHz and 19.6 kHz (ABEM Instrument AB, unpublished)[1]. Its 16.0 kHz

[1]Most VLF frequencies are allocated to military or governmental use, hence frequency tables are either unavailable or inofficial.

Description	Short form	Frequency range
ultra-low frequency	ULF	3–30 Hz
extremely low frequency	ELF	30–300 Hz
voice frequencies	VF	300 Hz–3 kHz
very low frequency	VLF	3–30 kHz
low frequency	LF	30–300 kHz
medium frequency	MF	300 kHz–3 MHz
high frequency	HF	3–30 MHz
very high frequency	VHF	30–300 MHz
ultra high frequency	UHF	300 MHz–3 GHz
super high frequency	SHF	3–30 GHz
extremely high frequency	EHF	30–300 GHz

Table 5.1: The electromagnetic spectrum at radio frequencies.

Frequency range	9–14 kHz	14–15 kHz	15–30 kHz
Description	Radionavigation systems (e.g. Omega, now obsolete)	Unallocated?	VLF transmitters for long-range military communication

Table 5.2: Spectrum of man-made VLF transmissions relevant to CR.

transmission is often by far the strongest VLF signal observed in the British Isles. Other sources in the lower VLF band include the now obsolete Omega radionavigation system. In order to avoid potential interference from such signals, the CR transmitter frequency should be chosen well away from any known frequencies of such origin. The frequency window between 14 and 15 kHz is regarded as suitable for this purpose (Table 5.2).

5.2 Array geometry

Now that the range of possible frequencies has been narrowed down to a suitable frequency of operation, the properties of the transfer impedance with regard to the remaining system parameters can be examined at this frequency. In this section, the functional dependence of the transfer impedance on array geometry is discussed for a typical frequency of operation of 15 kHz. Two different array geometries are considered, namely the inline and the equatorial configurations of the dipole-dipole array. Again, all calculations are based upon Equation 4.21. In principle, any of the array types known in conventional DC resistivity (Figure 3.3) can be employed also with electrostatic quadrupoles. In practice however, it seems advantageous that such a system be arranged in a dipole-dipole configuration for the following reasons:

- When operated at CR frequencies, classical DC resistivity arrays in Wenner or Schlumberger geometry can suffer from electromagnetic coupling between connecting wires. This is because the potential dipole is situated *between* the poles of the current dipole and hence current-carrying wires are likely to be in the vicinity of the wires of the potential dipole, especially if a single unit is used as power source and resistivity meter. This effect is well-known in IP surveys (Wait and Gruszka, 1986) and can be minimised by using a dipole-dipole configuration.

- For any capacitive sensor arrangement, the capacitance of the connecting wires to the actual sensors can also affect the measurement. This will be investigated in more detail in Section 5.4. The dipole-dipole configuration allows for transmitter and receiver units to be placed close to the sensors, thus keeping wire lengths to an absolute minimum.

5.2.1 Dipole separation

In analogy with the DC case, the CR transfer impedance is clearly a function of array dimensions. The relevant variables are dipole length and separation. While DC dipole-dipole arrays are often used with separations corresponding

to integer multiples $n \cdot a$ of the dipole spacing a, it is characteristic for the CR technique that dipole-dipole arrays may have arbitrary separations with rational n. Due to scalability it is sufficient to examine unit dipoles ($l = 1$ m) at increasing separations. In this study, array elevation was assumed constant at 1 mm.

5.2.1.1 Inline configuration

Figure 5.3 shows the variation of the complex potential in magnitude and phase with dipole separation for the inline dipole-dipole array. The corresponding real potentials for an equivalent DC array according to (3.13) are shown as dotted lines. Curves have been plotted for a range of resistivities representing values between 10^{-1} and 10^{3} Ωm. Separations considered range from $r = 1.1$ m to $r = 100$ m. Note that for the inline geometry it is necessary that $r > l$ (cf. Figure 4.12). For unit dipoles ($l = 1$ m), a separation between dipole midpoints of $r = 2$ m corresponds to all four poles being separated by the same distance (1 m), a configuration also known as the Wenner-γ array.
In accordance with expectations, higher magnitudes are observed in resistive environments while a conductive subsurface results in significantly lower voltages. A difference of five orders of magnitude in resistivity corresponds to a difference of up to two orders of magnitude in voltage. In resistive environments, the decrease in the CR magnitude with separation is practically linear on a log-log scale. For low resistivities and small separations however, the decrease is non-linear and a distinct deviation from the corresponding DC curves can be observed. Under these conditions, the magnitude of the CR potential is higher than the corresponding DC potential due to the influence of the quadrature component.
Phase angles are only accounted for in the CR potentials. In resistive environments, observed potentials are practically always in-phase, regardless of the separation. Separation plays a role in conductive environments, where in-phase behaviour is observed at larger distances, but significant phase shifts can occur at small separations, corresponding to the observed increase in magnitude. At extremely small separations the response tends towards quadrature ($-\pi/2$), i.e. the free space situation.
All magnitudes fall off by approximately three orders of magnitude across two orders of magnitude in separation. By setting a minimum voltage above which signal detection is considered realistic, a maximum separation for safe operation can be derived directly from the graph. For example, assuming that voltages of the order of 10^{-6} V can still be detected under favourable conditions, the maximum dipole separation in a 10 Ωm environment would be approximately 30 m.

5.2.1.2 Equatorial configuration

Figure 5.4 shows the same set of graphs for the equatorial dipole-dipole array. Note that the smallest separation is now $r = 0.1$ m, that is one order of magnitude smaller than for the inline configuration. Such small separations are

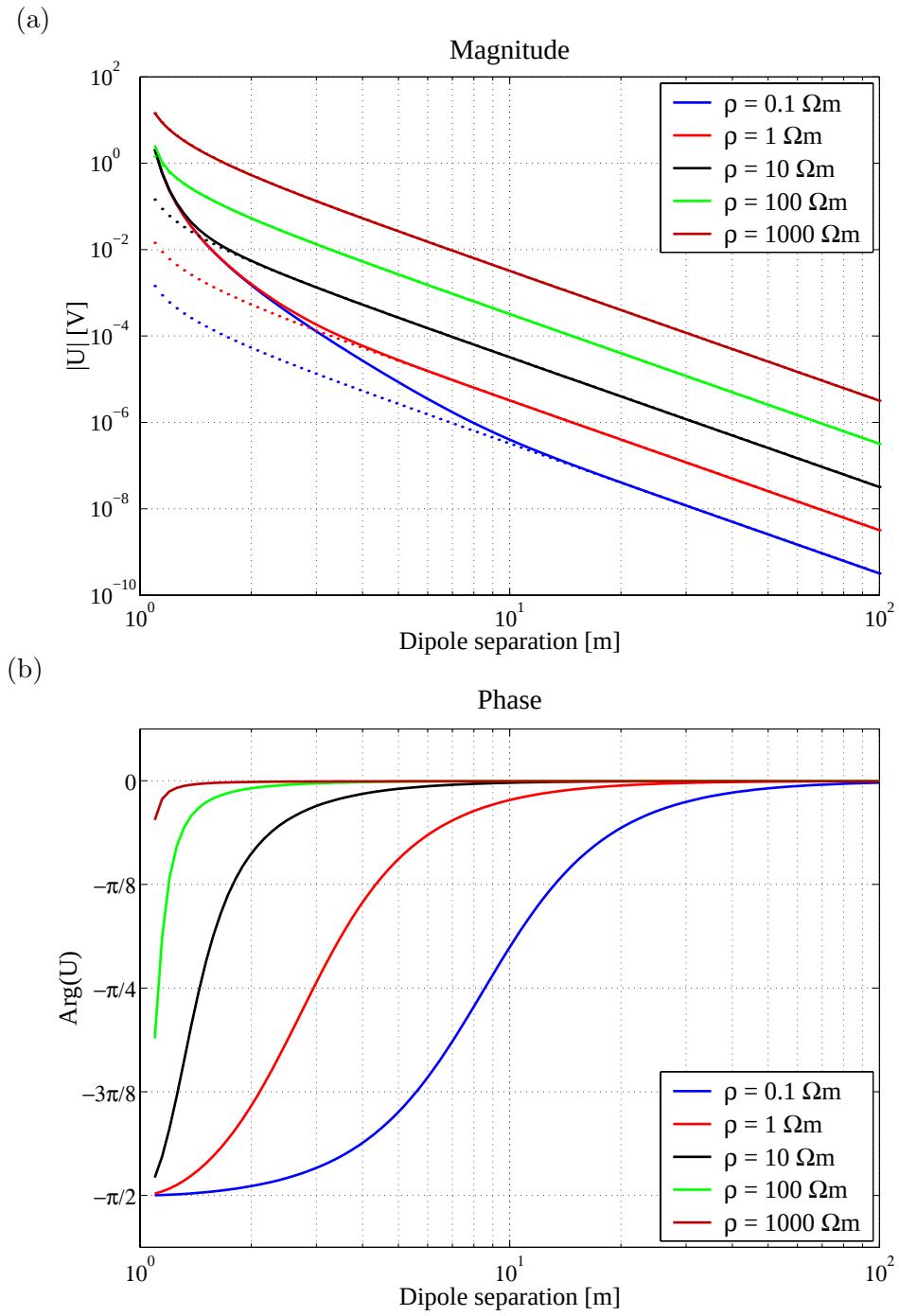

Figure 5.3: Variation of the complex potential with **dipole separation** for a capacitive array in **inline** configuration. Parameter: resistivity. Dipole length $l = 1\mathrm{m}$, array elevation $h = 1\mathrm{mm}$, $\varepsilon_r = 1$, $f = 15\,\mathrm{kHz}$, $I = 10\,\mathrm{mA}$. (a) magnitude, (b) phase. Values for an equivalent DC array are shown as dotted lines.

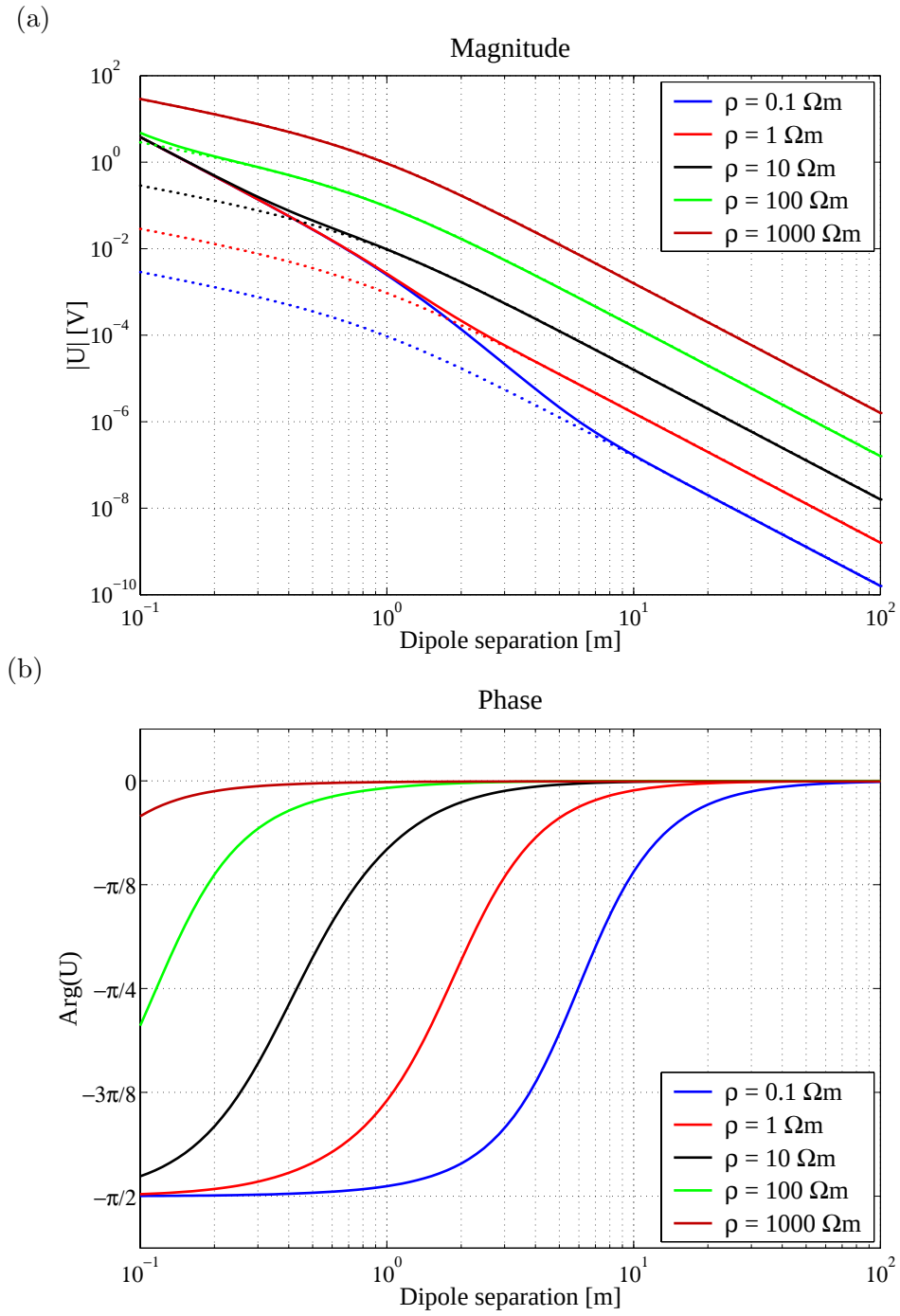

Figure 5.4: Variation of the complex potential with **dipole separation** for a capacitive array in **equatorial** configuration. Parameter: resistivity. Dipole length $l = 1\mathrm{m}$, array elevation $h = 1\mathrm{mm}$, $\varepsilon_r = 1$, $f = 15\,\mathrm{kHz}$, $I = 10\,\mathrm{mA}$. (a) magnitude, (b) phase. Values for an equivalent DC array are shown as dotted lines.

possible with equatorial arrays because the dipoles are no longer collinear, so that dipole separations may be smaller than dipole length, i.e. $r < l$. Again, curves have been plotted for separations up to 100 m. At comparable separations (i.e. in the range between 2 and 100 m), the magnitude curves for the equatorial configuration are very similar to those for the inline configuration, however the magnitude of the received voltage is smaller by a factor. This is consistent with the fact that the equatorial geometry uses the axis perpendicular to the main dipole symmetry axis, hence the "coupling" between potential and current dipole is expected to be weaker. As a consequence, observed potentials for the equatorial array are smaller than those observed with an inline array at comparable separations r. For the same injection current, the maximum dipole separations that can be achieved with equatorial geometry are also smaller. For example, for a voltage threshold of 10^{-6} V the maximum separation in a 10 Ωm environment would now be reduced to approximately 25 m. For low resistivities, a distinct deviation from the corresponding DC curves can again be observed at small separations. As in the case of the inline geometry, the magnitude of the CR potential is higher than the corresponding DC potential. The CR phase angles for inline and equatorial geometries are very similar at comparable separations (note the difference in horizontal scale between Figure 5.3 and Figure 5.4). However, as the equatorial configuration allows the use of separations smaller than the dipole length, one is more likely to encounter significant phase shifts with this geometry. For a given separation, the phase shift can increase dramatically as resistivity decreases. For example, a rectangular array with $r = 2$ m would observe phase angles of $-2.47 \cdot 10^{-3}$ or -0.14° at 1000 Ωm, $-8.17 \cdot 10^{-3}$ or -0.47° at 100 Ωm, $-79.9 \cdot 10^{-3}$ or -4.58° at 10 Ωm, -0.675 or -38.7° at 1 Ωm, and -1.45 or -82.9° at 0.1 Ωm.

5.2.2 Array elevation

In contrast to the DC case, elevation of the capacitive array above the surface now also has an influence on the transfer impedance. The size of this effect is important for the design of practical instruments, because the effective elevation of a real capacitive sensor can not always be accurately determined as the ground surface is not planar.
Without loss of generality, the only geometries considered here are four electrodes having the same elevation, i.e. the entire array is assumed at a constant height above ground. This is a reasonable assumption because the geometric factor and hence the transfer impedance do not change fundamentally if different electrodes have slightly different elevations (cf. Equations 4.23 and 4.24), as may be expected for measurements on natural surfaces (e.g. vegetation) and in uneven terrain. Again unit dipoles were considered due to scalability, this time however at a fixed separation of 2 m in the case of the inline array and 1 m in the case of the equatorial array. The former corresponds to a unit Wenner-γ array, the latter to a unit square array.

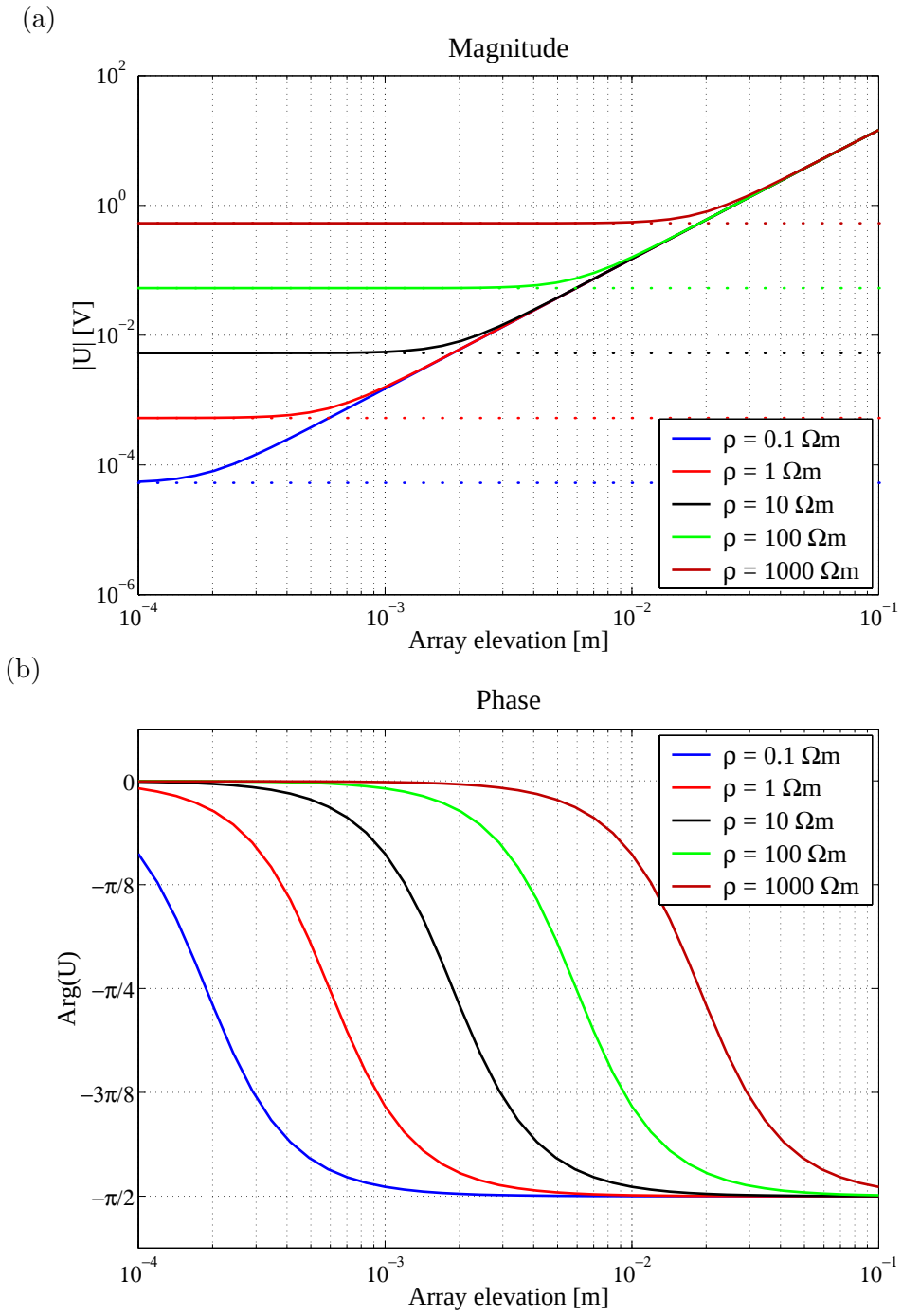

Figure 5.5: Variation of the complex potential with **array elevation** for a capacitive array in **inline** configuration. Parameter: resistivity. Dipole length $l = 1\mathrm{m}$, dipole separation $r = 2\mathrm{m}$, $\varepsilon_r = 1$, $f = 15\,\mathrm{kHz}$, $I = 10\,\mathrm{mA}$. (a) magnitude, (b) phase. Values for an equivalent DC array are shown as dotted lines.

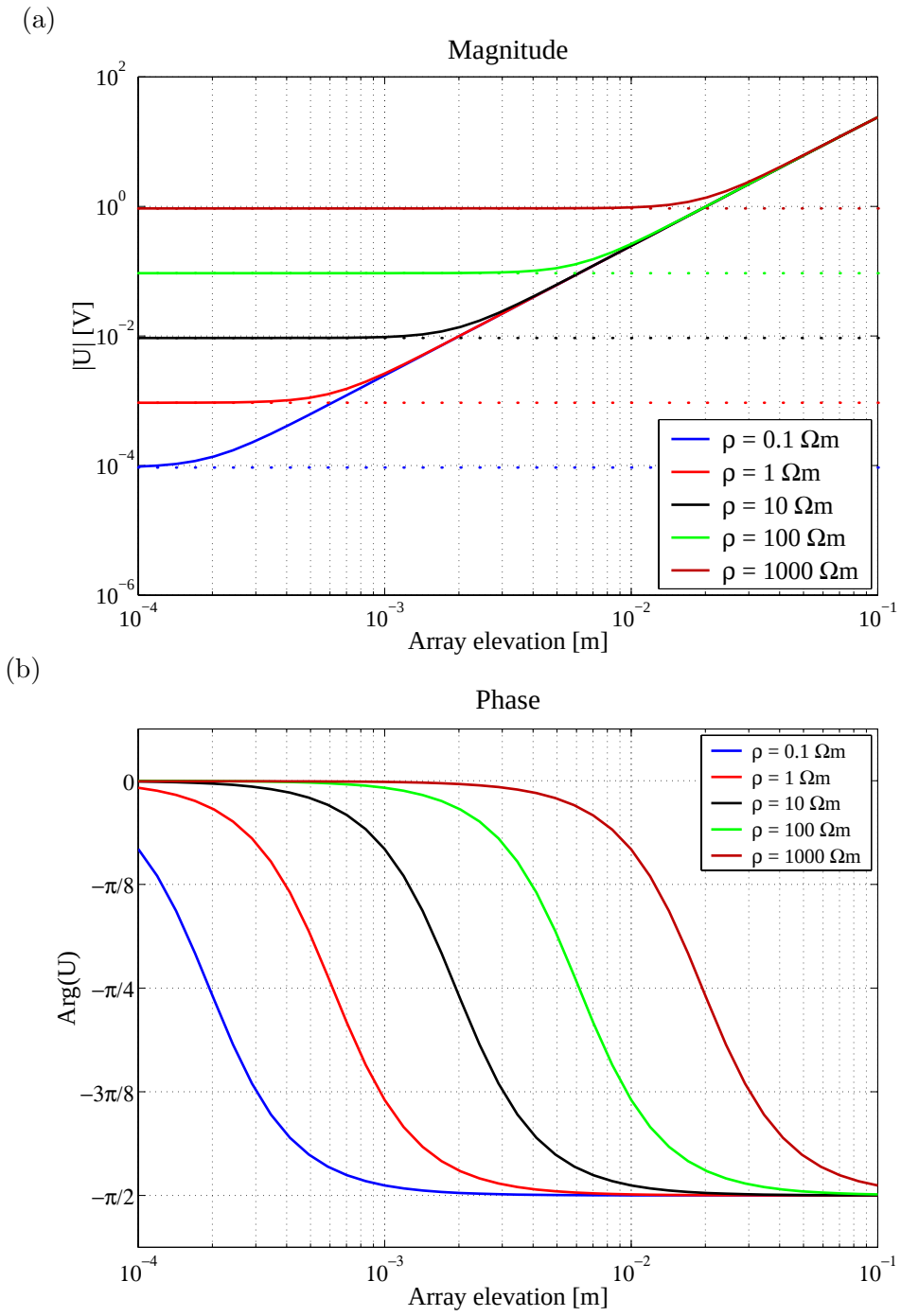

Figure 5.6: Variation of the complex potential with **array elevation** for a capacitive array in **equatorial** configuration. Parameter: resistivity. Dipole length $l = 1\mathrm{m}$, dipole separation $r = 1\mathrm{m}$, $\varepsilon_r = 1$, $f = 15\,\mathrm{kHz}$, $I = 10\,\mathrm{mA}$. (a) magnitude, (b) phase. Values for an equivalent DC array are shown as dotted lines.

5.2.2.1 Inline configuration

Figure 5.5 shows the variation of the complex potential in magnitude and phase with array elevation for the inline dipole-dipole array. The corresponding potentials for an equivalent grounded array are shown as dotted lines. As before, curves have been plotted for five different resistivities. The range of elevations considered is between 10^{-4} and 10^{-1} m, corresponding to capacitive sensors lying on, or close to, the ground.
In accordance with the DC case, the magnitude of the observed CR potential at small elevations is constant, and only a function of resistivity. This is an important observation because it means that minute changes in elevation, which may be difficult to account for in a practical field setup, have no significant effect on the result of the measurement. At larger elevations, magnitudes start to increase and eventually show asymptotic behaviour towards the free space value. The point where this occurs is a function of resistivity. In free space, the conducting earth is distant and hence the transfer impedance is no longer sensitive to resistivity. Large elevations must therefore be avoided. However, one has to bear in mind that throughout this parameter study the injected current is assumed constant, yet in practice an increase in sensor elevation is equivalent to an increase of impedance in the transmitter output circuit (Section 5.1.2). Realistically, the current (and hence the observed potential) must therefore decrease, unless additional power is provided by the generator.
The CR phase curves show a fundamental transition associated with the increase in magnitude. At small elevations the observed voltage is largely inphase, corresponding to the DC case with zero elevation. At larger elevations the quadrature component grows and the response undergoes a phase rotation of $-\pi/2$. Again, this corresponds to free space conditions where the CR transfer impedance is entirely in quadrature (cf. Equation 4.20).

5.2.2.2 Equatorial configuration

Qualitatively, the results are almost identical for the equatorial dipole-dipole array (Figure 5.6). Again, the magnitude of the observed CR potential is constant for small elevations and only a function of resistivity. The same asymptotic behaviour that is observed with the inline array is also found with the equatorial geometry. The phase curves are almost identical between both configurations. The difference between both sets of curves is due to the weaker "coupling" between current and potential dipoles in equatorial geometry. The CR and DC transfer impedances are generally lower for the equatorial configuration at comparable separations.

5.3 Electrical properties

The physical properties of the subsurface are the only genuine variables in the context of this study, while all other system design parameters will be fixed in a practical instrument. Any variation in the measured transfer impedance will then be attributed to a variation in the electrical properties.

5.3.1 Resistivity

The functional dependence of the CR transfer impedance on resistivity is assessed. It was shown in Chapter 4 that the use of audio frequencies for CR implies operation under a conductive regime ($\Omega \ll 1$, cf. Section 4.6.4.2). At these frequencies, CR must therefore be mainly sensitive to resistivity as opposed to dielectric properties. Unit dipoles at a range of separations in both inline and equatorial configuration are considered.

5.3.1.1 Inline configuration

Figure 5.7 shows the variation of the complex potential with resistivity in magnitude and phase for the inline dipole-dipole array. The corresponding potentials for an equivalent DC array are shown as dotted lines. Curves have been plotted for five different dipole separations, ranging between 2 m (corresponding to Wenner-γ) and 25 m. This range of separations is likely to be relevant to shallow site investigation studies. The array elevation is fixed at 1 mm. The range of resistivities considered is between 10^{-1} and $10^{3}\,\Omega$m.
In accordance with expectations, greater magnitudes are observed for shorter array separations. The DC potential grows linearly with resistivity in line with (3.14). The magnitude of the CR potential is observed to follow the DC curves almost everywhere except for low resistivities and at small dipole separations. There the CR curves flatten out and magnitudes remain at constant levels despite a further decrease in resistivity. This is due to the growing influence of the quadrature component. With decreasing dipole separation, the onset of this effect occurs at higher resistivities. For the range of parameters considered, CR magnitudes and DC potentials are only identical above resistivities of $\rho = 10\,\Omega$m. For smaller resistivities, the influence of the quadrature component is significant and a resistivity estimate based upon the magnitude would be inadequate. The phase curves reflect this transition. For high resistivities and large separations, the phase angle is close to zero, i.e. the observed potential is in-phase with the injected current. Towards low resistivities however, phase shifts occur and the response eventually moves into quadrature. The smaller the dipole separations are, the higher the resistivities at which this effect appears.

5.3.1.2 Equatorial configuration

Qualitatively, the same behaviour that was observed with the inline dipole-dipole array is also found with the equatorial configuration (Figure 5.8). For better comparison between the two configurations, a similar range of separations between dipole midpoints was considered, except that the smallest array in equatorial configuration is the unit square array ($r = 1$m). As observed previously, the main difference between the two configurations is that the potentials obtained with the equatorial configuration are generally lower than those obtained with the inline configuration for the same resistivity (and comparable dipole separations). The observation that, for the range of parameters considered, CR magnitudes and DC potentials are identical only above resistivities of $\rho = 10\,\Omega$m, applies also to the equatorial configuration.

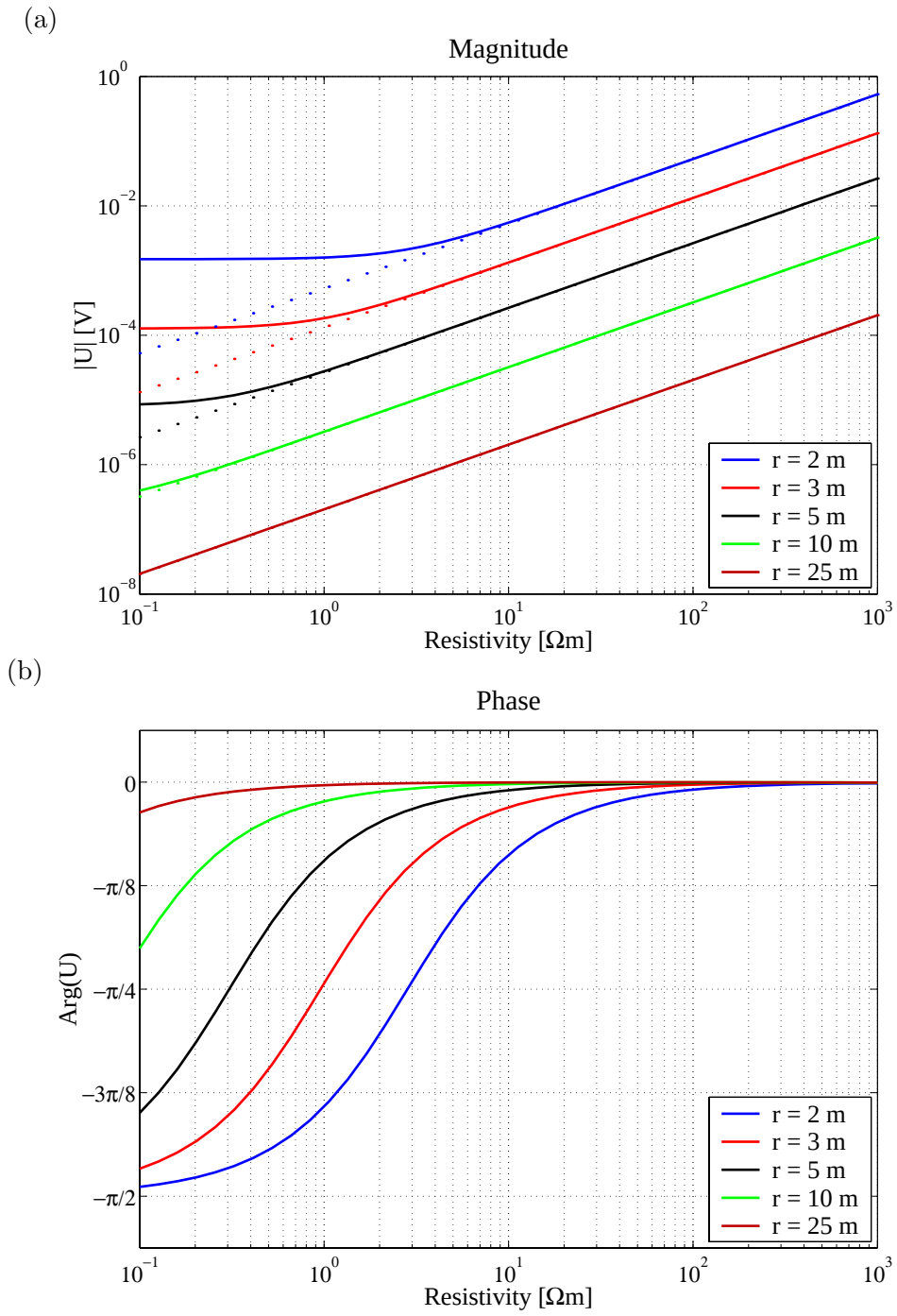

Figure 5.7: Variation of the complex potential with **resistivity** for a capacitive array in **inline** configuration. Parameter: dipole separation r. Dipole length $l = 1\mathrm{m}$, array elevation $h = 1\mathrm{mm}$, $\varepsilon_r = 1$, $f = 15\,\mathrm{kHz}$, $I = 10\,\mathrm{mA}$. (a) magnitude, (b) phase. Values for an equivalent DC array are shown as dotted lines.

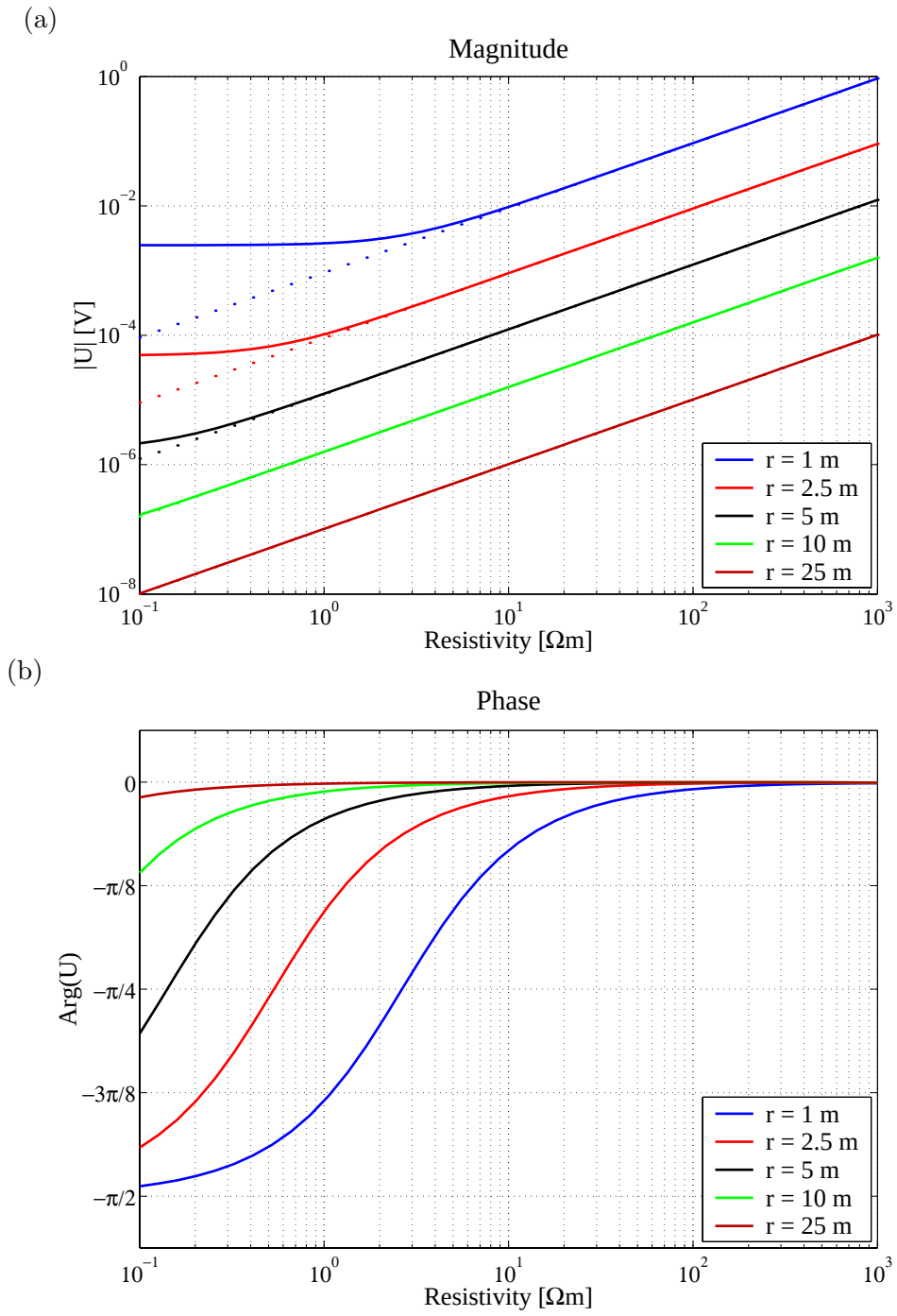

Figure 5.8: Variation of the complex potential with **resistivity** for a capacitive array in **equatorial** configuration. Parameter: dipole separation r. Dipole length $l = 1\mathrm{m}$, array elevation $h = 1\mathrm{mm}$, $\varepsilon_r = 1$, $f = 15\mathrm{kHz}$, $I = 10\mathrm{mA}$. (a) magnitude, (b) phase. Values for an equivalent DC array are shown as dotted lines.

5.3.2 Relative permittivity

The sensitivity of the CR technique towards dielectric properties is only marginal at audio frequencies. Measurable variation of the CR transfer impedance with relative permittivity at 15 kHz can only be obtained in highly resistive environments (Grard and Tabbagh, 1991; Tabbagh et al., 1993). For a study of this variation, a resistivity of $10^5\,\Omega$m has therefore been assumed, which exceeds the range considered previously by two orders of magnitude. Such ground conditions are not unrealistic, however the injection of sufficient amounts of current into a highly resistive earth is much more difficult. This practical limitation has been accounted for by assuming a lower injection current of 1 mA. The range of relative permittivities considered is between $\varepsilon_r = 1$ (free space value) and $\varepsilon_r = 80$ (water).

5.3.2.1 Inline configuration

Figure 5.9 shows the variation of the complex potential with relative permittivity in magnitude and phase for the inline dipole-dipole array. The corresponding potentials for an equivalent DC array, shown as dotted lines, are constant with respect to dielectric properties. Curves have been plotted for five different dipole separations, ranging between 2 m (Wenner-γ) and 25 m. The array elevation is again fixed at 1 mm.
Potentials can reach values up to approximately 5 V for the Wenner-γ array, but are significantly lower at long offsets ($\approx 2 \cdot 10^{-3}$V at 25 m). CR magnitudes match the corresponding DC value at $\varepsilon_r = 1$ before falling off by almost one order of magnitude towards higher ε_r.
The CR phase curves are identical for all separations. Starting at phase angles close to zero for $\varepsilon_r = 1$, the phase then rotates towards $-\pi/2$ and nearly reaches quadrature for $\varepsilon_r = 80$.

5.3.2.2 Equatorial configuration

Figure 5.10 shows the same set of graphs for the equatorial dipole-dipole array. Qualitatively, the results are identical with those of the inline configuration. The unit square array ($r = 1$ m) observes DC potentials with approximately twice the magnitude of those observed with the Wenner-γ array, which is in line with previous results. At long offsets, the equatorial array again observes smaller potentials than the comparable inline array.

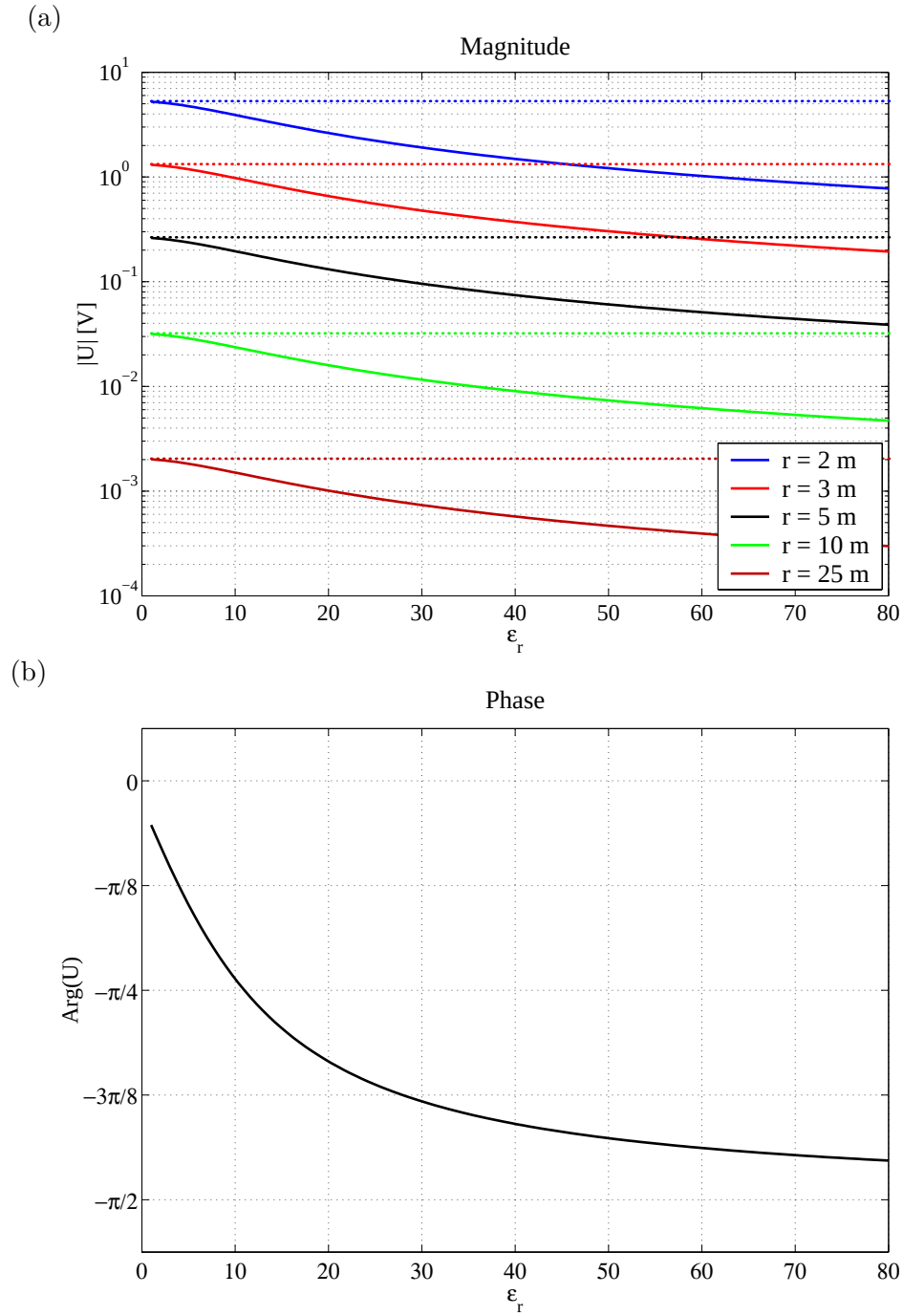

Figure 5.9: Variation of the complex potential with **relative permittivity** for a capacitive array in **inline** configuration. Parameter: dipole separation r. Dipole length $l = 1\mathrm{m}$, array elevation $h = 1\mathrm{mm}$, $\rho = 10^5\ \Omega\mathrm{m}$, $f = 15\,\mathrm{kHz}$, $I = 1\,\mathrm{mA}$. (a) magnitude, (b) phase. Values for an equivalent DC array are shown as dotted lines.

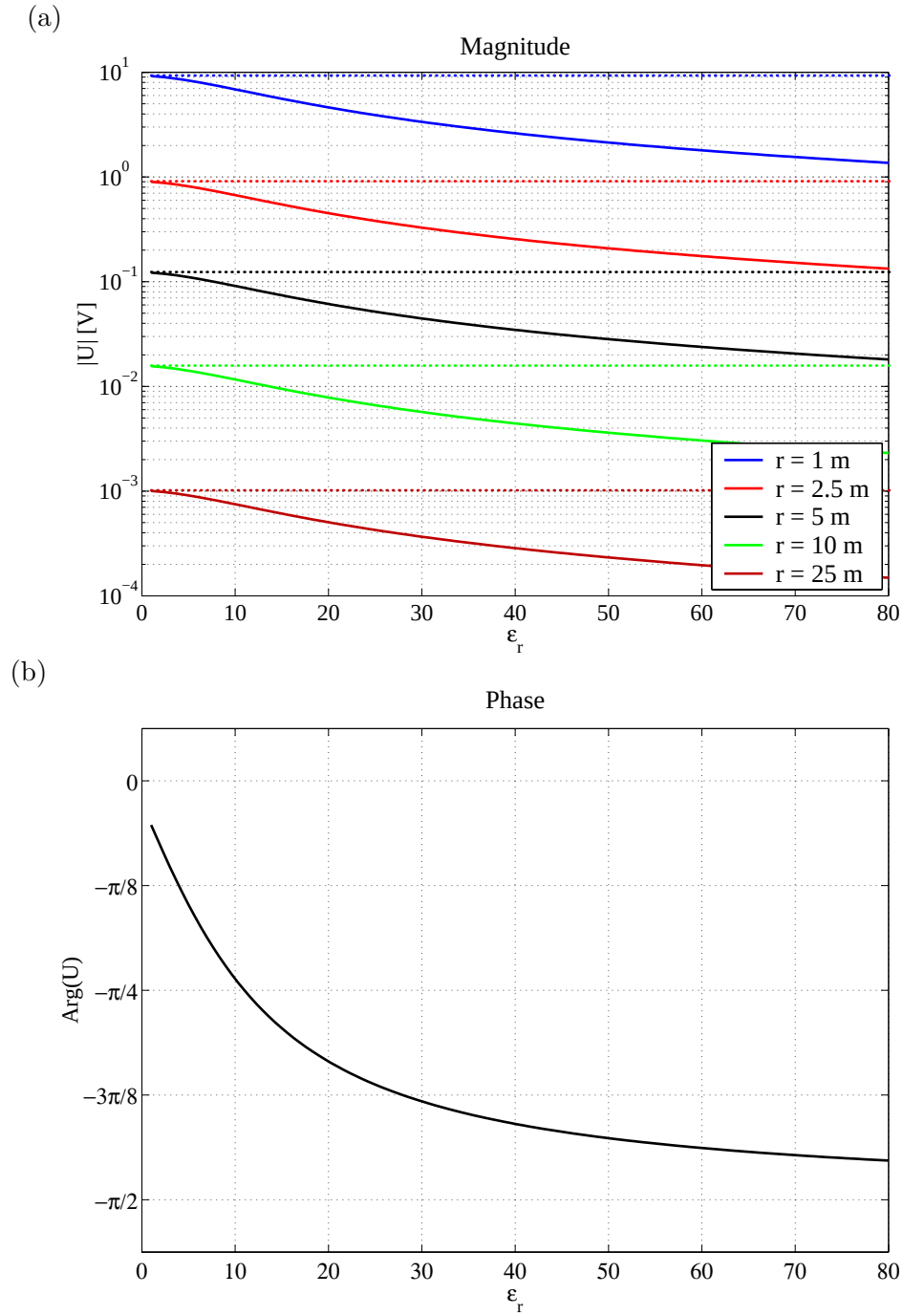

Figure 5.10: Variation of the complex potential with **relative permittivity** for a capacitive array in **equatorial** configuration. Parameter: dipole separation r. Dipole length $l = 1\mathrm{m}$, array elevation $h = 1\mathrm{mm}$, $\rho = 10^5\Omega\mathrm{m}$, $f = 15\mathrm{kHz}$, $I = 1\mathrm{mA}$. (a) magnitude, (b) phase. Values for an equivalent DC array are shown as dotted lines.

5.4 Modelling of capacitive sensors

The characteristics of a realistic capacitive sensor and the implications of its design for the CR measurement have not been discussed so far. This has been deliberate since it is clearly important to distinguish between general properties of the CR technique (i.e. the complex response predicted for an electrostatic quadrupole) and the particular properties of capacitive sensors. In this section, the properties of capacitive sensors will be examined more closely. The essential parameter of a capacitive sensor is its capacitance with respect to ground. The operational principle of CR is critically dependent on the sensor capacitance:

1. At the current dipole, the capacitance of the electrodes controls current injection into the ground. Greater capacitance is associated with a lower impedance so that higher currents may be injected at a given transmitter output power.

2. The potential dipole can be regarded as a passive probe sensing the electric field near the ground surface due to the current flow between the transmitter poles. The sensor capacitance is a measure for the degree of electrical coupling between the sensor and the ground.

An appraisal of capacitive sensors must therefore start with the evaluation of sensor capacitances, including their theoretical estimation and practical measurement. It is thought that a better appreciation of capacitive sensors may lead to enhanced understanding of the CR technique in general.

5.4.1 The capacitance of elementary geometric structures

In Section 5.1.2, the effective capacitance of generic capacitive sensors has been represented by the parallel-plate approximation. For a realistic sensor however, the parallel-plate model is too crude because it assumes plates of infinite area and neglects the influence of the fringing electric field at the corners and edges of a practical sensor. Two practical sensor types are plate-wire combinations and capacitive line antennas. In neither case can the parallel-plate formula be expected to provide an accurate estimate of sensor capacitance. The physical shape and design of the sensor controls not only its total effective capacitance, but also the spatial distribution of capacitive contact across the surface area covered by the sensor. Greater current densities can be expected in those areas of a sensor where the local impedance is low, i.e. in places with elevated local capacitance. Basic information about the spatial distribution of current flow can therefore be obtained by estimating capacitances of the component parts of a sensor.

The estimation of capacitances of elementary geometric structures is a well-known problem in other areas of applied physics. For example, one important application is the process of placing a large number of electronic components on an integrated circuit, otherwise known as VLSI[2]. In VLSI, the interaction of

[2] Very Large-Scale Integration

circuit elements with a substratum and each other is usually undesirable, but difficult to avoid. This interaction is mainly a function of mutual capacitance which can be assessed by modelling the elementary structures of a circuit.

5.4.1.1 Determination of capacitance

The capacitance of a conductor over a ground plane is determined by the geometric shape of the conductor's surface, its perimeter and the distance of the conductor from the surface. Essentially, the relation

$$C = \frac{Q}{U} = \frac{1}{U} \iint_S \sigma \, dS \tag{5.9}$$

is used to calculate capacitance, where S is the surface of the conductor and σ is the surface charge density. When a voltage U with respect to ground is applied, surface charges occur on both the ground plane and the conductor. Their density σ is a measure for the discontinuity of the normal component D_n of the dielectric flux density $\boldsymbol{D} = -\varepsilon_0 \varepsilon_r \nabla V$ (3.1, A.6):

$$D_{n_1} - D_{n_2} = \sigma \tag{5.10}$$

The potential V can be calculated from Laplace's equation by solving the associated boundary-value problem (Ringhandt and Wagemann, 1993).

5.4.1.2 Wire segment above a ground plane

Analytical solutions exist only for simple geometries. An infinite cylindrical conductor suspended over the ground plane (Figure 5.11) represents a two-dimensional problem where such a solution can be found. The capacitance per unit length of such a conductor is given by (Smythe, 1950; Yuan and Trick, 1982; Baxter, 1997)

$$C' = \frac{2\pi\varepsilon_0\varepsilon_r}{\ln\left(\frac{d+\sqrt{d^2-a^2}}{a}\right)} = \frac{2\pi\varepsilon_0\varepsilon_r}{\operatorname{acosh}\left(\frac{d}{a}\right)} \tag{5.11}$$

where a is the radius of the conductor and d the distance from its centre to the ground plane. The arrangement is a suitable model for a wire segment lying on the ground surface without having galvanic contact, for example due to insulation. Although expression (5.11) refers to a wire of infinite length, it is a good approximation for a finite wire segment if the length of the segment is far greater than the wire radius. C' must be multiplied by the length of the wire segment in order to obtain its total capacitance.

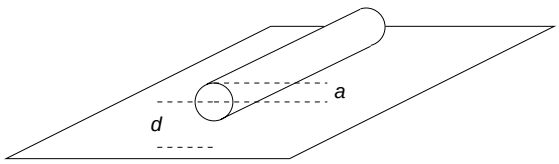

Figure 5.11: Cylindrical conductor above ground plane.

5.4.1.3 Finite-size plate above a ground plane

The other relevant geometry in the context of CR is that of a finite-size plate above a ground plane. This problem can only be solved numerically. An approximate functional expression for the capacitance of a rectangular plate of finite thickness was given by Sakurai and Tamaru (1983):

$$\begin{aligned} C = \varepsilon_0 \varepsilon_r \cdot \Big[& 1.15 \, \frac{w \cdot l}{h} \\ & + 1.40 \left(\frac{t}{h} \right)^{0.222} \cdot (2w + 2l) \\ & + 4.12 \left(\frac{t}{h} \right)^{0.728} \cdot h \Big] \end{aligned} \tag{5.12}$$

Here, w and l are the width and length of the plate, respectively, t its thickness and h the elevation of the bottom face above the ground surface (Figure 5.12). By comparing (5.12) to the parallel-plate approximation (5.6), it can be seen that the capacitance of a single plate is greater. This is because the opposing "plate" in the capacitor is now represented by the infinitely wide ground plane, so that the fringing fields at the edges and corners of the plate must be taken into account. The first term in Sakurai and Tamaru's expression corresponds to the parallel-plate term, raised by 15% (factor of 1.15). The second and third terms are due to the contribution from the edges and corners of the plate, respectively.

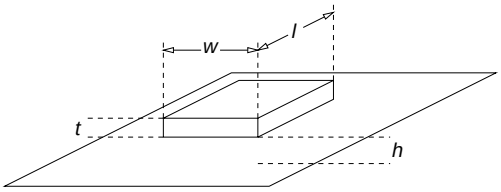

Figure 5.12: Finite-size rectangular plate above ground plane.

5.4.2 Application to capacitive sensors

As the capacitances of the component parts of a capactive sensor are now known, their relative contribution to the total sensor capacitance can be estimated for the sensor types introduced in Section 4.3.

5.4.2.1 The capacitive line antenna

A capacitive line antenna simply consists of a segment of wire or cable lying on the ground. The conducting part of the wire is separated from the ground by its sheathing and perhaps small air gaps where uneven ground prevents direct contact with the surface. Therefore, the line antenna has a well-defined finite capacitance against ground. The air gaps may be distributed more or less regularly along the length of the antenna, depending on the type of ground surface.

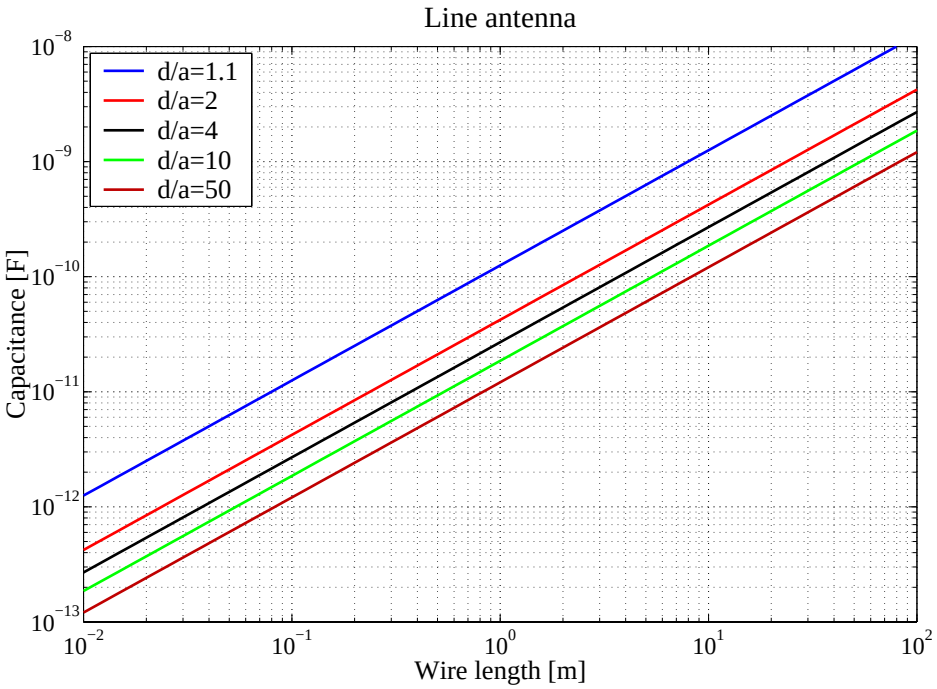

Figure 5.13: Capacitance of a capacitive line antenna as a function of length for different ratios d/a.

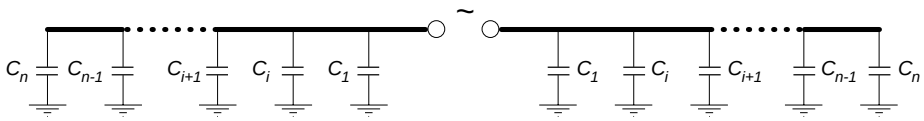

Figure 5.14: Equivalent circuit model of a line antenna dipole close to the ground.

The capacitance of an infinite line antenna is given by (5.11). For example, a line antenna with $d/a = 6$ (e.g. $d = 6$ mm, $a = 1$ mm, corresponding to a wire of 2 mm diameter elevated above ground with a 5 mm air gap) has a capacitance per unit length of 22.5 pF/m. The total capacitance of a finite-length antenna is obtained by multiplication of this factor with total antenna length. The graph in Figure 5.13 shows the capacitance of a line antenna as a function of its length for different ratios d/a. Capacitances are greater for smaller values of d/a, corresponding to the situation where the wire is closer to the surface. This is analogous to what is observed for a parallel-plate capacitor. Ratios much smaller than $d/a = 2$ are unrealistic. The results show that a suitable window of parameters exists where capacitive line antennas can be operated successfully. Still, for all relevant ratios of d/a, a total capacitance of 100 pF is only exceeded by line antennas with a length of several metres, particularly for $d/a \geq 2$. The discussion in Section 5.1.2 has shown that in order to keep the transmitter output impedance below a practical upper limit at audio frequencies, a sensor capacitance of the order of 1 nF is required. Capacitances much lower than 100 pF may be inadequate to provide sufficient capacitive coupling. It is therefore recommended that line antennas employed for CR measurements at those frequencies should have a minimum overall length of several metres.

The fact that the capacitance of a line antenna increases linearly with length can help explain the observation of a linear decrease in current along the antenna (Timofeev, unpublished, cf. Section 4.3.2). Consider a line antenna discretised into small segments of equal length, each of which has a distinct capacitance. A non-grounded dipole consists of two "poles" or antenna parts, each of which can be regarded as such a sequence of capacitors. The simplified equivalent electrical circuit model of such an antenna comprises n capacitors connected in parallel (Figure 5.14). The total capacitance of a symmetric non-grounded dipole is then given by the sum of the capacitances of the individual segments:

$$C_{\mathrm{LA}} = \frac{1}{2} \sum_{i=1}^{n} C_i \tag{5.13}$$

The division by two is due to the two poles connected in series with each other. In this model, an identical amount of current I_i leaks to the ground through each individual capacitive segment C_i:

$$I_i = \frac{U}{Z_i} = i\omega U C_i \tag{5.14}$$

where U is the voltage across the antenna, which is assumed to be constant in this model as the antenna itself represents an equipotential surface. The current observed at different positions along the antenna will then decrease linearly with distance according to (4.1), as the amount of current leaking into the ground is proportional to distance.

5.4.2.2 The plate-wire combination

A plate-wire combination comprises two component parts, a metallic sheet or plate and a segment of wire connecting the plate to the transmitter or receiver

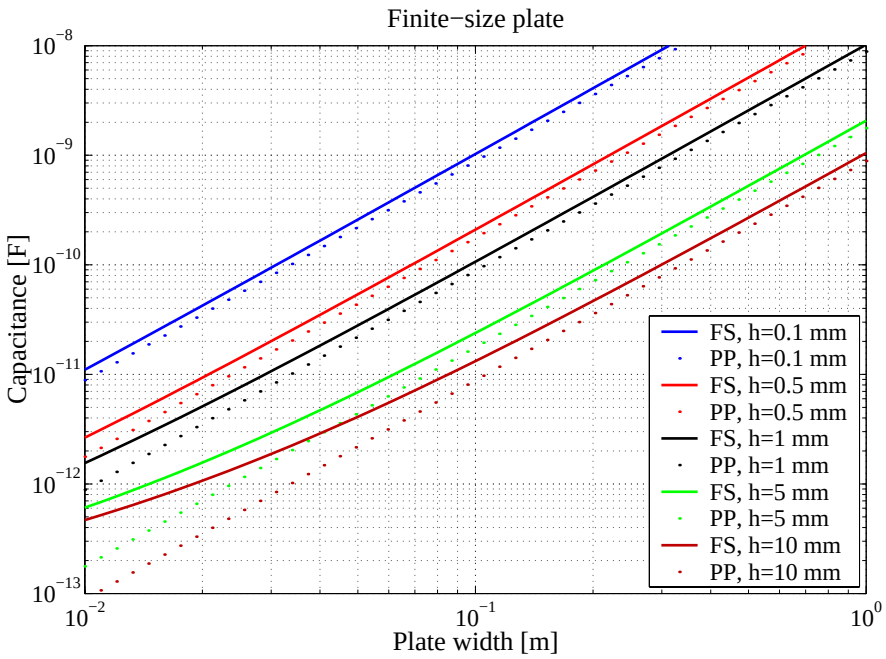

Figure 5.15: Capacitance of a square finite-size plate above ground as a function of its width for a range of elevations h. A thickness of $t = 1$ mm is assumed. Values for the corresponding parallel-plate model are plotted for comparison. FS: finite size, PP: parallel-plate.

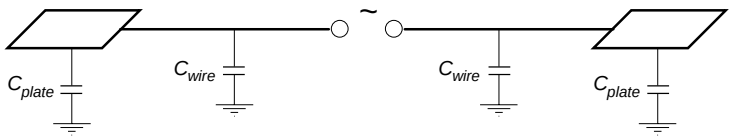

Figure 5.16: Equivalent circuit model of a plate-wire combination close to the ground.

units. In some practical sensor designs (e.g. CORIM™) the wire segment is mounted on a plastic mat in immediate vicinity of the ground surface. In that case both components of the plate-wire combination contribute to the total capacitance of the sensor. The relevant capacitances are those of a single plate (C_{Plate}) and of a single piece of wire (C_{Wire}), which must be examined separately.

A graph of the capacitance of a finite-size square plate above ground as a function of its width (and thus its surface area) is shown in Figure 5.15, together with the corresponding values for the parallel-plate model. The height h in the finite-size model corresponds to the inter-plate distance in the parallel-plate arrangement. In accordance with expectations, the finite-size capacitance is always greater than the parallel-plate capacitance. For small plates and larger elevations, the deviation of the finite-size capacitance from the parallel-plate model can be significant. As an example, typical plates may be $25\,\mathrm{cm} \times 25\,\mathrm{cm}$ in size with a thickness of 1 mm. At an elevation of 5 mm, such a plate would have a theoretical capacitance against ground of approximately 136.0 pF, according to (5.12). In contrast, the parallel-plate model yields a significantly smaller capacitance of 110.7 pF, corresponding to an error of nearly 20%.

As far as the wire element of the plate-wire combination is concerned, d/a ratios similar to those encountered with line antennas also apply for the connecting wires, hence such wires can be expected to have a similar capacitance per unit length. For example, a wire element close to the surface with a ratio of $d/a = 2$ would have a theoretical capacitance of 42.2 pF/m, while an elevated wire element with a ratio of $d/a = 10$ would only have 18.6 pF/m.

Analogous to remarks in the previous section, the individual contributions can be regarded as parallel capacitors in the equivalent circuit model (Figure 5.16). The total sensor capacitance for a plate-wire combination is then given by the sum of the individual values:

$$C_{\mathrm{PW}} = C_{\mathrm{Plate}} + C_{\mathrm{Wire}} \tag{5.15}$$

A practical dipole consists of two plate wire-combinations. The total sensor capacitance is therefore

$$C_{\mathrm{PW-Dipole}} = \frac{1}{2}(C_{\mathrm{Plate}} + C_{\mathrm{Wire}}) \tag{5.16}$$

due to the serial arrangement of the two elements.

The key objective in designing a plate-wire sensor is to make the relative contribution of the plate towards the total capacitance significantly greater than that of the wire element. In this case the partial impedance of the plate element can be expected to be much smaller than the partial impedance of the wire element, so that the majority of the current will be injected via the plate, in accordance with the theoretical concept of the electrostatic quadrupole. Figure 5.17 shows a general comparison between the capacitance of a standard plate ($25\,\mathrm{cm} \times 25\,\mathrm{cm}$, thickness $t = 1\,\mathrm{mm}$) and the capacitance of a unit line antenna (1 m length, wire radius $a = 1\,\mathrm{mm}$) as a function of the elevation d. It can be

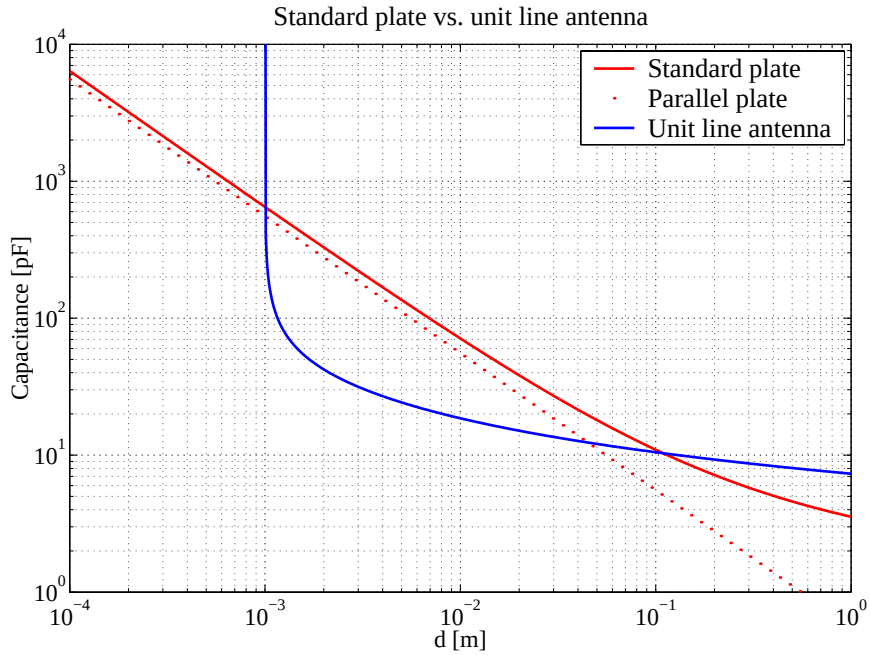

Figure 5.17: Comparison between the capacitance of a standard plate ($25\,\mathrm{cm} \times 25\,\mathrm{cm}$) and a unit line antenna (1 m length) as a function of elevation. Assumptions: plate thickness $t = 1\,\mathrm{mm}$, wire radius $a = 1\,\mathrm{mm}$. Values for the corresponding parallel-plate model are plotted for comparison.

seen that, for small elevations approaching 1 mm, the capacitance of the line antenna increases dramatically, eventually outgrowing the plate capacitance. This situation must be avoided, since the plate would forfeit its purpose, with the majority of the current being injected via the wire segment. Towards larger elevations, e.g. $d/a \geq 2$, the capacitance of the wire segment falls off rapidly and well below the capacitance of the standard plate. The capacitance of the latter decreases more slowly; for relevant elevations its fall-off is almost linear on a log-log scale. The "critical" level of 100 pF (see above) is reached at an elevation of $d \approx 7\,\mathrm{mm}$.

The results of this comparison show that the balance between the two components of the plate-wire arrangement is critical for the desired use of the sensor as a point pole approximation. Practical designs should aim to maintain very close contact between the plate and the ground surface, with effective elevations not exceeding a few millimetres. With regard to the wire segment instead, it is recommendable to raise the wire as much above the ground as possible in order to avoid any appreciable leakage of current along the connection to the plate. Installation of the wire on a mat in the immediate vicinity of the ground surface is to be discouraged. The use of very long plate-wire dipoles must also be approached with the necessary diligence as the relative influence of the wire segment grows with its length. Although dipoles employed in shallow site investigation studies are unlikely to be much longer than 10 m, extra care must be taken to assess the possibility of current leakage along connecting wires.

5.5 Discussion

The systematic study of design parameters in this chapter has provided an assessment of the practicality of CR measurements under quasi-static conditions. It is now possible to anticipate the likely performance of any practical instrument design. Given the large number of intertwined parameters associated with the CR technique, the feasibility of such measurements is by no means self-evident. However, the results of the parameter study suggest that a realistic set of parameters does exist which facilitates a capacitive measurement of resistivity under quasi-static conditions at scales applicable to environmental and engineering site investigations.

The frequency window of CR. The key parameter in CR is undoubtedly the frequency of operation. It has been shown in this chapter that a quasi-static CR measurement can only be successfully accomplished if two independent conditions are satisfied:

1. Induction numbers are low so that the quasi-static approximation applies, and

2. the frequency-dependent complex impedance of the injection circuit is sufficiently low to allow the passing of suitable electric currents.

While the induction number criterion is associated with an upper frequency limit, the impedance condition implies a lower frequency limit. It was found that both conditions can be met simultaneously in a loosely bounded frequency window in the VLF range. Under the assumptions discussed, this interval was found to range between 1 kHz and 25 kHz, however the limits can be extended at the expense of other parameters such as geometry. For example, higher frequencies than 25 kHz may be used with smaller array dimensions. Tabbagh et al. (1993) have suggested an upper frequency limit of 500 kHz for the quasi-static approximation to apply, however their judgement was based upon a 1 m square array and relatively high resistivities. The limits described here are less specific and apply to a site investigation context where greater array separations (i.e. greater depths of investigation) are required and more conductive environments may be encountered. Although not discussed by previous authors, the range of usable frequencies may be restricted further by the presence of competing natural or man-made electric signals in the same frequency band. In the UK, powerful emissions of long-range VLF transmitters near 16 kHz are of particular concern.

Geometric restrictions. Besides frequency, array geometry is the second most important factor controlling the CR transfer impedance. In contrast to the DC case, the CR response is also sensitive towards electrode elevation. Under quasi-static conditions, the functional dependence of the in-phase component of the CR transfer impedance on the lateral separation between current and potential dipole is nearly identical with the DC case. At low resistivities, small separations or large array elevations, the influence of the quadrature

component becomes measurable, resulting in a phase rotation and increased potential magnitudes compared to the DC case. Under extreme circumstances phase rotations can become so large that the transfer impedance is nearly in quadrature. The same would be true for very low frequencies. The reason for this effect lies in the sensitivity of the quadrature component to elevation, whose influence grows for small separations. In that case the geometric factor K^{ES} in (5.2b) becomes smaller against 1. It should be noted that this effect is purely electrostatic and not a result of electromagnetic induction.
This result has important consequences for the determination of resistivity from the measured transfer impedance. If only the magnitude of Z is measured, the CR technique will clearly overestimate resistivity at small array separations where CR magnitudes deviate from the DC potential (cf. Figures 5.3, 5.4). Under these circumstances, a correct resistivity estimate can only be obtained from the in-phase component of Z which is still in agreement with the DC value. The potential error introduced by the use of magnitudes will be larger in conductive environments. The implications for the design of a practical CR instrument are clear. If small array separations are to be used or measurements are to be performed on conductive ground, the fully complex transfer impedance must be measured, independent of the prerequisite of quasi-static conditions.

Significance of capacitance modelling. In the second part of this chapter, the properties of the capactive sensors themselves were studied by modelling the capacitance of their component parts. This is important because the electrostatic formalism makes no provision for the nature of the current injection or potential measurement. The key finding here is that the theoretical concept of point poles postulated in the electrostatic formalism has a practical realisation in the plate-wire sensor, provided that the plate dimensions are limited compared to dipole length. Despite the fact that some existing CR instruments use plate-wire sensors, this particular issue had not been previously addressed in the literature.
Capacitance modelling has also given insight into the properties of capacitive line antennas. It was found that such antennas must have a certain minimum length in order to be suitable as CR sensors. This is again due to the fact that a minimum capacitance is required to pass sufficient electrical current into the ground. The result also indicates that the electrostatic formalism cannot be applied to capacitive measurements with line antennas, since the assumption of point poles is inappropriate.

Fields of application for CR sensor types. The results of this chapter help to identify fields of application for both generic types of CR sensors. Due to the practical equivalence with point-poles, plate-wire sensors can be used to create classical electrode configurations known from the DC case, provided that the capacitance of the wire component is small against the capacitance of the plate. Typically, this means that the length of the wire is limited compared to the dimensions of the plate. If the connecting wire is lying on the ground, only dipolar configurations of the type ABMN are practical since configurations

of the type AMNB (e.g. Schlumberger, Wenner) or single-pole configurations (pole-pole, pole-dipole) would require long wire segments with significant capacitance. Plate-wire combinations are ideal for small-scale mobile arrays with compact dimensions. Such arrays could be usefully employed in shallow site investigation studies.
Meanwhile, the length of capacitive line antennas should not fall below a certain minimum for satisfactory operation. This requirement restricts their application to larger-scale arrays with dimensions of several tens of metres. In contrast to the plate-wire sensors, line antennas couple with the ground across their entire length, resulting in an averaging effect corresponding to the size of the antenna. Line antennas may therefore be less well suited for tomographic imaging applications where geometric accuracy is a key requirement for the plausibility of the inversion results. Nevertheless, line antennas can be useful if greater depths of investigation are required.

Chapter 6

Experimental validation of CR concepts

In previous chapters, the electrostatic formalism was established as the preferred theoretical framework for capacitive resistivity measurements in the quasi-static limit. A parameter study has shown that realistic conditions for practical CR measurements exist and has delivered criteria for instrument design. This chapter is dedicated to the experimental validation of the concepts developed only in theory so far. Initially, a newly developed prototype CR instrument is introduced as a practical implementation of an electrostatic quadrupole. Its measurement principle and specifications are discussed. Using this prototype instrument, a range of fundamental field experiments was conducted to assess the consistency between experimental data and theoretical predictions. The experimental approach was the following: firstly, the properties of real capacitive sensors were examined with respect to their dual role in the transmitter and receiver circuits. The effective capacitance of plate-wire sensors was measured and electrical field recordings were used to assess their wide-band reception properties. Secondly, the spatial properties of the observed complex transfer impedance were studied in a series of elementary surveys. Identical surveys were undertaken with conventional DC resistivity to assess the comparability of both techniques.

6.1 The BGS prototype CRI system

As part of the thematic research programme "Urban Regeneration and the Environment" (URGENT) funded by the UK's Natural Environment Research Council, the British Geological Survey has developed a prototype capacitive resistivity instrument for applications in the built environment. The BGS prototype CRI (Capacitive Resistivity Imaging) system is a straightforward implementation of the theoretical concept of an electrostatic quadrupole. Its major improvement over previous implementations of CR technology is that it measures the fully complex transfer impedance across the sensor array without the need for a reference potential. The instrument design is based upon modern signal detection technology. While commercial CR instruments may have been

taylored to match a particular application or fulfill a specific task, the BGS CRI system has been designed for research and offers utmost flexibility. The user has complete freedom of choice with regard to sensor type and array geometry. The transmitted signal can be tuned to a range of frequencies in the VLF band and output currents are variable. The system is designed for synchronous acquisition from multiple receiver channels and can perform both static and dynamic CR measurements.

6.1.1 Measurement principle

In CR, the task is to measure the electric potential associated with the injected fixed-frequency current, while establishing the phase relation between both signals. The harmonic waveform of a signal generator is to be amplified and injected into the ground. Only signals of this frequency are to be detected at the receiver. For this purpose, the BGS CRI system employs a measurement principle based on phase-sensitive signal detection, while significantly improving the signal-to-noise ratio of weak electric signals.
A schematic diagram of the setup of the BGS prototype CRI system is shown in Figure 6.1. On the transmitter side, a monochromatic sinusoidal signal is fed into a high-voltage, approximately constant power amplifier. This amplifier is designed to provide currents of the order of several mA when injected across capacitive electrodes. In dynamic applications, this current may vary significantly as the transmitter adapts to different surface conditions. It is therefore measured explicitly by means of a resistor in the current path of the capacitive sensor. The receiver unit contains the signal detection unit, measuring the in-phase and quadrature components of the observed potential with regard to the injected current. For this purpose, a phase reference is provided via a link to the transmitter. Basic signal conditioning is undertaken at the receiver dipole before presenting the potential to the signal detection unit. Crucially, the potential measurement is performed in floating mode without an external reference potential. Performance tests with other CR instruments have revealed that the use of such reference potentials (e.g. in conjunction with differential amplifiers) can cause considerable noise problems during towed-array operation. The in-phase and quadrature voltages provided are finally digitised using a 16-bit A/D data acquisition module and logged by a laptop PC. A voltage representing the measured current is obtained via a second link to the transmitter unit, digitised with each potential measurement and acquired synchronously as an additional data channel.

6.1.2 Specifications

The BGS prototype CRI system (Figure 6.2) is designed as a multichannel instrument for synchronous capacitive resistivity measurements with multiple receivers. By default, it operates at a frequency of approximately 14.2 kHz which can be varied within a small bandwidth. Injection currents can be regulated to an upper limit of approximately 30 mA. All components are powered by separate supplies to ensure galvanic decoupling. The use of 12 V batteries

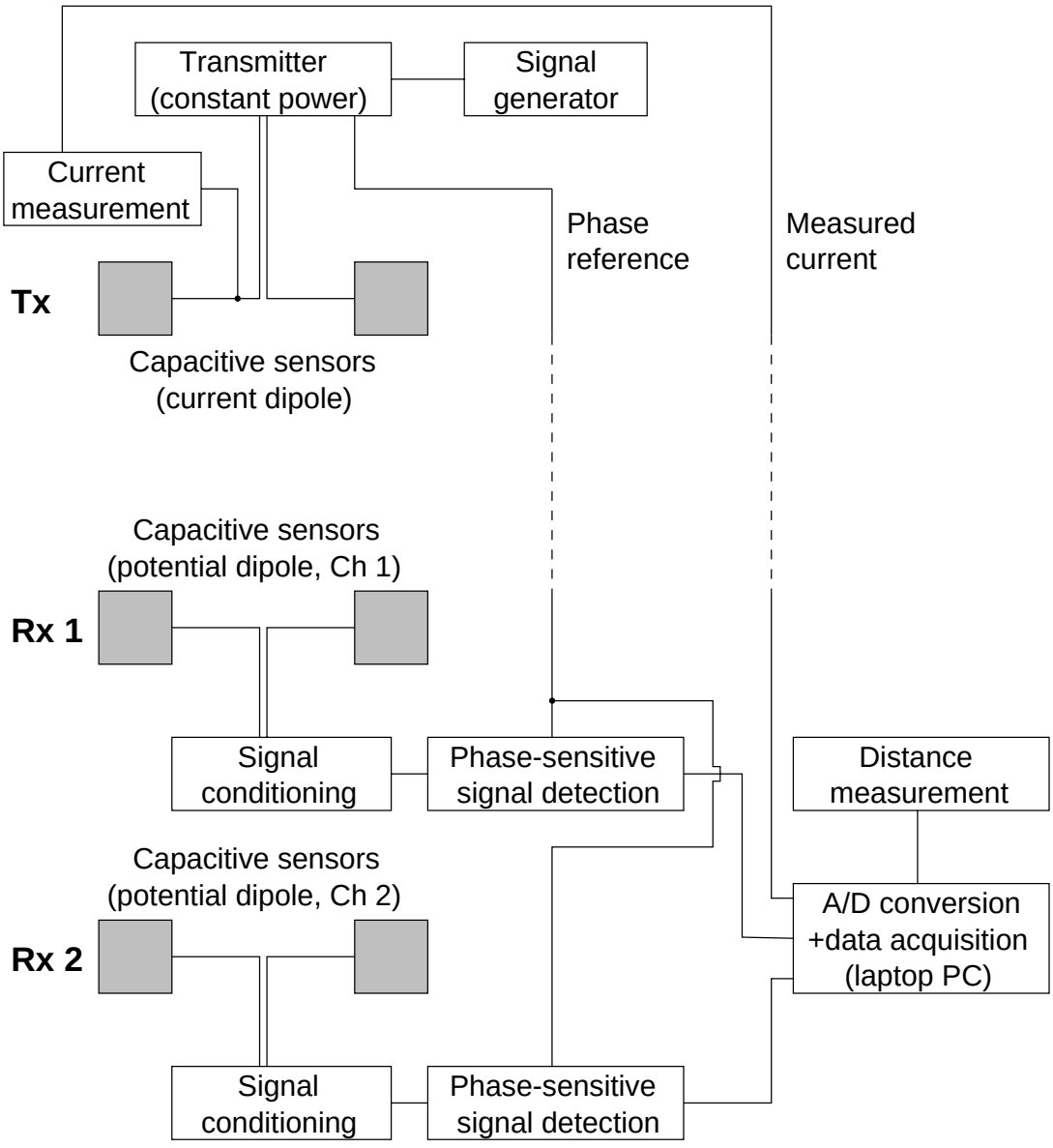

Figure 6.1: Schematic setup of the BGS CRI prototype system. Only two receiver channels are shown to demonstrate the principle.

guarantees flexible operation in the field.

Sensor types. In principle, there are no restrictions on the type of capacitive sensors connected to either the transmitter or receiver units of the BGS prototype CRI system. However, extensive testing has shown that simple plate-wire combinations are highly effective and valid realisations of point poles (cf. Section 6.2). This sensor type is used by default. The sensors consist of square metal plates, 25 cm × 25 cm in size and 2 mm thick, which are connected to the transmitter and receiver units by short segments of thin wire. The plates are encapsulated in plastic for electric insulation. Details of the transmitter unit and current dipole are shown in Figure 6.3, and a potential dipole is shown in Figure 6.4. Plate-wire sensors can be used for static surveys or mounted on towable platforms for mobile applications. In a static survey the array is stationary and the capacitive plates can be placed directly on the ground.

Signal conditioning. The electric potential observed at a receiver dipole is fed through an analogue bandpass filter and instrument amplifier located in the immediate vicinity of the sensors before being passed on to the signal detection unit, which is typically located some distance away from the current and potential dipoles. The cutoff frequencies of the bandpass filter (3 dB points) are approximately 1 kHz and 20 kHz. This bandpass filter serves two purposes. The lowpass component suppresses spectral energy from the upper VLF band and above. High-frequency EM noise is frequently observed on sites in the built environment. For example, a strong 60 kHz signal of unknown origin was regularly monitored during the development and testing of the CRI prototype at the BGS site in Keyworth. The highpass component suppresses the spectral energy of the mains frequency (50 Hz in the UK) as well as low-frequency motion-induced noise. Experiments have shown that motion-induced noise has a dominant low-frequency component of the order of 20 Hz.

Data acquisition and positioning. 16-bit A/D conversion and data logging is performed by an industry-standard data acquisition module controlled by a laptop PC. For static measurements, data acquisition is initiated manually by the operator. For towed-array applications, data acquisition is triggered by an odometer which is mounted behind the towing vehicle to provide distance information along a survey line. Data acquisition is then carried out at predefined sampling intervals, typically of the order of a few centimetres. Alternatively, Real-Time Kinematic Differential GPS has been used to trigger data acquisition at regular intervals and for navigation of the towing vehicle.

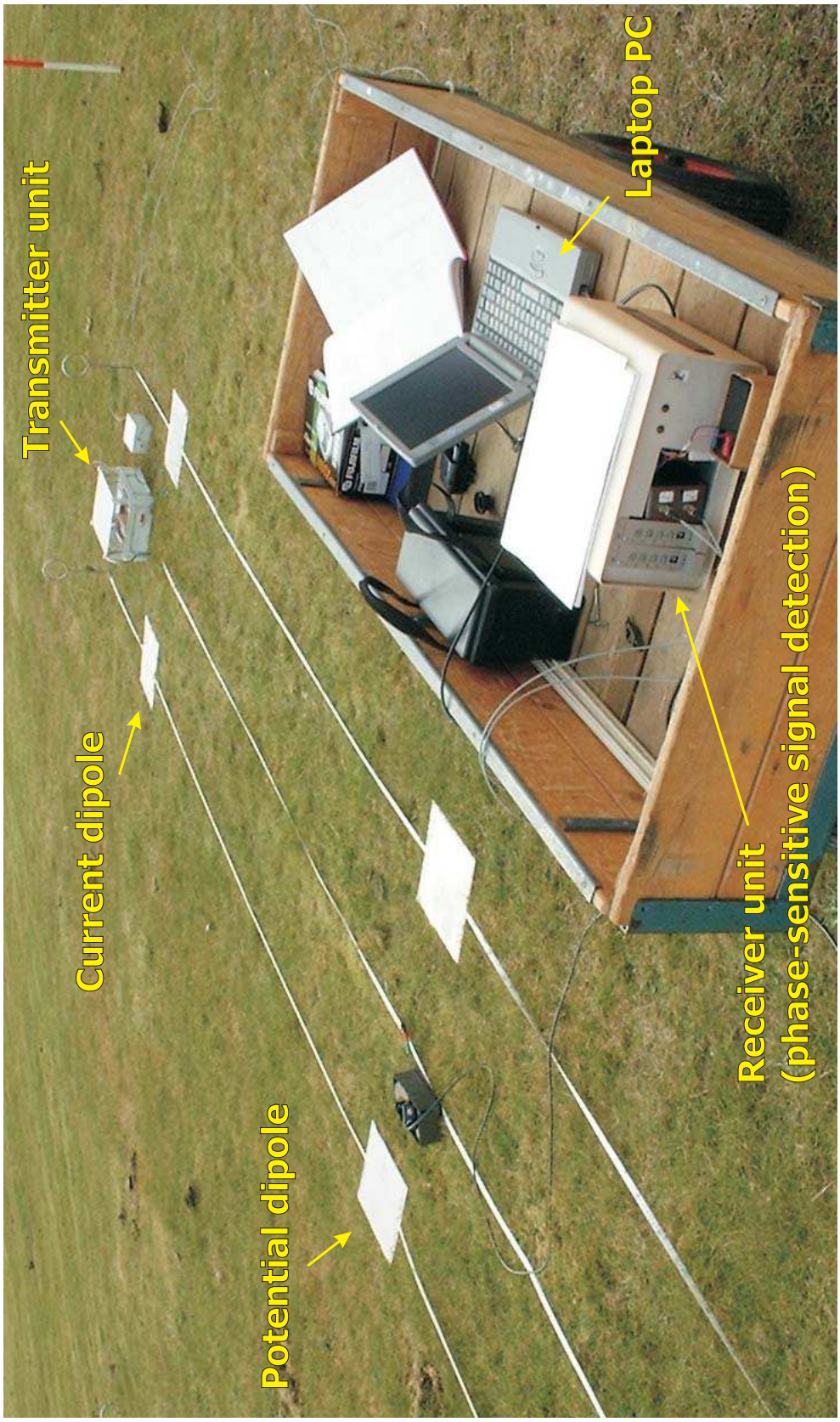

Figure 6.2: Static measurements with the BGS prototype CRI system in the field. ©NERC copyright.

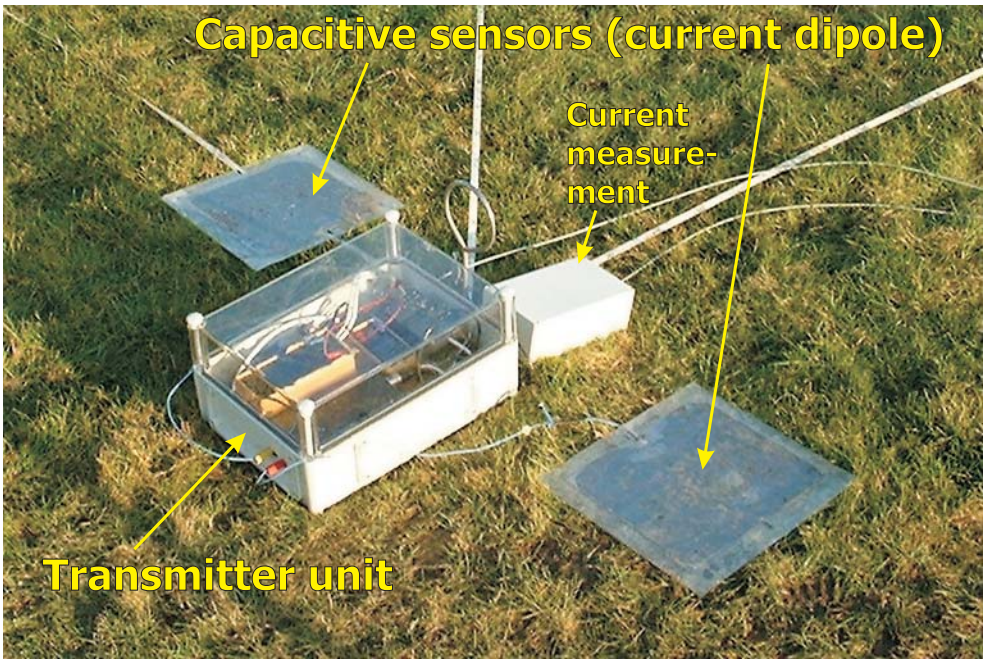

Figure 6.3: Transmitter unit and current dipole of the BGS prototype CRI system. ©NERC copyright.

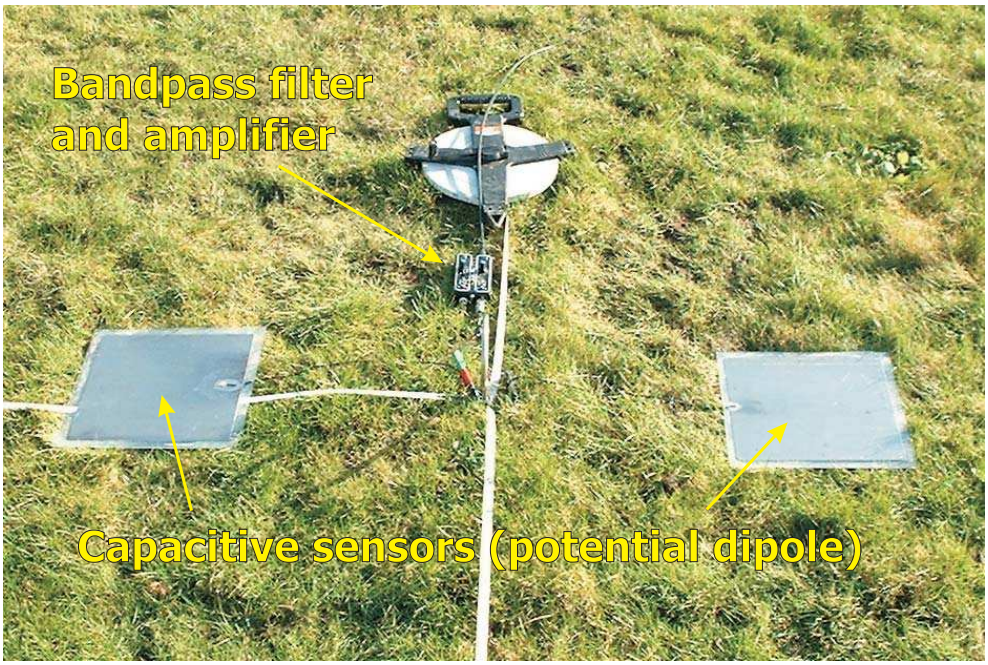

Figure 6.4: Potential dipole of the BGS prototype CRI system. ©NERC copyright.

6.2 Properties of real capacitive sensors

As part of the research for this thesis, the properties of plate-wire combinations as real capacitive sensors were examined more closely for the first time. This section describes the experiments that were undertaken for this purpose. The plate-wire combination was chosen because it was thought to reflect the concept of point poles as postulated by the electrostatic formalism. Firstly, the sensor capacitance was measured and compared to values inferred from the theoretical model in Chapter 5. Secondly, a comparative study between capacitive and galvanic electrodes was undertaken, which comprised the passive wideband monitoring of electric fields with a conventional grounded dipole and a nongrounded capacitive dipole.

6.2.1 Effective sensor capacitance and elevation

The effective capacitance of a plate-wire combination was determined in order to evaluate the applicability of the theoretical model described in Section 5.1.2. For this purpose, the reactive load at the transmitter output was measured directly. Besides the true (physical) elevation of the sensor above the surface, one of the uncertainties in capacitive resistivity measurements is the effective elevation relevant to the electrostatic calculation. From the measured sensor capacitance, an effective sensor elevation can be determined based upon the theoretical model. The following procedure was adopted for this purpose:

6.2.1.1 A practical measurement of capacitance

Plate-wire sensors were connected to the transmitter unit of the CRI system to form a current dipole of 1.5 m length. Thin metal plates (25 cm × 25 cm, 2 mm thickness) were used as capacitive electrodes and connection to the transmitter output was made by wires soldered to the nearest edge of the plate. The plates were laminated in plastic sheets to provide electrical insulation. The connecting wires were slightly raised above ground and kept as short as possible in order to keep their influence on the measurement to a minimum. The experimental setup is shown in Figure 6.5 a. All measurements were carried out on trimmed grass in a relatively homogeneous and conductive environment with an average

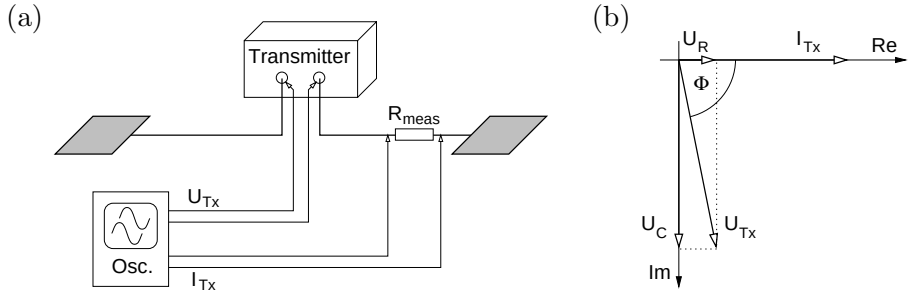

Figure 6.5: Experimental setup for the measurement of effective sensor capacitance (a) and representation of current and voltages in the complex plane (b).

near-surface resistivity of 25 Ωm. The test site and local geology is described in more detail in the following section. With the transmitter activated, the voltage at the terminals was measured by means of a high-voltage differential probe. The transmitter current was measured by means of the voltage drop across a resistor in the current path. Both signals were fed into a battery-powered hand-held oscilloscope in order to avoid interference by grounding the system to mains earth potential. The amplitudes of transmitter output voltage and current at the sensor and their phase relation were then measured on the oscilloscope. (Figure 6.5b).
Assuming that the complex impedance Z of the injection circuit can be split up into a reactive and a resistive part and the reactive part is purely due to capacitance (cf. Equation 5.4), the corresponding sensor capacitance C and resistance R can be estimated. The relevant equations are (cf. Figure 6.5b)

$$Z = X_C + R = \frac{U_{\mathrm{Tx}}}{I_{\mathrm{Tx}}} \qquad X_C = \frac{1}{i\omega C} = \frac{U_C}{I_{\mathrm{Tx}}} \qquad R = \frac{U_R}{I_{\mathrm{Tx}}} \tag{6.1}$$

The measurands are the total transmitter output voltage U_{Tx}, the total transmitter output current I_{Tx} and the phase angle Φ. Total sensor capacitance and ground resistance are calculated according to

$$C = \frac{I_{\mathrm{Tx}}}{\omega U_{\mathrm{Tx}} \sin \Phi} \qquad R = \frac{U_{\mathrm{Tx}} \cos \Phi}{I_{\mathrm{Tx}}} \tag{6.2}$$

Under the conditions described, the following results were obtained:

$$U_{\mathrm{Tx}} = 896\ \mathrm{V^{pp}} \qquad I_{\mathrm{Tx}} = 10.4\ \mathrm{mA^{pp}} \qquad \Phi = 81.8^\circ$$

Hence the total sensor capacitance, reactive impedance component and ground resistance are

$$C = 131.6\ \mathrm{pF} \qquad |X_C| = 85.2\ \mathrm{k\Omega} \qquad R = 12.3\ \mathrm{k\Omega}$$

The total sensor capacitance applies to the plate-wire dipole. A single pole has twice the capacitance of the combined arrangement since the two poles are connected in series. The single-pole capacitance of $C = 263.2$ pF is of the expected order of magnitude for a finite-size plate (cf. Section 5.4.2.2). In a controlled setup with raised wire segments, it is safe to assume that the contribution of the wire segment to the total sensor capacitance is negligible, i.e. the entire capacitance is provided by the plate. This assumption is necessary because the individual contributions of the two components (plate/wire) cannot be distinguished with this measurement technique. The experiment has also shown that the reactive impedance component associated with the capacitance of the sensor arrangement dominates ground resistance by a factor of 7. This result confirms the previous assumption of Section 5.1.2.2.

6.2.1.2 Determining effective elevation

The true (physical) elevation of the sensor above the ground surface is a theoretical parameter in the electrostatic model. Specifying a precise distance between

sensor and ground is unrealistic because imperfections of the real ground surface or small obstacles or surface vegetation will normally create an irregular elevation profile at microscopic level for each sensor. However, the measured sensor capacitance can be used to determine an effective elevation of the sensor. Although this value may not correspond to a true measurable elevation, it is the relevant value in electrical terms, which propagates into the effective geometric factor for the electrostatic quadrupole (cf. Section 4.6.3).
In the capacitance model for a finite-size plate (Section 5.4.1.3), the sensor capacitance is given by (5.12). This equation is a function of elevation h, however solving analytically for h is non-trivial and a numerical solution must be found. For a plate capacitance of $C = 263.2$ pF one obtains an effective plate elevation of $h = 2.54$ mm for the specific conditions on grass. This appears to be a sensible value which can be used for modelling purposes henceforth. The alternative parallel-plate model (5.6) gives an effective elevation of $h = 2.10$ mm, corresponding to an error of approximately 17%.

6.2.2 Wideband reception properties

When the electric field is measured by means of a horizontal dipole at the ground surface, the well-known continuity of the tangential electric field at the earth-air interface suggests that the result must be independent of whether the measurement is performed in air or in the ground. This conception allows the substitution of galvanically grounded electrodes by capacitive dipoles (Wait, 1995; Sapozhnikov, unpublished). In order to investigate this issue and to compare the performance of capacitive and galvanic dipoles in the relevant frequency range, wideband recordings of the electric field at the ground surface were undertaken. For this purpose, time series of the observed electric potential were recorded using both a grounded and a non-grounded dipole. The non-grounded dipole was represented by plate-wire sensors while conventional steel electrodes were used for the grounded dipole. Two different cases were considered. In the first part of the experiment, the natural background field was monitored. In the second part, the CRI transmitter was activated and its signal was monitored together with the background field.

6.2.2.1 Experimental setup

The experimental setup is shown in Figure 6.6. The dipoles were positioned in the vicinity of the CRI transmitter which acted as an artificial source for a sharp monochromatic VLF signal at 14.2 kHz. The transmitter dipole and the respective potential dipole were arranged in inline geometry. The length of the transmitter dipole was 1.5 m throughout the experiment and a plate-wire combination was used for current injection. The receiver dipoles were 1 m long and located at a distance of $r = 3$ m from the transmitter dipole. The grounded and non-grounded versions were deployed consecutively and observations were made with the transmitter switched on or off.
The observed potentials were passed through an analogue bandpass filter with a bandwidth of 1–20 kHz, amplified and recorded as time series using a sampling

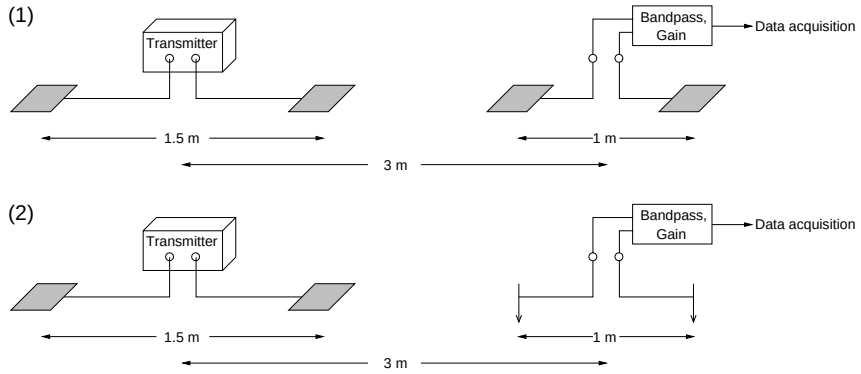

Figure 6.6: Experimental setup for wideband recordings of the electric field using grounded and non-grounded dipoles. (1) Non-grounded dipole (capacitive plate-wire sensor). (2) Grounded dipole (conventional steel electrodes).

rate of 100 kHz. Their individual length was chosen to be 4096 samples, corresponding to a registration time of 40.96 ms. Raw power spectra were calculated from these time series by a discrete Fast Fourier Transformation (FFT), using a Hamming window function (Oppenheim and Schafer, 1999).

6.2.2.2 Results and interpretation

Figures 6.7 and 6.8 show typical raw power spectra from individual time series registered during this experiment. The power spectral density has been plotted as a function of frequency in a range between 0 Hz (DC) and the Nyquist frequency of 50 kHz, which covers the relevant part of the VLF band.
Figure 6.7 represents the situation where the transmitter was switched off and the background field was recorded. The top panel shows a spectrum recorded with the non-grounded dipole, while the one at the bottom was recorded with the grounded dipole. Despite the different sensors employed, the two spectra have obvious similarities. Above the background noise, sharp spectral lines at identical frequencies between 15 and 30 kHz are clearly visible in both spectra. The spectral power of these signals is two to three orders of magnitude higher than that of the background noise. These spectral lines correspond to known VLF transmitters described in Section 5.1.3 (16.0 kHz = GBR, Rugby; 20.2 kHz = ICV, Italy; 24.0 kHz = NSS, USA?). A number of weaker spectral lines can also be identified on both diagrams, possibly due to local noise sources. The spectra have not been corrected for the filter response. The lowpass component of the bandpass filter appears to have the same effect on both sensor types. Between the 3 dB point at 20 kHz and the Nyquist frequency, a drop in the power spectral density by almost three orders of magnitude is observed for both dipoles.
Figure 6.8 shows corresponding spectra for the situation where the transmitter is active. Again, the two spectra are clearly similar. Due to its vicinity to the receivers, the strong CRI transmitter signal at 14.2 kHz is the prominent feature in the power spectra for both dipole types (approximately seven orders of

(a)

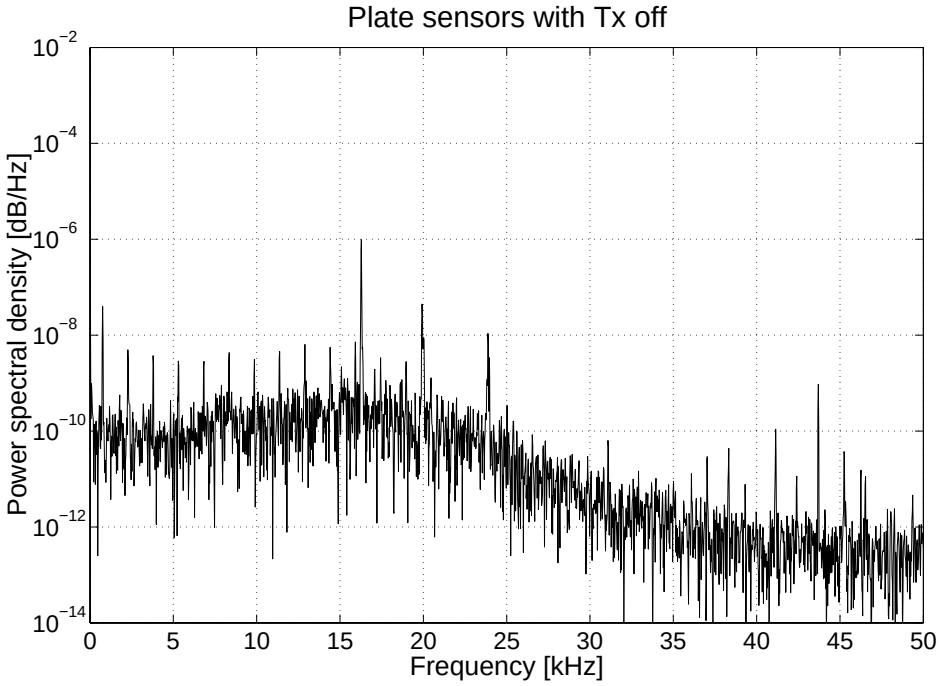

(b)

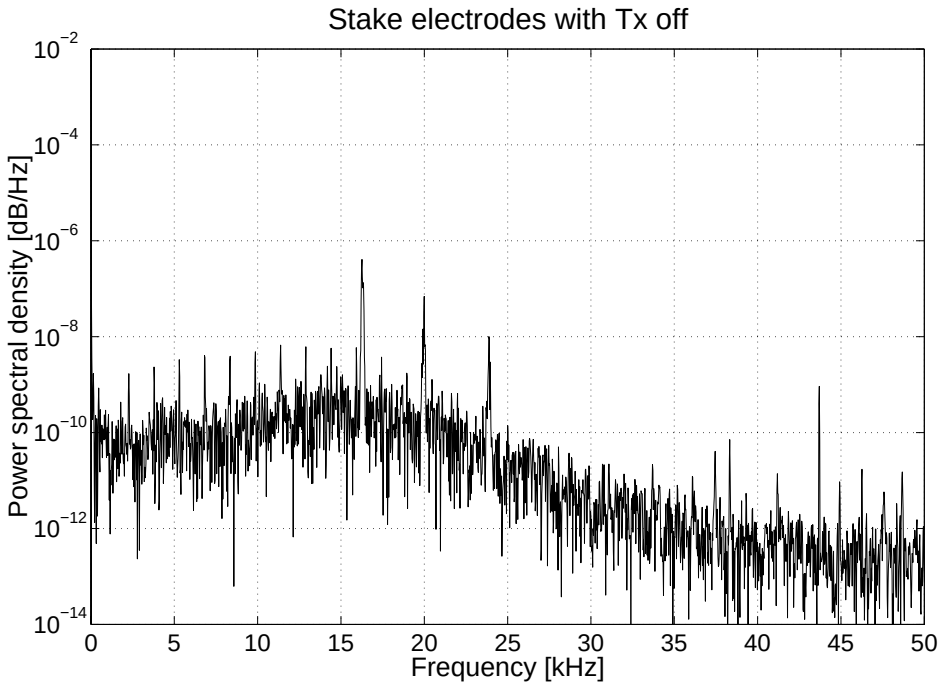

Figure 6.7: Raw power spectra of the observed potential from (a) plate sensors and (b) stake electrodes with the CRI transmitter switched off. Sampling frequency 100 kHz. Length of time series 4096 samples.

(a)

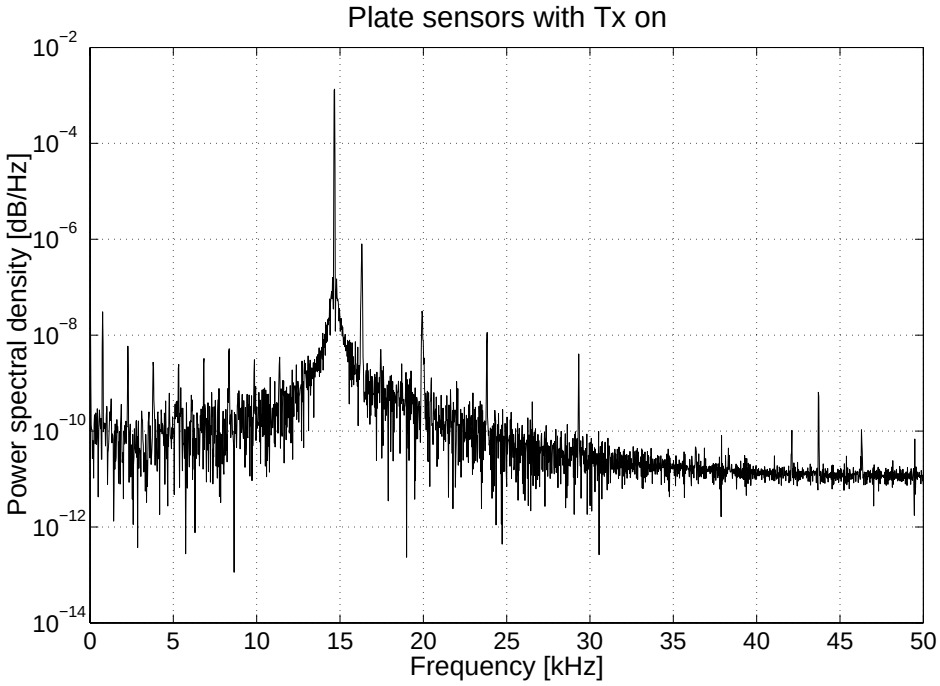

(b)

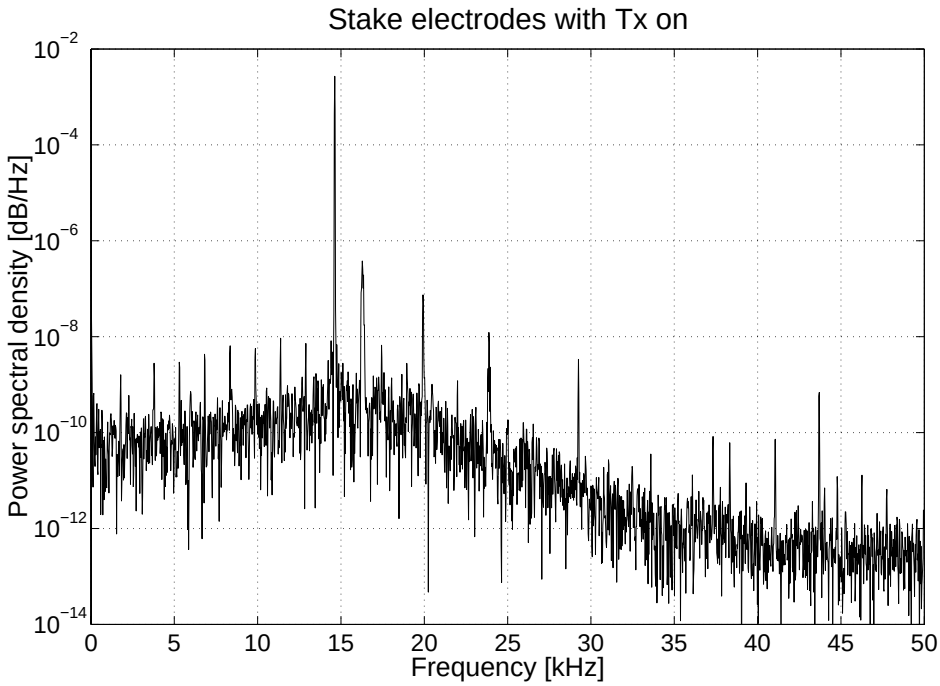

Figure 6.8: Raw power spectra of the observed potential from (a) plate sensors and (b) stake electrodes with the CRI transmitter switched on. Sampling frequency 100 kHz. Length of time series 4096 samples. Transmitter frequency 14.2 kHz.

magnitude above background noise). For the non-grounded dipole, the 14.2 kHz spectral line is not quite as sharp as for the grounded dipole. The broadening of the peak is due to leakage of spectral energy towards adjacent frequencies. It is unclear whether this is an effect of the sensor type or due to a temporary phenomenon during acquisition. The same spectral lines as observed without the transmitter are seen in the spectra again (16.0 kHz, 20.2 kHz, 24.0 kHz), while a new spectral line has appeared at approximately 29 kHz. This is likely to be the first harmonic of the CRI transmitter frequency. Virtually all minor line spectra observed before are still noticeable while the transmitter is active. In summary, the results of this simple semi-quantitative experiment suggest that the electric field observed with either non-grounded or grounded dipoles is very similar, hence non-grounded dipoles are suitable electric field sensors in the VLF range. Distinct monochromatic signals from VLF transmitters are observed in the same way by both a grounded and a non-grounded dipole, confirming the continuity of the electric field on either side of the ground-air interface.

6.3 Spatial analysis of the complex transfer impedance

A practical realisation of an electrostatic quadrupole is only conceivable if the concept of point poles can be simulated by realistic capacitive sensors. There is now sufficient evidence to suggest that plate-wire sensors can be a practical solution to this problem, provided that the plate capacitance dominates over that of the wire segment. Consequently, a capacitive resistivity measurement based on plate-wire sensors should be accurately described by the electrostatic formalism. The experimental validation of this fundamental concept with a practical CR instrument has been a substantial part of the research presented in this thesis. The following experimental approach was pursued: in a homogeneous environment with known electrical properties, the fully complex transfer impedance (Equation 4.35) was measured in a series of elementary surveys with basic array geometries and compared to theoretical values calculated with the electrostatic formalism (Equation 4.21). Two classes of experiments were carried out:

1. Moveout surveys were conducted to analyse the variation of the transfer impedance with distance and to assess the practicality of CR measurements across a range of separations with varying signal-to-noise conditions.

2. Directional surveys were conducted to analyse the variation of the transfer impedance with azimuth between transmitter and receiver to verify the dipolar character.

All measurements were performed with the BGS prototype CRI system using plate-wire sensors. The surveys were conducted in static mode, i.e. sensors were placed on the ground surface and current and potential readings taken at fixed positions. The results were then used to calculate $|Z|$ and $\mathrm{Arg}(Z)$.

6.3.1 Description of the test site

The study described in this section was carried out on soft ground (grassland) in order to facilitate comparison with results from conventional DC resistivity surveys. A test area on the site of BGS headquarters in Keyworth (Nottinghamshire, UK) was selected for this purpose.

6.3.1.1 Site geology

The surface geology of the Keyworth area is characterised by the presence of clay-rich sedimentary rocks, deposited in arid continental and transitional marine conditions during the late Triassic and early Jurassic periods (Charsley et al., 1990). The BGS headquarters is situated at the base of the "Rhaetic escarpment" and is underlain at shallow depths by gypsiferous mudstones of the Mercia Mudstone Group. The site is founded directly on the so-called Cropwell Bishop Formation (CBp), which is part of the top end of the Mercia Mudstone Group (Wealthall, 1999). The CBp comprises red-brown and sometimes grey-green mudstones and siltstones and commonly contains evaporates such as gypsum. On the BGS site these mudstones are found in thick deposits (10s of metres) overlain only by a thin soil cover (0.3–1 m). Parts of the site have been landscaped using surplus material excavated during construction.

6.3.1.2 Electrical properties

The geological setting of the Keyworth site creates favourable conditions for the testing of electrical techniques. Even though some areas contain reworked material, the near-surface mudstone deposits represent a uniform and isotropic background with average resistivities of approximately 20 Ωm within the top few metres of ground. Previous coverage of the actual test area by conventional resistivity surveys had shown that the ground is reasonably homogeneous. The area is also known not to contain any artificial anomalies (foundations, services, or similar).

6.3.2 Variation with distance: moveout surveys

Based on the reasoning set out in Section 5.2, the equatorial and inline configurations of the dipole-dipole array were employed for the experiments as two complementary geometries. In the first set of experiments, the variation of the complex transfer impedance with distance was examined. For this purpose, moveout surveys were conducted during which the transmitter dipole remained at a fixed position while the receiver dipole was moved away progressively. In a laterally homogeneous environment, this procedure is equivalent to a centred resistivity sounding (cf. Section 3.1), but helps economise on the necessary array movements. Unit dipoles (1 m length) were employed throughout. Static measurements of the injected current and the in-phase and quadrature components of the observed potential were made at increasing dipole separations, ranging from the smallest separation possible up to separations of 10 m and greater. The transfer impedance was calculated for each separation, making

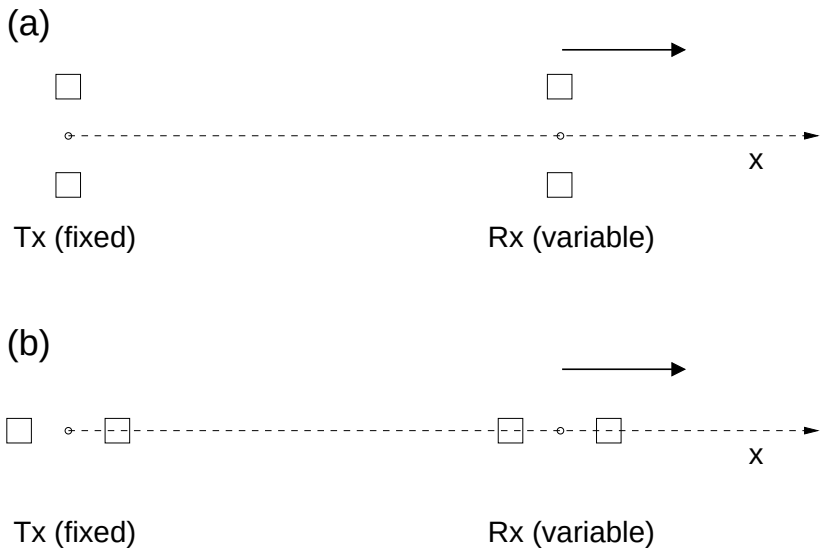

Figure 6.9: Moveout survey to determine the variation of the transfer impedance with distance. (a) equatorial configuration, (b) inline configuration.

the results independent of possible current fluctuations during the experiment. For a statistical assessment of the stability of the measurement over time, automated readings were taken at each location at a rate of 10 Hz. Those values were then stacked to obtain a mean and standard deviation. Injection currents of approximately 9 mA were used throughout the experiment.
The measured data were then compared with the response predicted by the electrostatic formalism. The two remaining variables in the experiments are resistivity and array elevation, for which only expected values are known. For the purpose of this study, it was anticipated that average resistivities of $\rho \approx 20\,\Omega$m would be observed, and that the effective array elevation h would be of the order of millimetres, following the findings of Section 6.2.1. Model curves for the complex transfer impedance (Equation 4.21) were calculated for each array geometry. In order to assess the sensitivity of the results towards either of the two parameters, the variation of the halfspace model with both was considered in order to obtain an optimal fit. Initially, elevation was kept constant while resistivity was varied within a range of values, and vice versa.

6.3.2.1 Equatorial configuration

The first survey was carried out with current and potential dipoles in equatorial configuration (Figure 6.9a). In this geometry, the minimum dipole separation is only limited by the physical dimensions of the plates, hence a minimum separation of 0.3 m between the dipole axes could be employed. Separations were increased stepwise so that distances were approximately evenly spread on a logarithmic scale. A maximum dipole separation of 12 m was found to be practical under the given circumstances, although it is likely that larger separations could be achieved with a greater transmitter dipole moment, i.e. the use

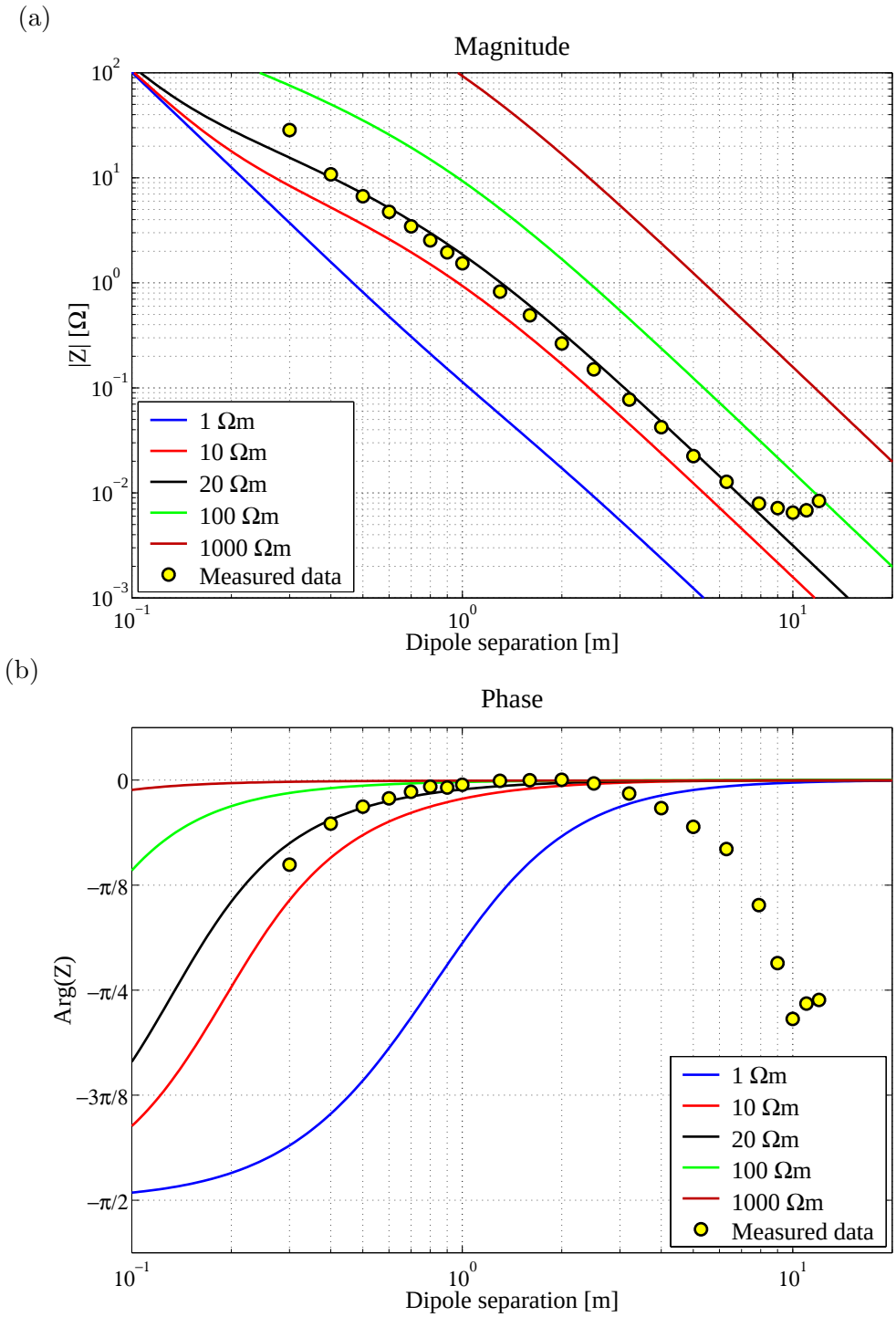

Figure 6.10: Complex transfer impedances for the moveout survey in equatorial configuration: comparison of measured data with quasi-static model (model parameter: resistivity; array elevation fixed at $h = 0.5\,\mathrm{mm}$). (a) magnitude, (b) phase.

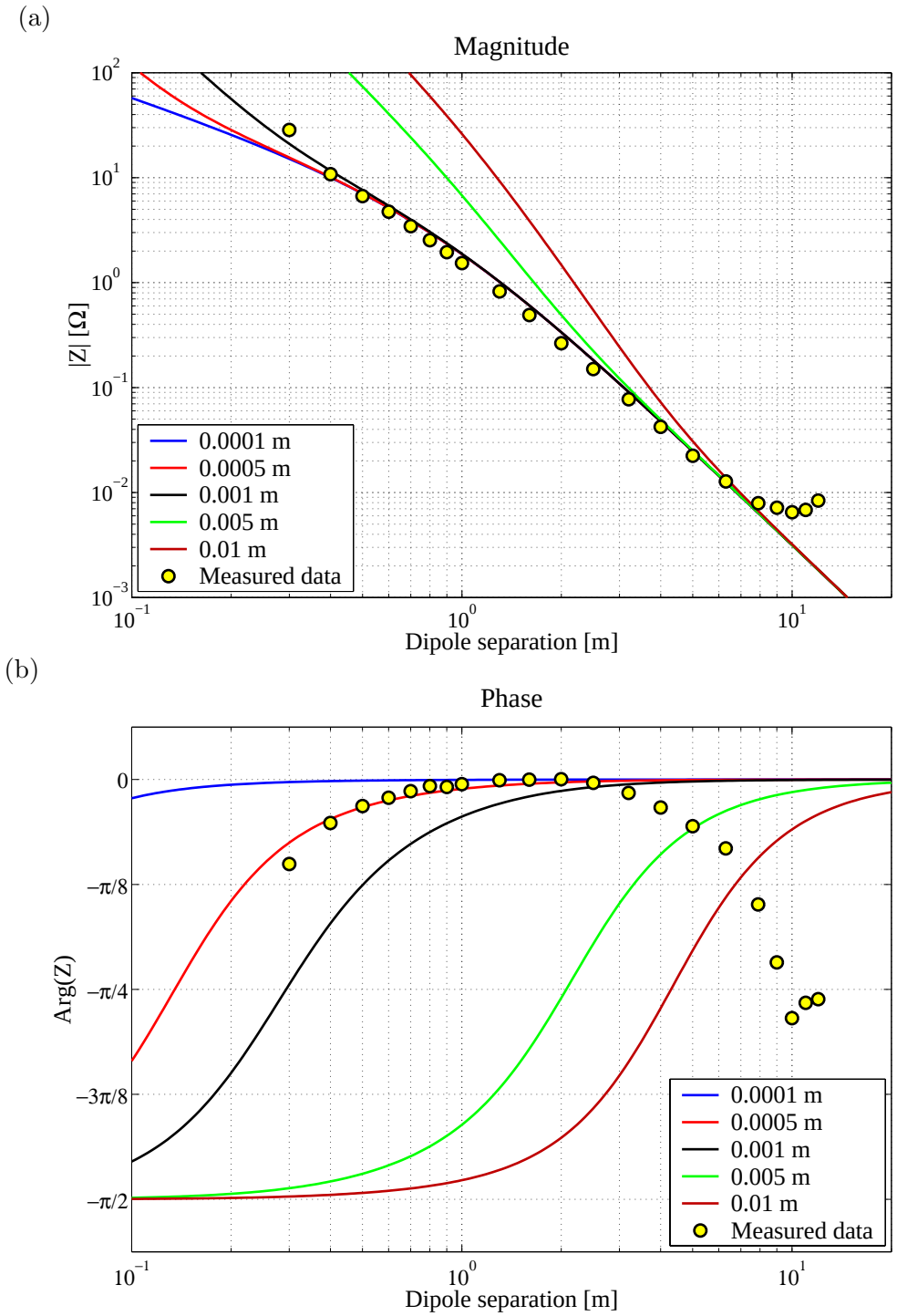

Figure 6.11: Complex transfer impedances for the moveout survey in equatorial configuration: comparison of measured data with quasi-static model (model parameter: elevation; resistivity fixed at $\rho = 20\,\Omega\mathrm{m}$). (a) magnitude, (b) phase.

of stronger injection currents or longer dipoles. A more resistive environment than $\rho = 20\,\Omega$m would also facilitate the use of larger separations.

The results of the equatorial survey are summarised in Figures 6.10 and 6.11. Magnitude and phase of the measured transfer impedance were superimposed on the calculated curves for the homogeneous halfspace. All graphs have been plotted using a log-log (or semi-log) scale. The measured data (coloured circles) represent the mean value of 100 stacked readings at each location. In all cases the standard deviation was found to be within the radius of the circle. In Figure 6.10, resistivity is the free model parameter while the array elevation h is kept constant at 0.5 mm. The model resistivities cover a range of values from a conductive regime ($1\,\Omega$m) to a resistive regime ($1000\,\Omega$m), including the expected value of $20\,\Omega$m. Dipole separations range between 0.3 m and 12 m. Figure 6.11 shows the same measured data, but the free model parameter is now elevation, while resistivity is assumed constant at $20\,\Omega$m. Model elevations range from 0.1 mm to a maximum of 10 mm, including the expected value of 0.5 mm. Greater elevations are not realistic because high impedances in the transmitter output circuit would cause a decrease in current.
The distinct separation of the model curves in Figure 6.10a reflects the sensitivity of the magnitudes towards resistivity. For the variation with elevation (Figure 6.11a), the effect on the magnitude is less pronounced and a significant effect can only be observed for $h > 1$ mm. In practice, the magnitude measurement is therefore expected to be less sensitive towards array elevation than towards resistivity. Instead, the phase is highly sensitive towards elevation (Figure 6.11b), but to a lesser extent towards resistivity (Figure 6.10b), at least for separations greater than dipole length ($r > l$). The sensitivity of the phase towards elevation is due to the sensitivity of the quadrature component towards the geometric factor (cf. Figure 4.14b).

The optimal fit between the measured datapoints and the theoretical curves is observed for a resistivity of $\rho = 20\,\Omega$m (black solid curve in Figures 6.10) and an elevation of $h = 0.5$ mm (red solid curve in Figure 6.11). For the magnitudes, the fit with respect to both resistivity (Figure 6.10) and elevation (Figure 6.11) is best for separations between 0.4 m and 8 m. In that interval measured magnitudes follow the optimal curve very closely, considering the variation over three orders of magnitude. At $r = 0.3$ m, the measured magnitude exceeds the theoretical value by a significant amount. This effect is most likely due to the breakdown of the point-pole concept for finite-size plates at these extremely small separations. For a plate width of 0.25 m and a separation of the plate midpoints of 0.3 m, the actual separation between the edges of the transmitter and receiver plates is only 5 cm. This discrepancy leads to an overestimation of the measured magnitude compared to the theoretical value. At separations above 8 m, the measured magnitude deviates from the optimum model curve towards significantly higher values. The effect is thought to be real because the deviation is smooth and unlikely to be related to the measurement process. Its onset can also be observed in the phases. There, the measured data fit the model curves best between 0.4 m and 3 m. Large phase angles are ob-

served at the smallest separations. This effect is predicted by quasi-static theory (cf. Section 5.2.1), but has never been confirmed experimentally in the literature. Phase recedes with increasing separations until a minimum is reached at 2 m. However, instead of maintaining in-phase behaviour as predicted by the quasi-static model, phase angles begin to increase again, suggesting a sudden increase in the quadrature component. Phase grows smoothly and reach values of $|\varphi| > \pi/4$ beyond 10 m. The growth of the quadrature component is also observed in the magnitudes. The effect on the magnitudes is only noticeable at larger separations. The phenomenon is attributed to inductive effects starting to become relevant in the relatively conductive environment (Benderitter et al., 1994; Tabbagh and Panissod, 2000). The induction number (3.30) is approximately 0.105 at $r = 2\,\mathrm{m}$ and 0.529 at $r = 10\,\mathrm{m}$ ($f = 14.2\,\mathrm{kHz}$, $\sigma = 0.05\,\mathrm{Sm}^{-1}$). Benderitter's criterion is still just about fulfilled (cf. Section 4.6.2), but the quasi-static approximation has reached its limits and the response of the CR array is more adequately described by electromagnetic theory (cf. Section 4.7).

6.3.2.2 Inline configuration

The second experiment was carried out with current and potential dipoles in the inline configuration (Figure 6.9b). In this geometry the dipole separation is limited by the actual dipole lengths, hence a minimum separation of 1.3 m was employed. Due to the stronger coupling in inline configuration, slightly larger separations are possible than those achieved with the equatorial array. A maximum dipole separation of 15 m was found to be practical with the inline array.

The results of the moveout survey in inline configuration are summarised in Figures 6.12 and 6.13. The graphs are presented in analogous fashion to those for the equatorial data. In Figure 6.12 resistivity is a free model parameter while elevation is again kept constant at 0.5 mm. The range of model resistivities considered has been the same as before. Dipole separations range between 1.3 m and 15 m. Figure 6.11 shows the same data, but elevation is now the free model parameter while resistivity is kept constant. The range of elevations considered was the same as in the equatorial case.
The optimal fit is again observed for a resistivity of $\rho = 20\,\Omega\mathrm{m}$ and an elevation of $h = 0.5\,\mathrm{mm}$). For the magnitudes, the fit with respect to both parameters is best for separations between 1.4 m and 9 m. Similar to the equatorial case, the measured magnitude exceeds the theoretical value significantly at the shortest separation ($r = 1.3\mathrm{m}$). The reason for the overestimation is likely to be the same as before. At $r = 1.3\,\mathrm{m}$ the plate edges of the current and potential dipoles are only separated by 5 cm, thus introducing a geometric distortion. At separations greater than 9 m, magnitudes are again observed to deviate smoothly from the optimum model curve towards higher values. The phases reflect this deviation, with measured data matching the optimum model curve best between 1.4 m and 4 m. Large phases are again observed at small separations, in accordance with expectations. A minimum is reached at 2.5 m, however beyond 4 m the phases start to grow again due to a rise in the quadrature component. Similar to the

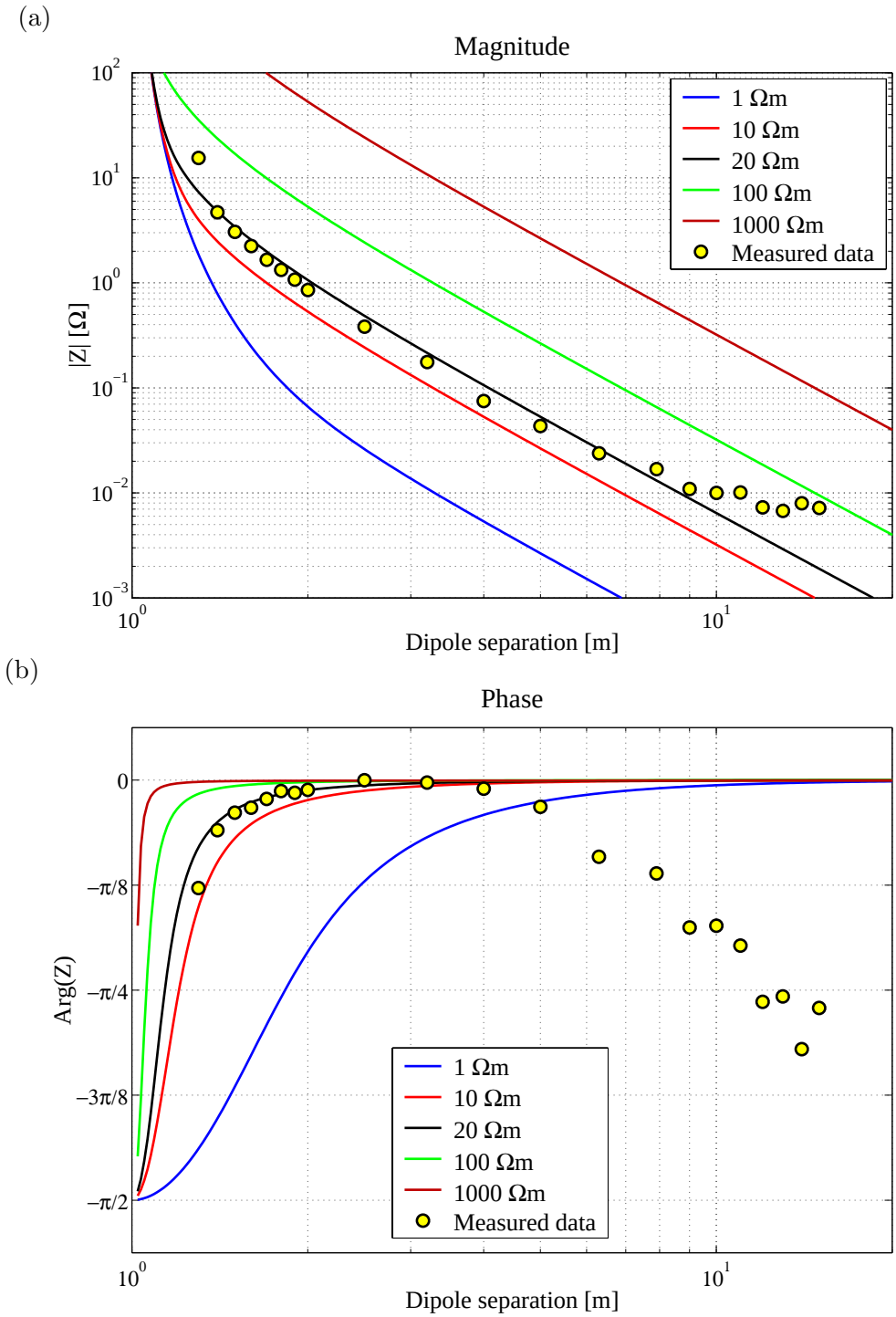

Figure 6.12: Complex transfer impedances for the moveout survey in inline configuration: comparison of measured data with quasi-static model (model parameter: resistivity; model elevation fixed at $h = 0.5\,\mathrm{mm}$). (a) magnitude, (b) phase.

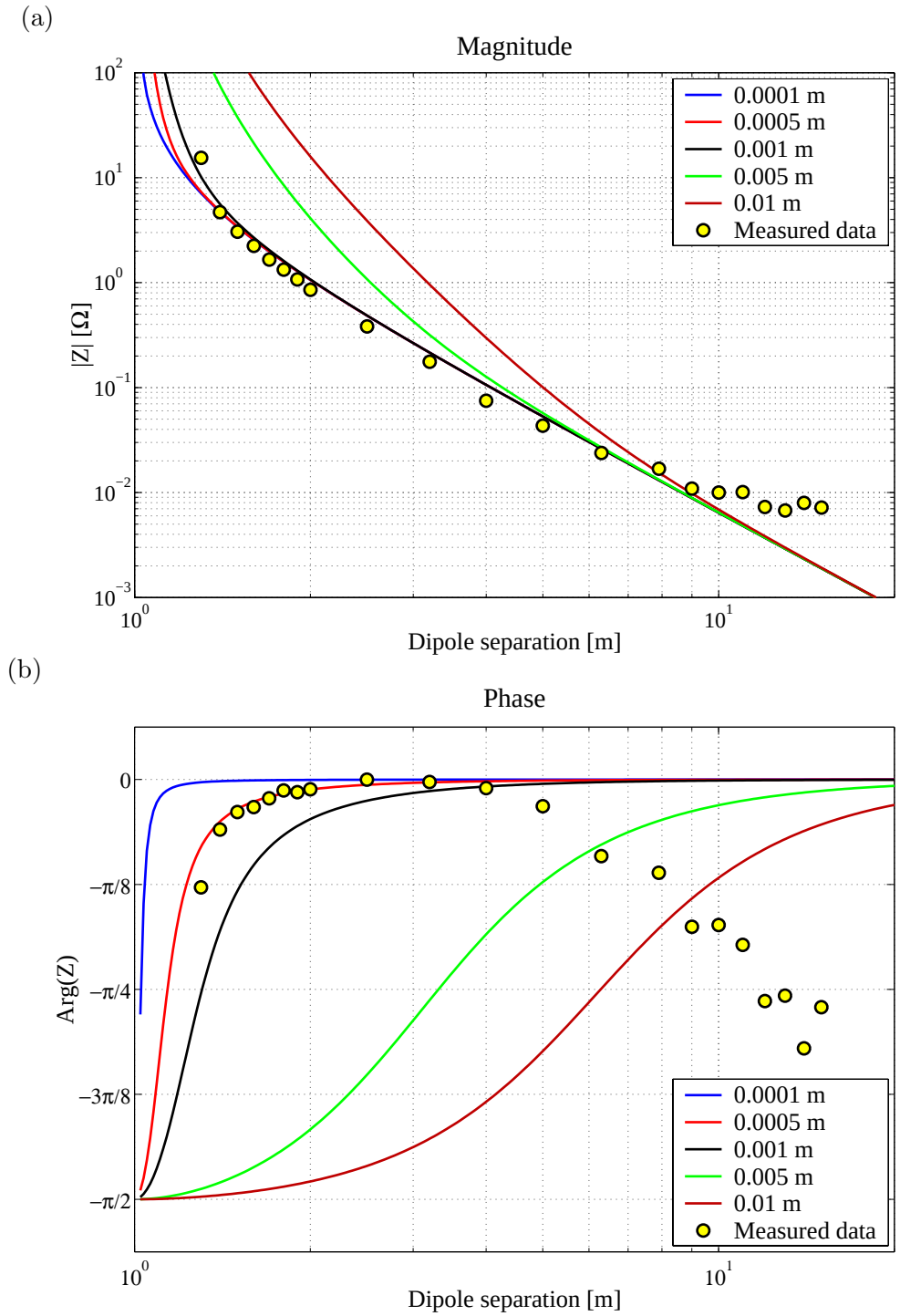

Figure 6.13: Complex transfer impedances for the moveout survey in inline configuration: comparison of measured data with quasi-static model (model parameter: elevation; model resistivity fixed at $\rho = 20\,\Omega\mathrm{m}$). (a) magnitude, (b) phase.

equatorial case, phases of $|\varphi| > \pi/4$ are reached beyond 12 m. Interpretation of this effect by the onset of electromagnetic induction is analogous to the equatorial case.

6.3.3 Comparison with DC resistivity

The acid test for any new technique that measures a well-known parameter is the direct comparison with a traditional measurement. For this purpose, identical moveout surveys were undertaken on the same profile with conventional DC resistivity. CR and DC measurements were performed in immediate succession to ensure identical conditions for both types of surveys. The DC instrument employed was an ABEM Terrameter™ SAS 300 C with standard stainless steel electrodes. This instrument is designed to inject a user-selectable switched DC current. The switching frequency of 0.2 Hz is equivalent to a cycle time of 5 s. An injection current of 10 mA was used for smaller separations before upgrading to 20 mA for larger separations. The manually operated Terrameter can stack successive measurements and displays the (real) transfer impedance ($Z = U/I$) for each individual repetition.

6.3.3.1 Equatorial configuration

The DC resistivity moveout surveys were performed in exactly the same way as their CR counterparts. The stake electrodes were inserted at positions corresponding to the plate centres of the plate-wire sensors used in the CR survey. Figure 6.14 shows the direct comparison between capacitive and DC resistivity data for the equatorial surveys. Initially, the transfer impedances are examined for both techniques. In the case of DC resistivity, the transfer impedance is a real number which must be compared to the in-phase component (Re Z) in the case of CR (cf. Section 4.6.5.3). This comparison is shown in Figure 6.14a. More subtle differences become apparent if geometry is brought in and the impedances are transformed into apparent resistivities. Figure 6.14b shows the comparison between CR and DC apparent resistivities calculated from the above impedances. Both CR and DC apparent resistivities were calculated according to Equation 3.14, using Re Z and the DC geometric factor (3.23).
The impedance curves overlay well on the log-log scale, however in an interval between 0.6 m and 3 m the DC readings are found to exceed the CR values slightly. In contrast, the CR datum point with the shortest separation has a significantly higher value than the corresponding DC reading. This is due to the overestimation of Z at short separations as discussed in the previous section. At longer separations (4–6 m), both curves overlay well. The maximum dipole separation for the CR measurements at which a stable reading was obtained (10 m) is significantly greater than the separation achieved with DC resistivity (6.3 m). This result is despite the higher dipole moment of the DC current dipole, demonstrating the superior signal detection capabilities of the CRI system at low signal-to-noise ratios.
In the apparent resistivity curves the above effects are amplified. Both datasets show a relatively constant level between 0.5 m and 3 m, corresponding to ex-

(a)

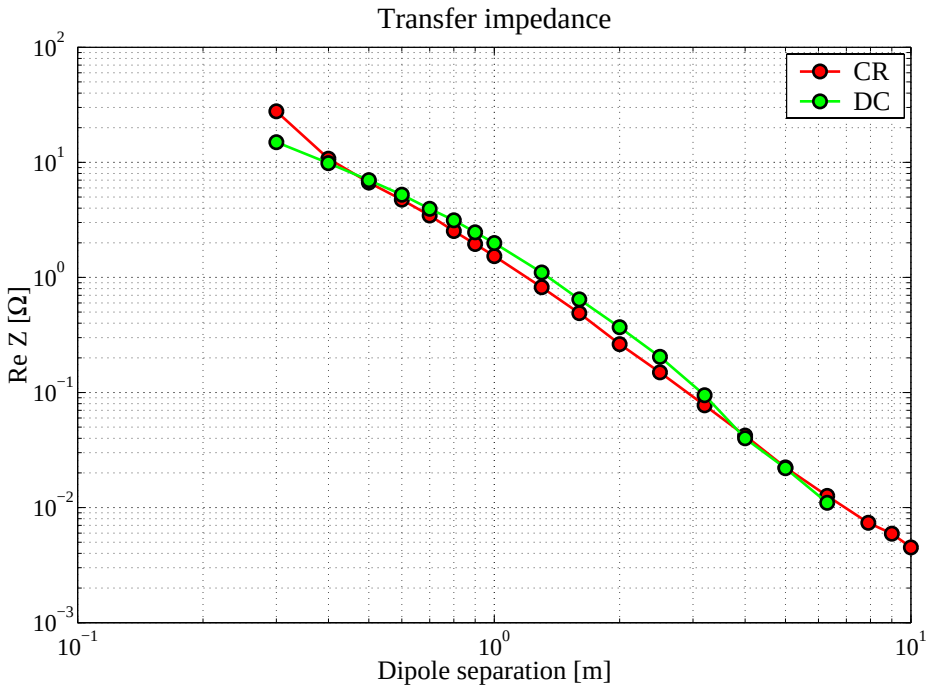

(b)

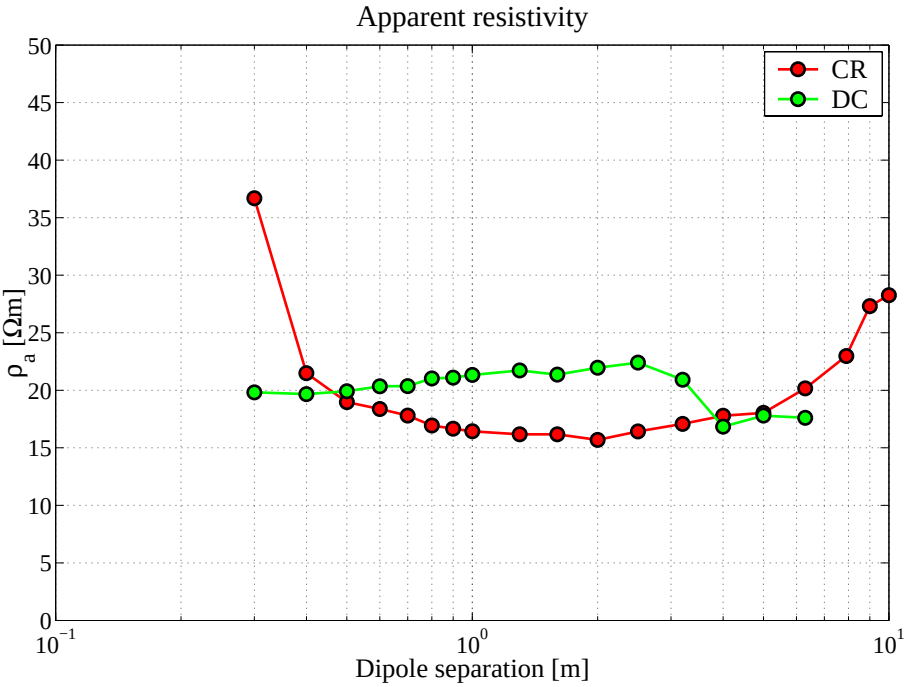

Figure 6.14: Direct comparison between CR and DC resistivity data: moveout survey in equatorial configuration. (a) magnitude of transfer impedance, (b) apparent resistivity.

(a)

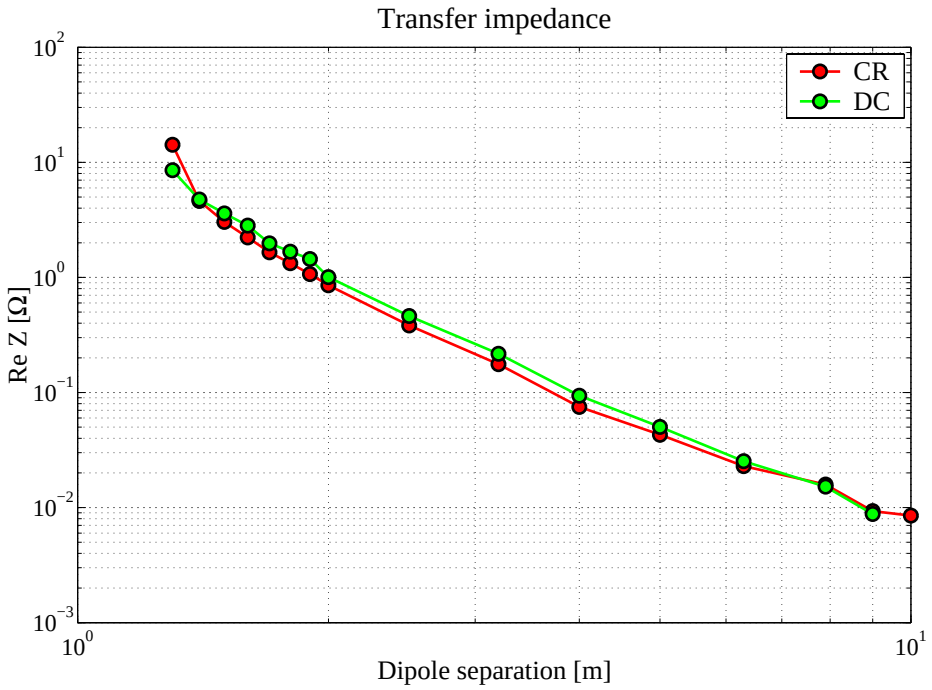

(b)

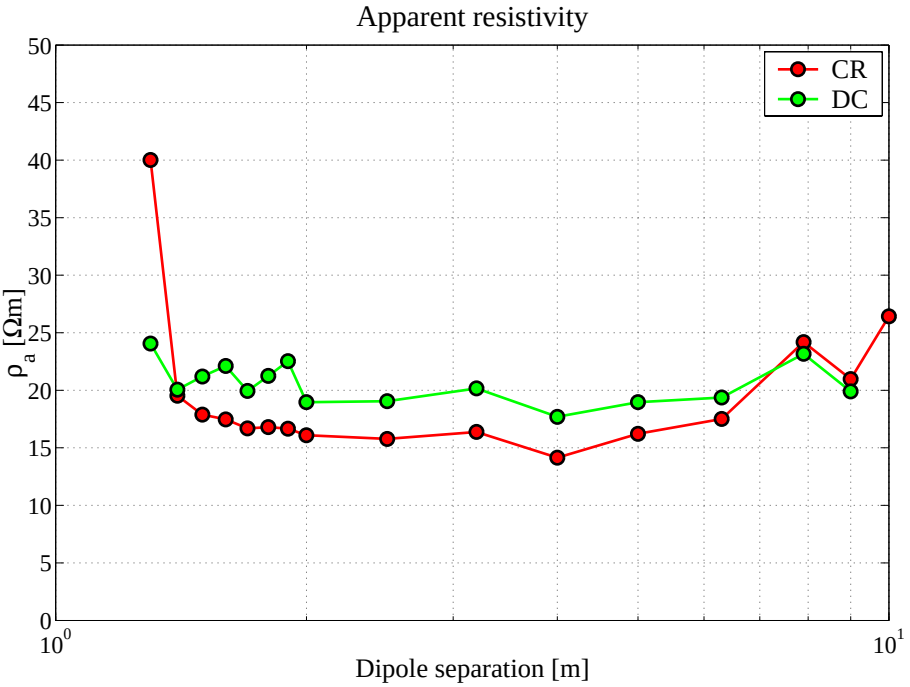

Figure 6.15: Direct comparison between CR and DC resistivity data: moveout survey in inline configuration. (a) magnitude of transfer impedance, (b) apparent resistivity.

pectations about the near-surface uniformity of the test area. In this interval, the DC value is slightly above the anticipated 20 Ωm, while the CR value is below that level. These results indicate that, at these low levels of difference, a more precise calibration may be required for both systems. At 4 m the DC value drops to the CR level. From 6 m onwards, the CR value grows steadily, corresponding to the increase in magnitudes observed earlier. This effect is unlikely to be related to geology, but rather due to the overestimation of apparent resistivity because of inductive effects.

6.3.3.2 Inline configuration

Due to stronger coupling, the inline configuration offers slightly more favourable conditions for both instruments. The comparison betwen capacitive and DC resistivity data for the inline survey is shown in Figure 6.15. Again, the impedance curves overlay well but for DC values being slightly elevated once more. An overestimation of Z at the smallest separations is again observed in the CR data, confirming that the effect can be observed with different array geometries. The apparent resistivity curves show that both datasets are highly correlated between 2 m and 9 m. Both techniques resolve the same fine structure, e.g. a slight depression at $r = 3$ m and a small high at $r = 8$ m. The DC curve matches the anticipated 20 Ωm level, while the level of the CR curve is found to be slightly lower. The upward trend in the CR data at 10 m is again attributed to the onset of inductive effects.

6.3.4 Variation with azimuth: directional survey

In the second set of experiments the directional variation of the CR transfer impedance was examined. For these surveys the location of the current dipole remained fixed at the origin while the potential dipole was rotated around the current dipole on a circular arc, i.e. at a fixed separation, maintaining a constant mutual orientation between the two dipoles. Two complementary configurations are possible, in which current and potential dipoles have either parallel or perpendicular orientation (Figure 6.16). These types of surveys were expected to give additional information about the shape of the source field generated by the current dipole. This field is expected to have dipolar characteristics and its azimuthal variation should therefore produce a characteristic response, which can be predicted for a quasi-static quadrupole using the electrostatic formalism. Experimental confirmation of this prediction by a practical CR measurement would further strengthen the confidence in the technique and demonstrate the universal applicability of the electrostatic formalism under the conditions discussed in Chapter 5.

In analogy with the moveout surveys, a series of static measurements were carried out at a range of azimuth angles. Unit dipoles were employed and a separation of 5 m between the midpoints was used. Theoretical responses were calculated in the same manner as before. In the context of the directional surveys, the complex transfer impedance can be regarded as a periodic function

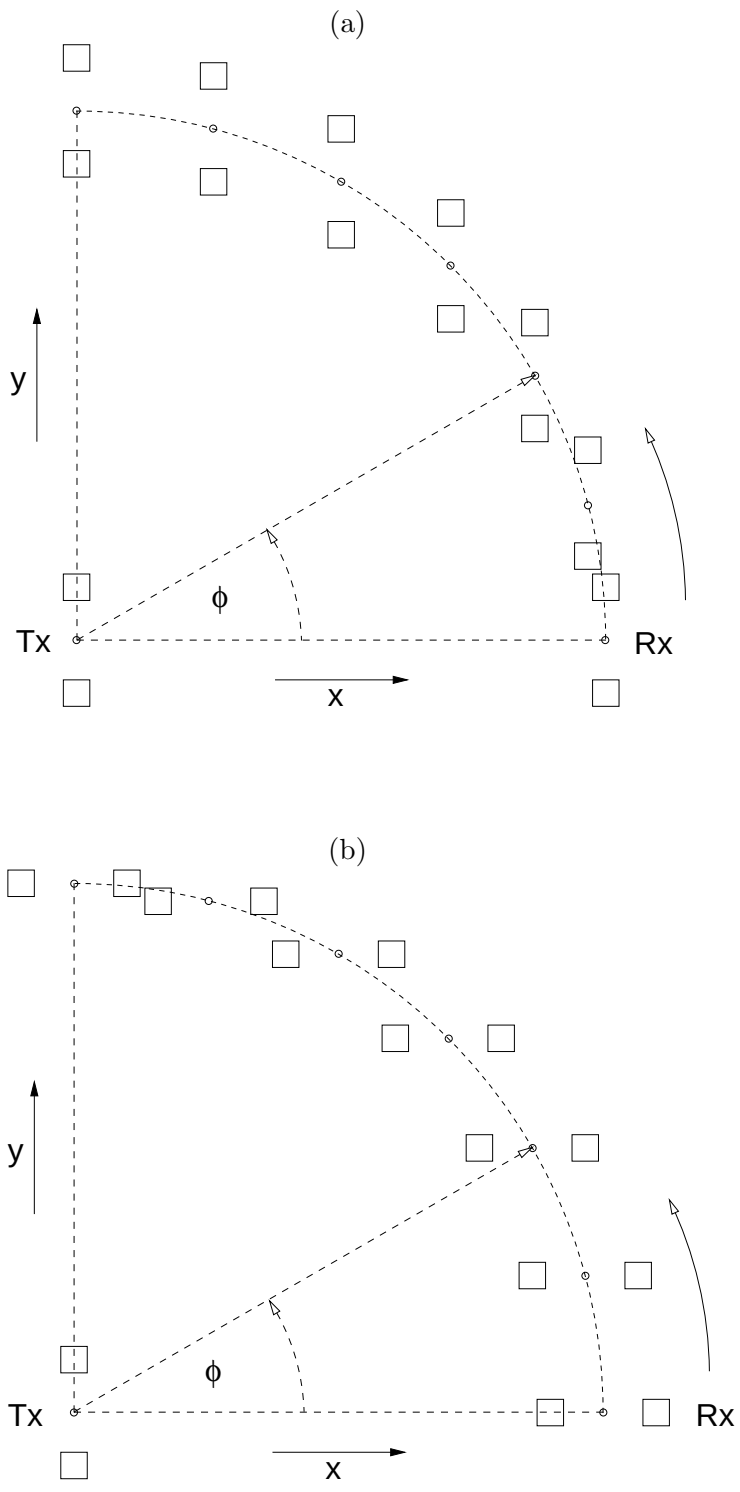

Figure 6.16: Directional survey to determine the azimuthal variation of the transfer impedance. (a) parallel configuration, (b) perpendicular configuration.

of the azimuth ϕ. For reasons of symmetry it is therefore sufficient to restrict the survey to a quarter-circle, i.e. $\phi \in [0° \ldots 90°]$. The surveys were carried out at a different time of the year than the moveout surveys, hence slightly different conditions were anticipated.

6.3.4.1 Parallel configuration

The first survey was carried out with current and potential dipoles in a parallel configuration (Figure 6.16a). Starting from an equatorial position ($\phi = 0°$), The azimuth ϕ was increased in steps of 5° until an axial or inline position ($\phi = 90°$) was reached. The results of this survey are summarised in Figures 6.17 and 6.18. In contrast to the moveout surveys, all graphs are now displayed as a function of azimuth on a linear scale. In Figure 6.17, resistivity is the free model parameter while elevation is kept constant at 1 mm. The same measured data are shown in Figure 6.18, but now elevation is the free model parameter while resistivity is kept constant at 25 Ωm. An angular interval of 180° is shown, centered around an azimuth of $\phi = 45°$, to capture the periodicity of the response. The magnitude has two distinct maxima, an absolute maximum at $\phi = 90°$ and a secondary maximum at $\phi = 0°$. These are consistent with the interpretation of the axial configuration as the position of maximum coupling, while the equatorial configuration only represents a local maximum. Between the two maxima the magnitude has a zero and the phase changes quadrants ($\phi \approx 36°$). In similar fashion to the previous results, the variation of the magnitude with resistivity (Figure 6.17a) is strong while the effect of elevation on magnitude (Figure 6.18a) is much weaker. The variation of the phase with resistivity (Figure 6.17b) is relatively weak, while its variation with elevation (Figure 6.18b) is clearly stronger.

Due to the seasonal change in ground conditions, the optimal fit between measured data and calculated model curves is now observed at $\rho = 25\,\Omega$m. The match between measured magnitudes and the optimal curve at $\rho = 25\,\Omega$m (Figure 6.17a) is remarkably good. The minimum near $\phi = 36°$ is reproduced correctly by the experimental data, however at a slightly lower azimuth. Figure 6.18a shows that measured magnitudes match a range of possible elevations smaller than 5 mm. As far as phases are concerned, interpretation of the results is not as straightforward. At a dipole separation of 5 m, calculated phases are very small, while a slight increase in the measured phase had already been observed in the moveout surveys at that distance. The measured phases were therefore not expected to fit the models particularly well. However, in the parallel configuration they were found to be of the expected size and were observed to follow the change in quadrants predicted by the model curves (Figures 6.17b, 6.18b).

6.3.4.2 Perpendicular configuration

The second survey was carried out with current and potential dipoles in perpendicular configuration (Figure 6.16b), but otherwise following the same pro-

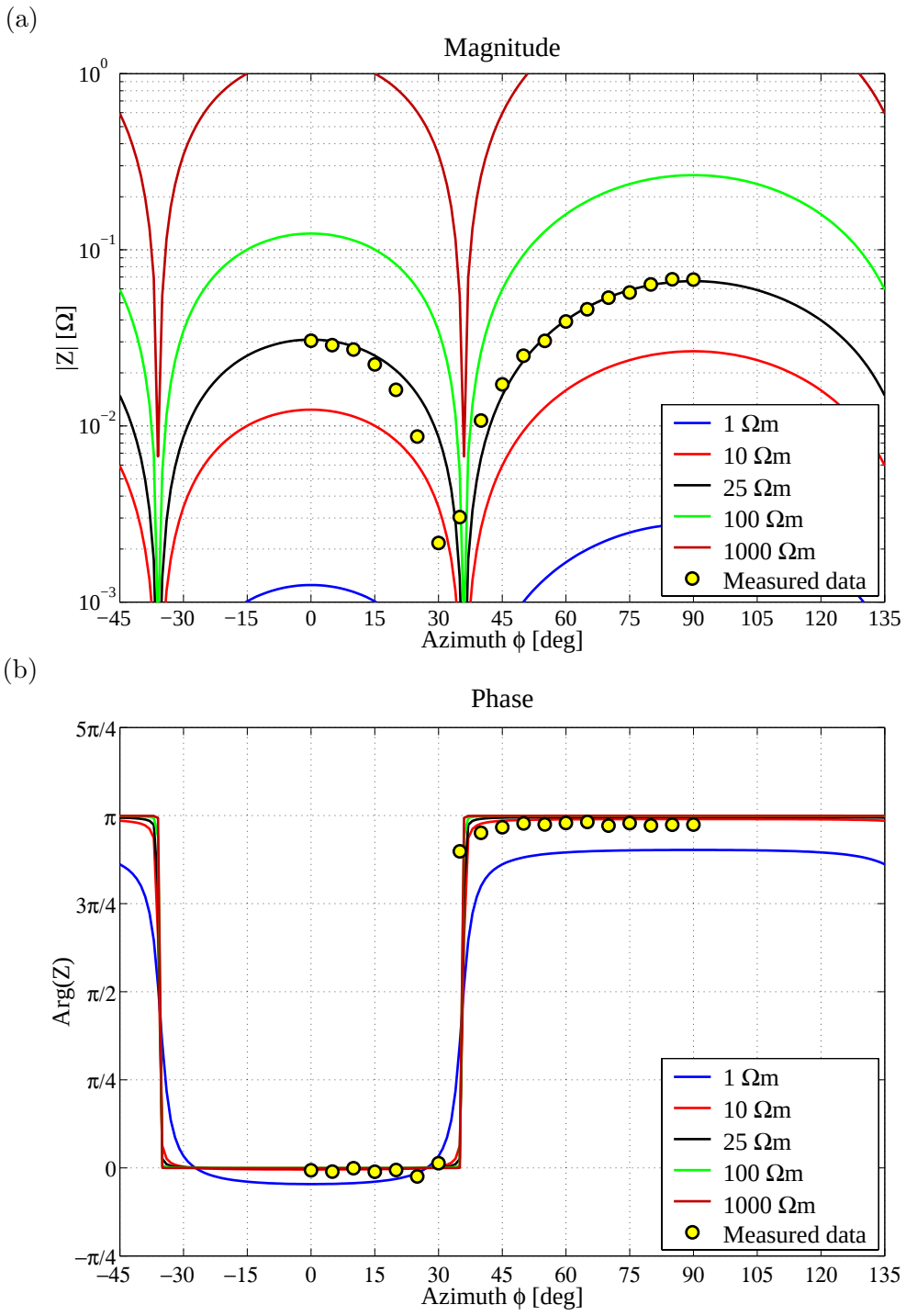

Figure 6.17: Transfer impedances for the directional survey in parallel configuration: comparison of measured data with quasi-static model (model parameter: resistivity; model elevation fixed at $h = 1\,\mathrm{mm}$). (a) magnitude, (b) phase.

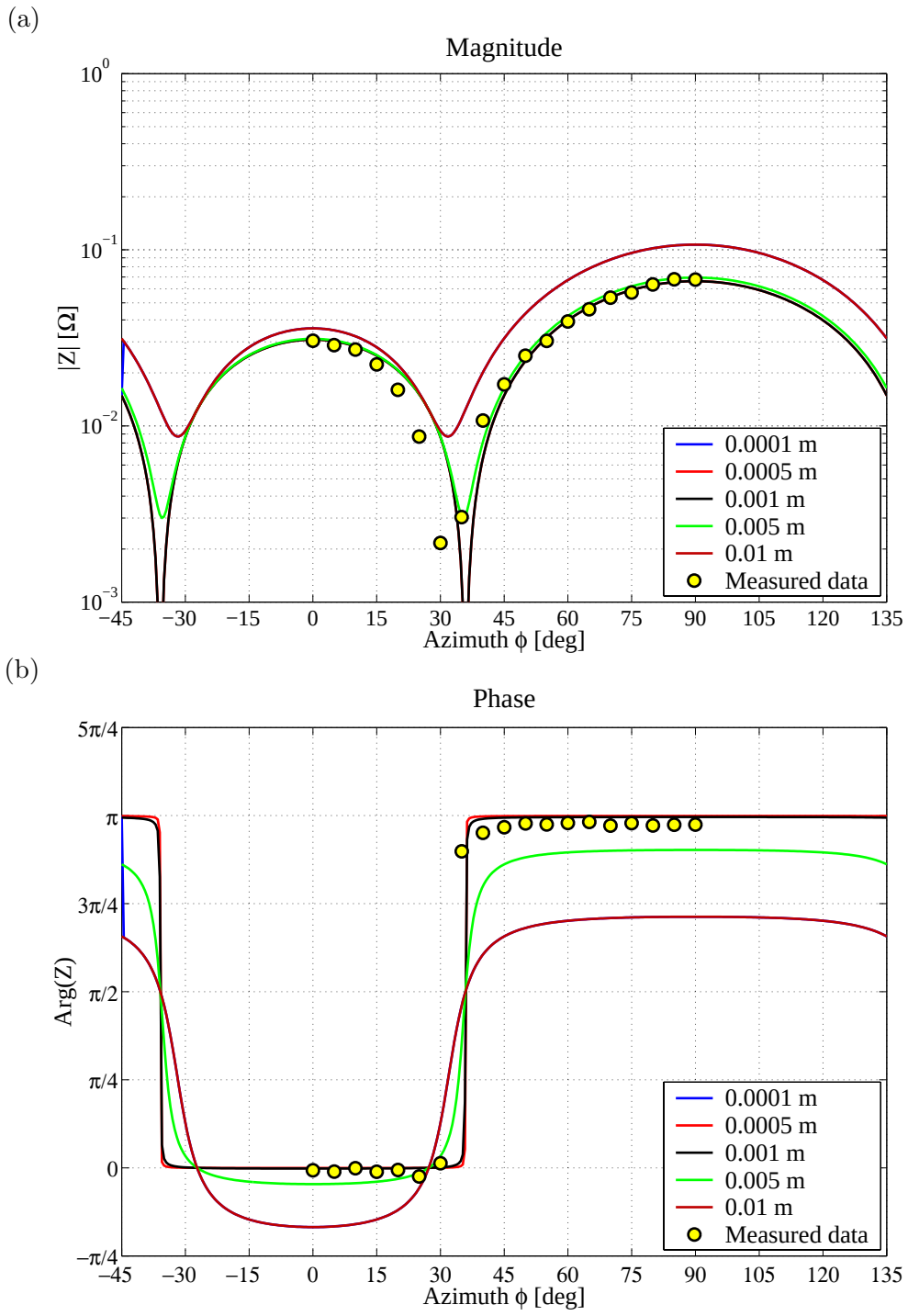

Figure 6.18: Transfer impedances for the directional survey in parallel configuration: comparison of measured data with quasi-static model (model parameter: elevation; model resistivity fixed at $\rho = 25\,\Omega\mathrm{m}$). (a) magnitude, (b) phase.

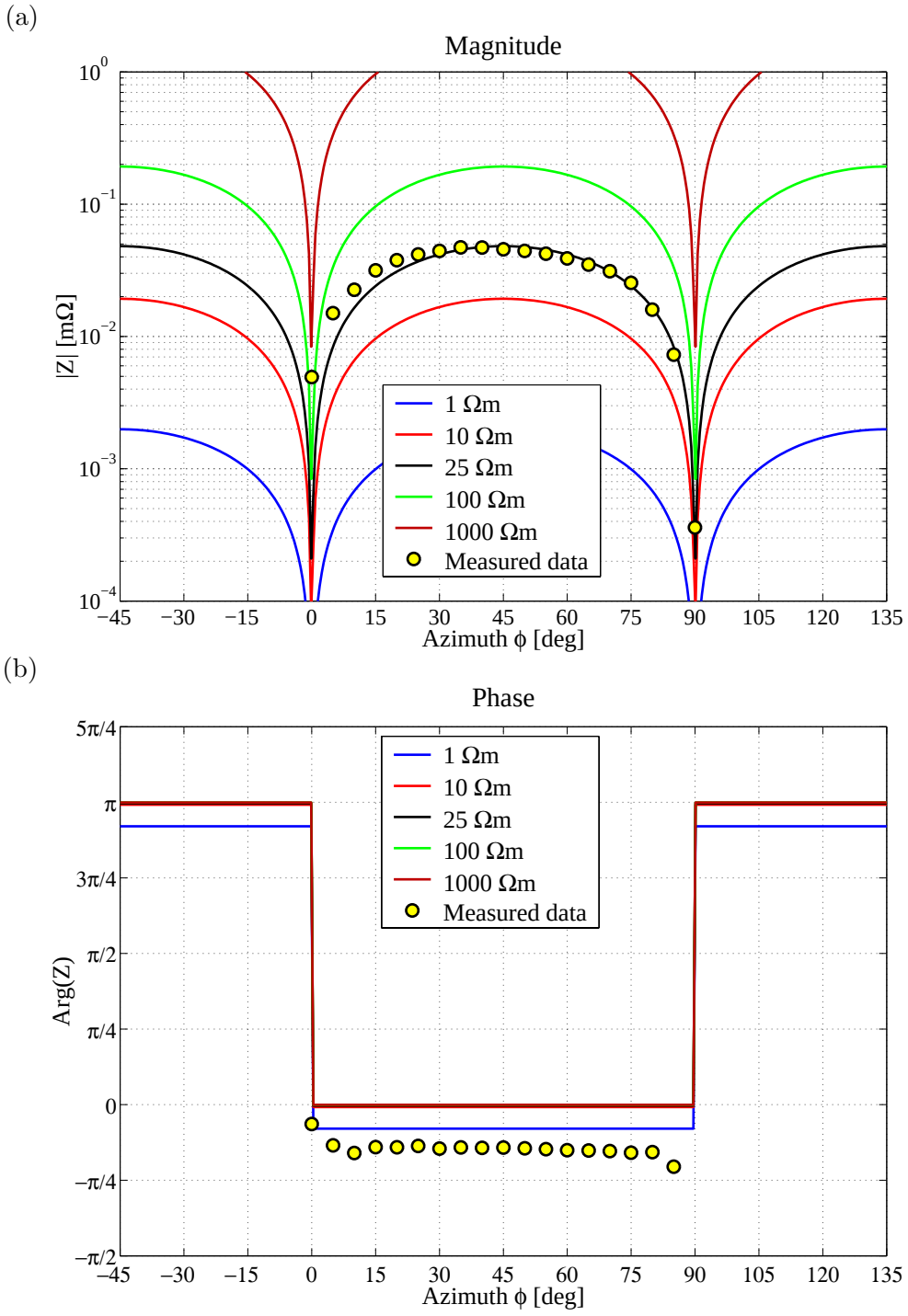

Figure 6.19: Transfer impedances for the directional survey in perpendicular configuration: comparison of measured data with quasi-static model (model parameter: resistivity; model elevation fixed at $h = 1\,\mathrm{mm}$). (a) magnitude, (b) phase.

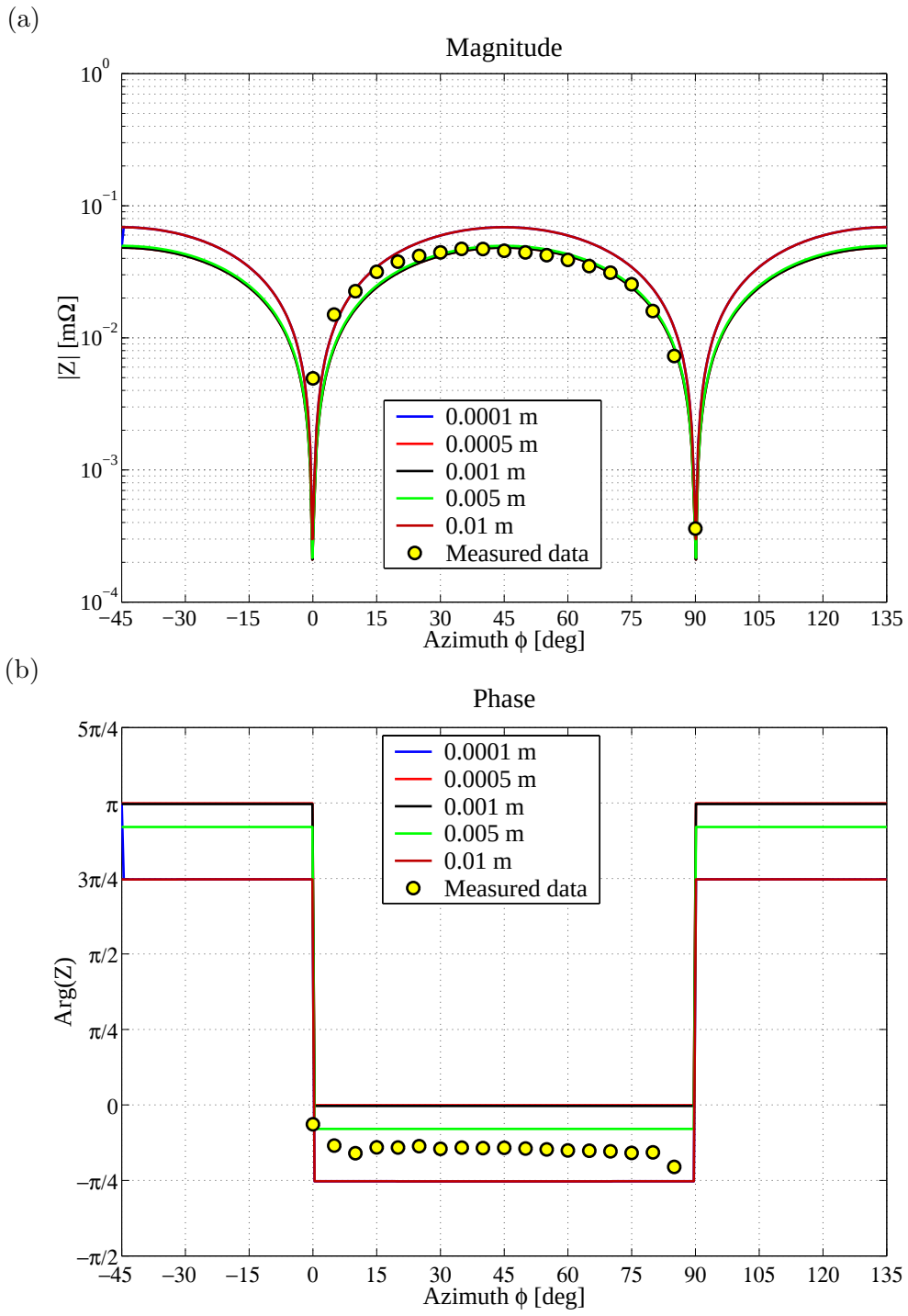

Figure 6.20: Transfer impedances for the directional survey in perpendicular configuration: comparison of measured data with quasi-static model (model parameter: elevation; model resistivity fixed at $\rho = 25\,\Omega\mathrm{m}$). (a) magnitude, (b) phase.

cedure as in the parallel case. The results of this survey are summarised in Figures 6.19 and 6.20. In Figure 6.19, the free model parameter is resistivity while elevation is kept constant at 1 mm. The same measured data are shown in in Figure 6.20 but now elevation is varied while resistivity is kept constant at $\rho = 25\,\Omega$m. In contrast to the parallel configuration, the response of the perpendicular case is now symmetric about $\phi = 45°$. The magnitude has a central maximum at $\phi = 45°$ and zeros at $\phi = 0°$ and $\phi = 90°$. At these azimuths the phase changes quadrant, but is constant otherwise. Magnitude and phase show the same sensitivity towards resistivity and elevation that was observed already for the parallel configuration. The sensitivity of the magnitude towards resistivity (Figure 6.19a) is strong while its sensitivity towards elevation (Figure 6.20a) is much weaker. In contrast, the variation of the phase with resistivity (Figure 6.19b) is relatively weak, while its variation with elevation (Figure 6.20b) is much stronger.

As in the case of the parallel configuration, the optimal fit is again observed at a resistivity of $\rho = 25\,\Omega$m. The measured magnitudes match the model curve remarkably well except for a slight asymmetry in the magnitudes towards smaller angles (Figure 6.19a). The zeros at $\phi = 0°$ and $\phi = 90°$ are reproduced accurately by the measured data. Analogous to the parallel case, Figure 6.20a shows that measured magnitudes match a range of possible elevations smaller than 5 mm. The phases are found to be constant and very stable with azimuth, however at a slightly greater value than predicted by the optimum curves (Figures 6.19b, 6.20b). This effect is consistent with observations from the moveout surveys that the quadrature component becomes noticeable for separations greater than 4 m.

6.4 Discussion

In this chapter, the validity of fundamental concepts of the capacitive resistivity technique has been assessed in detail. A study of this kind was only made possible by the construction and evaluation of a prototype CR instrument that can measure the fully complex transfer impedance and accurately record phase information. This had been impractical previously due to the lack of suitable instrumentation. The availability of the BGS prototype CRI system has enabled the conduct of a series of detailed experiments under controlled conditions. The results of this assessment and their implications for the practical application of the CR technique are discussed in the following.

Novelty of the instrument. The BGS prototype CRI system represents the successful realisation of a fully complex CR measurement. Its measurement principle is based on the phase-sensitive detection of minute fixed-frequency signals under noisy conditions. This is crucial for the reliable estimation of amplitude and phase of the transfer impedance at larger array separations and in environments with elevated levels of ambient noise. It is the only known instrument of its kind to employ a floating ground reference, i.e. the complex

potential at the receiver dipole is measured without the need for a fixed reference potential. Somewhat contrary to the idea of a capacitive measurement, galvanic reference electrodes had to be employed in previous designs (e.g. the CORIM™ system). The floating measurement is an important step forward in terms of instrument design and a prerequisite for successful operation of towed arrays on artificial surfaces, where a galvanically coupled reference is known to cause difficulties. Conceptually, the CRI system is intended for simultaneous acquisition on multiple receiver channels. The system is flexible with regard to sensor type and configuration and can be used for the dynamic acquisition of multi-offset high-resolution resistivity data from towed arrays. This application is discussed in detail in Chapter 7.

Real capacitive sensors. Studying the practical properties of real capacitive sensors has led to an improved understanding of fundamental issues associated with the CR measurement. The effective sensor capacitance of a plate-wire combination has been measured directly in the field. The results have shown that the reactive part of the impedance of the injection circuit is dominant over the ground resistance, i.e. the transmitter current is primarily a function of the sensor capacitance, which in turn is directly determined by the surface area of the sensor and its proximity to the ground surface. It has also been shown that an effective sensor elevation can be deduced from the measured sensor capacitance using simple capacitance models. Although this elevation is theoretical and based on an idealised ground surface, good correlation with practical elevations has been observed. This can be regarded as further proof that the fundamental assumptions of the CR technique are consistent.
A study was undertaken to compare the capabilities of capacitive sensors and galvanic electrodes with respect to wideband measurements of the electric field. A non-grounded dipole and a grounded dipole were used to monitor the ambient electric field at VLF frequencies. Experimental data of this kind are rarely found in the literature. The fundamental issue of whether grounded and non-grounded dipoles are equivalent sensors for the electric field at the ground surface has been the subject of controversial discussion in the past (Wait, 1995). Results of the present study, although qualitative, indicate that both dipole types measure similar fields and are likely to be equivalent in the context of CR measurements.

Spatial analysis of the transfer impedance. A detailed spatial analysis of the complex transfer impedance was carried out to assess the applicability of the electrostatic formalism to practical CR measurements. The analysis involved a series of elementary surveys over relatively homogeneous ground. Magnitude and phase of the transfer impedance (Z) were measured as functions of array separation and azimuth and compared to model curves calculated with the electrostatic formalism. Assessments in such detail were previously impractical due to the lack of instrumentation to perform phase-sensitive capacitive measurements. The free model parameters were resistivity and elevation. The moveout surveys included measurements at unusually short separations in order to examine characteristic phase shifts under such conditions. The azimuthal surveys

were regarded as additional control due to the directional sensitivity of Z.

The results of the analysis show that there is remarkable agreement between the measured data and the quasi-static model. The moveout surveys suggest that this agreement applies to a wide range of distances except for extremely short and beyond relatively long separations. In both moveout and azimuthal surveys, the optimal fit with respect to resistivity corresponded with expected values from previous experience with the test area (20–25 Ωm). Array elevation mainly affects the quadrature component (and hence the phase) of Z and has limited influence on the magnitudes. Models with effective elevations under 1 mm appeared to fit the measured data best.
In the moveout surveys, Z (and hence ρ_a) was consistently overestimated at extremely short array separations due to geometric effects caused by the finite plate size. The predicted occurrence of large phases at moderately short separations has been confirmed by the experiments. At separations of several times the dipole length, the onset of inductive effects was consistently observed in all datasets. These effects are expressed by a significant increase in magnitude and an associated phase rotation away from zero phase. Consequently, apparent resistivities are also overestimated at long offsets. The effect on ρ_a has previously been reported by Benderitter et al. (1994). The remaining discrepancies between measured data and the quasi-static model are attributed to the expected aberration of the real subsurface from a truly homogeneous halfspace. Comparative surveys with conventional DC resistivity have shown reasonable agreement between both techniques, however DC levels for ρ_a were slightly elevated compared to CR. Absolute calibration of the two systems was not attempted.

Chapter 7

Dynamic measurements with towed CR arrays

Dynamic data acquisition is a procedure well known in the context of many other geophysical methods (e.g. marine seismics, airborne geophysics, ground penetrating radar). A truly dynamic, continuous (as opposed to stop-and-go) measurement process is the most effective in terms of ground coverage and can provide densly sampled datasets. These have the potential to reveal more detailed information about the ground than coarser static data. As far as resistivity methods are concerned, the use of dynamic techniques is limited. For DC resistivity in particular, the problem of maintaining galvanic contact at all times must be overcome. Data obtained by dynamic DC measurements (cf. Section 3.1.5) are often affected by high noise levels due to temporary variations in galvanic contact (Sørensen, 1996). On artificial ground, the situation is worse due to high contact impedances, making dynamic DC techniques unsuitable for surveys in the built environment. Dynamic capacitive measurements are an ideal alternative to DC, providing a means of collecting high-density resistivity data independent of surface conditions. A key advantage of CR is that its measurement principle facilitates a dynamic mode of operation. In dynamic CR, apparent resistivity data are acquired continuously from a towed array of capacitive sensors.

In this chapter, the fundamental concepts associated with the use of towed CR arrays are discussed. The operational characteristics of available towed-array instruments are examined. Apparent resistivity profiles acquired by towed-array CR represent a novel type of geophysical data with distinct attributes. Typical examples of towed-array CR data are shown and their properties examined, for example with respect to data quality and repeatability of measurements. It is demonstrated that sampling intervals of the order of centimetres are possible without the need for data reduction. Resistivity data with such densities are unprecedented in applied geophysics. Finally, basic data processing techniques relevant to towed-array CR are discussed, including the suppression of towing-induced noise and the removal of levelling errors.

7.1 Fundamental concepts

7.1.1 Synchronous multi-channel acquisition

A towed CR array consists of multiple capacitive sensors in a fixed geometrical arrangement, mounted on some kind of towable mechanical platform such as a trailer, frame, mat or carpet. The entire unit is then pulled along manually by an operator or towed by a vehicle. Current and potential dipoles are moved synchronously and kept at a constant separation. Single-channel systems consist of one receiver dipole and thus can only provide data for one single dipole separation at a time. Multi-channel systems with several receivers can obtain n data series for n dipole separations synchronously, thus investigating n effective depths in a single pass of the instrument.
The use of multi-offset towed CR arrays gives rise to different survey techniques analogous to those described in Sections 3.1.3 and 3.1.4, including multi-offset resistivity profiling, multi-offset resistivity mapping and resistivity tomography. The potential increase in productivity by using multi-offset towed arrays as opposed to single-array acquisition is obvious. It should be noted that, besides greater efficiency, there is no fundamental difference between synchronous acquisition with multi-channel arrays and the sequential acquisition by multiple passes with a single-channel system. A characteristic property of towed-array measurements is that surveys are necessarily conducted along linear profiles. Survey progress is therefore always directional. This has important consequences for areal mapping and 3D imaging surveys (discussed in Chapter 8). In this chapter, only individual profiles will be considered.

7.1.2 Continuous spatial sampling

A key parameter in resistivity profiling is the sampling interval, i.e. the distance along the survey profile at which readings from the same array geometry are taken. In DC resistivity, the horizontal sampling interval is a function of the electrode arrangement. For convenience, surveys are usually designed such that electrode movement is minimal. In a multi-electrode setup with a large number of equally spaced electrodes, the minimum horizontal sampling interval associated with any particular array configuration is then equal to the electrode spacing along the profile. For dynamic measurements with towed arrays however, lateral sampling is independent of the electrode arrangement and can be significantly denser ("continuous"). If all channels on a multi-offset system are scanned synchronously, the sampling interval is the same for all array configurations. Practical data acquisition implies that sampling will be regular either in time or space.

Constant-frequency sampling. Constant-frequency sampling produces data at regular intervals in time. A potential disadvantage of this approach is that spatial sampling along the survey profile becomes irregular if the towing speed varies. Figure 7.1 shows synthetic apparent resistivity profiles sampled at a constant frequency. The usual procedure is to record marker points (fidu-

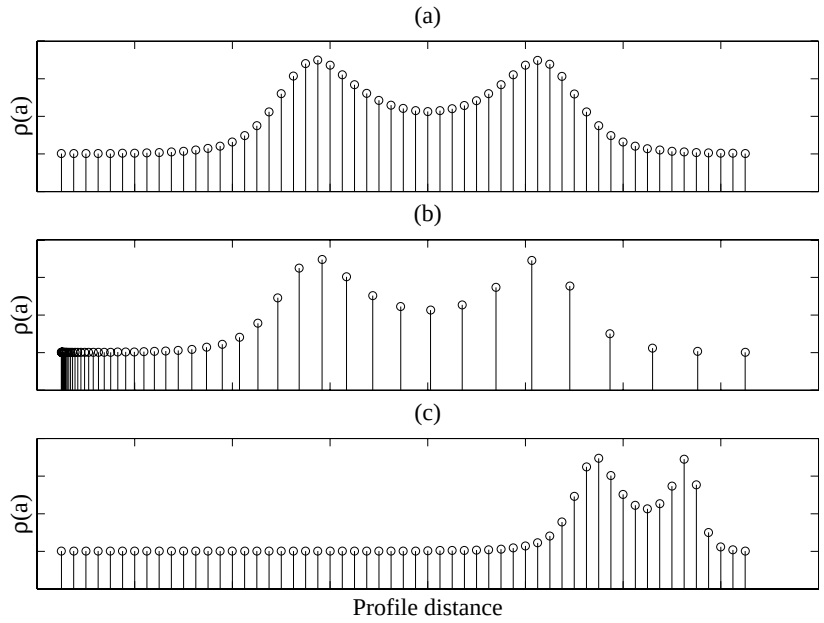

Figure 7.1: Positional errors in apparent resistivity profiles arising from variations in towing speed during constant-frequency sampling. (a) Sampling at constant speed. (b) Sampling at increasing speed ($v \propto t^3$). (c) Reconstruction of profile (b) by assuming constant sampling intervals.

cials) at greater distances on the survey line, between which the sampled data are then distributed equally by linear interpolation. Equally-spaced data are only obtained at constant towing speeds (Figure 7.1a). A variation in towing speed leads to irregular sampling (Figure 7.1b) and consecutive reconstruction of the profile by linear interpolation between fiducials leads to distortion or loss of spatial information (Figure 7.1c).

Constant-distance sampling. Many data processing and interpretation schemes (e.g. filtering, spatial Fourier analysis or resistivity modelling and inversion algorithms) require equally spaced data. Regular sampling in space from the outset is therefore advantageous to avoid resampling and potential loss of information at a later stage. Equally-spaced data can be obtained by triggering the acquisition at predefined distance intervals. A distance measurement may be realised by an odometer attached to the sensor array or towing vehicle. An odometer comprises a wheel that produces a well-defined number of electronic pulses per revolution.
Alternatively, data acquisition may be controlled remotely by external navigation aids such as Differential GPS (cf. Chapter 8) or automated surveying equipment such as self-tracking laser theodolites (Lehmann and Green, 1999).

Minimum sampling interval and spatial averaging. The horizontal sampling interval cannot be arbitrarily small. The maximum rate at which individual resistivity readings can be obtained is limited by the time constant τ of the measurement process itself. This time constant is a function of the frequency of operation and depends on the measurement principle. The same restriction applies to DC resistivity, where low-frequency AC resistivity meters are commonly used to avoid compensation for electrode self-potential (Hesse et al., 1986). Cycle times between 8 ms (125 Hz) and 15 s (0.067 Hz) are in use with common instruments, so that measurements can be made with typical time constants ranging from a few milliseconds to several seconds. In the case of CR, cycle times are significantly smaller due to the use of frequencies in the VLF range (e.g. 66.7 μs at 15 kHz). Dynamic measurements on such a short time scale require rapid adaptation of the injected current, which is invariably associated with induced EM fields. By examining the response of conductive ground to current injection in the form of a step function, Hesse et al. (1986) were able to show that typical time scales for the decay of induced fields are of the order of 1–2 μs. Even over a time scale of a single current cycle, the influence of the induced field can therefore be neglected.
At typical towing speeds of 2.5 km/h, a time constant of the order of $\tau = 10\,\text{ms}$ as used by faster DC instruments corresponds to a distance of approximately 7 mm over which a single measurement is performed while the array is moving at constant speed. For dynamic DC resistivity measurements, spatial sampling at the (sub-)centimetre scale therefore requires the construction of resistivity metres that can make a single measurement per current cycle (Hesse et al., 1986). In the case of CR however, the same time constant corresponds to hundreds of current cycles at VLF (e.g. 150 cycles at 15 kHz). Conceptually, phase-sensitive signal detection in conjunction with spatial sampling at the centimetre scale is therefore possible.
As a consequence of the finite time required for each measurement during towed-array CR data acquisition, readings are not actually obtained at a fixed position in space but over a small distance. This fundamental averaging effect is inherent to dynamic measurements. However, even greater averaging is associated with the finite size of capacitive sensors. The electric potential is determined for an area of ground corresponding to the size of the individual sensor. In the case of capacitive plates, this means that individual readings represent an average over the plate width. In the case of line antennas, the averaging effect applies to the entire length of each dipole.

7.1.3 The dipole-dipole geometry

The choice of array geometry is a fundamental decision for towed-array resistivity measurements. While the use of a static multi-electrode setup (cf. Figure 3.7) allows data acquisition with a variety of geometries on the same profile without changing the electrode arrangement, data acquisition from a towed array is only practical with a constant geometry. It is therefore desirable to use a geometry with versatile properties. Some electrode geometries are generally unsuitable for towed CR arrays. The use of remote electrodes (pole-pole and

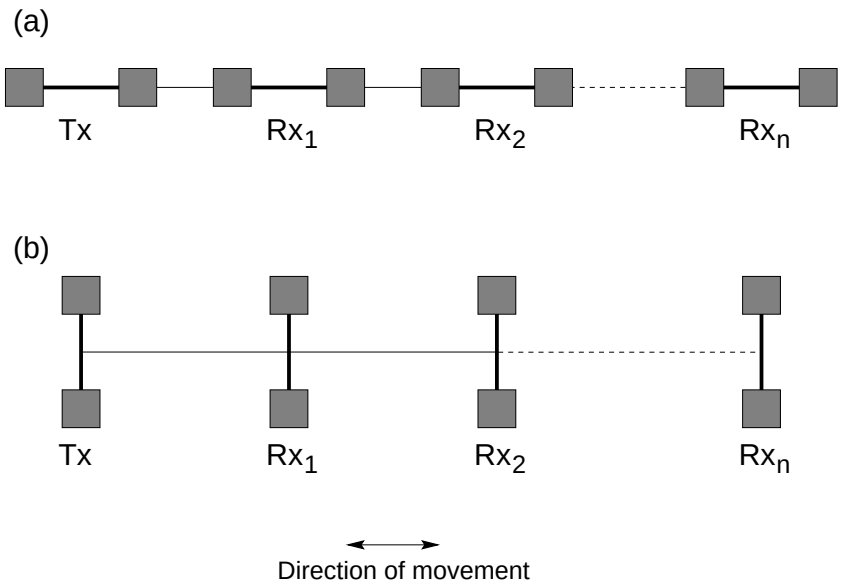

Figure 7.2: Configuration of a towed CR array with one transmitter and multiple receivers in dipole-dipole geometry. (a) Inline, (b) equatorial array.

pole-dipole arrays) is commonplace in the DC technique and such geometries have even been used in conjunction with mobile DC arrays (Panissod et al., 1998). However, their application to towed CR arrays is impractical because of the length of connecting wires required for the remote poles. The classical Wenner and Schlumberger arrays are equally problematic because the potential dipole is located between the current electrodes. In a towed array, such an arrangement would invariably be susceptible to mutual inductive coupling between transmitter and receiver wiring.
Consequently, the dipole-dipole array is the only array type that is suitable without restriction for dynamic CR measurements. The dipole-dipole geometry is therefore an integral part of the concept of towed CR arrays. The two generic configurations are the inline and equatorial dipole-dipole arrays (Figure 7.2). These have the following properties:

Depth of investigation. In analogy to DC resistivity, the depth of investigation of the CR technique is constrained by the overall size of the electrode array. For comparison between different geometries, the depth of investigation can be quantified by the same absolute depth scales that are used in DC resistivity, for example the "median depth" defined by Edwards (1977, cf. Section 3.1.4.2). At small separations, the median depth of the inline dipole-dipole array is only marginally smaller than for other array types (cf. Table 3.2). It is however significantly smaller than the median depth of the equatorial array. With respect to overall array size L, the equatorial array has by far the largest median depth compared to the other array types ($\approx L/3$).

Sensitivity distribution. The DC sensitivity indicates the change in measured potential due to a change in resistivity of a particular volume of the subsurface. It is a function of array geometry and represents a meaningful quantity in any interpretation process (Spitzer, 1998). The sensitivity for a defined electrode array configuration can be expressed as the inner product of the current densities $\mathbf{j}^l$ and $\mathbf{j}^m$ produced by a current source of strength I at the source position l and the receiver position m, respectively, integrated over the perturbed volume τ_n (Geselowitz, 1971):

$$\Phi_{lmn} = \frac{1}{I} \iiint_{\tau_n} \mathbf{j}^l \mathbf{j}^m d\tau_n \tag{7.1}$$

Sensitivity analysis can help assess the spatial resolution capabilities of a particular electrode geometry, yet very few results have been published in the open literature (Spitzer, 1998; Loke, 1999). In order to compare the two elementary configurations, 3D distributions of the DC sensitivity were calculated for the inline and equatorial dipole-dipole arrays. Results for the inline dipole-dipole array are shown in Figure 7.3. The near-vertical contour pattern (Figure 7.3b) reveals that this configuration is very sensitive to lateral changes in resistivity, but relatively insensitive to vertical changes (Loke, 1999). Results for the equatorial dipole-dipole array are shown in Figure 7.4. The sensitivity contour pattern is more horizontal with a greater lateral extent (Figure 7.4c). This means that the equatorial array is likely to be more sensitive to vertical changes and less to lateral ones. These characteristics affect the information content of data acquired with different array geometries and are likely to affect any quantitative interpretation, for example by inverse modelling. The results demonstrate that the choice of geometry is a significant factor in designing a towed CR array.

Signal strength. A clear disadvantage of the dipole-dipole array is the fact that observed potentials are very small at large separations (i.e. large n-factors). A comparison of the two elementary configurations shows that the inline geometry represents the configuration of "maximum coupling" between current and potential dipoles. The coupling in the equatorial configuration is weaker than for the inline geometry, hence a weaker signal is observed at comparable dipole separations. In the case of the inline configuration, the potential is inversely proportional to r^3 (cf. Equation 3.22). The only remedy for this problem is to increase the transmitter dipole moment by using a longer dipole or stronger currents or to use larger potential dipoles in order to obtain a stronger signal. Panissod et al. (1997a) have described an improved type of equatorial array in which the length of the potential dipoles increases with their distance from the current dipole. The resulting configuration is V-shaped and is referred to as the "Vol-de-canards" array[1].

Manoeuverability/handling. Clearly, a towed multi-channel array must be easily manoeuverable in practice, particularly when deployed on sites with space

[1] vol de canards (fr.) = flight of the ducks (refers to V-shaped formation).

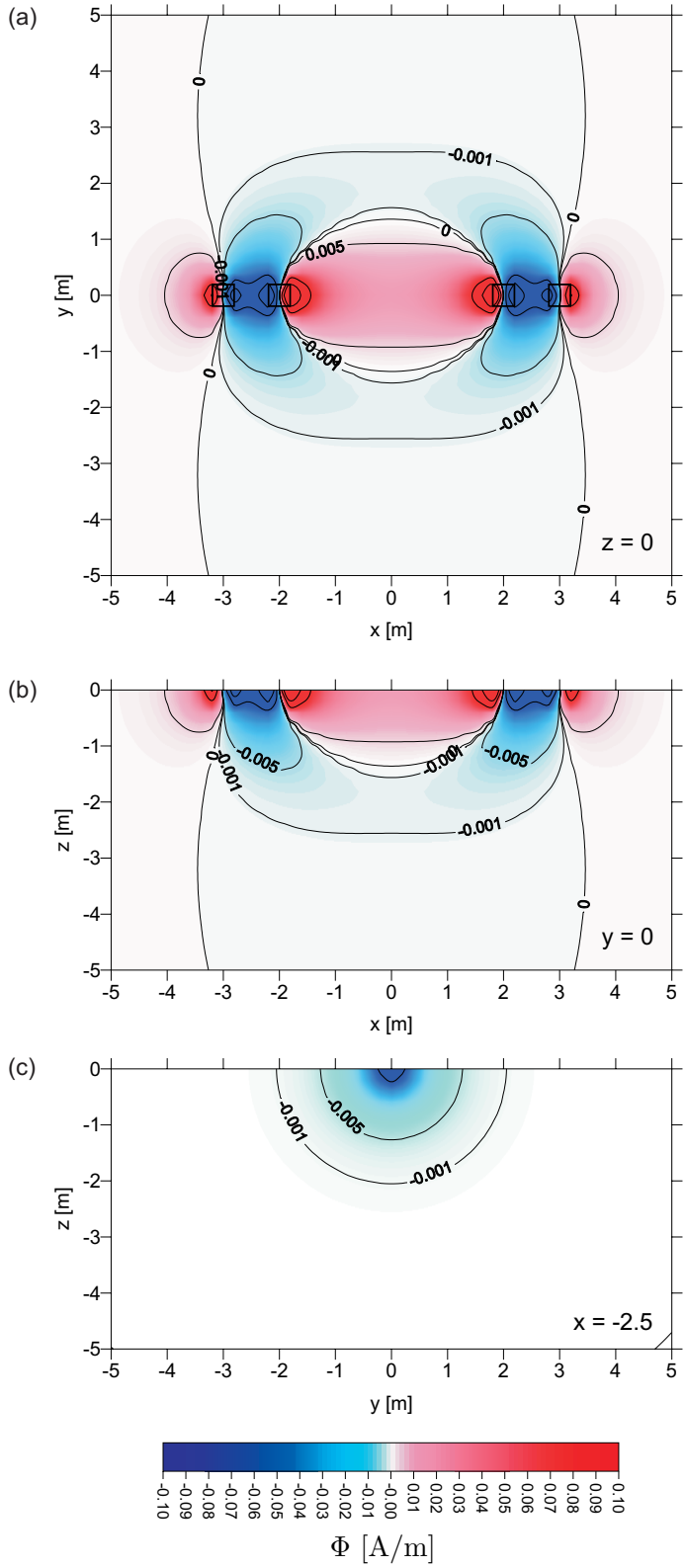

Figure 7.3: 3D distribution of DC sensitivity for the inline dipole-dipole array ($l = 1\,\mathrm{m}$, $r = 5\,\mathrm{m}$) in a homogeneous halfspace. (a) xy plane, $z = 0$; (b) xz plane, $y = 0$; (c) yz plane, $x = -2.5$.

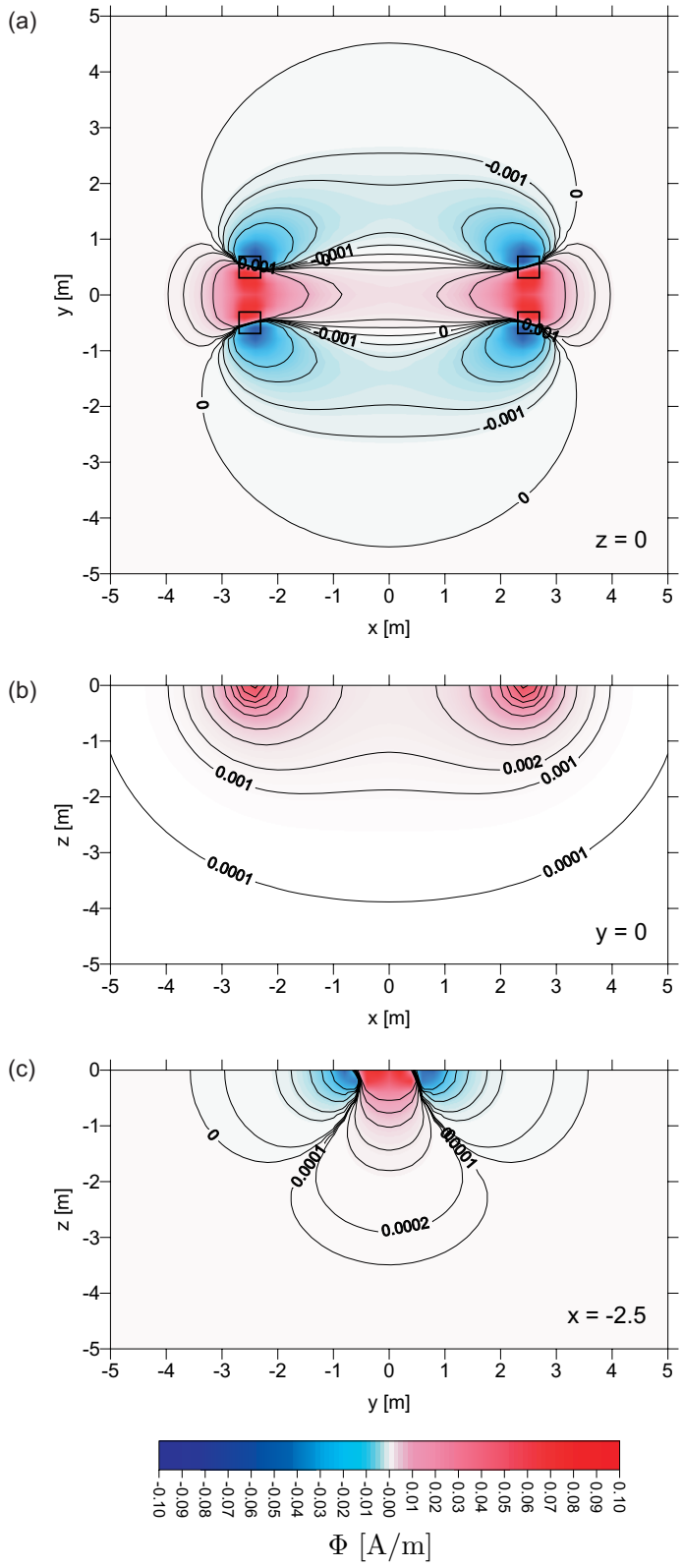

Figure 7.4: 3D distribution of DC sensitivity for the equatorial dipole-dipole array ($l = 1\,\mathrm{m}$, $r = 5\,\mathrm{m}$) in a homogeneous halfspace. (a) xy plane, $z = 0$; (b) xz plane, $y = 0$; (c) yz plane, $x = -2.5$.

restrictions. The physical dimensions and weight of the array must therefore be limited. Surveys on smaller, confined sites may require more compact arrays for easier manoeuvring than surveys on vast open spaces. The equatorial geometry allows the construction of very compact arrays because dipoles can be arranged at shorter distances relative to dipole size. The inline array requires more space between the dipoles and is therefore bigger by default. However, the overall length and width of the array is also directly linked to its depth of investigation. Consider an inline and an equatorial array with $l = 1\,\mathrm{m}$, $r = 2\,\mathrm{m}$, respectively. Then the overall length L of the inline array equals 3 m, while for the equatorial array $L = 2\,\mathrm{m}$. The nominal depth of investigation (median depth) for the inline array is 0.42 m, while for the equatorial array it is 0.72 m (cf. Table 3.2). Despite the equatorial array being shorter, its nominal depth of investigation is greater than that of the inline array.
In contrast, the inline geometry facilitates the construction of streamlined arrays with less mechanical resistance against dragging. The use of capacitive line antennas allows for the construction of a special kind of towed array. If the antenna material (e.g. coaxial cable) is robust enough to withstand mechanical stress, the antenna itself may form part of the tow line. The current and potential dipoles can then simply be lined up to an array which can be pulled without the need for a mechanical platform. The OhmMapper™ system is an example where such a design has been realised (cf. Figure 4.6).

7.2 Operational characteristics of towed CR arrays

As part of this research, numerous test measurements with different CR instruments have been performed over a period of three years to examine the properties of capacitive resistivity data obtained with towed arrays. Commercially available instruments (OhmMapper™ and CORIM™) were evaluated over periods of several weeks each and a variety of surveys was undertaken on a number of different sites. In addition, a substantial amount of work has gone into the development and testing of the BGS prototype CRI system. The CRI system has also been used for a limited number of evaluation surveys on different sites. A complete discussion of all data is clearly beyond the scope of this thesis. Instead, representative examples will be discussed that demonstrate the operational characteristics of individual instruments as well as towed CR arrays in general. All the examples shown use raw data as recorded in the field.

7.2.1 OhmMapper™

The OhmMapper™ is based upon the use of capacitive line antennas (Figure 7.5 and Section 4.4.1). In its default configuration, a coaxial-cable array comprising a transmitter unit and a receiver unit are pulled along the ground by a walking operator (Figure 7.6). Transmitter and receiver are galvanically separated by a non-conducting rope segment. The front end of the receiver dipole is connected to a tow line which in turn is attached to a harness worn by the operator. The tow line also acts as a data link for the communication between a data logger (a hand-held console carried by the operator) and the receiver unit.

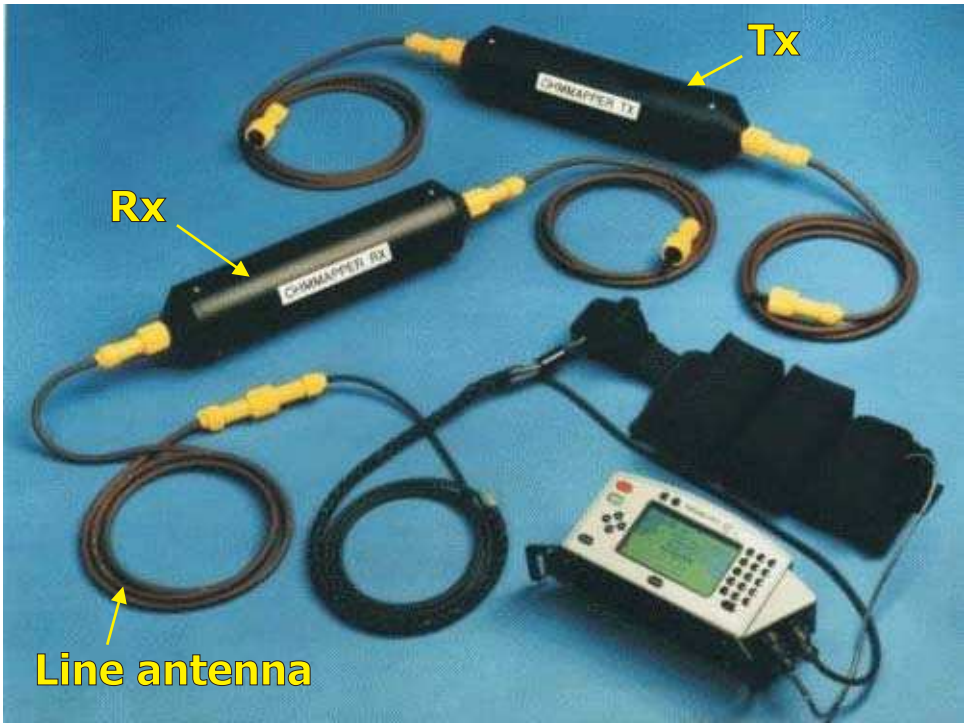

Figure 7.5: Components of the OhmMapper™ system. Photo: Geometrics Inc.

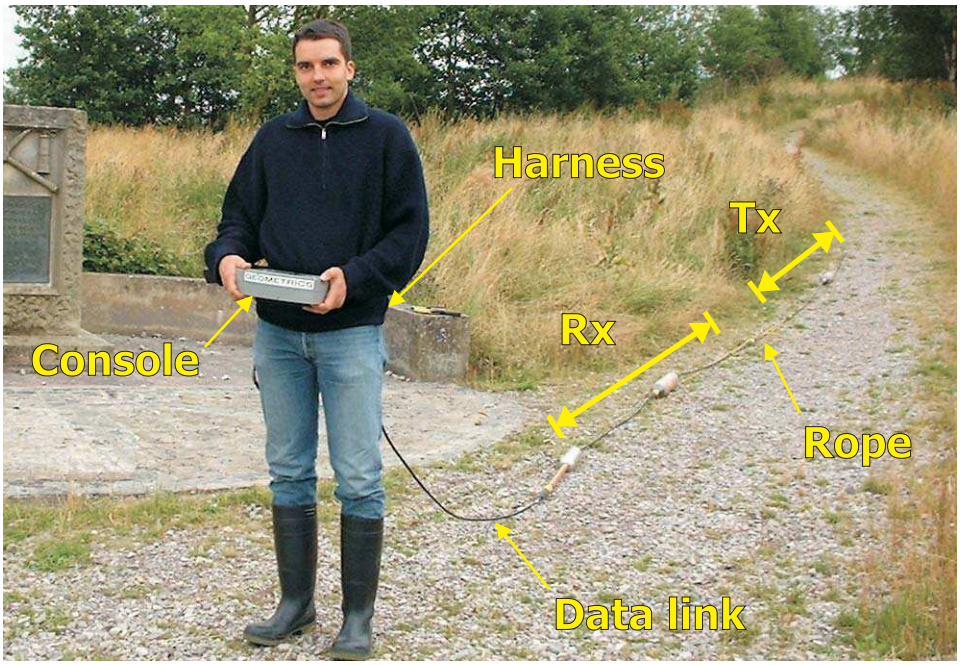

Figure 7.6: The OhmMapper™ system in field operation.

The transmitter operates at a frequency of 16.5 kHz and has an output power of up to 2 W. The output current can range between 0.125 mA and 16 mA. It is automatically adapted to local conditions by the transmitter and maintained at constant level. As there is no electrical link between transmitter and receiver units, information about the current setting is modulated onto the carrier signal and decoded by the receiver for subsequent calculation of the transfer impedance. From the receiver, data are sent digitally to the console via a serial link. Data are sampled at a user-selectable, constant rate of up to 2 Hz, i.e. a minimum cycle time of 0.5 s. At average walking speeds of 2–2.5 km/h, the minimum horizontal sampling interval is therefore around 30 cm. In order to establish a spatial reference between the recorded data and the survey profile, fiducial marks can be recorded during the acquisition, which are stored alongside corresponding datum points. Spatial distortion of the profile (cf. Section 7.1.2) can thus be kept to a minimum.

7.2.1.1 Data quality

The OhmMapper™ system was tested in a variety of environments to assess the data quality under different survey conditions. Typical apparent resistivity profiles recorded during those tests are shown in Figures 7.7–7.10. The maximum sampling rate of 2 Hz was used throughout in order to obtain the highest lateral resolution possible.

Grass. The first example (Figure 7.7) was recorded on grass over landscaped ground on a test area at the BGS site in Keyworth (cf. Section 6.3.1). Dipoles of 10 m length and a rope of 10 m ($l = 10$, $r = 20$) were used on this occasion. Up to a profile distance of 105 m, the observed apparent resistivities reflect the well-known background value of approximately 20 Ωm on this site. Variations between adjacent datum points are of the order of 1–2 Ωm and the total variation over this first section of the profile is within a range of between 16 and 25 Ωm. The remaining section of the profile between 105 m and 145 m has a different character and shows considerable variation in apparent resistivity. A "W"-shaped anomaly centred at 127 m is observed, which corresponds to the crossing of a small, gently sloping embankment. This section of the profile is contaminated by towing noise in the form of spikes, i.e. individual outliers with values many times greater or smaller than the background resistivity. Although spikes with small values can occur, the vast majority is associated with very large values. These "positive" outliers are a characteristic of the OhmMapper™ system and are observed in many datasets. They are likely to be associated with situations in which one of the line antennas is lifted off the ground due to vertical stress on the tow line, for example at the foot of a slope.

Grass/concrete. Figure 7.8 shows a profile recorded over an abandoned mineshaft at the Minnie Pit, Silverdale, Staffordshire. The mineshaft is backfilled with rubble and has a diameter of approximately 6 m. At the surface it is covered by a concrete cap with a diameter of approximately 10 m. The shaft is surrounded by grassland. The apparent resistivity profile runs across the

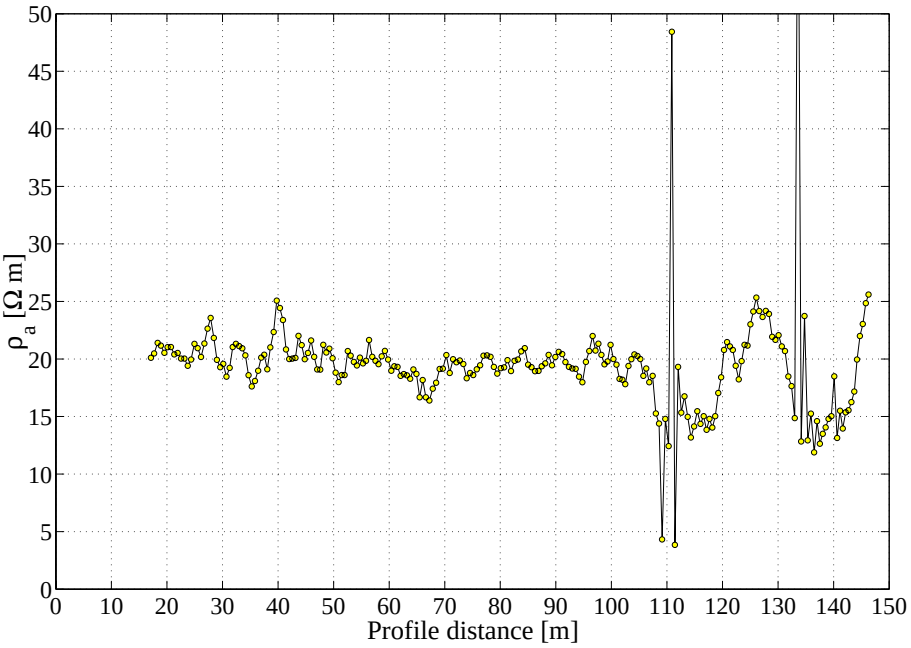

Figure 7.7: OhmMapper™ apparent resistivity profile on grass (BGS test site). Dipole length 10 m, rope length 5 m, sampling rate 2 Hz.

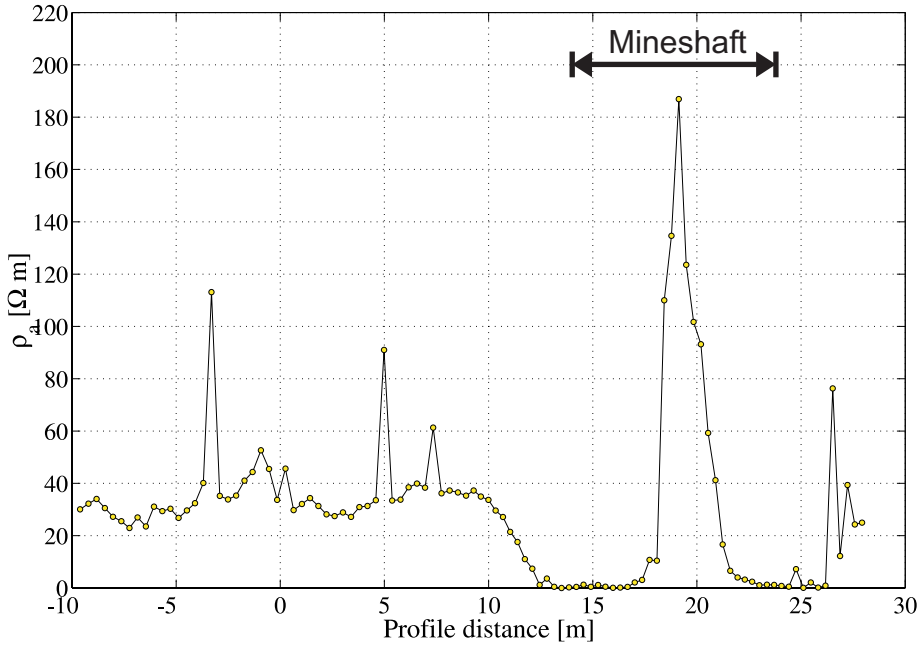

Figure 7.8: OhmMapper™ apparent resistivity profile over an abandoned mineshaft (Minnie Pit, Silverdale). Dipole length 5 m, rope length 4 m, sampling rate 2 Hz.

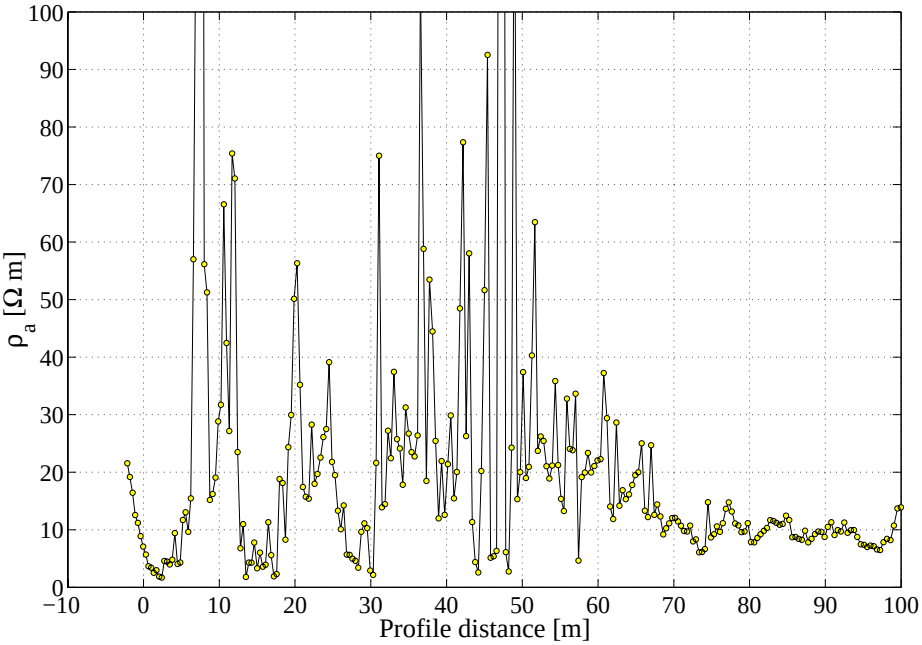

Figure 7.9: OhmMapper™ apparent resistivity profile on a dirt track (British Gas site, Aylestone Road, Leicester). Dipole length 5 m, rope length 2 m, sampling rate 2 Hz.

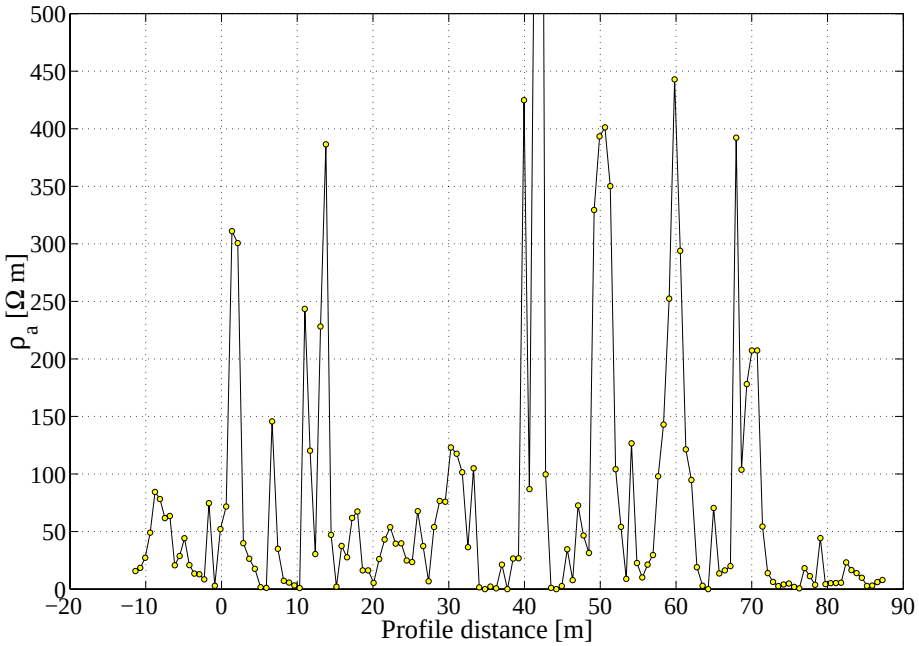

Figure 7.10: OhmMapper™ apparent resistivity profile on a tarmac road (British Gas site, Aylestone Road, Leicester). Dipole length 5 m, rope length 5 m, sampling rate 2 Hz.

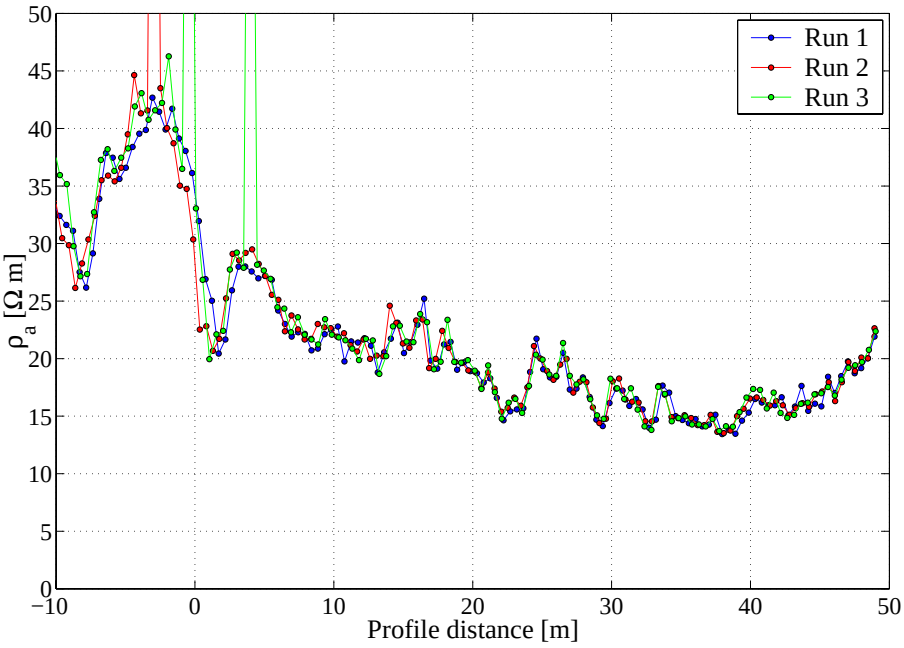

Figure 7.11: OhmMapper™ repeatability test: apparent resistivity profiles on grass.

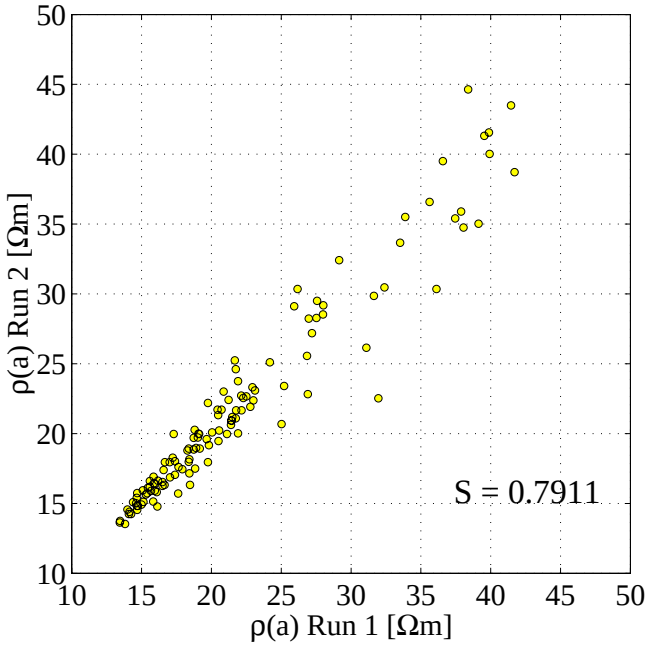

Figure 7.12: Correlation between repeated OhmMapper™ profiles: cross-plot of runs 1 and 2.

centre of the shaft and was measured with 5 m dipoles and 4 m of rope ($l = 5$, $r = 9$). In profile coordinates, the shaft is centred at 19 m, with the concrete cap extending between 14 m and 24 m. The shaft is represented by a large resistive anomaly ($\approx 190\,\Omega$m), surrounded by a "halo" of extremely low apparent resistivities ($\leq 2\,\Omega$m). The spatial wavelength of this anomaly is slightly larger than the surface extent of the cap. The background material, likely to be made ground, has an average resistivity of approximately 35–40 Ωm. The profile is almost free of noise, except for some outliers similar to those discussed above. No obvious difference in character can be observed for the transition between the two surface materials.

Dirt track. A profile recorded on a dirt track over some suspected underground storage tanks is shown in Figure 7.9. The track is situated on a site owned by British Gas at Aylestone Road, Leicester. While parts of the profile are of good quality (beyond 60 m), the majority of the dataset is buried in high-amplitude noise. The USTs are expected to be located in the first half of the profile (0 to 40 m). Some variation in background resistivity appears to be present in that section, but the intensity of the corresponding anomalies cannot be accurately determined without further processing.

Tarmac road. Finally, Figure 7.10 shows a profile recorded on a stretch of tarmac road. The road is also part of the British Gas site at Aylestone Road, Leicester. The data obtained on this type of surface have slightly different properties. High amplitude features are no longer composed of individual spikes, but may now comprise a sequence of several samples. Tarmac data recorded with the OhmMapper™ appear to have a higher variance, with apparent resistivities covering a wider range of values (0.5–650 Ωm). However, it cannot be ruled out completely that the observed response is biased by electromagnetic coupling with metallic conductors (e.g. services, reinforcements). On-road surveying with the OhmMapper™ is generally not without difficulty because of the sometimes uneven running of the towed array due to diminished lateral guidance and mechanical friction on tarmac or concrete.

7.2.1.2 Repeatability

A series of repeatability tests was carried out in order to assess the consistence of repeated resistivity measurements with the OhmMapper™. Figure 7.11 shows an apparent resistivity profile on grass, for which data were repeatedly acquired in three consecutive runs. The three resulting profiles were superimposed on each other and data from different runs are represented by different colours.
Good consistency between the individual datasets is observed. The results suggest that not only large features such as the resistive anomaly at the beginning of the profile (centred around -3 m) are reproduced, but also small structures with higher wavenumbers such as those between 12 m and 35 m. Even features supported only by a single datum point (e.g. at 27 m) appear to be repeatable. Figure 7.12 shows a scatterplot for the apparent resistivities observed in Runs 1 and 2, confirming the good correlation between the two datasets. The

correlation coefficient for these two runs is 0.7911. Agreement exists between consecutive runs despite the expected inaccuracies in positioning the array. This is an important observation since it is unlikely that a towed instrument will follow exactly the same track on the ground when a survey line is repeated.

7.2.2 CORIM™

The CORIM™ is a 6-channel instrument based upon capacitive plate sensors. In its default configuration, an equatorial array comprising one transmitter dipole and six receiver dipoles, is pulled along the ground by a towing vehicle. Plate-wire sensors are mounted on wing-shaped plastic mats together with the transmitter or receiver units. The dipoles have a flexible mechanical connection, so that the array can follow a curved tow path. The array is designed with a separation of 1 m between each dipole (cf. Figure 4.7), so that the separation between consecutive receivers and the transmitter ranges from 1 m (Rx 1) to 6 m (Rx 6). The dipole length is 1.5 m. With this array design, the maximum effective depth z_{eff} of the CORIM™ system is approximately 2.3 m (Table 7.1). The receiver at the front end of the array has the longest offset and is attached to a small trailer carrying a 12 V battery and a control unit connected to a laptop PC. The transmitter is located at the rear end of the array to avoid cross-talk on the wiring between receivers and the control unit.
The transmitter operates at a frequency of 12 kHz and can generate output currents ranging from 2 mA to 8 mA. The current is user-selectable according to field conditions and is regulated to maintain a constant level. The current setting must be manually altered in the control software. Potentials at the receiver dipoles are measured by means of differential amplifiers, for which a reference potential is obtained by a galvanic connection to ground. For this purpose, the receiver unit is connected to the metallic connectors between the mats which have direct contact with the ground surface. A/D conversion is performed at the receiver units and data from all six channels are sent to the control box and transferred to the PC, where data are stored and graphically displayed during acquisition. Data can be sampled at user-selectable intervals between 0.2 m and 2 m. The distance measurement is realised by an odometer mounted on the trailer and attached to one of its wheels. System tests have shown that satisfactory data quality at the minimum sampling interval of 0.2 m can only be achieved at extremely low speeds smaller than 1 km/h. At average speeds of 2.5 km/h the minimum sampling interval that can be employed is 0.3 m. Pulling the instrument with a Land Rover in first gear at low transmission ratio was found to provide the best results.

7.2.2.1 Data quality

The CORIM™ system was tested in a variety of environments to assess the data quality under different survey conditions. Typical apparent resistivity profiles recorded during those tests are shown in Figures 7.15–7.19. Data were acquired on all six receiver dipoles simultaneously, i.e. for separations of 1 m to 6 m. Apparent resistivities are plotted at the respective array mid-points.

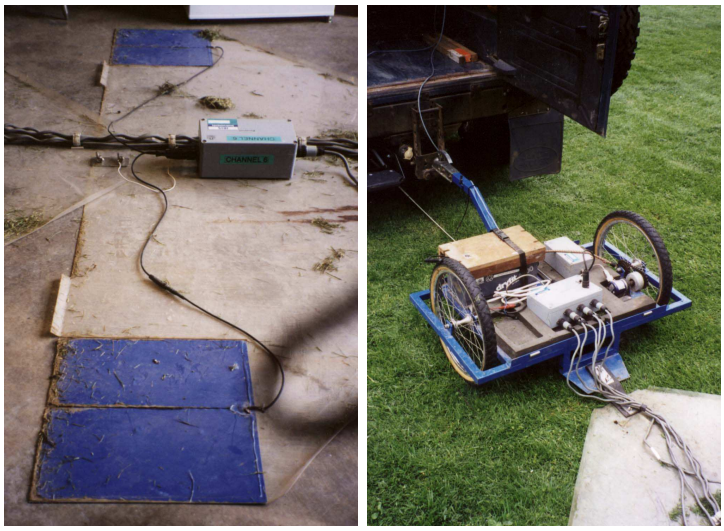

Figure 7.13: Components of the CORIM™ system. Left: receiver dipole; right: trailer with control unit, battery and odometer.

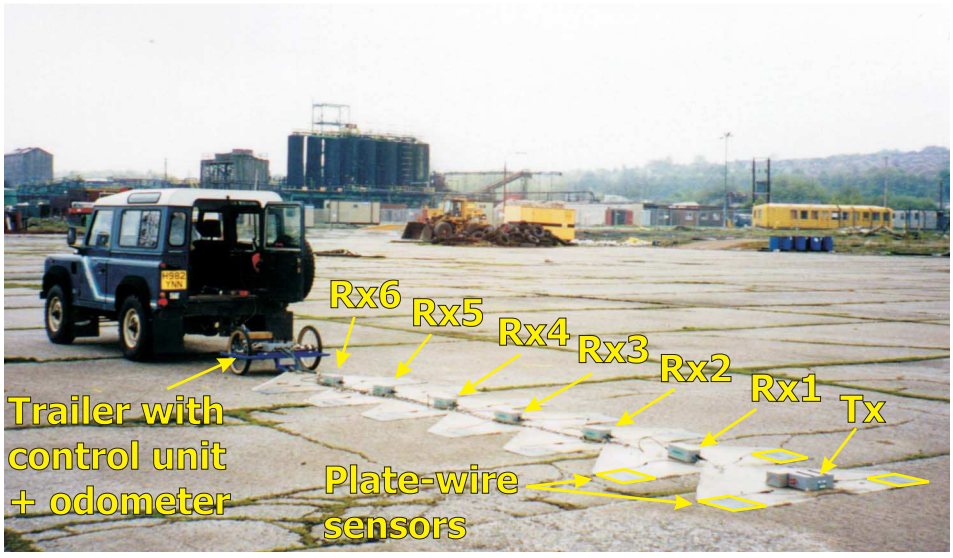

Figure 7.14: The CORIM™ system in field operation.

Receiver	l [m]	r [m]	n	z_{eff} [m]
Rx 1	1.5	1.0	0.667	0.45
Rx 2	1.5	2.0	1.333	0.86
Rx 3	1.5	3.0	2.000	1.21
Rx 4	1.5	4.0	2.667	1.58
Rx 5	1.5	5.0	3.333	1.96
Rx 6	1.5	6.0	4.000	2.33

Table 7.1: Dimensions of the CORIM™ system and effective depths of investigation.

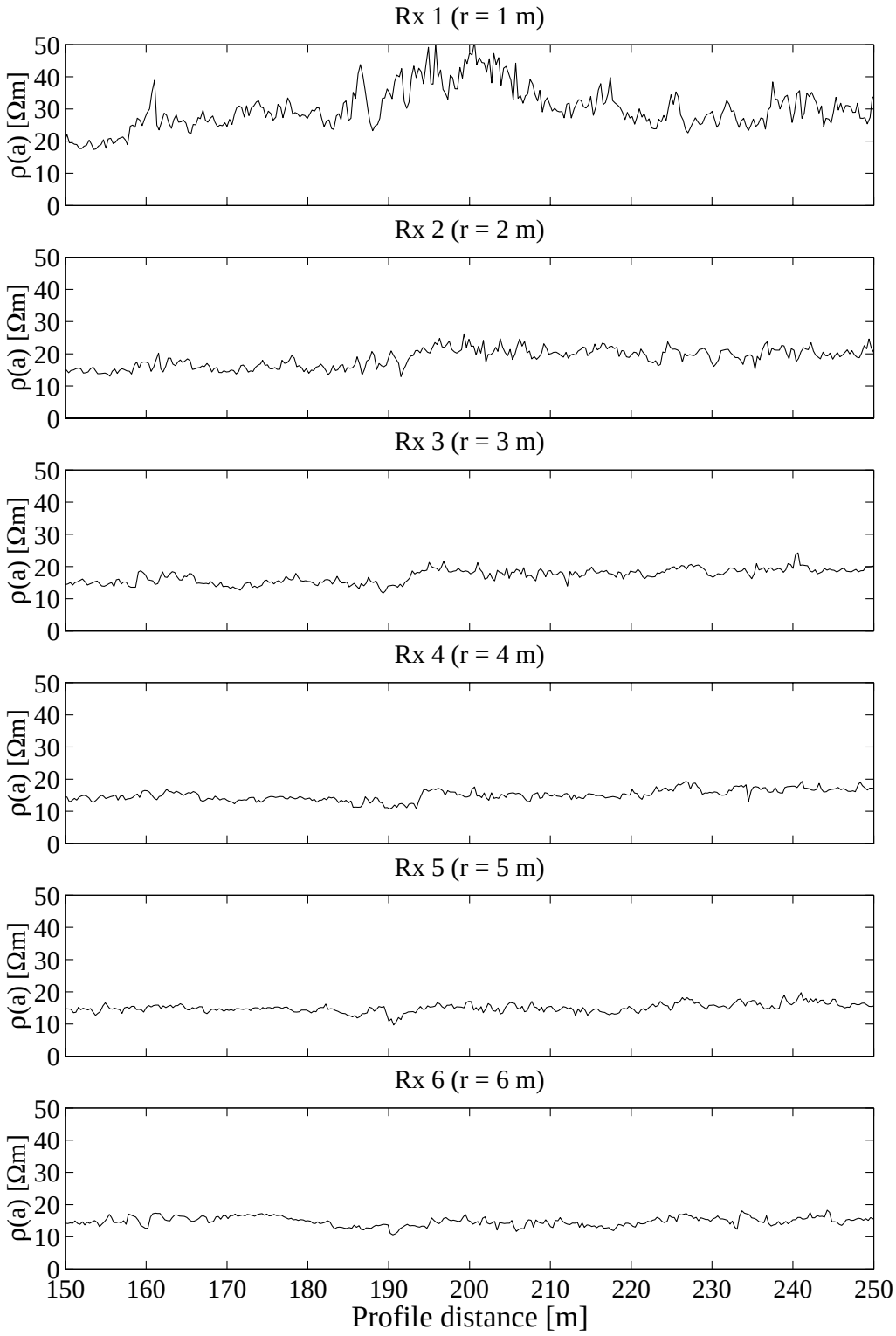

Figure 7.15: CORIM™ apparent resistivity profile on grass (BGS test site). Dipole length 1.5 m, separations $1 \ldots 6\,\mathrm{m}$, sampling interval 0.3 m.

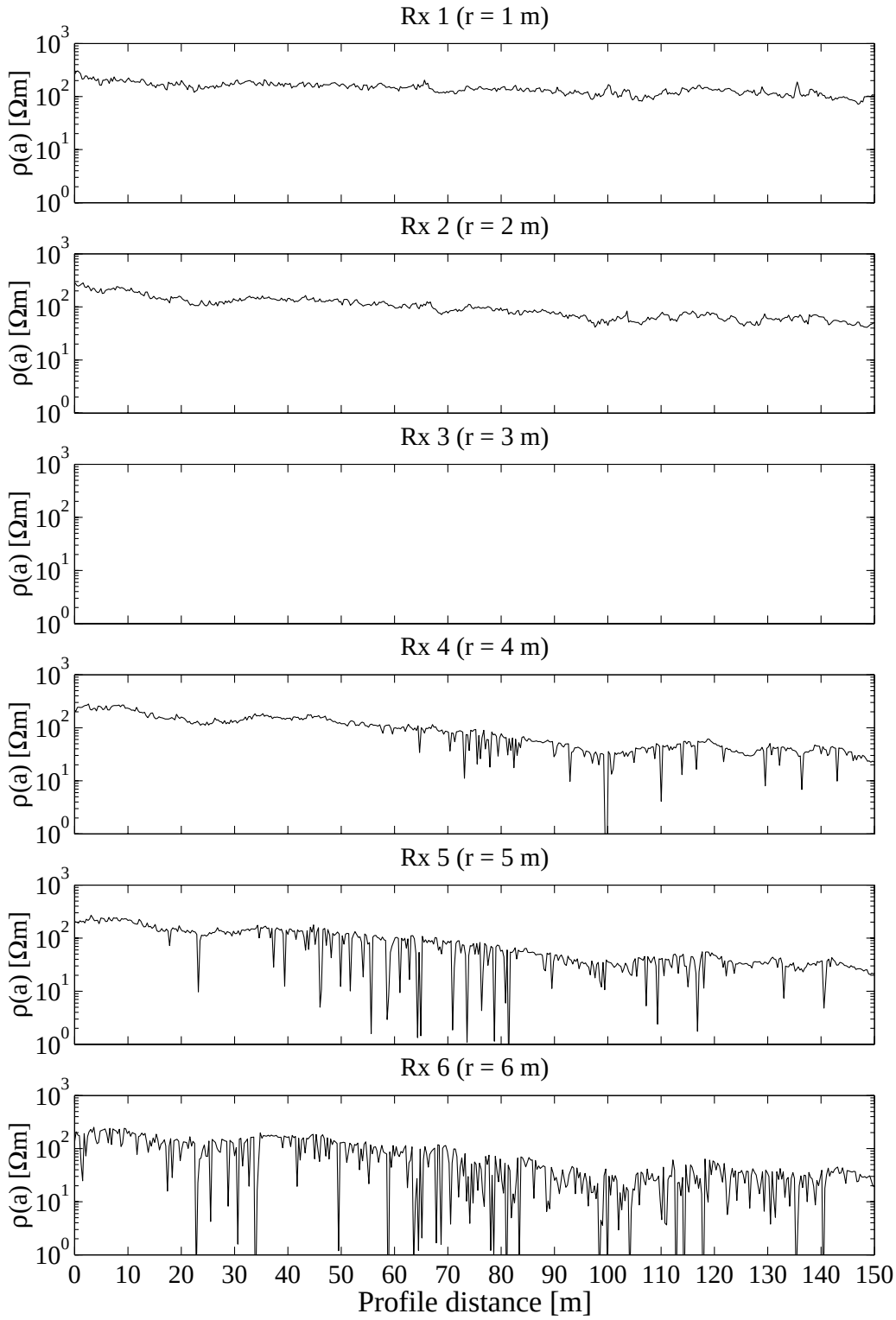

Figure 7.16: CORIM™ apparent resistivity profile on grass affected by towing noise (Chetwynd Barracks training site). Dipole length 1.5 m, separations $1 \ldots 6\,\mathrm{m}$ (Rx 3 non-operational), sampling interval 0.3 m.

A sampling interval of 0.3 m was used throughout, i.e. the resolution of the apparent resistivity profiles is close to the maximum that can be achieved with this instrument.

Grass. The first example (Figure 7.15) was recorded on the test site at BGS headquarters in the same area and under similar conditions as previously described (cf. Section 7.2.1). Apparent resistivity data from a 100 m profile are shown, with the shortest separation (Rx 1, $r = 1$ m) plotted in the top panel and the longest separation (Rx 6, $r = 6$ m) in the bottom panel. Except for the shortest separation, all profiles show little variation in ρ_a, reflecting the relatively homogeneous ground on large parts of the site. The average apparent resistivity observed is found to be decreasing slightly with increasing separation. The anticipated background resistivity level of 20 Ωm is observed on Rx 2 and Rx 3. Receivers 4, 5 and 6 detect gradually lower values, with the average ρ_a at Rx 6 being approximately 15 Ωm. In contrast to the longer offsets, data from Rx 1 ($z_{\text{eff}} = 0.45$ m) show significantly more variation, with observed resistivities ranging from approximately 20 Ωm to 50 Ωm. This variation is likely to be due to the shallow depth of investigation of Rx 1. At depths smaller than 0.5 m, the electrical properties of the subsurface are likely to be inhomogeneous due to variations in soil compaction, water content and other pedological parameters. No obvious contamination by towing noise can be seen in the data. The variation in ρ_a over distances of the order of the sampling interval (rarely more than 10 Ωm between adjacent samples) seems genuine, especially for the shorter array separations. At the longest separation, the data appear to have the smallest variance. These observations are in agreement with expectations for an earth response where long-offset arrays should see smoother data with less high-wavenumber variations. However, towing noise was frequently observed on other occasions. Long separations (Rx 5, Rx 6) and, surprisingly, also the shortest offset (Rx 1) were most likely to be affected. In contrast to what was observed for the OhmMapper™, the characteristic towing noise observed with the CORIM™ consisted of low resistivity spikes ("dropouts"). An example is given in Figure 7.16, which shows a profile recorded on grass at the Chetwynd Barracks training site, Nottingham. There, receivers 4, 5 and 6 were severely affected by this characteristic noise.

Grass/concrete. Figure 7.17 shows apparent resistivity profiles recorded over a concealed void at the EIGG test site at the University of Leicester. As the survey line is only 35 m long, individual datum points were marked with a coloured symbol to clarify the true resolution. The void is centred at a profile distance of 35 m and is represented by a sealed plastic tank with a volume of 0.12 m^3, buried at 0.3 m dept under a concrete slab. In the direction of the survey line, the slab is 2 m wide. The remainder of the test site is grassland, with a surface layer of topsoil approximately 0.3 m thick, grading down into Boulder Clay. The clay background is associated with resistivities of approximately 30 Ωm (Rx 2–Rx 6), while the topsoil is more resistive at 40–50 Ωm (Rx 1). The target is associated with a distinct anomaly observed at

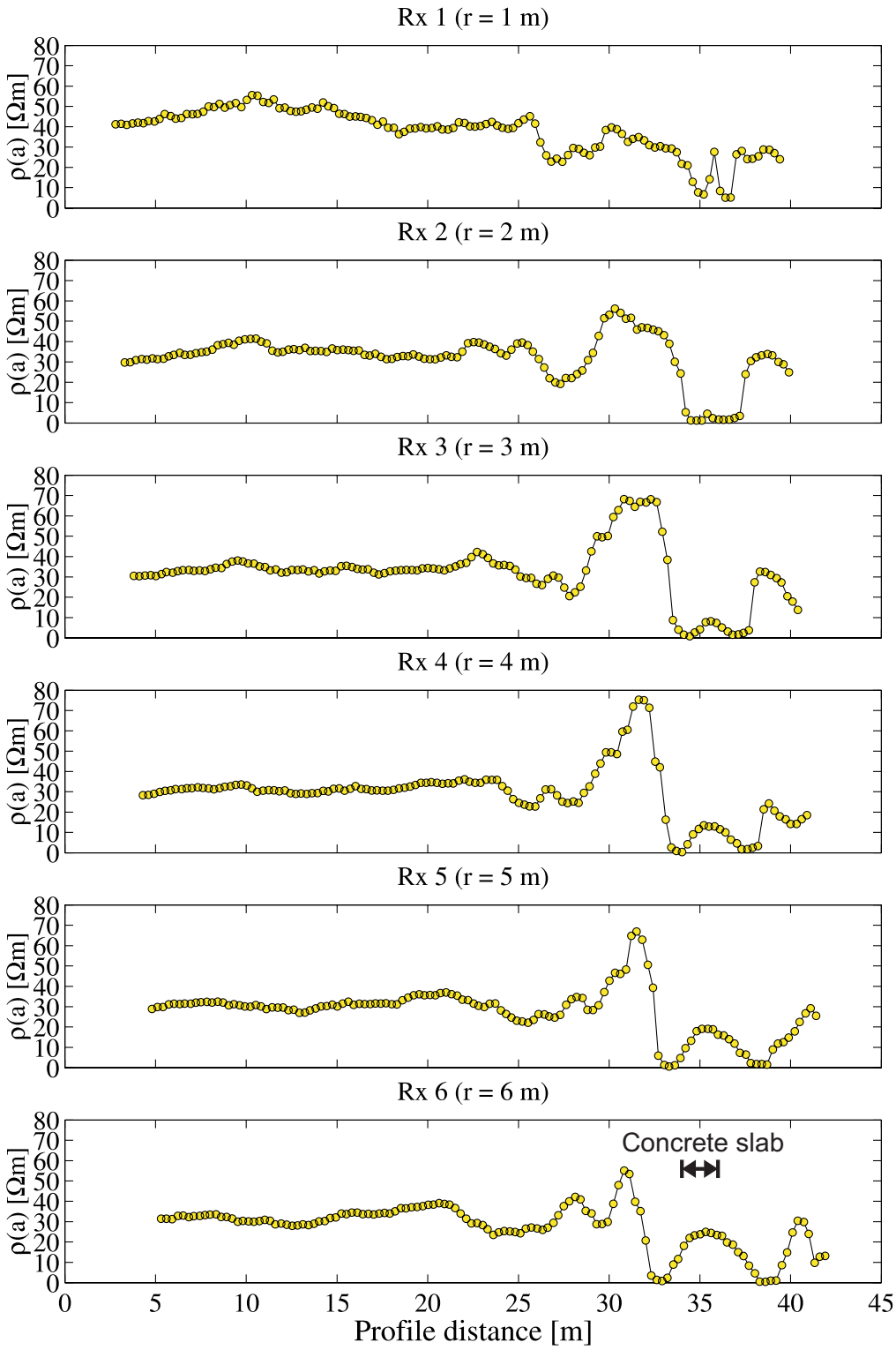

Figure 7.17: CORIM™ apparent resistivity profile on grass/concrete over a void (EIGG test site). Dipole length 1.5 m, separations $1 \ldots 6$ m, sampling interval 0.3 m.

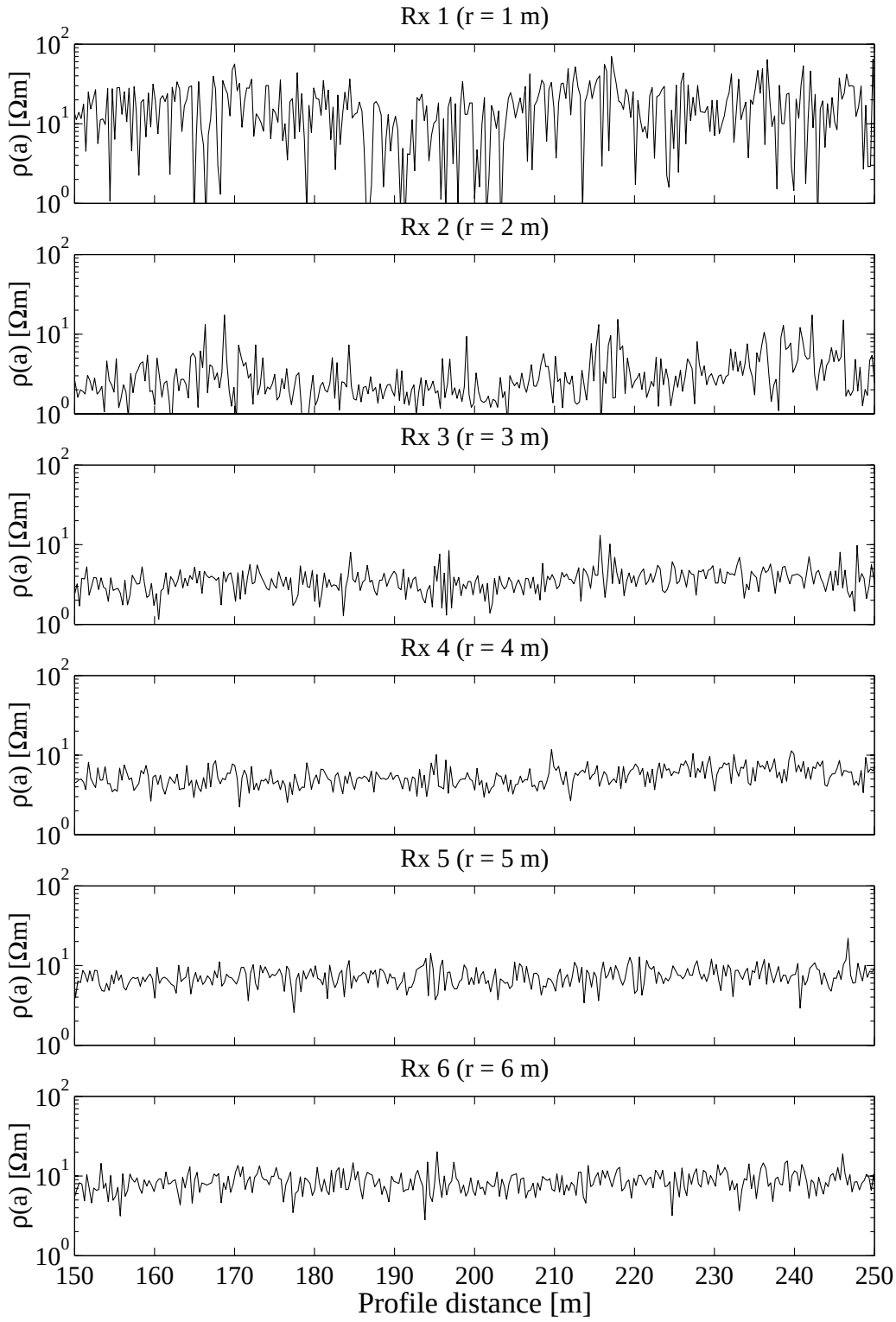

Figure 7.18: CORIM™ apparent resistivity profile on a tarmac road (BGS site). Dipole length 1.5 m, separations $1 \ldots 6$ m, sampling interval 0.3 m.

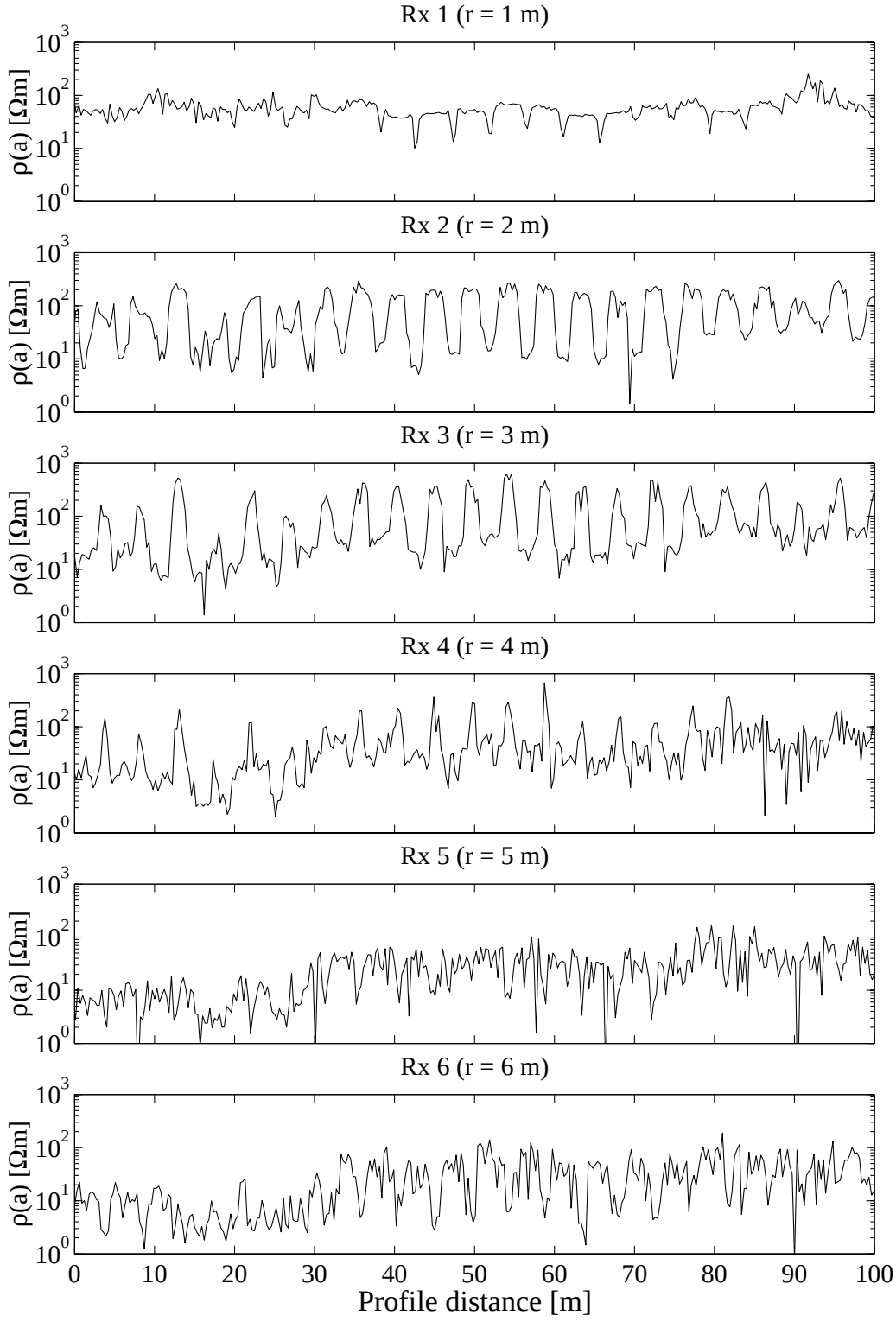

Figure 7.19: CORIM™ apparent resistivity profile on reinforced concrete (Avenue coking plant, Chesterfield). Dipole length 1.5 m, separations $1 \ldots 6$ m, sampling interval 0.3 m.

all six separations. The anomaly is symmetric and "W"-shaped, with the two minima reaching very low resistivities $< 5\,\Omega$m. The centre of the anomaly is a local maximum, but its resistivity is smaller than the background resistivities observed in the vicinity of the target. The edges of the target are associated with maxima in ρ_a. The spatial wavelength of the anomaly is greater than the lateral extent of the target and grows with increasing dipole separation. Again, the dataset is apparently unaffected by towing noise.

Tarmac road. The next example (Figure 7.18) was recorded on a stretch of tarmac road at the BGS site. Data quality is poorer than on grass in the sense that road data have a much higher variance (n.b. the logarithmic scale). Quite surprisingly, the highest variance is observed for Rx 1, and variance reduces gradually on consecutive receivers. Apparent resistivities are comparatively low ($\approx 20\,\Omega$m on Rx 1, $> 10\,\Omega$m on Rx 2–6), which may indicate that the data reflect the properties of the subbase rather than the road surface. Data of this quality would have to undergo rigorous processing before it could be used for quantitative interpretation such as inverse modelling.

Concrete. Finally, a profile recorded on an area covered with large segments of concrete is shown in Figure 7.19. The area is part of the derelict Avenue coking plant near Chesterfield. The concrete slabs are approximately 5 m × 9 m in size, of significant thickness (30–50 cm) and reinforced. The area is thought to be underlain by waste products from the production process. Again, the data are of high variance, but in this instance the variation appears to be caused by the nature of the concrete slabs. A periodic signature with a wavelength corresponding to the width of the individual segments is observed on all channels, the signal being most prominent on Rx 2 and Rx 3. This variation in apparent resistivity is obviously associated with the reinforcement, which is likely to be interrupted at segment boundaries. Such data should be treated with caution as they are potentially affected by EM coupling noise.

7.2.2.2 Repeatability

The consistency of measurements with the CORIM™ system was assessed in a series of repeatability tests. Figure 7.20 shows apparent resistivity profiles recorded at the EIGG test site in Leicester on a survey line close to the one discussed earlier (Figure 7.17). Profiles resulting from two consecutive runs were superimposed onto each other, with each run represented by markers of a different colour. A detailed view of this dataset for Rx 2 only is shown in Figure 7.21. The two datasets are very consistent, however some discrepancies are notable. The absolute level of ρ_a is well reproduced except for some isolated parts of the profile. Figure 7.22 shows a scatterplot for the apparent resistivities observed in the two consecutive runs, confirming the good correlation between the two datasets. The correlation coefficient for the two runs is 0.9646.
Sometimes small high-wavenumber features observed in one of the runs are not reproduced by the other (cf. Figure 7.21). Such inconsistencies are likely to be due to inaccurate positioning of the array on the survey line. It was found that

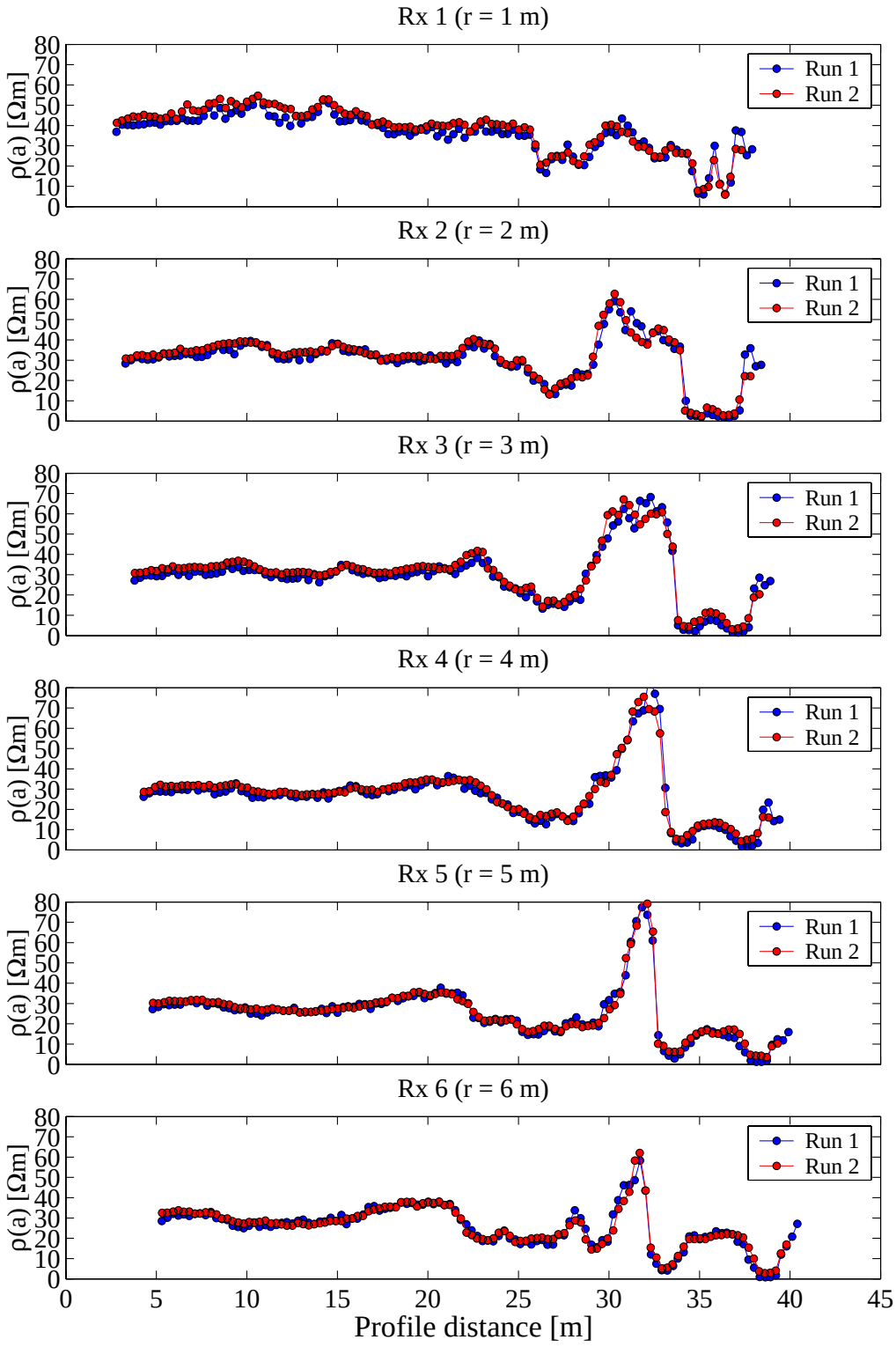

Figure 7.20: CORIM™ repeatability test: apparent resistivity profiles over a void (EIGG test site). Sampling interval 0.3 m.

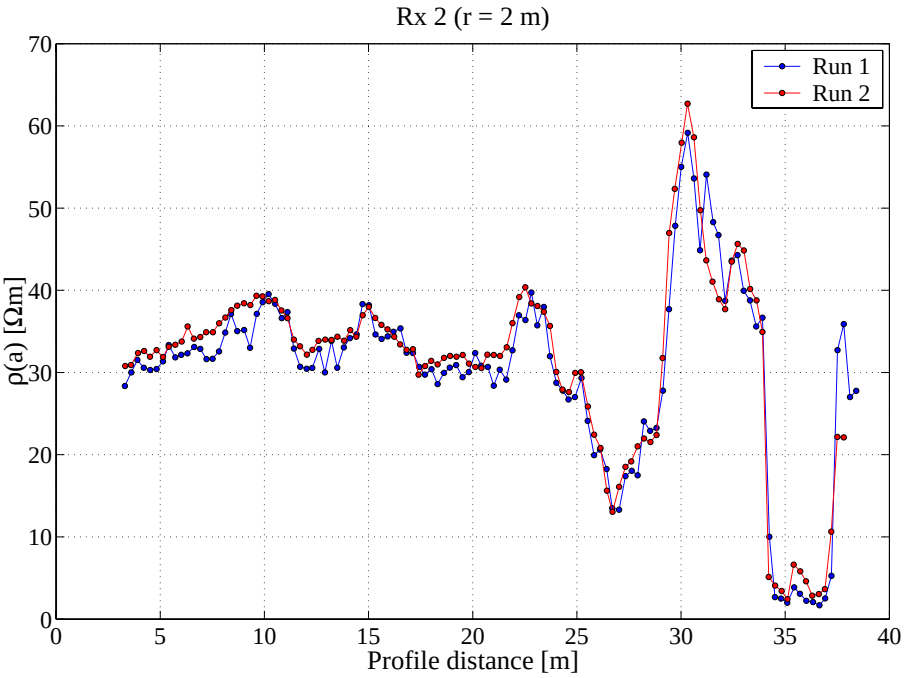

Figure 7.21: Detail of Rx 2 ($r = 2\mathrm{m}$) for the CORIM™ repeatability test. Sampling interval 0.3 m.

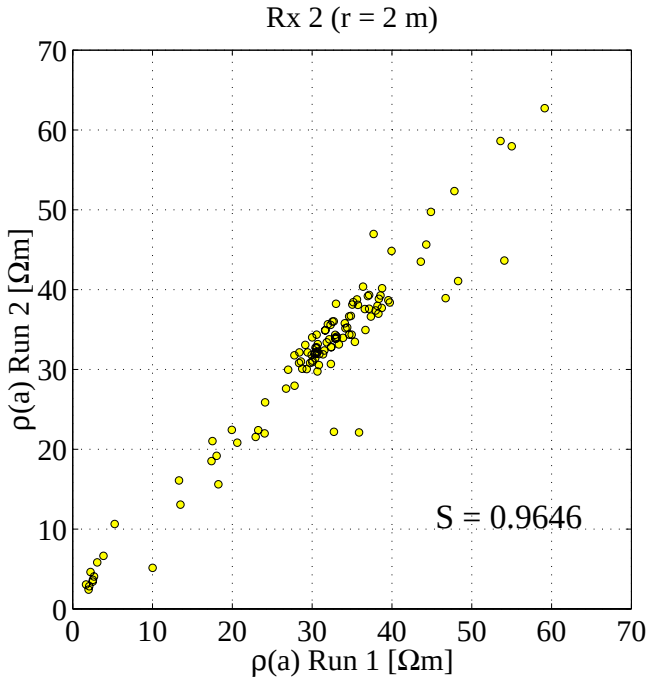

Figure 7.22: Correlation between repeated CORIM™ profiles for Rx 2.

visual navigation with the towing vehicle allowed for an accuracy of ±10 cm with respect to the intended survey line. Such navigational errors can explain the observed discrepancies in the apparent resistivity data.

7.2.3 BGS CRI system

In contrast to the commercial instruments, the BGS CRI system can be used to examine the properties of the complex transfer impedance obtained from dynamic measurements. Such data are unavailable in the open literature and are shown here for the first time. For the towed-array setup of the CRI system, an equatorial dipole-dipole configuration was chosen due to its compactness in combination with a superior depth of investigation. Transmitter and receiver dipoles have a length of 1.5 m. So far, the system has been operated with up to three receivers synchronously. Such an arrangement is sufficient to demonstrate the principles of multi-channel acquisition, but development is still ongoing and it is planned to incorporate additional channels. The receiver dipoles were arranged at approximately regular distances on a logarithmic scale. The default separations of the BGS CRI system together with the corresponding depths of investigation are shown in Table 7.2.

Receiver	l [m]	r [m]	n	K_{DC}	z_{eff} [m]
Rx 1	1.5	1.6	1.067	18.585	0.71
Rx 2	1.5	4.0	2.667	197.365	1.58
Rx 3	1.5	8.0	5.333	1467.364	3.10

Table 7.2: Dimensions of the BGS CRI system and effective depths of investigation.

Plate-wire combinations are used as capacitive sensors, mounted onto thin polyethylene sheets. The sheets, each of which comprises one dipole, are then interconnected by spacers of variable length. The sheets serve two purposes. Firstly, they provide a rigid structure and mechanical support in order to maintain a constant array geometry while the system is in motion. Secondly, their use minimises any changes in separation between the plate sensors and the ground surface (i.e. the array elevation in electrostatic terms). The sheets are cut into the shape of delta wings to minimise resistance against obstacles on the ground and to allow easier turning of long arrays. The transmitter is located at the rear end of the array to avoid interference. It operates at a default frequency of 14.2 kHz and output currents between 6 mA and 10 mA were found to be practical on a variety of surfaces. A small trolley accommodates the transmitter unit and batteries, thus minimising mechanical stress on the transmitter wing. Amplifiers and filter units are mounted on the receiver wings. No ground reference is necessary due to the floating measurement principle. The measured potentials together with the measured injection current are transferred to a receiver unit inside the towing vehicle, where they are digitised and stored on a laptop PC. The acquisition is triggered by an odometer attached to the towing vehicle. A typical sampling distance of 5 cm was used for most surveys, which

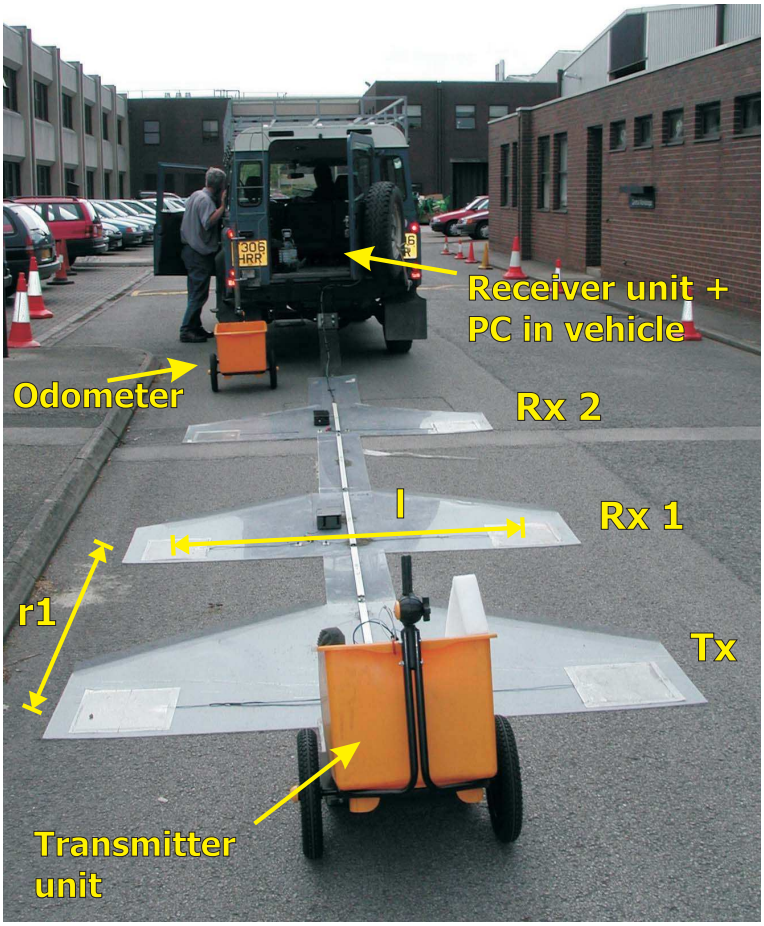

Figure 7.23: The BGS CRI system in field operation on a tarmac road using two receivers. ©NERC copyright.

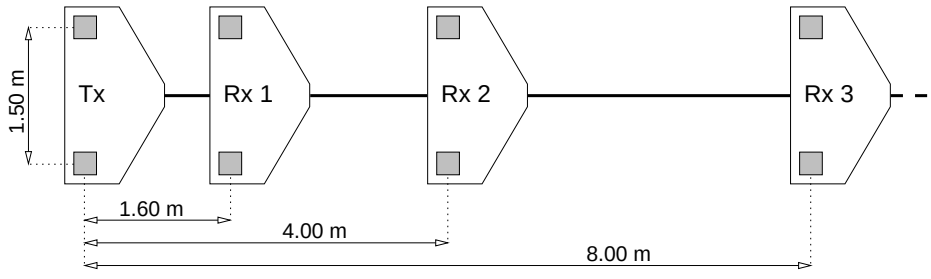

Figure 7.24: Geometry of the BGS CRI system in a towed-array setup with three receivers.

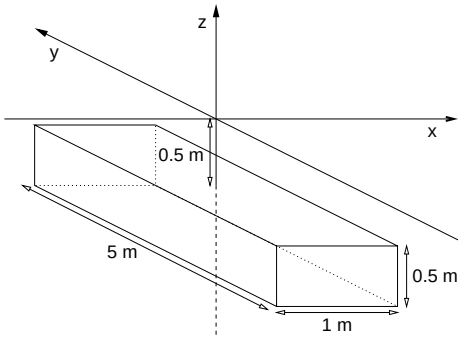

Figure 7.25: Geometry of the shallow concrete target at the BGS test site.

corresponds to a resolution 5–6 times higher than what is possible with commercial equipment. Such sampling intervals were found to be compatible with typical towing speeds of 2.5 km/h and time constants of the order of 10–30 ms for the phase-sensitive signal detection.

7.2.3.1 Data quality

Tests were carried out in a variety of environments to examine the dynamic properties of the transfer impedance and to assess the data quality obtained with the CRI system under different survey conditions. Typical datasets recorded during those tests are shown in Figures 7.26 to 7.30.

Grass. The first example was recorded on grass on the test area at the BGS site in Keyworth over one of two newly constructed artificial targets. This facility had not been available during previous instrument tests. Large blocks of concrete were installed at shallow depth to simulate electrically resistive features such as foundations or voids on a scale suitable for towed CR arrays. The geometry of the target used for this test is shown in Figure 7.25. The concrete block is 5 m long, 1 m wide, 0.5 m thick and is buried at 0.5 m depth. The survey line was orientated perpendicular to the long axis of the target, coincident with the x-axis in the diagram. The centre of the target is located at a profile distance of approximately 5.80 m.
The recorded data are shown in Figures 7.26 and 7.27 for Rx 1 ($r = 1.6$ m) and Rx 2 ($r = 4$ m), respectively. The top three panels (a–c) show the in-phase and quadrature components of the complex transfer impedance together with the alternative interpretation as magnitude and phase. The measured injection current is shown in (d). The apparent resistivity (e) was calculated with Equation (4.42), using the in-phase component of the observed potential in conjunction with the DC formula. The general quality of the raw data is remarkably good, considering the high resolution (≈ 40 samples between each pair of gridlines). Beginning and end of the profile are situated on uniform ground with apparent resistivities between 20 and 25 Ωm. For both offsets, the signature of the resistive concrete target can be recognised near the centre of

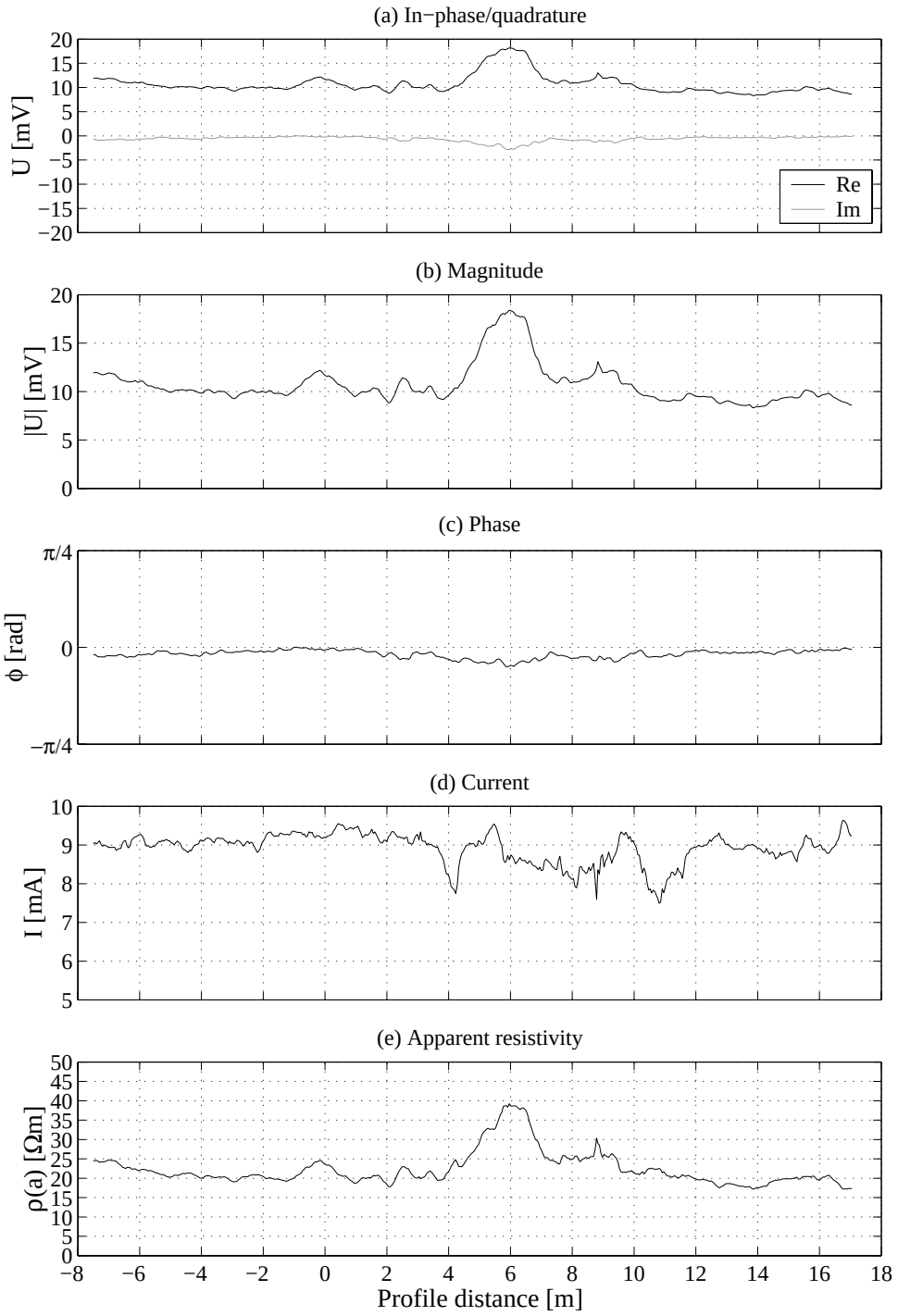

Figure 7.26: CRI apparent resistivity profile on grass (BGS test site), Rx 1 ($r = 1.6\,\mathrm{m}$), dipole length 1.5 m, sampling interval 5 cm. (a) complex potential (in-phase and quadrature), (b) magnitude, (c) phase, (d) current, (e) apparent resistivity.

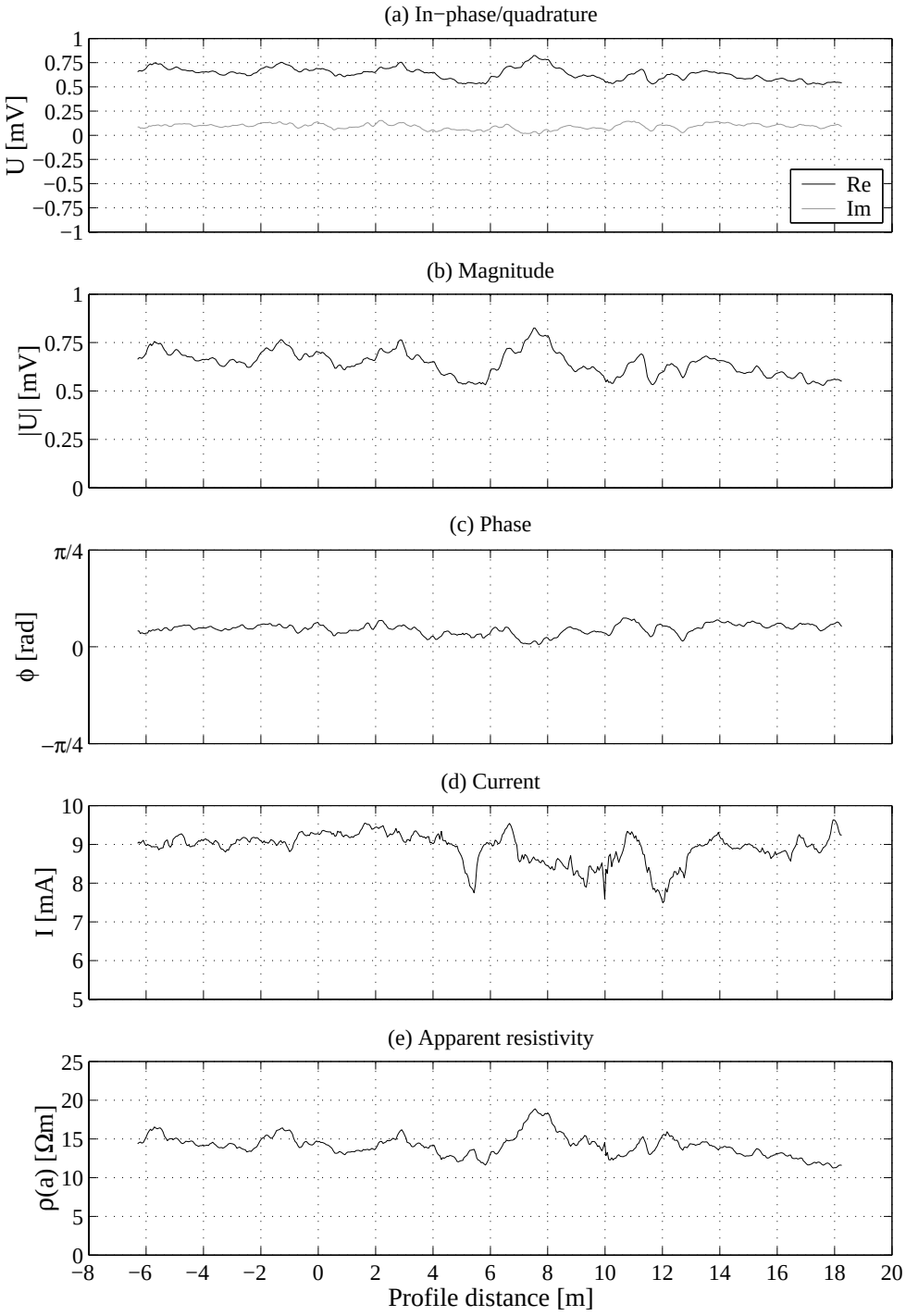

Figure 7.27: CRI apparent resistivity profile on grass (BGS test site), Rx 2 ($r = 4\mathrm{m}$), dipole length 1.5 m, sampling interval 5 cm. (a) complex potential (in-phase and quadrature), (b) magnitude, (c) phase, (d) current, (e) apparent resistivity.

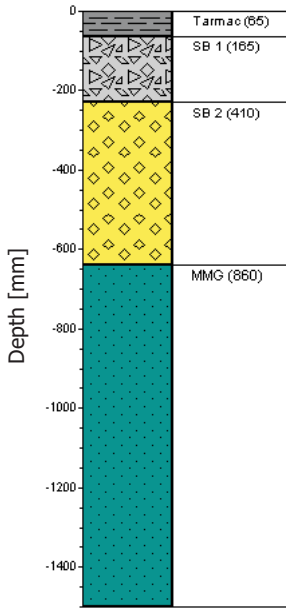

Figure 7.28: Vertical layering of the sub-base of a road at the BGS site. SB1 = sub-base 1; SB2 = sub-base 2; MMG = bedrock (Mercia Mudstone).

the profile. On Rx 1, the maximum in ρ_a centred at 5.80 m reaches a value of approximately twice the background resistivity at 40 Ωm. The signature on Rx 2 is more subtle, mainly because the equatorial array at longer offsets generates weaker, M-shaped anomalies over resistive targets (cf. Chapter 8). The maximum in the in-phase component of the potential is accompanied by a small but significant anomaly in the quadrature component. Over homogeneous ground, the quadrature is close to zero in agreement with expectations.

Tarmac road. Further trials were carried out on a stretch of tarmac road on the BGS site (cf. Figure 7.23). Typical apparent resistivity profiles recorded on that occasion are shown in Figures 7.29 and 7.30. Again, two different dipole separations are considered. Figure 7.29 shows data acquired at $r = 1.6$ m, while those in Figure 7.30 were acquired at $r = 4$ m. The road is known to contain a number of buried services, including sewers and a high-voltage power cable, however the exact location of the features was indeterminate. A schematic cross-section through the structure of the road sub-base is given in Figure 7.28. The short-separation data (Figure 7.29) are of outstanding quality. The transfer impedance is highly dynamic, but has very low variance (a–c). Apparent resistivity values (e) range from approximately 15 Ωm to nearly 300 Ωm, reflecting the complexity of the road as an engineered structure. A number of well-defined anomalies (-0.5 m, 10.5 m, 25.5 m and 27.5 m) are likely to be associated with the services mentioned above. This assumption is supported by the fact that the effective depth of investigation of the short-offset array coincides roughly with the interface between the lower sub-base and the underlying geology (cf. Table

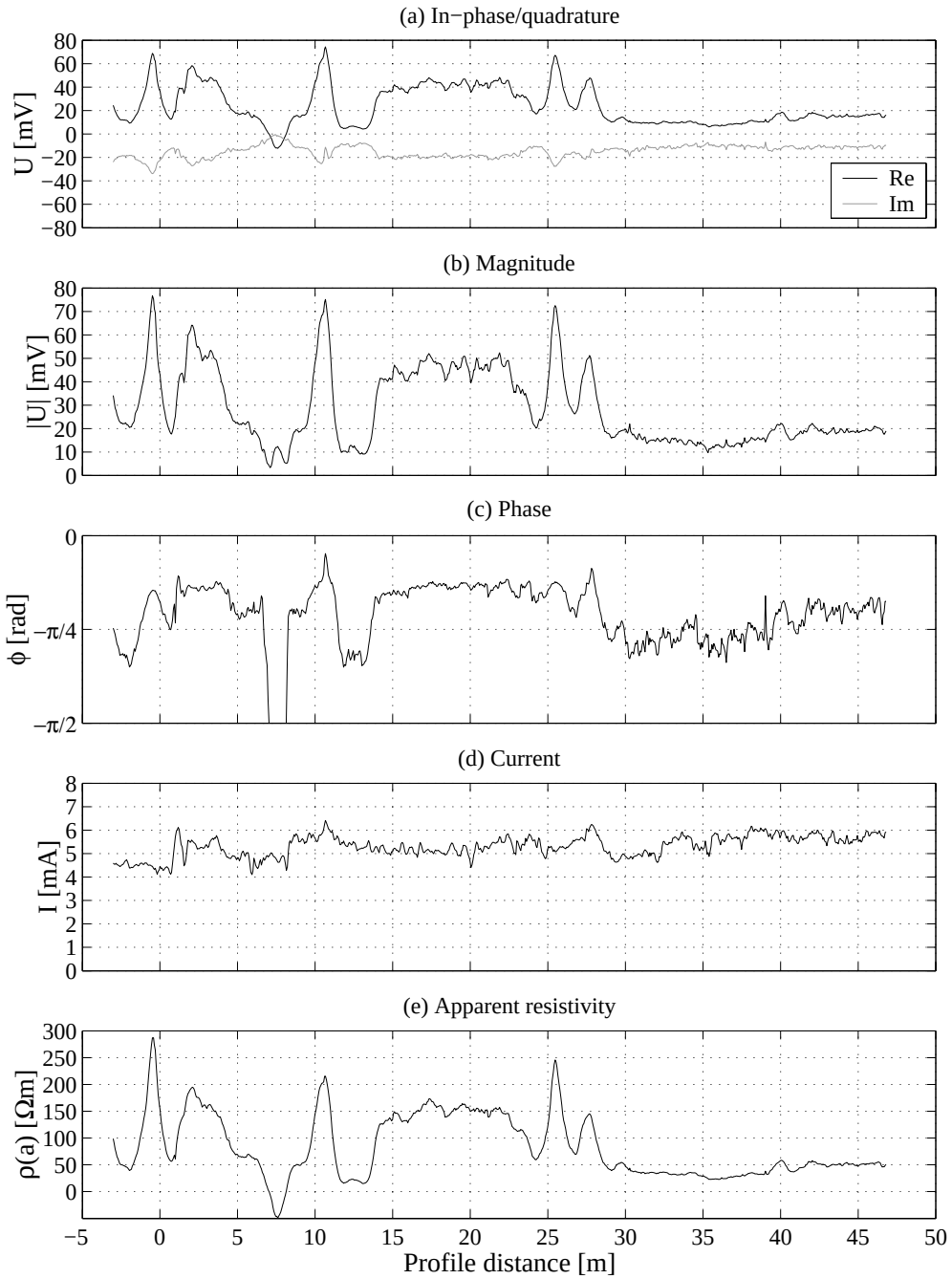

Figure 7.29: CRI apparent resistivity profile on a tarmac road (BGS site), Rx 1 ($r = 1.6\,\mathrm{m}$), dipole length 1.5 m, sampling interval 5 cm. (a) complex potential (in-phase and quadrature), (b) magnitude, (c) phase, (d) current, (e) apparent resistivity.

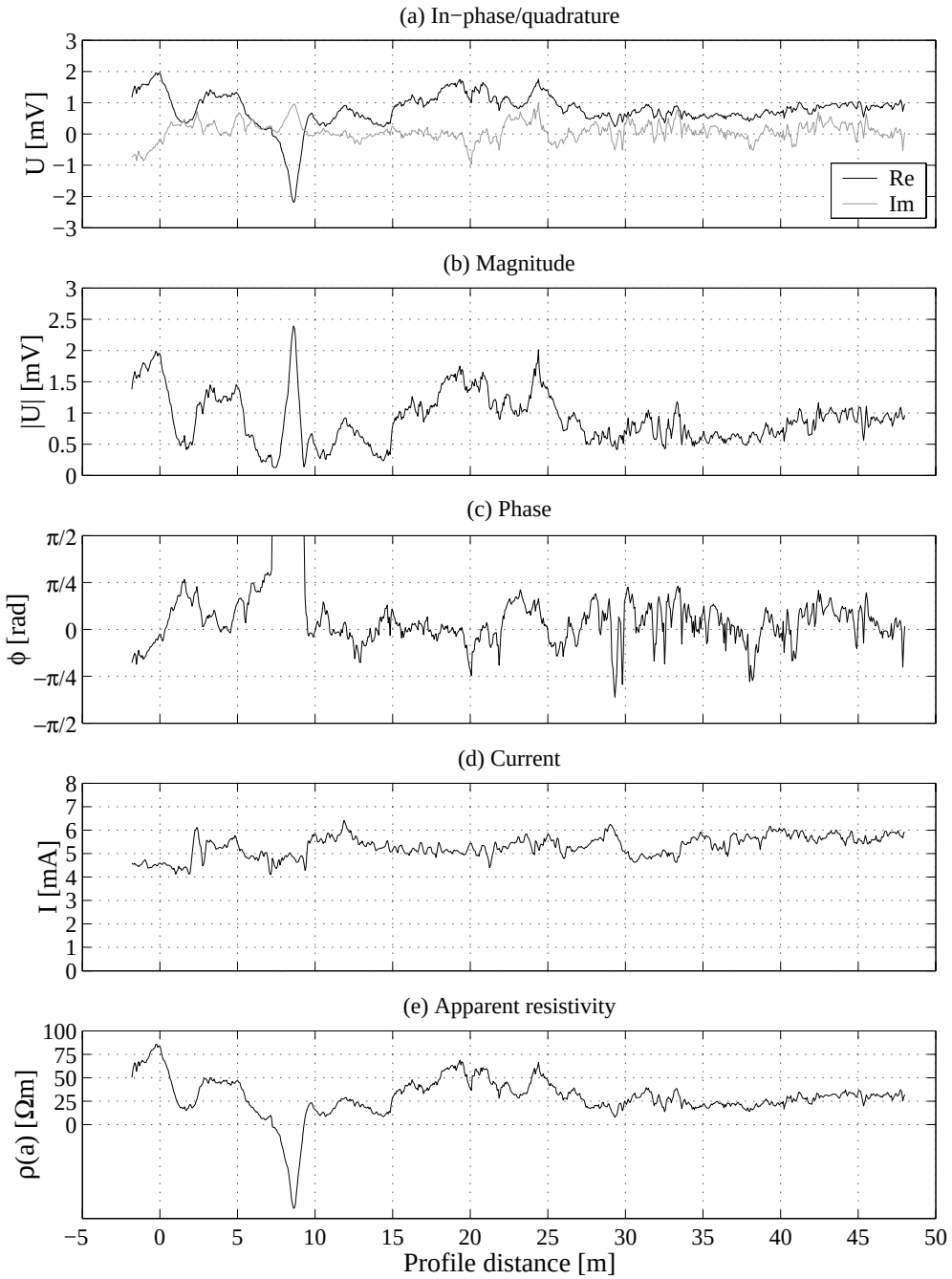

Figure 7.30: CRI apparent resistivity profile on a tarmac road (BGS site), Rx 2 ($r = 4\,\mathrm{m}$), dipole length 1.5 m, sampling interval 5 cm. (a) complex potential (in-phase and quadrature), (b) magnitude, (c) phase, (d) current, (e) apparent resistivity.

7.2). This is a typical burial depth for roadbed services. A feature at 7.5 m, associated with a negative in-phase component (and hence a negative apparent resistivity) is thought to correspond to a crossing power cable. In its vicinity, the response of the CR array is likely to be affected by EM coupling rather than quasi-static current flow. The substantial drop in apparent resistivity between 22 m and 30 m may suggest a change in the composition of the sub-base. This is supported by visual evidence on the road surface, where a boundary between two sections of tarmac was noticed.
The long-offset data (Figure 7.30) are less dynamic and have a slightly higher variance. Some features that were observed in the short-offset data can still be recognised, including the anomaly at 7.5 m, which is now associated with an even stronger negative response (Figure 7.30e).

7.2.3.2 Repeatability

Repeatability tests were carried out to assess the consistency of measurements undertaken with the CRI system. Figure 7.31 shows apparent resistivity profiles of two consecutive runs on a tarmac road on the same survey line as the one shown previously in Figures 7.29 and 7.30. The agreement between the two runs is quite remarkable. Scatterplots for the apparent resistivities observed in these two runs (Figure 7.32) confirm the high degree of correlation between the datasets. The correlation coefficients for the two runs are 0.9976 for Rx 1 and 0.9858 for Rx 2.

7.2.3.3 Comparison with DC resistivity

Finally, an experiment was undertaken to directly compare dynamically measured CRI data with conventional DC resistivity profiles. A DC resistivity traverse was acquired over the shallow concrete target on the BGS test site on the same survey line that had been used for the CRI survey (cf. Section 7.2.3.1). A conventional multi-electrode DC resistivity acquisition system was employed for this purpose. In order to simulate the equatorial geometry used with the CRI system, two rows of electrodes with a separation of 1.5 m were installed parallel to the survey line. A unit electrode spacing of 0.4 m was used as a common divisor of both CRI separations (Rx 1 = 1.6 m, Rx 2 = 4 m). The acquisition system was then programmed to measure apparent resistivities consecutively across pairs of dipoles with constant separation along the survey line. Thus, resistivity traverses for two equatorial dipole-dipole arrays with $l = 1.5\text{m}$ and $r_1 = 1.6\text{m}$, $r_2 = 4\text{m}$ were obtained at a sampling interval of 0.4 m. Such coverage is already unusually dense for typical site investigation surveys with DC resistivity, yet the CRI dataset has still a much higher resolution at approximately eight CRI samples per DC electrode spacing.
Figure 7.33 shows the results of the comparison for the short (a) and the long offset (b). Again, the centre of the target is located at a profile distance of approximately 5.80 m. The overall shape of the traverse is identical for both techniques and agreement is observed down to the scale of one DC electrode separation. However, the amount of additional detail contained in the CRI

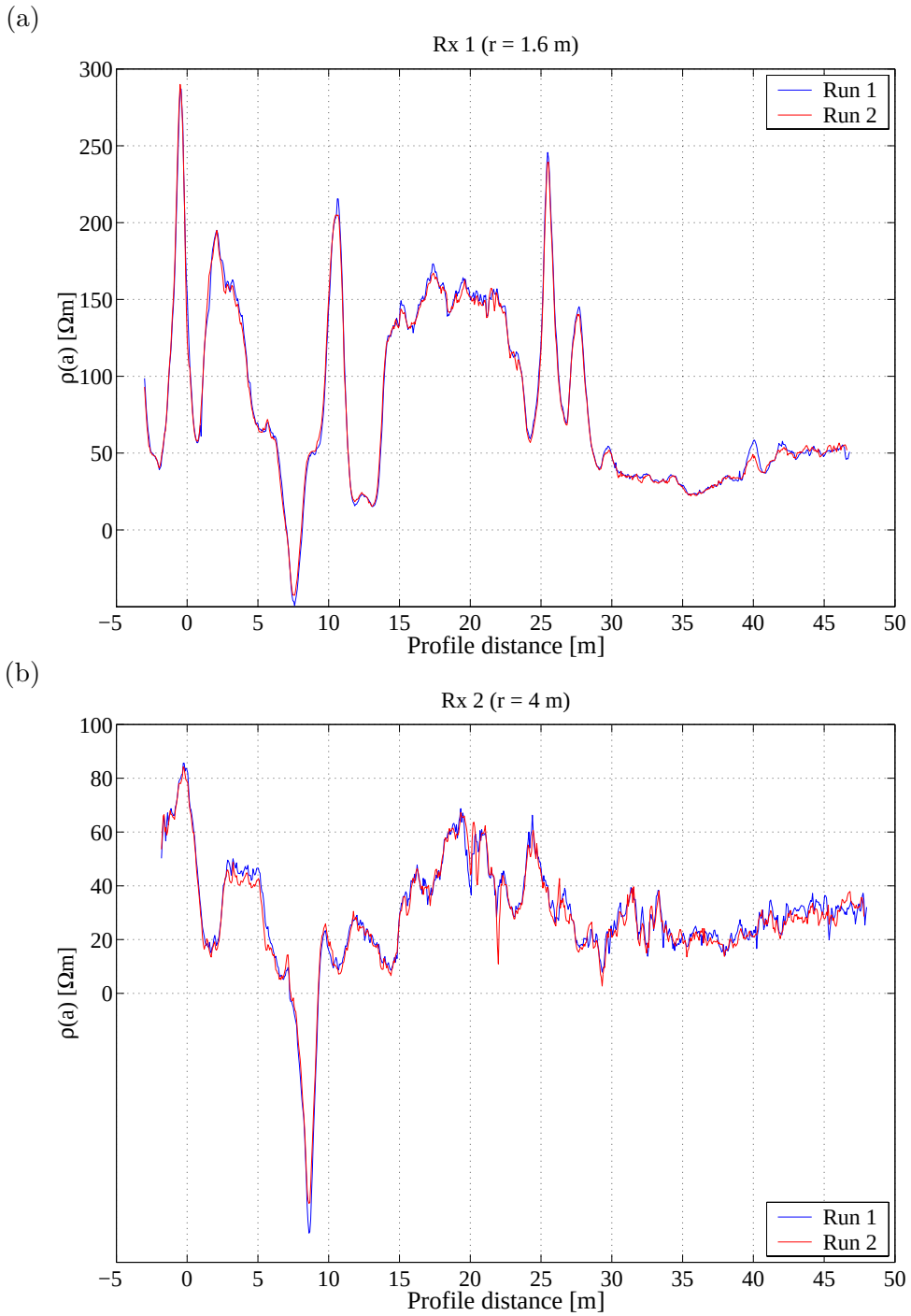

Figure 7.31: CRI repeatability test: apparent resistivity profiles on a tarmac road. (a) Rx 1 (r = 1.6 m); (b) Rx 2 (r = 4 m).

(a)

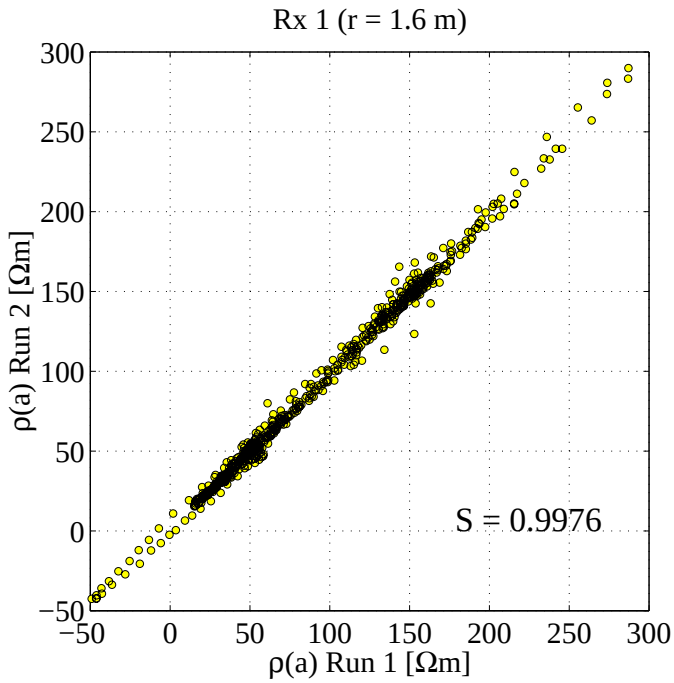

(b)

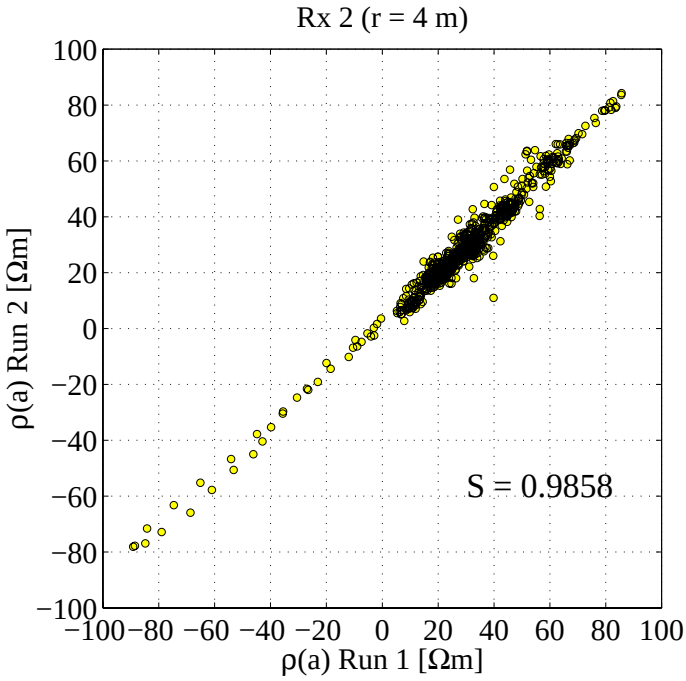

Figure 7.32: Correlation between repeated CRI profiles. (a) Rx 1 (r = 1.6 m); (b) Rx 2 (r = 4 m).

(a)

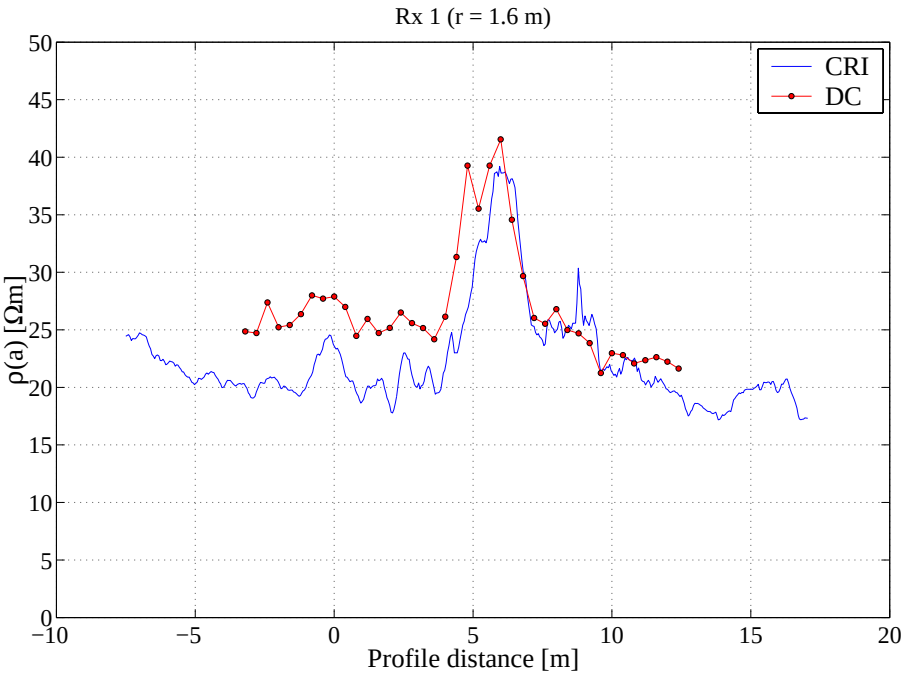

(b)

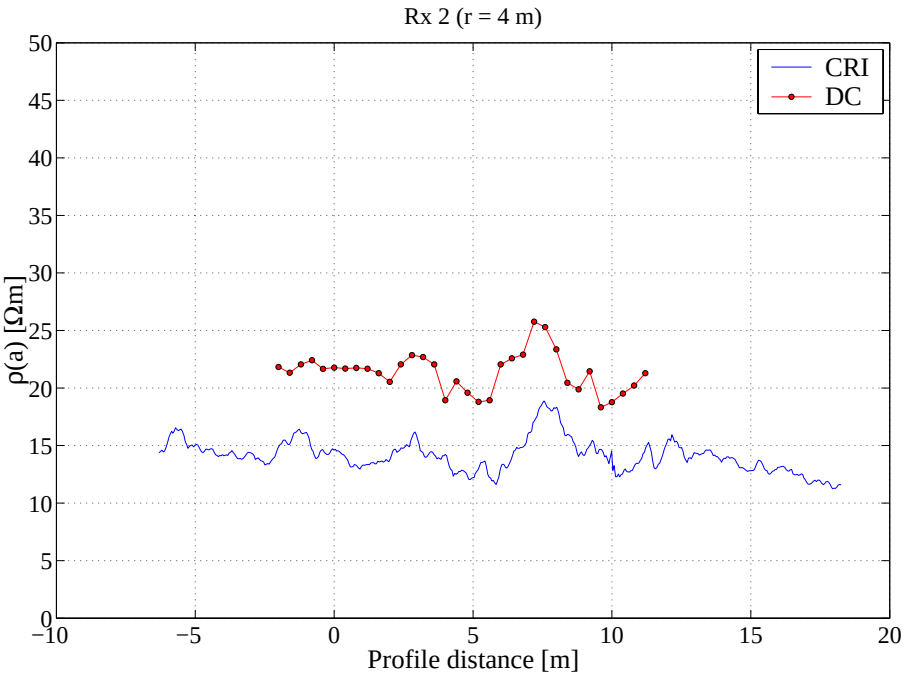

Figure 7.33: Comparison between a CRI profile over the shallow concrete target and the corresponding DC resistivity traverse. (a) Rx 1 ($r = 1.6\,\mathrm{m}$); (b) Rx 2 ($r = 4\,\mathrm{m}$).

profile is obvious. The relative amplitudes between the extrema over the target and the uniform background are found to be consistent for both techniques.

7.3 Basic processing of towed-array CR data

The processing of dynamically acquired CR data must address a number of issues that are not usually problematic in the context of static measurements. The two most important of these are the occurrence of motion-induced noise and levelling errors between consecutive profiles. Despite being generally uncommon in resistivity methods, such effects can be mitigated by the application of data processing techniques well known from other areas of geophysics. In this section, potential problems with data quality in towed-array CR are highlighted and adequate processing techniques presented.

7.3.1 Suppression of motion-induced noise

The examples in the previous section have shown that the operation of towed CR arrays can be affected by motion-induced noise of variable character and intensity. Characterisation of the noise encountered is therefore critical for the design of adequate suppression procedures.

7.3.1.1 Noise characterisation

Towing noise is known to severely affect the dynamic resistivity measurement by conventional DC techniques (Sørensen, 1996). Typical noise observed in Pulled-Array Continuous Electrical Profiling (cf. Section 3.1.5.2) was found to have RMS amplitudes of approximately 60 Ωm, corresponding to a signal-to-noise ratio of 1 over a 60 Ωm halfspace (Munkholm et al., 1995; Munkholm, 1996). For more conductive subsurfaces, the PA-CEP signal would then be completely buried in noise. Under such conditions, statistical processing and heavy data reduction are inevitable. In the case of PA-CEP, only one value per 80 samples is stored (i.e. one per second), which approximately corresponds to a sampling interval of 1 m. Munkholm et al. (1995) were able to show that the PA-CEP noise has a non-Gaussian, long-tailed distribution and a non-white spectrum. It is often affected by high amplitude noise bursts. Conventional running mean filters are not optimal for such data. Instead, robust stacking schemes were found to be most suitable for the processing of PA-CEP data (Munkholm et al., 1995).
In the case of CR, noise characteristics are more favourable due to the absence of galvanic contact and associated electrochemical effects. As the examples in Section 7.2 have shown, CR noise appears to be primarily a function of the instrument design and measurement principle. The assessment of CR noise should be instrument-specific. An example of such an assessment for the CORIM™ system is given in the following. Figure 7.34 shows noise data recorded with the CORIM™ on grass over a 200 m profile at a sampling interval of 0.3 m. The data were acquired by measuring the potential (a) at a receiver dipole (here: $r = 2\,\mathrm{m}$) without any current injection. Equivalent apparent resistivities

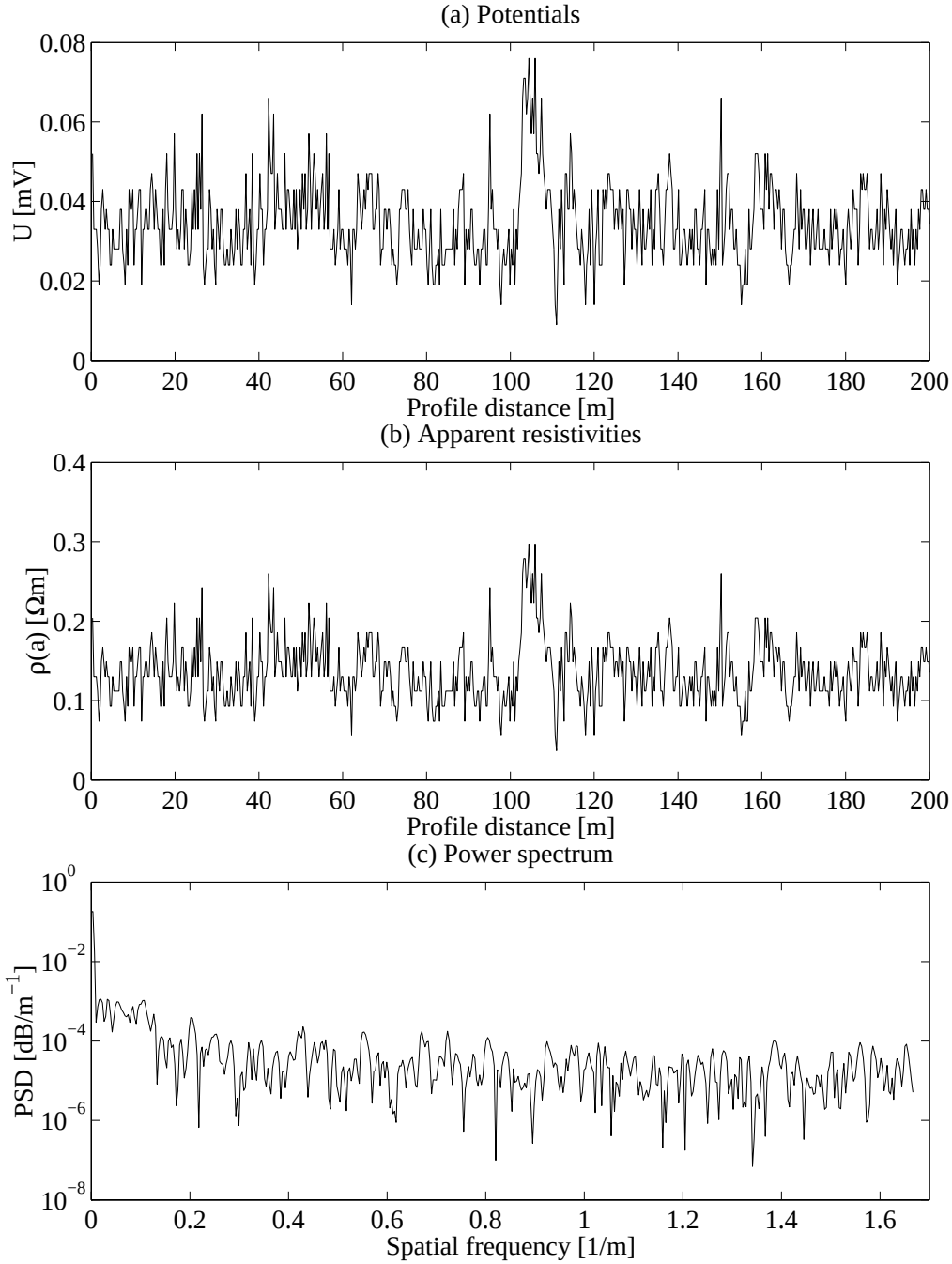

Figure 7.34: Evaluation of CR noise data: CORIM™ potentials measured without current injection (Tx off). (a) Potentials over a profile of 200 m (sampling interval 0.3 m). (b) Potentials converted into apparent resistivities for $I = 8\,\mathrm{mA}$. (c) Spatial power spectral density of noise potentials.

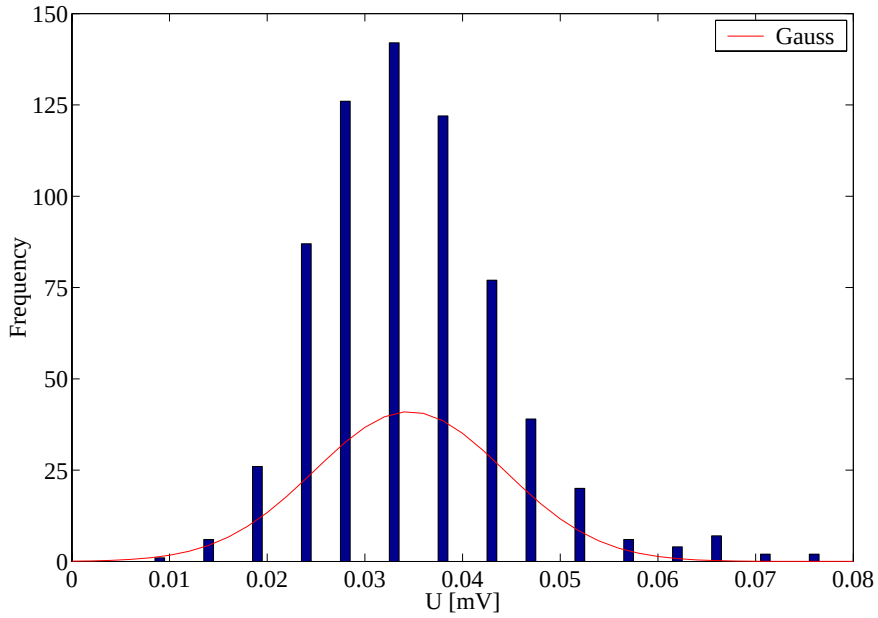

Figure 7.35: Statistical distribution of CORIM noise potentials as a binned histogram compared to a Gaussian distribution with the same mean and standard deviation.

(b) have been calculated for an injection current of 8 mA. The spatial power spectrum (c) shows that the noise is nearly white, except for an increase at low spatial frequencies (≤ 0.2). The RMS amplitude of the CORIM™ noise is 0.036 mV in the case of the potentials and 0.14 Ωm in the case of the apparent resistivities, which is close to the maximum resolution of the instrument. The voltage steps corresponding to the least significant bit of the A/D conversion can be recognised in the data. The occurrence of such low noise levels suggests that there are circumstances in which high signal-to-noise ratios (≥ 100) may be achieved in towed-array CR measurements, even in more conductive environments where signal amplitudes are low. This concept has been confirmed by numerous field experiments with the available CR instruments. However, it must be stressed that the noise analysis presented here is not representative of all field conditions. Experience has shown that there are situations where much higher proportions of towing-induced noise are observed. Instruments such as the CORIM™ which use a reference potential obtained by galvanic contact are particularly prone to such noise, especially on dry and resistive surfaces such as roads and pavements (cf. Figures 7.9, 7.10 or 7.18). Data acquired with the BGS CRI system show that a "floating" measurement gives rise to much higher signal-to-noise ratios on those surfaces.
The statistical distribution of the CORIM™ noise data is shown in Figure 7.35, superimposed on a Gaussian distribution with the same mean and standard deviation. Although the amplitudes are not comparable due to the finite discretisation of the sampled data, the noise distribution has clearly the same shape as the corresponding Gaussian distribution.

7.3.1.2 Despiking

Examples presented in Section 7.2 have shown that individual outliers (spikes) are a characteristic type of motion-induced noise which may contaminate CR data. Such noise spikes can assume either high (Figures 7.7, 7.9, 7.10) or low values (Figure 7.16), but typically not a mixture of both. The occurrence of such spikes can be explained by either the temporary breakdown of the injection current in the transmitter circuit caused by a sudden increase in contact impedance, or a momentary saturation of the receiver. The statistical properties of this type of noise are such that traditional filtering methods (convolution filters, running averages) are sub-optimal. The power contained in the spikes will not be reduced but merely smeared out over an interval. More robust filtering techniques are therefore required.

Trimming techniques, which simply truncate data above or below a defined threshold value based upon the statistical distribution of the entire dataset, are not straightforward as the data may have a high natural variance, for example due to near-surface inhomogeneities or sharp lateral contrasts in subsurface properties. At the same time, geoelectric profiles are generally known to be smoothly varying signals where sharp spikes (i.e. individual outliers) cannot occur. It is therefore expected that some form of predictive filtering may be suitable for despiking such datasets. Predictive filters are designed to "predict" the signal based upon previously extracted segments in a continual manner along the profile. Such filters were used by Munkholm et al. (1995) to recover PA-CEP data submerged in long-tailed noise. However, while their application required a reduction of the dataset by a factor of 80, the despiking of CR data by predictive filters need not result in any reduction at all.

The simplest case of a predictor filter is one where the conditions demand that the signal must not change by more than a certain variation factor from one sample to the next (Munkholm, 1996). Such a filter has been implemented and tested on CR datasets. Let $(x_1, \ldots, x_N)$ a signal of length N samples, and x_n the sample to be predicted. Then the average $\bar{x}$ of the first $n-1$ samples $x_1 \ldots x_{n-1}$ is calculated. For a user-determined variation factor $p > 0$, predictor bounds $\bar{x} + p \cdot \bar{x}$ and $\bar{x} - p \cdot \bar{x}$ are calculated and compared to the sample x_n. If the measured sample x_n falls outside of the predictor bounds it is reassigned the value of the high or low predictor bound, depending on whether it fell above or below the bounds. The process is repeated for sample x_{n+1} and the average of $x_2 \ldots x_n$. The procedure continues along the profile until the final sample has been predicted. The possibility of applying this filtering strategy to data acquired in real-time is obvious. For post-processed data, the directional bias may be reduced by repeating the procedure in the opposite direction and taking the average of the two results.

An example of applying the predictor to a typical CR dataset contaminated by noise spikes is shown in Figure 7.36. The raw data (a) cover a wide range of values over the length of the profile and have high local variance associated with features of limited spatial extent, for example at a profile distance between 170 m and 190 m. The challenge of filtering is to retain as much of this information as possible while at the same time reducing the power of the noise

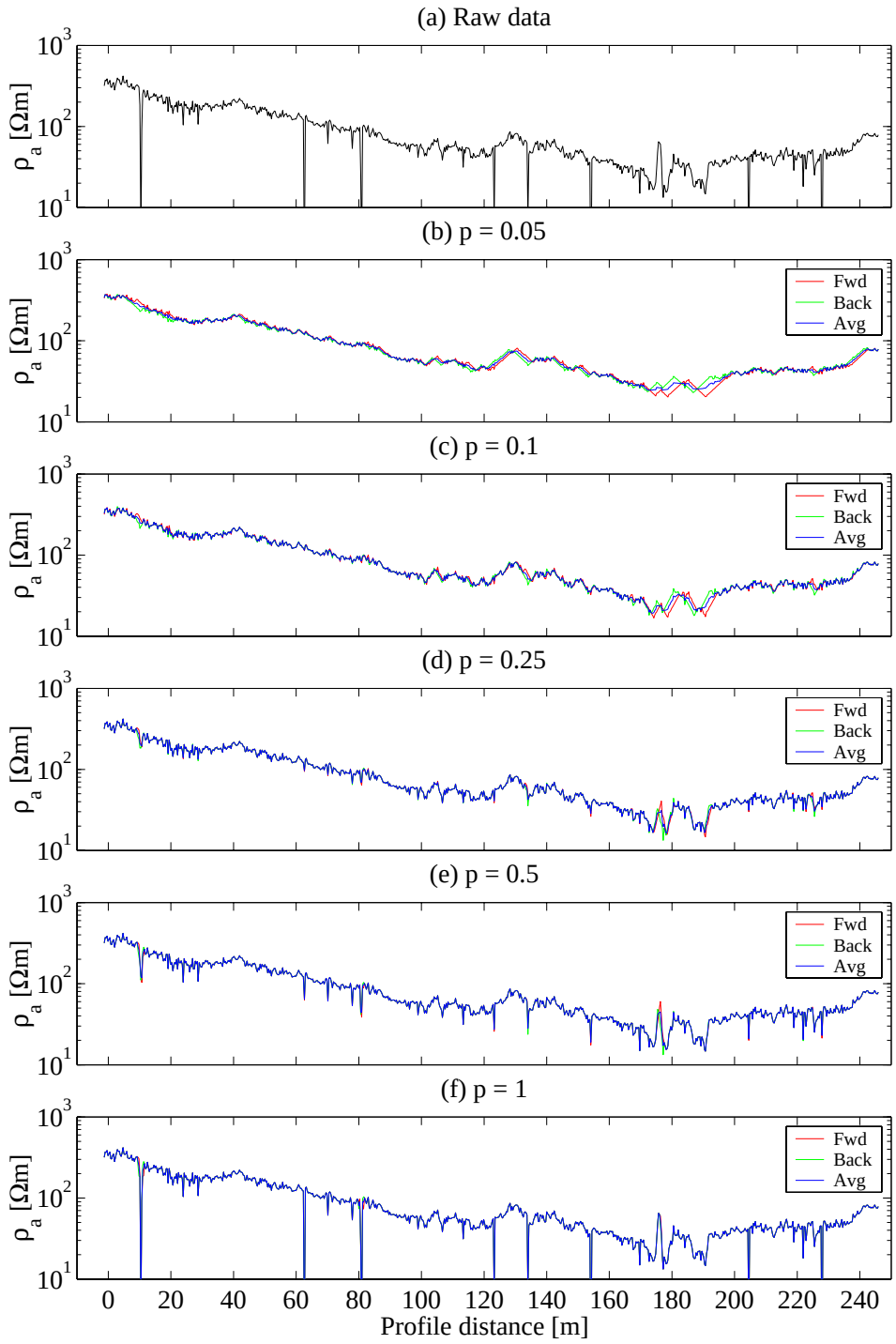

Figure 7.36: Predictive filtering of CR profile data contaminated by noise spikes. (a) Raw data; (b)–(f) filtered data using a predictor length of $n = 3$ and a range of variation factors $0.05 \leq p \leq 1$.

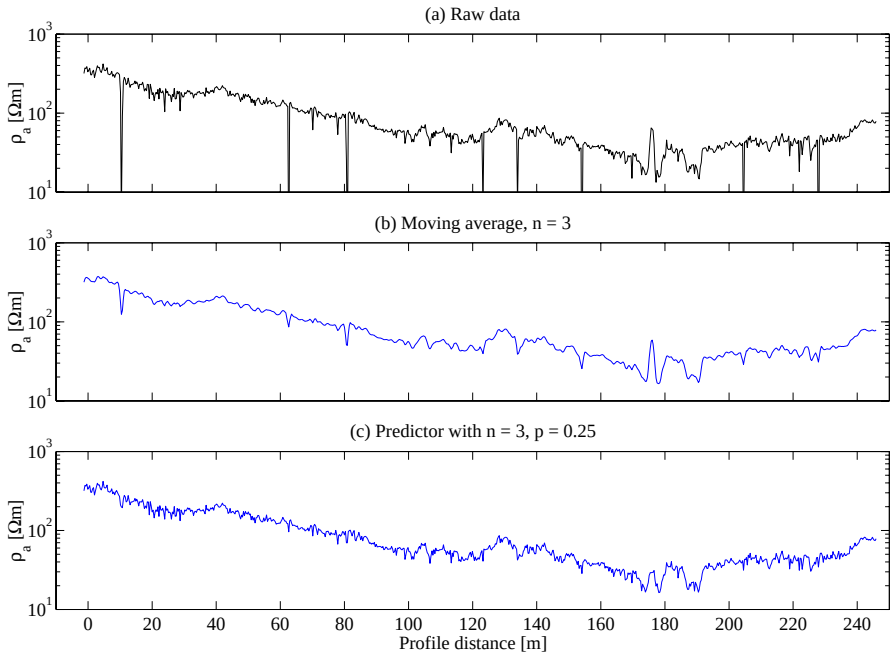

Figure 7.37: Comparison between conventional and predictive filtering of CR profile data. (a) Raw data; (b) filtered data using a 3-point moving average filter; (c) filtered data using the predictor with $n = 3$, $p = 0.25$.

spikes. A predictor of length $n = 3$ was then applied twice, once from left to right ("forward", red line) and once from right to left ("back", green line). The average of the two runs is shown by the blue line. As the data were sampled at a constant distance of 0.3 m, the predictor length $n = 3$ corresponds to a distance of 0.9 m on the ground over which the resistivity of the subsequent sample is predicted. Tests have shown that shorter predictors ($n = 1, 2$) result in a noisier response, while the response of longer predictors ($n \geq 4$) may get distorted by the presence of short-wavelength features or steep gradients in resistivity. However, the predictor performance depends largely on the width of the predictor bounds determined by the variation factor p. The influence of this factor on the predictor response can be seen in Figure 7.36b–f, where p has been varied between 0.05 and 1. A variation of 5% results in the removal of all noise spikes and a generally smooth response (b), however short-wavelength features (e.g. at 175 m) are suppressed also. A variation of 100% leaves the dataset almost unchanged (f), i.e. nearly all measured data, including the noise spikes, are within the range of predicted values. The optimal setting for p is somewhere in between these extremes and a function of the variability of the data. A setting of $p = 0.25$ (d) has been found to be the best compromise between spike removal and preservation of signal content.

A comparison between a conventional averaging filter and the predictor filter is shown in Figure 7.37. Panel (b) shows the result of applying an unweighted 3-point moving average to the same dataset as before. Below, a predictor

with $n = 3$, $p = 0.25$ has been applied (c). The difference in performance is obvious: while high-wavenumber content of the signal is dispersed by the moving average filter and spread across neighbouring samples, the majority of this information is retained by the predictor filter. At the same time, spike removal is more comprehensive with the predictor filter, particularly for large spikes (i.e. extreme outliers), for example at a profile distance of 10 m.
Adequate recovery of steep gradients in the data presents a challenge to any type of filter. In this respect, the moving average filter appears to have a slight advantage over the predictor. This can be seen by the example of the anomalous feature at 175 m, which is preserved better by the moving average filter than by the predictor.

7.3.2 Correction of levelling errors

Field experience has shown that, besides motion-induced noise, CR datasets can be affected by levelling errors. Data acquired consecutively, for example on adjacent survey lines, may have slightly different absolute levels. This problem is well-known in the context of airborne resistivity methods (Huang and Fraser, 1999). In CR, the origin of levelling errors is strongly related to instrument design, and errors observed with different CR systems may be of variable size. Levelling errors indicate an erroneous measurement of the electric potential which may be due to spurious reference potentials. In areal surveys where data are acquired on parallel lines, levelling errors result in line-to-line offsets, i.e. a misalignment between neighbouring survey areas. Such offsets may lead to gross inconsistencies in mapping and imaging applications and must therefore be removed by suitable processing techniques.

7.3.2.1 Basic statistics and empirical levelling

A dataset recently acquired in a towed-array CR survey at Chetwynd Barracks, Nottingham, may serve as an instructive example for the problem of levelling errors and their removal. The CORIM™ instrument was used to collect multi-offset apparent resistivity data (6 channels, equatorial array) on a site approximately 2.5 ha in size. The site is situated on alluvial river terraces in the Trent Valley, and comprises a marked transition between sand and gravel deposits in the valley and solid geology dominated by Triassic Sandstones on higher ground. A total of 49 lines of up to 250 m length, perpendicular to the strike of the Alluvium, were completed during the survey. The survey was conducted in a bidirectional manner, i.e. adjacent lines were acquired in opposite directions. An inter-line spacing of 2 m was employed and data were sampled at intervals of 0.3 m. The survey area was on grassland and predominantly flat in the south, with the northern part gently rising. It contains very few features visible at the surface, but a number of buried foundations of previous buildings and infrastructure is thought to be present on site.
The raw CR data were despiked on the basis of individual lines. After filtering, data were positioned and gridded before shaded image maps of apparent resistivity were produced. It was found that the maps were severly biased by

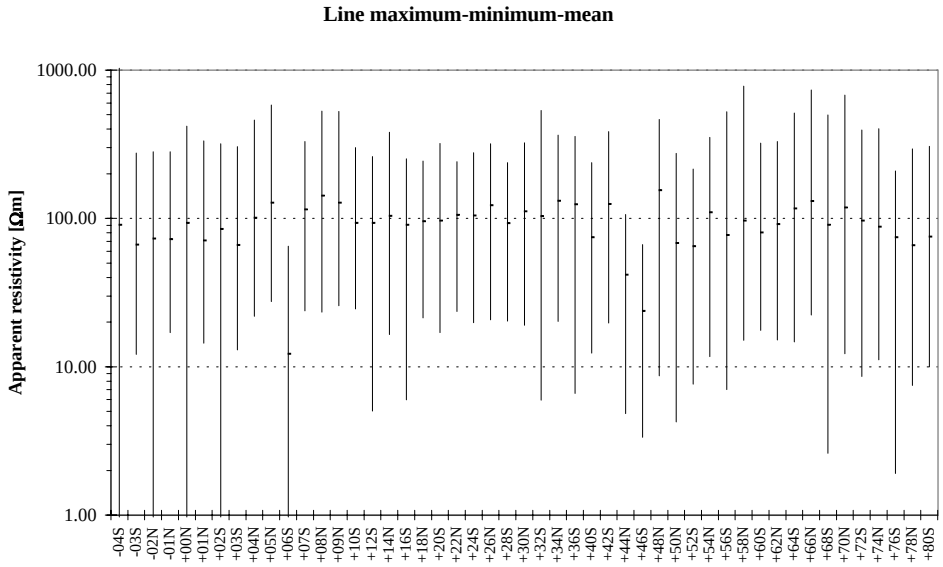

Figure 7.38: Elementary line-based statistics (high-low-mean) for the towed-array CR survey at Chetwynd Barracks.

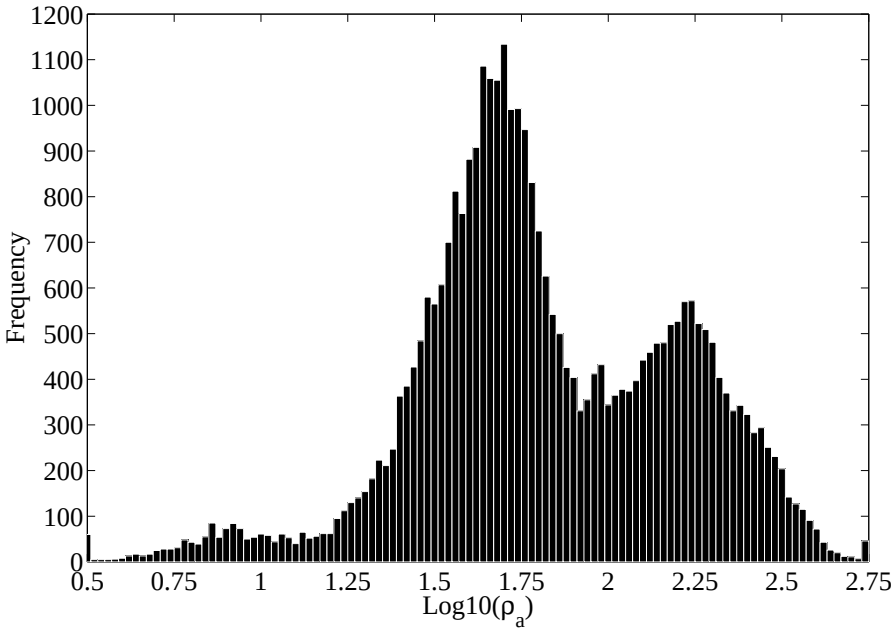

Figure 7.39: Histogram of apparent resistivities for the towed-array CR survey at Chetwynd Barracks.

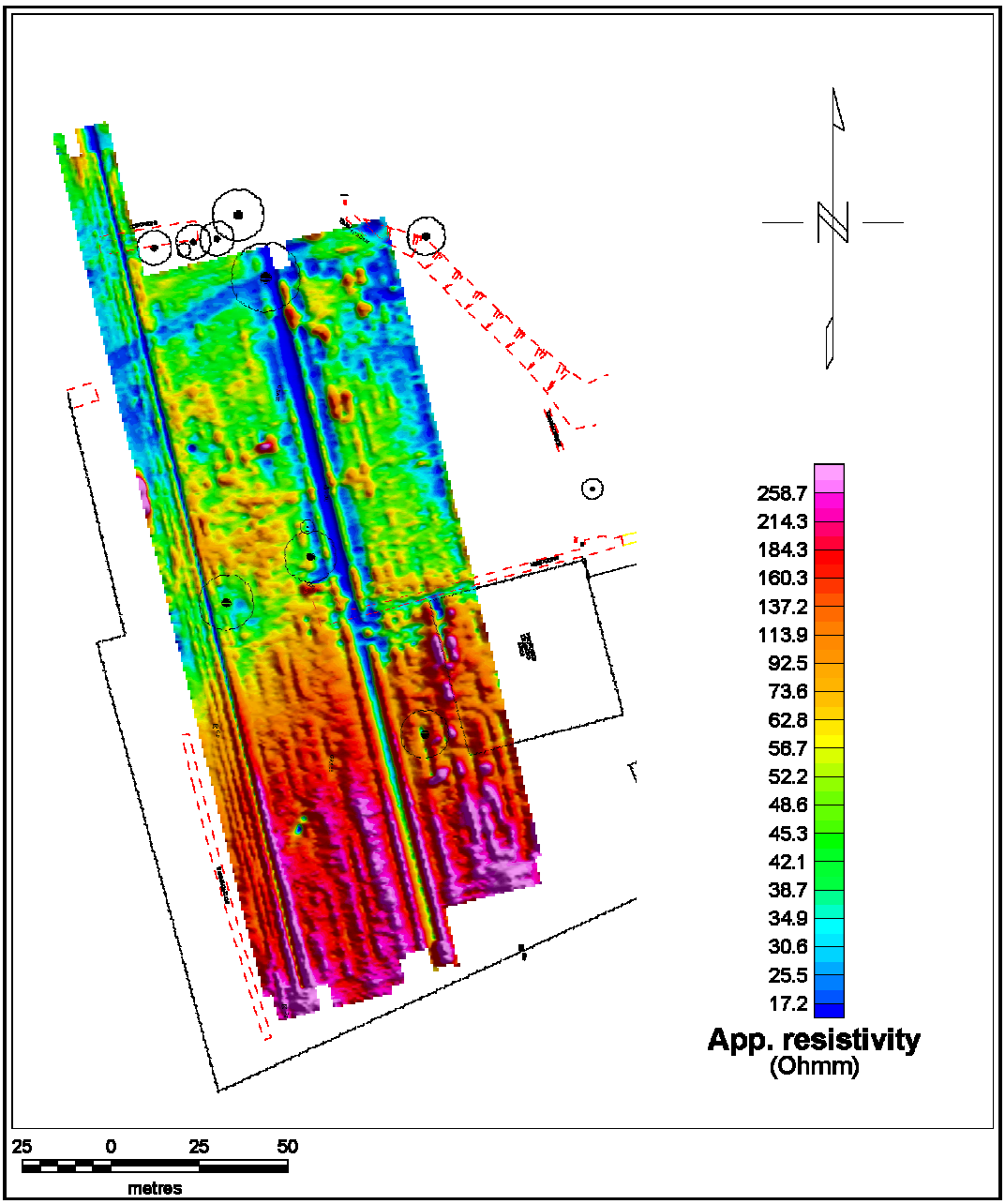

Figure 7.40: Apparent resistivity map (raw data) obtained from a towed-array CR survey at Chetwynd Barracks.

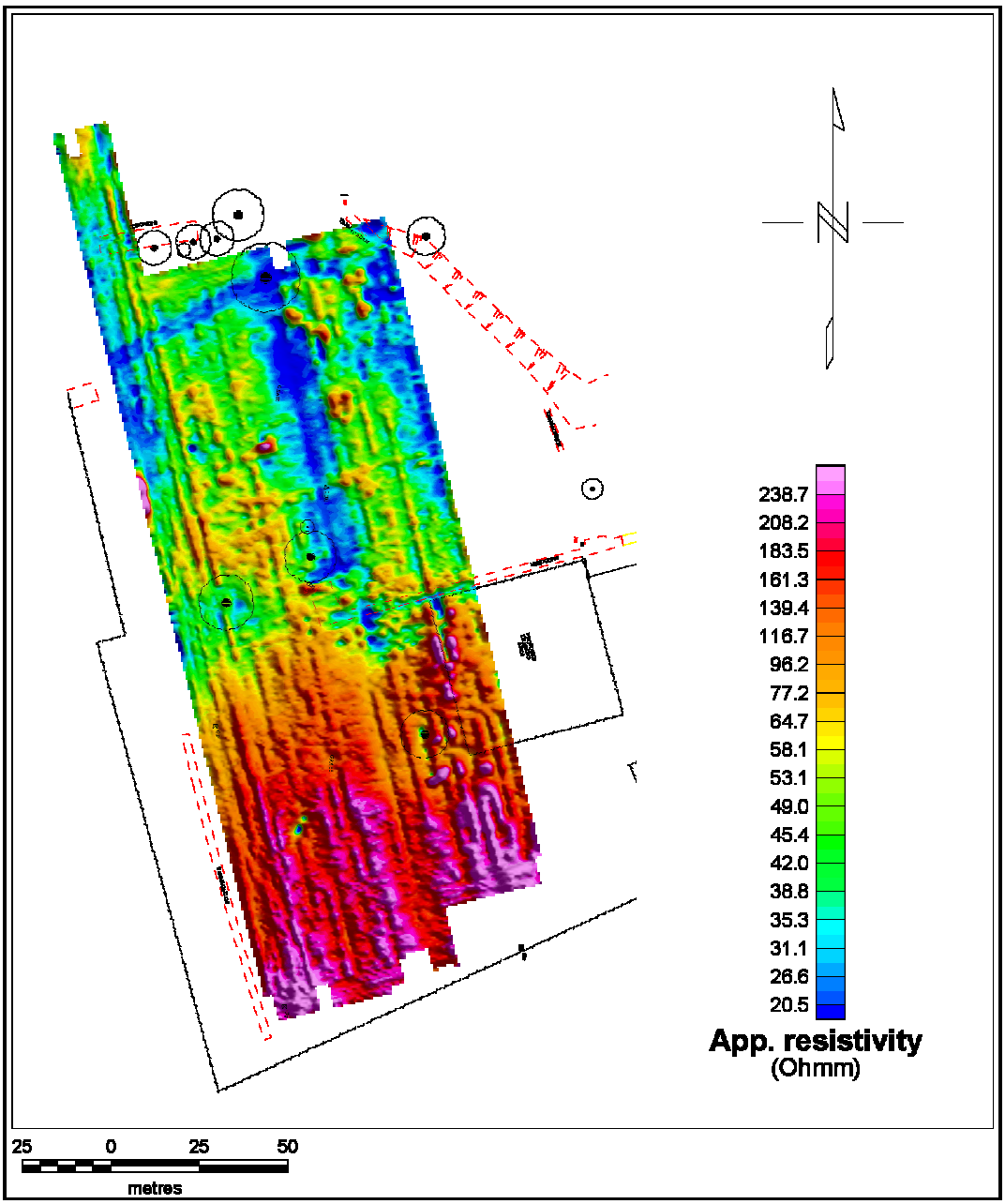

Figure 7.41: Apparent resistivity map of the Chetwynd Barracks site after empirical levelling.

levelling errors. These are best seen by examining the basic statistical properties of the dataset. Elementary statistics for Rx 4 ($l = 1.5$ m, $r = 4$ m) are given in Figures 7.38 and 7.39. The graph in Figure 7.38 shows the average resistivities (mean value) along with the maximum and minimum values (high-low-mean diagram) for all survey lines on a logarithmic scale. Significant outliers at +06S, +44N and +46S are immediately obvious, however other lines seem to have more subtle offsets. The levelling errors appear to be unrelated to the fact that the acquisition mode was bidirectional. Figure 7.39 shows the statistical distribution of the entire dataset for Rx 4 as a binned histogram for the apparent resistivities. The two large maxima at approximately 1.7 ($\approx 50\,\Omega$m) and 2.25 ($\approx 180\,\Omega$m) are due to the presence of two characteristic zones dominated by drift geology in the south and solid geology in the north. The higher resistivities are associated with the alluvial sands and gravels at the bottom of the valley, while the lower resistivities are associated with clayey deposits found upslope. The low-resistivity tail of the distribution, with a faint maximum at approximately 0.9 ($\approx 8\,\Omega$m), is mainly caused by the levelling errors. A shaded image map of the original dataset can be seen in Figure 7.40, where the levelling errors have caused characteristic stripes in the direction of the survey lines.
For airborne surveys using potential field methods such as gravity or magnetics, the usual approach to the removal of levelling errors is the acquisition of tie-lines perpendicular to the original survey lines. By comparing data at line intersections, levelling errors can be detected and level-shifts applied to the respective survey lines. For the towed-array CR technique however, this approach is not valid due to the directionality of the measurement. In the case of a heterogeneous subsurface, tie-line data may rightfully have different apparent resistivity values at intersections with the original survey lines. For the Chetwynd Barracks dataset, an empirical levelling technique was therefore considered as an initial remedy.
Rather than considering individual points on the survey lines sampled along profiles perpendicular to the original survey direction (sometimes referred to as pseudo-ties), the tie-line approach was emulated by examining the statistical averages (mean values) of each survey line (cf. Figure 7.38). By fitting a low-order polynomial to the sequence of mean values, the approximate levels of the erroneous lines were determined and respective level-shifts applied to those lines. Alternatively, if the levelling errors are more subtle, all survey lines may be level-shifted so that their respective mean values match the values on the regression curve. The outcome of this empirical levelling procedure is shown in Figure 7.41. The resulting apparent resistivity map is a major improvement on the original data, however residual errors remain visible in the form of cross-line ripple.

7.3.2.2 Micro-levelling by directional filtering

The removal of residual levelling errors from pre-leveled data, usually referred to as "micro-levelling", demands a slightly more sophisticated approach. Minty (1991) has suggested a technique for the micro-levelling of aeromagnetic data based on directional filtering which applies to towed-array CR data without

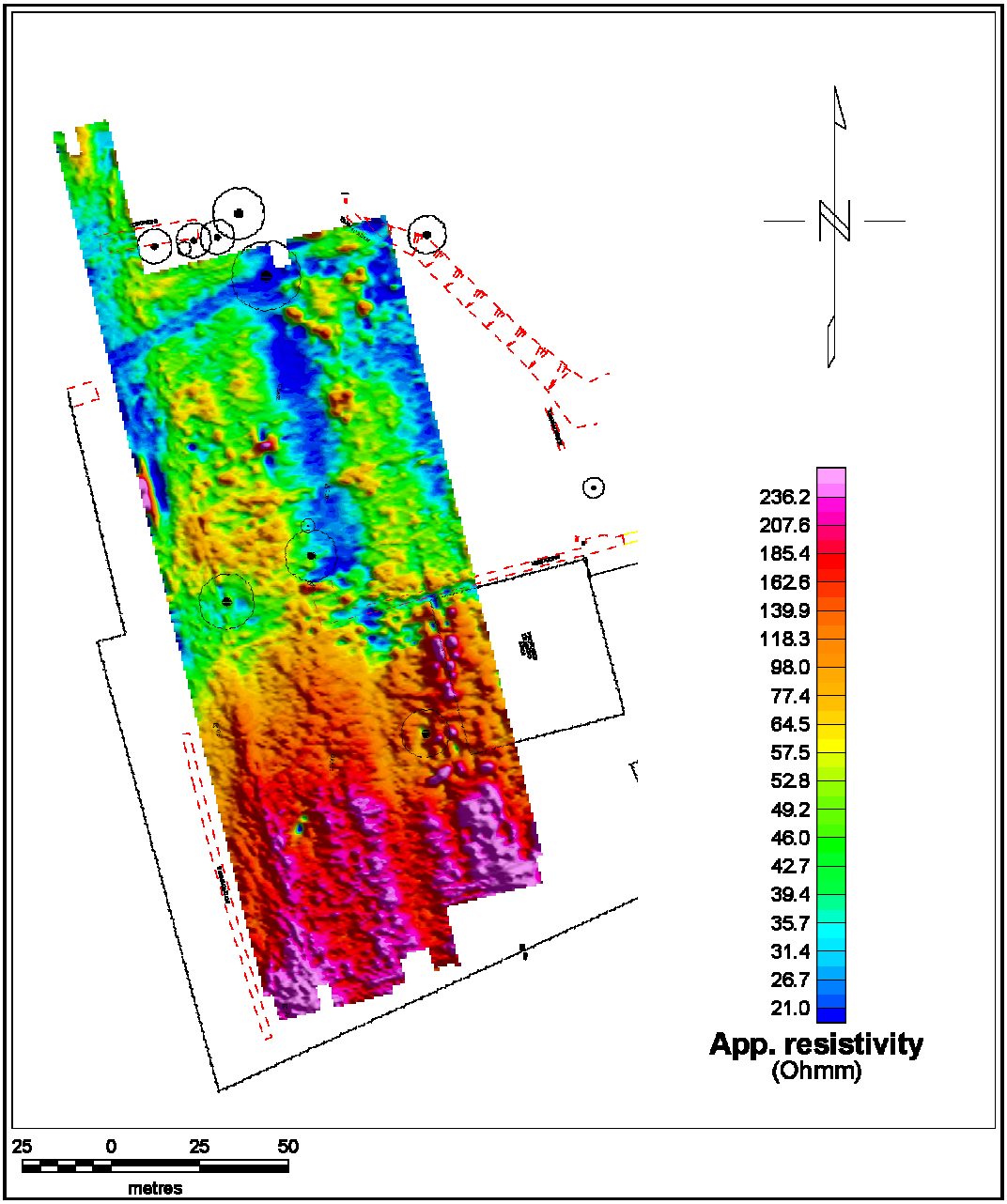

Figure 7.42: Decorrugated apparent resistivity map of the Chetwynd Barracks site after micro-levelling.

modification and has been used here to demonstrate the similarities between the processing of airborne geophysical and towed-array CR data. Rather than individual survey lines, a regular two-dimensional grid of apparent resistivity data is now considered. For convenience, the grid spacings are chosen to correspond with the sampling interval in profile direction, and with the inter-line spacing in the perpendicular direction. On gridded datasets, two-dimensional directional filters can be designed to pass or reject linear features of varying strikes (Fuller, 1967). Minty's technique makes use of the fact that the anomalies introduced by inadequate levelling have a distinct spectral signature. They are characterised by a wavelength in profile direction much greater than the inter-line spacing, and a wavelength perpendicular to the profile direction of precisely twice the inter-line spacing. They can be removed from the grid by applying the following sequence of directional filters (Minty, 1991):

1. The original grid (grid A) is low-pass filtered in the direction of the survey lines and the result is stored in grid B.

2. Grid B is then high-pass filtered in the direction perpendicular to the survey lines and the result is stored in grid C.

3. Grid C is finally subtracted from grid A.

After application of the two directional filters with perpendicular orientation, grid C contains only the elongated anomalies associated with the levelling errors. After subtraction from the original grid, these anomalies should be largely removed. This procedure has been successfully applied to the Chetwynd Barracks dataset. Figure 7.42 shows the decorrugated apparent resistivity map after micro-levelling. Virtually all levelling-related anomalies have been removed so that the true subsurface information contained in the data can be fully appreciated. In contrast to tie-line levelling, Minty's technique is non-rigorous and cannot distinguish between levelling errors and real elongate anomalies parallel to the survey line direction. It must therefore be applied with care.

7.4 Discussion

In this chapter, the feasibility of making high-density dynamic capacitive resistivity measurements with towed arrays has been demonstrated both by conceptual considerations and practical experiments. It has been shown that, beyond the limited capabilities of existing CR instruments, reliable dynamic measurements of the fully complex transfer impedance are possible with towed arrays. Consequently, towed-array CR has many similarities with other truly dynamic geophysical techniques.

Fundamental concepts of dynamic CR measurements. Synchronous multi-channel acquisition allows the simulation of multi-electrode DC resistivity profiling surveys with a single pass of a towed CR array. In contrast to DC profiling however, data acquisition with CR arrays is not restricted to a finite set of electrode positions, thus making "continuous" spatial sampling possible. It was shown that minimum sampling intervals for the CR technique may be of the order of 1 cm. At such small sampling intervals, CR has an advantage over the DC technique due to the much higher frequency of operation, which allows for a statistically sound measurement of the transfer impedance at realistic towing speeds, while a DC measurement is limited to single-cycle estimates. The two generic array configurations (inline and equatorial dipole-dipole array) have different properties with regard to depth of investigation, sensitivity distribution and practical handling under field conditions. The equatorial configuration has the greatest depth of investigation relative to array dimensions and allows the construction of compact multi-offset arrays. Its disadvantage is a slightly reduced signal strength compared to its inline counterpart.

Operational characteristics of towed CR arrays. The operational characteristics of towed CR arrays were assessed by evaluating existing CR instruments as well as the newly designed BGS CRI system. The instruments considered share many similarities, but distinct differences were also observed. All are capable of acquiring high-quality, highly repeatable data with low levels of towing-induced noise, given suitable surface conditions. For the commercially available instruments, these characteristics are restricted to the magnitude of the transfer impedance. Evaluation of the CRI system has shown that the same or indeed a superior level of quality and repeatability is possible for a measurement of the fully complex response.
Significant differences were discovered in the performance on artificial surfaces such as tarmac and concrete. While the data quality obtained with the CRI system is even better in such environments than on natural surfaces such as grass, the commercial instruments tend to have some difficulty with these conditions. For the CORIM™ system as the nearest relative to the CRI system, the observation of elevated noise levels on tarmac and concrete is attributed to the use of reference potentials obtained via galvanic contact. This concept is somewhat contrary to the intended use of CR in the built environment. Instead, the fully floating measurement principle of the CRI system proves the feasibility of low-noise measurements under such conditions. The OhmMapper™ does not

require any galvanic coupling and can generally provide good quality data on roads and pavements. However, the mechanical properties of the towed inline array may result in erratic dynamic behaviour when towed on those surfaces, which may have detrimental effects on the consistency and repeatability of the measurement. Towed arrays with equatorial geometry were found to provide better dynamic stability. The use of capacitive line antennas is likely to result in spatial averaging and datasets obtained with the OhmMapper™ must be interpreted with care when using processing schemes designed for point electrodes. The true potential of towed-array CR measurements is revealed by the quality of the data obtained with the BGS CRI system. Its main strength is its outstanding performance on flat surfaces such as roads, where highly repeatable, low-noise resistivity measurements are possible at ultra-high densities. Extensive trials have shown that the information content of the CRI response is likely to be significant at all scales, i.e. even at high wavenumbers. Such repeatability at centimetre level is clearly a novelty for near-surface geophysical data. Comparisons with conventional DC resistivity profiling data have demonstrated the equivalence of towed-array CR measurements with conventional DC traverses, highlighting the considerable amount of additional detail contained in CR data.

Quality issues associated with towed-array CR data. Motion-induced noise is one of the potential problems that may be associated with towed-array CR data. The character and intensity of such noise is a function of the measurement principle employed by individual CR instruments and the properties of the ground surface. Low-noise conditions are required for the acquisition of high-density resistivity data without the need for spatial reduction.
The process of signal detection is the primary stage of noise suppression in CR. Consequently, typical CR noise levels at the recording stage are likely to be far smaller than those observed in dynamic DC measurements. However, disruption of the capacitive coupling caused by movement of the sensors over rough terrain can introduce high-intensity noise, usually expressed as individual outliers (spikes). While conventional filtering techniques are inappropriate for the suppression of such noise, predictive filtering was found to give useful results with towed-array CR datasets. A predictor based on parts of the previous signal can remove the outlier noise component while retaining relevant high-wavenumber information in the data. Such filters produce datasets that are much more adequate for quantitative interpretation schemes than the contaminated raw data. The nature of the predictor filter also allows for dynamically acquired data to be processed in real time.
A second potential problem are levelling errors affecting CR data acquired on neighbouring profiles. Their intensity and frequency of occurrence appears to be mainly dependent on instrument design. It is acknowledged that the tests described here have used "new" (on the market) CR instruments and improvements will be made as the subject and methodologies progress. Data processing techniques well-known in airborne geophysics were usefully applied to corrugated CR datasets, highlighting the similarities between towed-array CR and airborne data acquisition.

Chapter 8

Electrical imaging with multi-offset towed-array CR

High-density multi-offset towed-array CR surveys provide a novel type of geophysical data for which designated processing and interpretation techniques do not exist. In this chapter, the use of such data for tomographic resistivity imaging will be examined. It will be shown that, due to the equivalence between resistivities determined by the CR and DC methods, well-known DC interpretation schemes may be applied to CR datasets with some adaptations. However, despite such close relationships with fixed-electrode DC data, datasets acquired with multi-channel towed CR arrays have specific characteristics which must be taken into account for adequate processing and interpretation, particularly if the latter is to be carried out "on-the-fly". These properties are discussed in the first part of this chapter.
Later it is shown how different DC resistivity inversion algorithms with increasing levels of complexity can be applied to the interpretation of multi-offset towed-array CR data. At the simplest level, such data may be regarded as continuous vertical electrical soundings (CVES) which can form the basis of a quasi-2D interpretation. Using a fast 1D inversion algorithm, the suitability of this approach for ERT is examined. Subsequently, the requirements for a full 2D resistivity inversion of towed-array CR data are described. In this context, the use of smoothness-constrained least-squares inversion is considered. The use of towed-array CR for 3D ERT presents the greatest challenges for data processing and inversion and is discussed in the final part of this chapter.

8.1 Properties of multi-offset towed-array data

8.1.1 Fixed-electrode versus towed-array acquisition

The acquisition of fixed-electrode multi-offset DC resistivity data is typically carried out with automated multi-channel systems using lines or grids of electrodes spaced at regular intervals (e.g. Griffiths and Turnbull, 1985; Griffiths et al., 1990). Current and potential electrodes are moved along the profile by activating consecutive electrode positions along a multi-core cable. The conse-

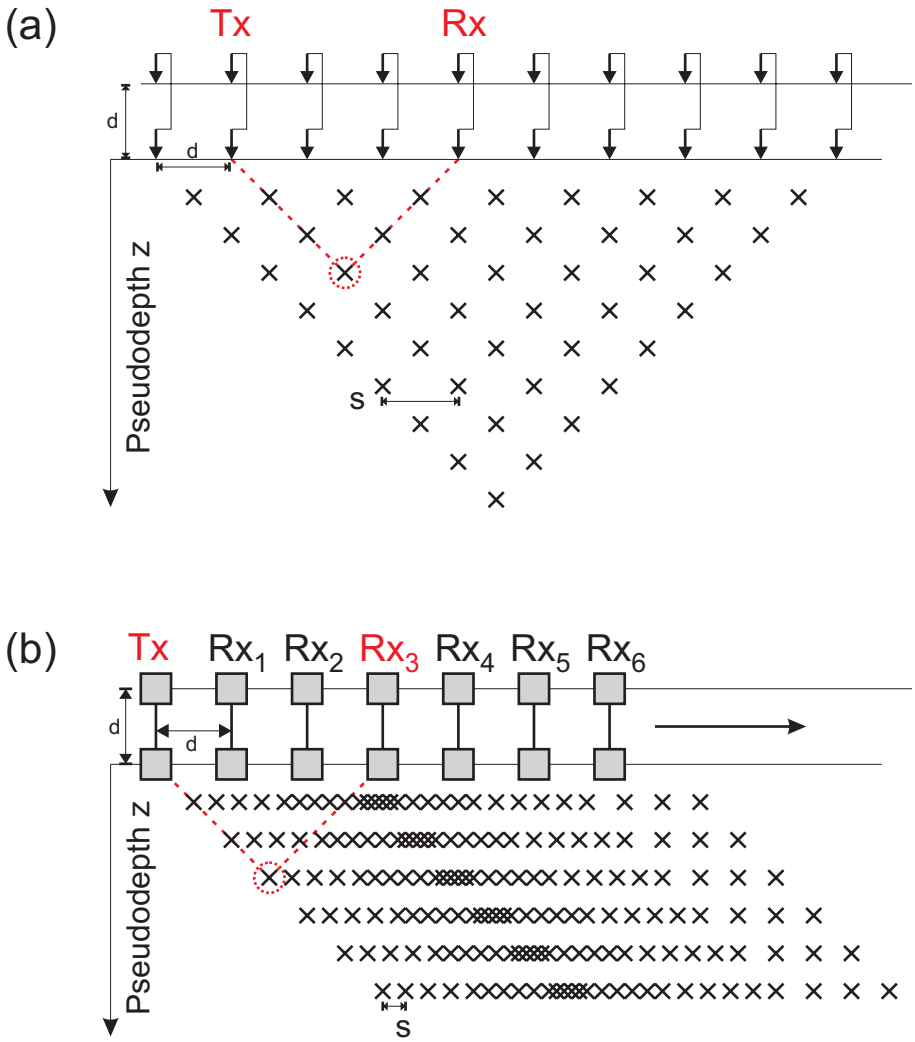

Figure 8.1: Distribution of datum points in the distance-pseudodepth plane as obtained with fixed-electrode and towed-array data acquisition using equatorial dipole-dipole geometry. (a) Fixed-electrode acquisition with constant electrode spacing d. (b) Towed-array acquisition with constant array spacing d, but variable sampling interval Δs.

quences of this methodology are:

1. The lateral sampling distance for a given array geometry is constant, i.e. the ground is probed at regular intervals along the profile. The locations of apparent resistivity datum points associated with individual electrode configurations follow a regular pattern in the distance-pseudodepth plane (Figure 8.1a).

2. Due to the regularity of the electrode grid, dipole size and array separation are always integer multiples of the fundamental electrode spacing. Hence, vertical sampling of the subsurface through extending the electrode spread is also discrete and limited to well-defined depths.

3. The distribution of datum points in the apparent resistivity pseudosection typically has triangular or trapezoidal shape (Figure 8.1a).

It is obvious that for fixed-electrode resistivity data, lateral and vertical sampling of the subsurface are interdependent and predetermined by the fundamental electrode spacing d. This specific property of multi-offset DC data is heavily used in interpretation schemes. In electrical resistivity tomography, the use of regular electrode spacings justifies a non-uniform, but laterally regular discretisation of model grids (e.g. Barker, 1992). Some filtering techniques also make use of equally-spaced acquisition. Acworth and Griffiths (1985) have used an expanded offset filter based on the equal distances between electrode positions to process tripotential apparent resistivity profiling data.
Towed-array acquisition (DC as well as CR) lacks such a well-defined spatial reference. Whilst the geometry of the towed electrode array is constant, its position on the ground is variable. An important aspect of the interpretation of multi-offset towed-array CR data is therefore to reliably establish the spatial allocation of apparent resistivities acquired from the moving array, so that individual readings can be accurately positioned in the distance-pseudodepth plane. Characteristics of the towed-array approach are:

1. The lateral sampling distance in towed-array CR can be far smaller than the dimensions of the electrode array and may vary according to towing speed along the profile or sampling frequency in time (Figure 8.1b).

2. Towed arrays may have a more flexible geometry than fixed-electrode grids, i.e. array size and separations do not have to be integer multiples of some fundamental distance. Vertical sampling of the subsurface is therefore equally flexible.

3. The distribution of datum points in the apparent resistivity pseudosection can have the shape of a parallelogram, provided the current dipole is located at one end of the array (Figure 8.1b).

Consequently, lateral and vertical sampling of the ground are no longer interdependent in towed-array acquisition, nor are they predetermined by fundamental geometric properties. It is this greater flexibility which requires an adaptation of conventional DC interpretation schemes to handle multi-offset towed-array CR data.

8.1.2 Relation between array offsets and sampling interval

An obvious hindrance for the direct interpretation of multi-offset towed-array CR data as individual 1D soundings is the fact that the datum points obtained from one scan of the multi-offset array do not fall on a vertical line in the distance-pseudodepth plane. Data sampled in consecutive scans must therefore be collated into soundings in order to obtain spatially accurate resistivity-depth profiles. This is particularly critical if processing and interpretation is to be carried out "on-the-fly".

In most near-surface applications it is desirable to sample multi-offset towed-array CR data at a constant interval Δs if no prior information about the subsurface is available. In practical towed-array CR instruments, this sampling interval is typically identical for all receiver channels, i.e. short-offset data is obtained at the same Δs as long-offset data. In contrast to DC resistivity, this sampling interval may be much smaller than the geometric dimensions of corresponding electrode configurations. The relation between the sampling interval and the dipole offsets determines the position of the datum points in the distance-pseudodepth plane and is therefore crucial for the applicability of DC interpretation techniques. The possible scenarios are shown in Figure 8.2 for the simple case of an array with linearly increasing offsets ($d_i = i \cdot d_0$, $i = 1 \ldots n$) and equatorial dipole-dipole geometry, as implemented by the CORIM™ instrument. Using this configuration, the problem is reduced to the relation between the basic offset d_0 and Δs. If the ratio between the two is an integer multiple greater than one, datum points acquired by consecutive scans from multiple offsets eventually coincide laterally, i.e. they plot vertically above each other in the distance-pseudodepth plane (e.g. $d_0/\Delta s = 4$, Figure 8.2a). If, however, this ratio is non-integer, the lateral coincidence is lost and the pattern in the distance-pseudodepth plane becomes irregular (e.g. $d_0/\Delta s = 3.\overline{3}$, Figure 8.2b). If the ratio is equal to one, i.e. the sampling interval equals the basic offset ($d_0/\Delta s = 1$), lateral coincidence is only partially achieved and only datum points from every other offset plot vertically above each other (Figure 8.2c). For the purposes of this chapter it will be assumed that the first case applies, i.e. the basic offset is an integer multiple of the sampling interval. For all other cases, a viable alternative is to resample the apparent resistivity profiles of individual channels so that lateral coincidence is achieved.

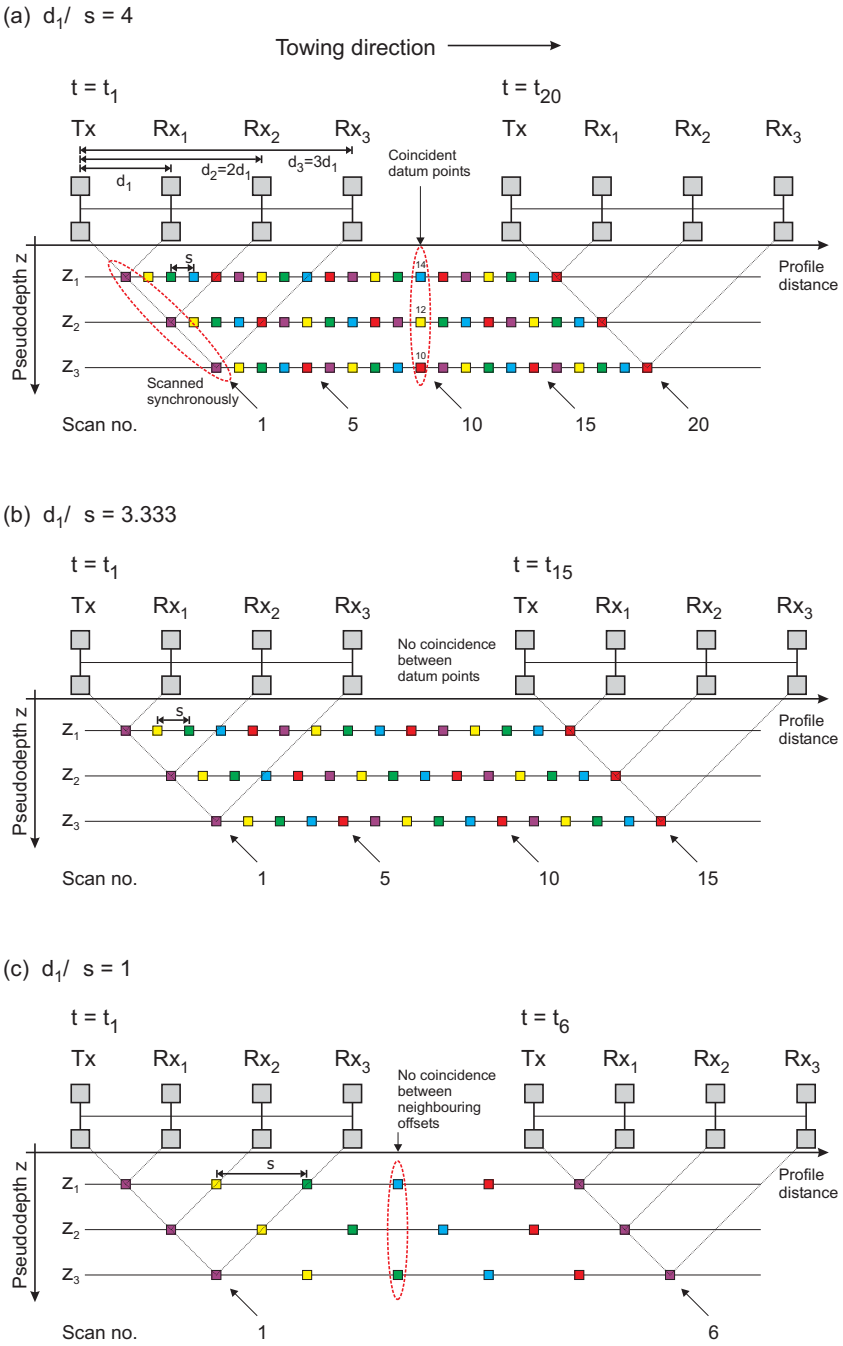

Figure 8.2: The relation between offsets and sampling interval and its influence on the lateral coincidence between datum points in the distance-pseudodepth plane for a towed CR array with equatorial dipole-dipole geometry and linearly increasing offsets ($d_i = i \cdot d_0$, $i = 1 \ldots n$). Datum points of the same colour are measured synchronously. (a) $d_0/\Delta s = 4$. If d_0 is an integer multiple greater than one of the sampling interval Δs, datum points from different offsets coincide laterally. (b) $d_0/\Delta s = 3.\overline{3}$. For non-integer multiples, datum points from different offsets do not coincide laterally. (c) $d_0/\Delta s = 1$. If the sampling interval equals the basic offset, only datum points from every other offset coincide laterally.

8.2 Quasi-2D interpretation

Multi-offset apparent resistivity data acquired on a linear profile can be interpreted in a maximum of two dimensions, i.e. the resulting resistivity-depth models will be either 1D or 2D. In this section it is demonstrated how such models can be derived from multi-offset towed-array CR data. Initially, a technique based on continuous 1D modelling and inversion is tested with regard to its potential for quasi-2D interpretation of such datasets. Quasi-2D techniques are not sufficiently accurate in regions with a highly irregular resistivity distribution (Dahlin, 1993). Conceptually however, they are extremely fast and can thus be applied in real-time, i.e. for "on-the-fly" interpretation in the field. Fully two-dimensional interpretation is more demanding and requires the full dataset to be available at once.

8.2.1 Continuous Vertical Electrical Sounding

Horizontal profiles of multi-offset resistivity data can be regarded either as independent profiles for individual channels with different depths of investigation or as a sequence of discrete vertical soundings at individual "stations". In the latter case, interpretation is analogous to a situation in which an expanding electrode spread is employed to investigate the subsurface below a single point on the survey line. The simplest approach to the interpretation of multi-offset resistivity profiling data is therefore to regard the profile as a sequence of discrete stations at which individual vertical electrical soundings (VES) are performed. For a geometrically correct sounding, apparent resistivity readings from multiple offsets must be grouped and centred around a fixed point on the traverse. This data subset can then be regarded as a classical VES curve by plotting apparent resistivity versus depth. Such curves are often interpreted by layered 1D models (cf. Chapter 3). By selecting consecutive points along the traverse it is possible to construct a quasi-2D model from a sequence of adjacent 1D soundings. This procedure has been branded Continuous Vertical Electrical Sounding (CVES) by van Overmeeren and Ritsema (1988) and was used by the authors in connection with expandable multi-electrode cables attached to an automated data acquisition system. The cables were deployed using a "roll-along" technique and had take-outs at constant spacings, connected to a regularly spaced sequence of electrodes. This methodology made data collection by means of the Wenner Offset (Barker, 1981) and Wenner Tripotential (Carpenter, 1955; Carpenter and Habberjam, 1956) techniques particularly attractive. CVES can be expected to give reliable results in areas with limited variation in resistivity, but must be regarded with caution where rapid changes occur. This is because depth interpretation is strictly 1D, so that 2D or 3D effects remain unaccounted for.
The construction of VES curves from multi-offset towed-array CR data requires the compilation of overlapping measurements sharing the same centre, i.e. groups of datum points which plot on vertical lines in the distance-pseudodepth plane. Assuming that data are sampled at a constant interval Δs and all dipole separations are integer multiples of that distance, a group of da-

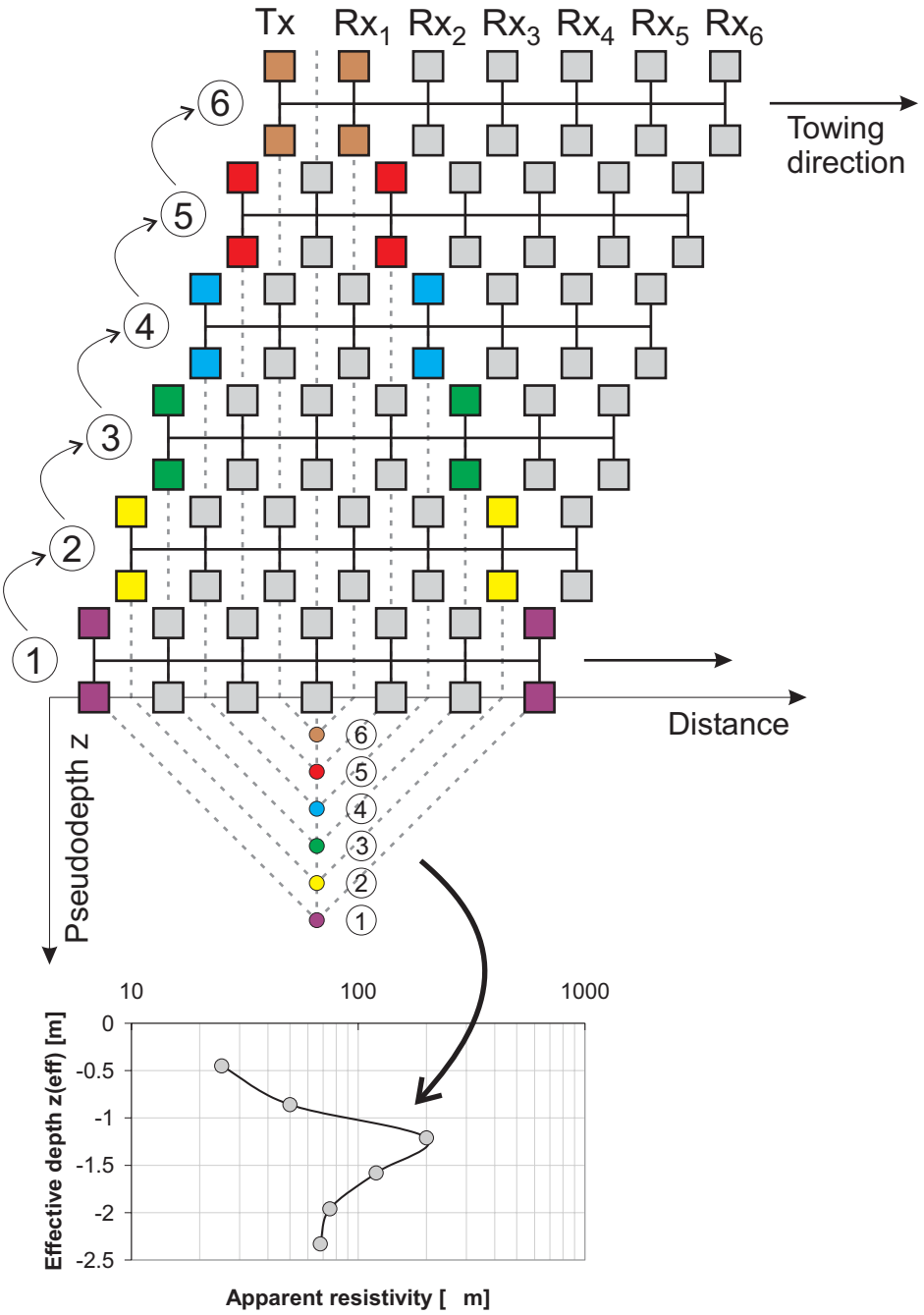

Figure 8.3: Compilation of overlapping measurements for the construction of a VES curve from multi-offset towed-array CR data.

tum points, including one from each offset, exists which has a common centre point and can be used to construct a VES curve (cf. Section 8.1.2). Figure 8.3 shows this procedure for a system with CORIM™ geometry, i.e. six receivers arranged at linearly increasing offsets. Such an array provides apparent resistivity data for six different depths of investigation, i.e. the associated VES curve is defined by six points. It can be seen in the diagram that the necessary measurements must be taken sequentially at six different locations, starting with the longest offset (here Rx_6). The VES curve for the station considered is only complete when the shortest offset has passed the centre point of the sounding. The VES curve can then be interpreted by a 1D model. Multilayer resistivity-depth models are a classical approach to solving the 1D problem and a variety of automated inversion methods is available for fitting such models to electrical sounding data.

8.2.2 Zohdy's inversion

A particularly fast iterative method for obtaining a layered 1D resistivity-depth model directly from a VES curve was described by Zohdy (1989) for the case of Schlumberger and Wenner soundings. In the following, the algorithm will be referred to as Zohdy's inversion. It takes advantage of the property of equivalence among multilayer media and, in contrast to other methods, is fully automatic and does not require a starting model, i.e. an initial guess of the number of model layers, their thicknesses or their resistivities. Conceptually, Zohdy's inversion is based on a number of specific properties observed with all theoretical sounding curves for horizontally stratified, laterally homogeneous media, regardless of the number of layers or the resistivity distribution with depth. These properties are (Zohdy, 1989):

1. Computed apparent resistivities are always positive.

2. The form of the sounding curve follows the form of the true resistivity-depth curve.

3. The maximum change in apparent resistivity always occurs at an array spacing that is larger than the depth at which the corresponding change in true resistivity occurs, i.e. a sounding curve is "out-of-phase" with the true resistivity-depth curve and shifted towards greater depths.

4. The amplitude of a sounding curve is always less than or equal to the amplitude of the true resistivity-depth curve.

5. If the true resistivity of a thick layer in a multilayer model is changed, the apparent resistivity along a corresponding segment of the sounding curve also changes accordingly.

As a consequence of these properties, it is evident that model layer depths derived from a measured sounding curve must be shifted to the left in order to bring the assumed layering more or less in phase with the true resistivity-depth distribution. Additionally, the assumed resistivities must be adjusted

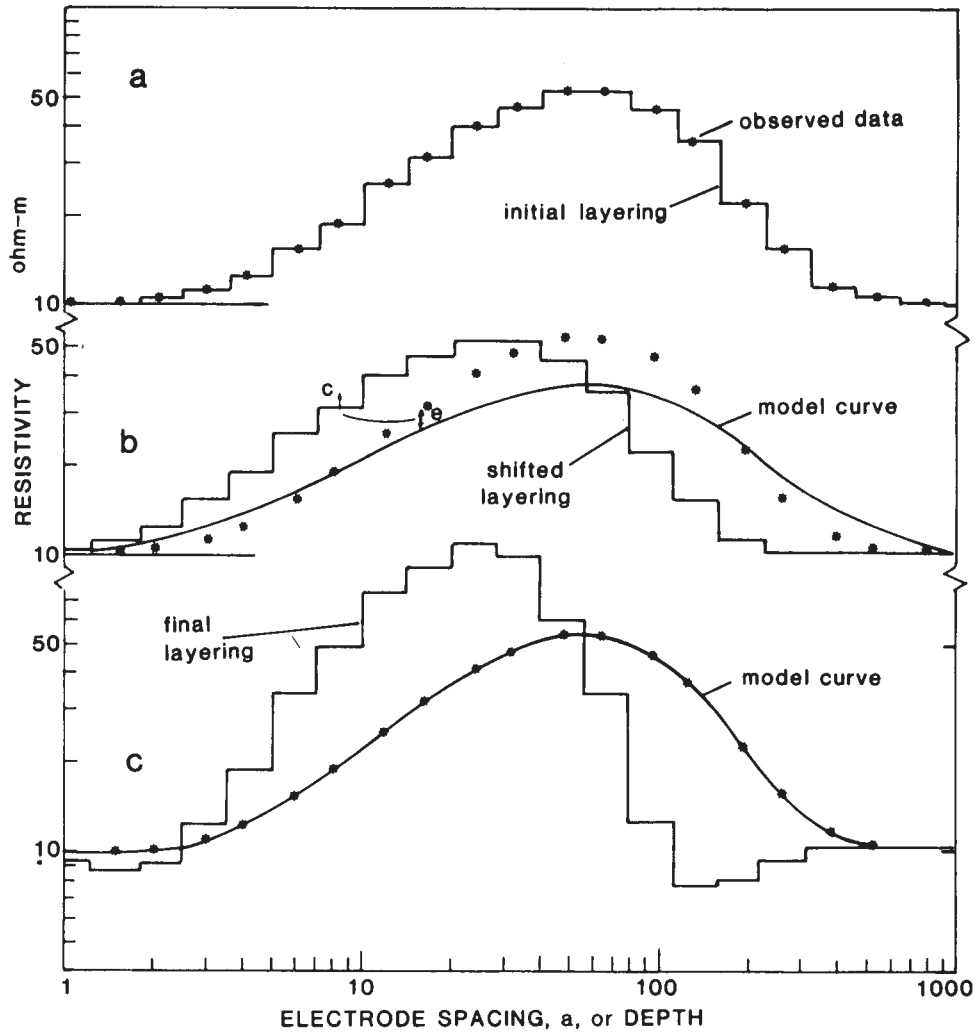

Figure 8.4: The principle of Zohdy's inversion algorithm (Barker, 1992): (a) Observed data and initial layering. (b) Shifted layering and resulting model sounding curve. (c) The final layering and resulting model curve.

to approximate the amplitude of the true resistivities. The essence of Zohdy's algorithm is therefore to determine the appropriate amount by which to shift the depths and adjust the resistivities, without prior knowledge of the true resistivity-depth distribution. The iterative procedure relies on the following initial assumptions:

- The number of layers in the model equals the number of digitised points on the observed curve.
- The depths of the model layers are equal to the digitised electrode spacings which are equally spaced on a logarithmic scale.
- The true resistivities of the starting model equal the observed apparent resistivities.

The inversion is then carried out in two iterative parts:

Depth determination. The following calculation is performed to determine the depth shift required in order to bring the assumed layering and the unknown layering "in-phase": Firstly, a theoretical sounding curve is computed for the current multilayer model by convolution. The RMS error is computed as a measure of the difference between the observed and calculated apparent resistivities. Subsequently, all layer depths are decreased by a small arbitrary amount (e.g. 10 %). A new sounding curve with an associated new RMS error is then computed and the two RMS errors are compared. If the new RMS is smaller, then the shallower depths are closer to the true, but unknown, depths than the original ones. This procedure is repeated until the RMS is minimised, i.e. any further reduction of the depths would shift the layering too far.

Resistivity determination. Once the optimum set of depths is determined, the model resistivities must be adjusted to optimise the fit. The following process is performed for each datum point on the observed and calculated sounding curves: if the computed apparent resistivity at the j-th spacing is less (or greater) than the corresponding observed apparent resistivity, the corresponding true resistivity of the j-th layer is increased (or decreased) so that the calculated apparent resistivity will approach the observed one. A layer resistivity is adjusted according to

$$\rho_{i+1}(j) = \rho_i(j)\frac{\bar{\rho}_0(j)}{\bar{\rho}_{ci}(j)} \tag{8.1}$$

where i is the number of the iteration, j is the index of layers and spacings, $\rho_i(j)$ is the j-th layer resistivity at the i-th iteration, $\bar{\rho}_{ci}(j)$ is the calculated apparent resistivity at the j-th spacing for the i-th iteration, and $\bar{\rho}_0(j)$ the observed apparent resistivity at the j-th spacing. A new sounding curve is then calculated using the adjusted layer resistivities. A new RMS error is now computed and compared to the previous one. The procedure is repeated until the calculated curve matches the observed one as closely as possible.

8.2.3 Application to towed-array CR data

The application of Zohdy's inversion to towed-array CR data required several adaptations as the original algorithm was only designed for Schlumberger and Wenner DC soundings. Zohdy (1989) rather vaguely states that, besides these two configurations, the five properties described on p. 212 also apply to most, but not all, dipole-dipole sounding curves for horizontally stratified media. In the light of the intended application to CR, this statement required some clarification. Das and Ghosh (1973) found that, for horizontally stratified media, i.e. a layered earth, apparent resistivities ρ_a obtained with the azimuthal dipole-dipole array for different angles θ (cf. Figure 3.4) are the same as, and equivalent to, those measured with a Schlumberger array. This equivalence explicitly applies to the equatorial dipole-dipole array which is a special case of the azimuthal dipole-dipole array for $\theta = \pi/2$. However, it does *not* apply to the inline (or polar) dipole-dipole array. The consequences are:

- Equatorial dipole soundings yield the same VES curves as Schlumberger soundings over a horizontally stratified earth.
- Existing Schlumberger curves may be used for the interpretation of equatorial dipole soundings.
- The forward filters used to calculate VES curves from a layered model are the same for the Schlumberger and equatorial dipole geometries.
- Zohdy's inversion applies to equatorial dipole soundings without change and can be used for the interpretation of multi-offset towed-array CR data acquired with equatorial geometry.

Other issues arise from the fact that a VES curve obtained from multi-offset towed-array CR data may have a rather different character from a VES curve obtained from conventional DC soundings. In the case of towed-array CR the number of dipole offsets is determined by the number of receiver dipoles available, which is likely to be much smaller than the number of spacings on a classical DC sounding curve. The resulting CR sounding curve is only defined by a limited number of points.

The forward part of Zohdy's algorithm calculates the theoretical sounding curve by linear filtering (Ghosh, 1971a,b). Zohdy uses the improved filter described by O'Neill (1975) which uses six points per logarithmic decade and thus provides higher accuracy for stronger resistivity contrasts. The six-point filter is thought to be commensurate with the electrode spacings used in conventional DC soundings and considered optimal for defining the form of a sounding curve (Zohdy, 1989). In the context of this chapter, the CORIM™ array geometry is used as an example for a multi-offset towed CR array. The six CORIM™ channels provide a sufficient amount of data in a single pass of the instrument to be interpreted as resistivity soundings. However, as the VES data are spaced at linear rather than regular logarithmic intervals, they must be resampled to

Receiver no.	1	2	3	4	5	6
Dipole separation [m]	1.00	2.00	3.00	4.00	5.00	6.00
Sampling distance [m]	1.00	1.47	2.15	3.16	4.64	6.81

Table 8.1: Spacings at which CORIM™ VES curves were resampled to match the six-point forward filter.

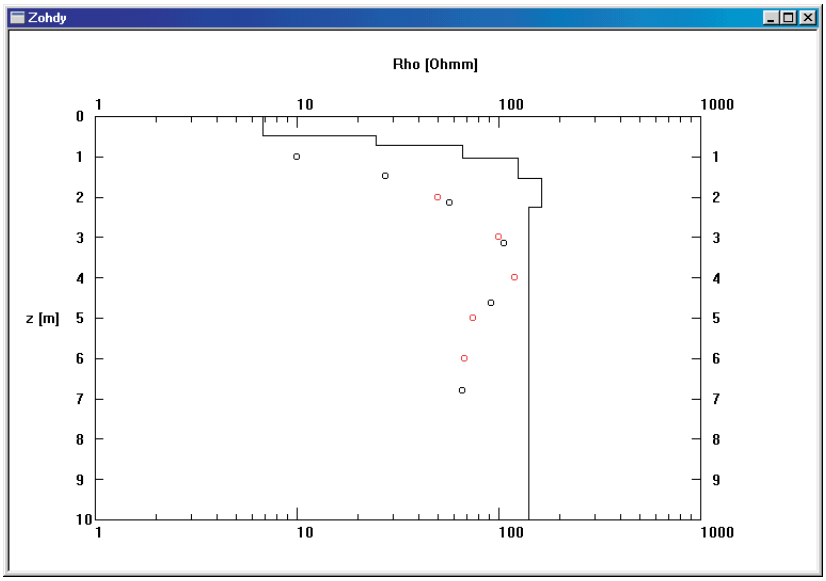

Figure 8.5: Example of Zohdy's inversion applied to a VES curve derived from CR data. Red markers: measured data. Black markers: resampled data. Black line: 1D Zohdy model.

comply with the forward filtering process. Table 8.1 shows suitable spacings.

Figure 8.5 shows the result of Zohdy's inversion applied to a single VES curve extracted from towed-array CR field data. The measured data are plotted at a pseudodepth of r, indicated by red markers. This curve was resampled at the locations given in Table 8.1 by means of cubic spline interpolation. Zohdy's algorithm was then used to determine a 6-layer 1D resistivity model, indicated by the black line in Figure 8.5. The properties of this model reflect the simplified approach taken by Zohdy's technique. The shape of the resistivity-depth function resembles that of the VES curve. The number of layers is always identical to the number of sampling points on the VES curve. The maximum model resistivity occurs at a shallower depth compared to the VES curve and is larger than the measured maximum.

8.2.4 Examples

The use of Zohdy's inversion for the interpretation of towed-array CR data will now be demonstrated in two examples. The first example is a synthetic dataset representing a vertical contact under a homogeneous surface layer. This example can help assess to what extent Zohdy's algorithm is able to reconstruct simple resistivity contrasts. The second example is a field dataset representing a simple geological transition. Due to its inherent 1D nature, the Zohdy method cannot be expected to produce accurate models of a highly inhomogeneous subsurface. In the context of CR however, it can be used as a real-time indicator in the field for the presence of anomalous zones which may then be interpreted more accurately by post-survey modelling.

8.2.4.1 Synthetic data: shallow vertical contact

The resistivity model considered for this example consists of a shallow vertical contact buried beneath a uniform, moderately resistive surface layer (Figure 8.6). The contact is between a more resistive (50 Ωm) and a more conductive (10 Ωm) halfspace, corresponding to a resistivity contrast of 5:1. The fundamental information about this model that one would hope to retrieve from any

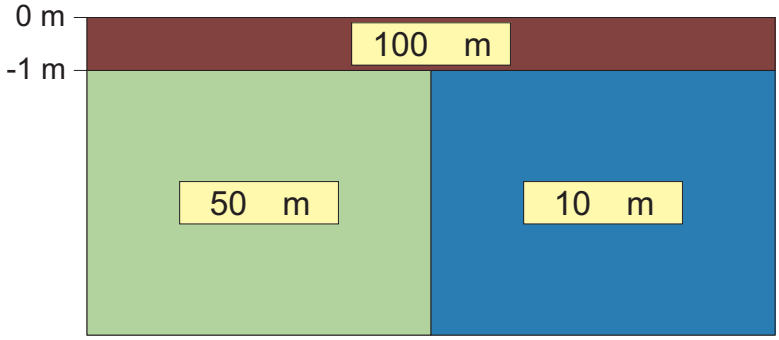

Figure 8.6: Cross-section through the resistivity model of a shallow vertical contact.

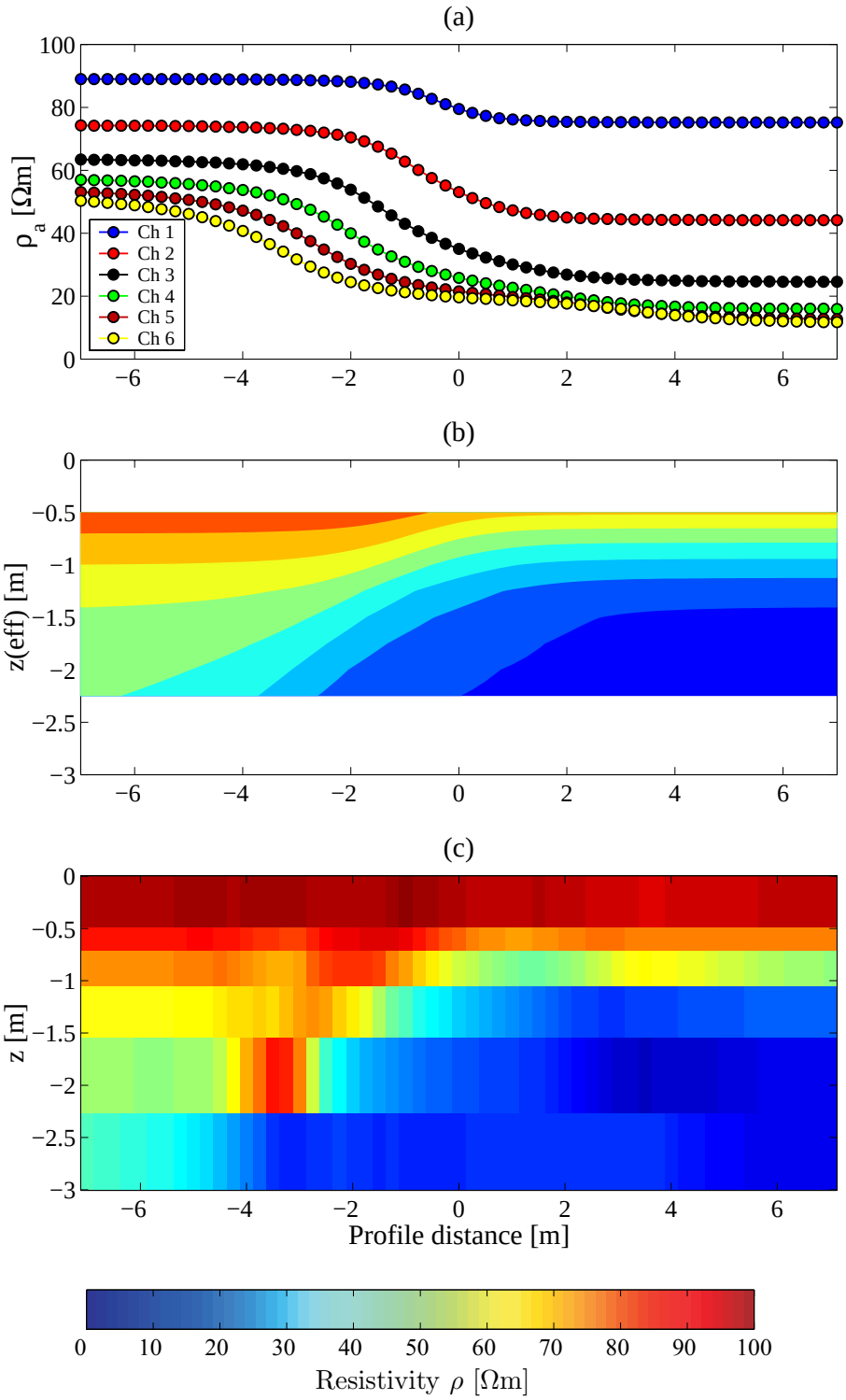

Figure 8.7: Quasi-2D interpretation of synthetic towed-array CR data with CORIM™ geometry. (a) Apparent resistivity profiles of modelled data (vertical contact at 0 m). (b) Apparent resistivity pseudosection of modelled data. (c) Zohdy model.

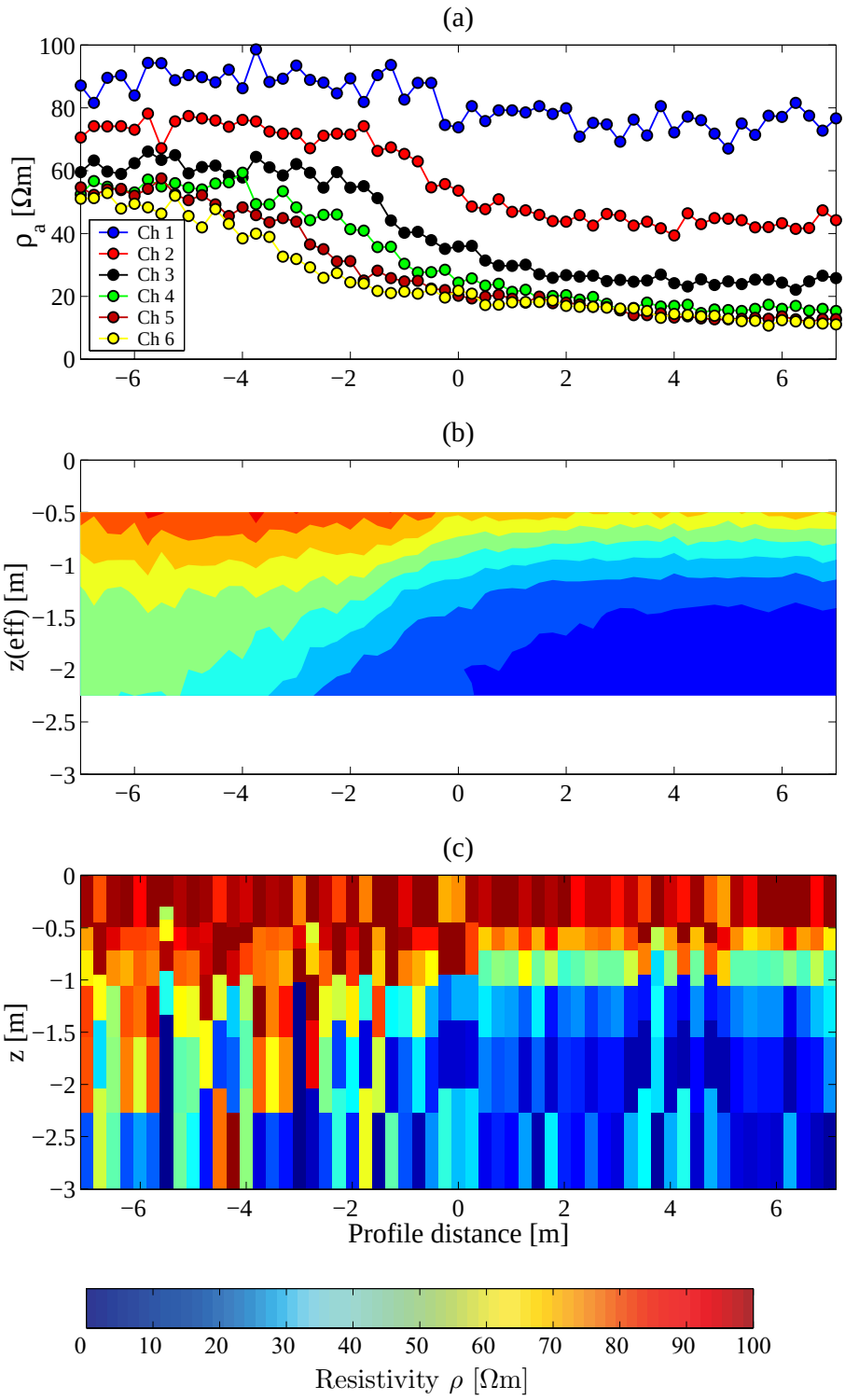

Figure 8.8: Quasi-2D interpretation of synthetic towed-array CR data with added Gaussian noise. (a) Apparent resistivity profiles of modelled data (vertical contact at 0 m, 5% noise added). (b) Apparent resistivity pseudosection of modelled data. (c) Zohdy model.

measured data are (a) the depth of the anomaly (here the vertical contact), (b) its lateral location and (c) an estimate of the true resistivities involved.
Synthetic apparent resistivity data for a six-receiver system with CORIM™ geometry were obtained using a finite-difference DC resistivity forward modelling algorithm by Spitzer (1995). Simulating towed data acquisition required the calculation of apparent resistivities at a large number of positions and small intervals (e.g. 0.25 m) so that a relatively fine model discretisation was necessary to achieve sufficient numerical accuracy. Spitzer's algorithm allows the use of non-uniform grids and arbitrary electrode positions relative to model nodes so that computational expense could be kept to a minimum. The resulting (noise-free) apparent resistivity profiles for all six channels are shown in Figure 8.7a, where the position of the vertical contact is at a profile distance of 0 m. All datum points are centred on the respective array midpoints. Figure 8.7b shows the same data in the form of a contoured apparent resistivity pseudosection, in which the apparent resistivity values from different array spacings have been plotted at their respective pseudodepths (median depth z_{med}, cf. Section 3.1.4.2 and Table 7.1). The inverted dataset (Zohdy model) is shown in Figure 8.7c as a continuous sequence of layered 1D models, in which the model layers are represented by narrow bars coloured according to their model resistivities.

Noise-free response. The model response (profiles and pseudosection) shows a pronounced transition between the two quarterspaces which can be recognised in all channels. The wavelength of the transition is of the order of more than twice the dipole offset of the respective array. This effect of "smear-out" of spatial information in measured data is well-known in resistivity methods. The objective of any inversion algorithm is to reverse this process and to reconstruct a "true" model of the subsurface where the feature causing the "smearing" effect is focused and relocated to its original position. This is the fundamental difficulty that any real-time approach to CR data interpretation is faced with, considering that only data acquired up to the current position of the array is available for interpretation.
The pseudosection (Figure 8.7b) shows the basic qualitative properties of the underlying model in terms of the transition from a more resistive to a more conductive region. The receiver with the longest offset (Rx 6) measures apparent resistivities which are very close to the true model resistivities. However, information about the depth of the transition, which only occurs below the surface layer at 1 m, is vague and an interpretation based purely on the pseudosection would probably lead to a false conclusion about the depth and vertical extent of the anomalous zone. The true geometry of the contact and its lateral position are unclear from the pseudosection, but might perhaps be guessed from the apparent resistivity profiles as a result of the symmetry of the response.
Compared to the pseudosection, the Zohdy model (Figure 8.7c) gives additional clues with regard to the nature of the true model. Although the Zohdy model does not (and cannot be expected to) reconstruct the vertical contact itself, it clearly confirms the continuity of the surface layer, leaving anomalous regions confined to the lower part of the model. The Zohdy layer depths remain un-

changed throughout the profile and only the layer resistivities have been altered. In agreement with the true model, the topmost Zohdy layer ($0 \geq z > -0.5$) is estimated at a resistivity close to 100 Ωm. The next layer ($-0.5 \geq z > -0.74$) is only slightly more conductive, but still laterally coherent. Only the third Zohdy layer ($-0.74 \geq z > -1.08$) shows a distinct lateral change near a profile distance of 0 m. This depth corresponds well with the depth of the contact in the true model. Below this depth, the resistivities in the right-hand part of the Zohdy model are estimated relatively accurately at values of the order of 10 Ωm. The left-hand part is dominated by an artefact in the form of a diagonal resistive feature. The leftmost region of the model shows approximately correct resistivities around 50 Ωm. The slightly poorer definition of the left model part may be due to the smaller resisitivity contrast between the surface layer and the base of the model.

Noisy response. The quality of the result can change dramatically if contamination of the data by measurement noise is considered. Figure 8.8 shows the results of the Zohdy inversion for the same dataset as before, after 5% of stochastic noise with Gaussian distribution has been added to the modeled apparent resistivity values. While the effect of the noise on apparent resistivity profiles (Figure 8.8a) and pseudosection (Figure 8.8b) is moderate, the model obtained from the Zohdy inversion (Figure 8.8c) is highly sensitive towards changes in data quality. Although the sharp vertical contrast at 1 m depth is still recognisable in the Zohdy model, the vertical contact and the associated lateral transition between the more resistive and the more conductive zone is now less obvious.

8.2.4.2 Field data: river terraces at Chetwynd Barracks

The second example consists of a field dataset collected with the CORIM™ system at the Chetwynd Barracks training site, Chilwell, Nottingham. Apparent resistivity data from six receivers were acquired on a linear profile along river terraces on a gently sloping hillside on the fringes of the Trent River valley. The area is underlain by Triassic mudstones. The profile was approximately 150 m long and extended from clay-rich deposits upslope into alluvial sands and gravels in the valley. This geological setting is responsible for a gradual transition from conductive ground on the hillside into resistive material in the valley.
Unfiltered apparent resistivity profiles are shown in Figure 8.9a using a logarithmic scale. The survey started on the hillside and continued downslope into

Layer	Description	Depth [m bgl]
1	Loose, soft, amorphous, loamy topsoil	0.0–1.0
2	Sandy clay with occasional gravels	1.0–6.5
3	Alluvial gravel deposits	6.5–9.0

Table 8.2: Approximate ground lithology at Chilwell Barracks at the bottom of the slope.

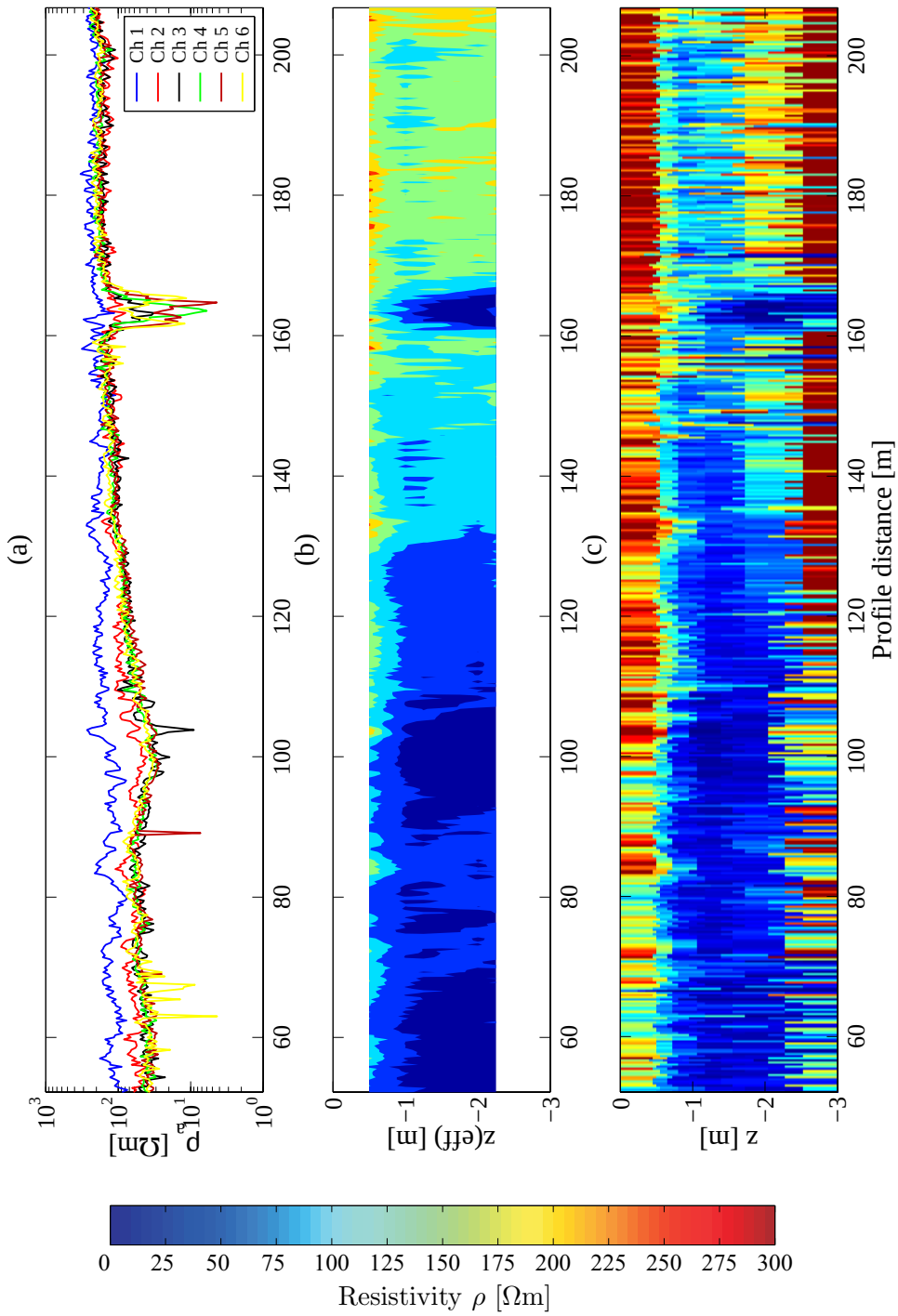

Figure 8.9: Quasi-2D interpretation of towed-array CR field data acquired with the CORIM™ system. (a) Apparent resistivity profiles. (b) Apparent resistivity pseudosection. (c) Zohdy model.

the valley. Over the course of the profile, apparent resistivity values increase from under 100 Ωm to 200–250 Ωm. A zone of anomalously low resistivities on all channels at profile distances between 160 m and 170 m is associated with a buried segment of concrete pipe that serves as an artificial shallow target for geophysical testing. The raw data are of good quality and are only marginally affected by motion-induced noise in the form of outliers on individual channels. The same data displayed as a contoured apparent resistivity pseudosection (Figure 8.9b) clearly show the gradual transition between the two geological regimes, yet in a rather qualitative manner. There is some indication of a more resistive surface zone along the profile.
Similar to what was found for the synthetic data, the Zohdy model (Figure 8.9c) despite its simplicity provides additional clues to the true nature of the subsurface. It suggests the presence of a surface layer of between 0.5 m and 0.7 m thickness, which becomes increasingly resistive as the profile continues downslope. The highest resistivities of 300Ωm and more are recorded in the valley beyond a profile distance of 170 m. In the valley, the highly resistive surface layer coincides with a resistive layer at depth ($z < -2$ m). This layer does not appear to be present further upslope (up to a profile distance of approximately 120 m).

8.3 2D interpretation

In areas with a complex subsurface, the application of 1D sounding methods to quasi-2D interpretation is more likely to be inadequate and interpretation of multi-offset resistivity data by two- or three-dimensional methods will be more appropriate (e.g. Keller, 1993). Under circumstances where real-time (or on-site) data processing and interpretation is not required, a full post-survey 2D interpretation of linear profile data is nearly always preferable to the quasi-2D approach (Dahlin, 1993). Methods relevant to the 2D interpretation of towed-array CR data are described in this section.

8.3.1 2D iterative least-squares inversion

2D automated interpretation techniques seek to optimise observed multi-offset apparent resistivity data against a two-dimensional earth model. This process is crucial for the concept of 2D resistivity imaging (Griffiths and Barker, 1993) or 2D ERT. Different methods for the automated interpretation of arbitrary resistivity distributions are available. Early approaches were limited to specific model geometries, so that a priori knowledge about the subsurface was required (Pelton et al., 1978a; Tripp et al., 1984; Smith and Vozoff, 1984). Barker (1992) introduced a 2D algorithm using simple parameter adjustments similar to Zohdy's 1D inversion. A true "inversion" of an arbitrary resistivity distribution however involves the calculation of the sensitivity distribution for the chosen model (in the form of the Jacobian matrix), which takes into account how changes in the model parameters (i.e. model resistivities) affect individual apparent resistivity datum points.
For the purposes of interpreting multi-offset towed-array CR data, a modern,

fully automated resistivity inversion algorithm (RES2DINV; Loke and Barker, 1995) based upon the least-squares optimisation method (Lines and Treitel, 1984) has been considered. RES2DINV is cell-based, i.e. the subsurface is divided into a number of model cells so that either the finite difference or finite element methods are applicable. In order to optimise the fit between resistivity model and a set of m measured data values, an initial model is modified in an iterative manner so that the difference between the model response $\mathbf{f} = (f_1, f_2, \ldots, f_m)^T$ and the observed data $\mathbf{y} = (y_1, y_2, \ldots, y_m)^T$ is reduced[1]. The difference is given by the discrepancy vector $\mathbf{g} = \mathbf{y} - \mathbf{f}$. The n model parameters can be represented by the vector $\mathbf{q} = (q_1, q_2, \ldots, q_n)^T$. For a least-squares optimisation, the modification of the model parameters must be such that the sum of squares error $E = \mathbf{g}^T\mathbf{g} = \sum_{i=1}^{m} g_i^2$ is minimised. A reduction of this error can be achieved by solving the following Gauss-Newton equation for the model parameter change vector $\Delta\mathbf{q}$ (Lines and Treitel, 1984):

$$\mathbf{J}^T\mathbf{J}\Delta\mathbf{q} = \mathbf{J}^T\mathbf{g} \tag{8.2}$$

where $\mathbf{J}$ is the Jacobian matrix of size $m \times n$ of partial derivatives. The elements of the Jacobian are given by

$$J_{ij} = \frac{\partial f_i}{\partial q_j} \tag{8.3}$$

i.e. the change in the ith component of the model response due to a change in the jth model parameter. Once the parameter change vector has been determined for an iteration k, a new model is then obtained by

$$\mathbf{q_{k+1}} = \mathbf{q_k} + \Delta\mathbf{q_k} \tag{8.4}$$

In order to avoid unrealistic changes to the model due to potential near singularities of the product $\mathbf{J}^T\mathbf{J}$, the Gauss-Newton equation (8.2) is modified according to

$$(\mathbf{J}^T\mathbf{J} + \lambda\mathbf{I})\Delta\mathbf{q} = \mathbf{J}^T\mathbf{g} \tag{8.5}$$

where $\mathbf{I}$ is the identity matrix and λ is a damping factor. This modification is commonly known as the Marquardt-Levenberg or ridge regression method (Lines and Treitel, 1984). It has been successfully used in the inversion of resistivity data with a small number of model parameters, e.g. resistivity soundings with a small number of layers. For large numbers of model parameters however, such as encountered in 2D and 3D resistivity inversion models with many cells, this method can produce erratic resistivity distributions with spuriously high or low resistivity zones. To overcome this problem, an additional constraint can be introduced which demands model smoothness. This type of approach has become known as Occam's inversion (Constable et al., 1987; deGroot-Hedlin and Constable, 1990). The mathematical form of the smoothness-constrained least-squares method involves a further modification to the Gauss-Newton equation (8.5) (Ellis and Oldenburg, 1994a):

$$(\mathbf{J}^T\mathbf{J} + \lambda\mathbf{F})\Delta\mathbf{q} = \mathbf{J}^T\mathbf{g} - \lambda\mathbf{F}\mathbf{q} \tag{8.6}$$

[1]The vector $\mathbf{x}^T$ denotes the transpose of $\mathbf{x}$.

where $\mathbf{F} = \alpha_x \mathbf{C_x^T C_x} + \alpha_y \mathbf{C_y^T C_y}$ and $\mathbf{C_x}$ and $\mathbf{C_y}$ are the smoothing matrices in the x- and y-directions, respectively. α_x and α_y are the relative weights given to the smoothness filters in these directions.

Equation 8.6 represents an l_2-norm smoothness-constrained optimisation, i.e. the *square* of the spatial changes, or roughness, of the model resistivity values is minimised. This is the default mode of operation of RES2DINV and applies to models where the true subsurface resistivity is expected to vary in a smooth and gradational manner. For a "blocky" subsurface, i.e. if the subsurface contains a number of more or less homogeneous regions with sharp boundaries between them, an l_1-norm optimisation method that minimises *absolute* changes (Claerbout and Muir, 1973) tends to give significantly better results. This mode of operation ("robust inversion") has been found useful for the interpretation of resistivity datasets from environmental and engineering investigations involving engineered subsurface targets.

8.3.2 Application to towed-array CR data

The application of fully automated resistivity inversion algorithms such as RES2DINV to towed-array CR data holds a number of potential pitfalls. These are mainly related to the different nature of towed-array datasets compared to fixed-array resistivity data (cf. Section 8.1). The first important issue is that RES2DINV (like similar algorithms) assumes a regularly spaced sequence of electrode positions along the survey profile. The lateral discretisation of the model in RES2DINV uses constant cell widths while the vertical discretisation can be adapted according to the median depths of the measured data. If any of the array separations of the towed CR array are not suitable integer multiples of the lateral sampling distance during the CR survey, it may not be possible to select a reasonably large electrode spacing in RES2DINV which can accommodate all possible sensor positions along the profile. Although it is always possible to select a very small fundamental electrode spacing to fulfill the criterion (e.g. $d = 0.01$ m), small spacings d will inevitably increase the overall model size by a large factor which may render the model unmanageable. For example, if a single four-point array with a spacing of $r = 1$ m were used to acquire data at a sampling distance of $\Delta s = 0.3$ m, a fundamental electrode spacing of $d = 0.1$ m would have to be selected in order to accommodate all the positions taken up by the current and potential electrodes during the profile run. Over a profile of 100 m length, a model with 1000 electrode positions would thus be required to interpret the dataset as a whole. The upper limit of permissible electrodes in RES2DINV is presently of that order. Yet, not all electrode positions defined in the model would actually be associated with datum points because of the sub-optimal choice of d. Had a sampling distance of $\Delta s = 0.25$ m been employed, an optimal fundamental electrode spacing of $d = 0.25$ m could be used to define the model and merely 400 electrodes would suffice to interpret the 100 m profile as a whole. Matters may be even more complicated if multi-offset arrays are used and the individual array separations are "incompatible" whereby they do not share a common denominator. If towed-array CR datasets

are to be interpreted by 2D resistivity inversion, it is recommended that the lateral sampling distance of the towed-array survey is adjusted to the array geometry employed (cf. Section 8.1.2).
The second important issue about towed-array CR datasets is the fact that the number of available array offsets with present towed-array CR instruments is comparatively small compared with the number of offsets typically employed in a conventional 2D DC resistivity survey. In other words, the depth coverage of multi-offset towed CR arrays tends to be less dense, so that the vertical resolution of 2D models derived from towed-array CR data may be limited to a smaller number of model layers. Since the lateral sampling density of a towed-array survey may be very high, this may lead to some degree of disproportion between the lateral and vertical discretisations of the 2D model. When inverting towed-array CR data, it is therefore recommendable to carefully design the model mesh by hand, without relying on advanced features such as automatic mesh generation.

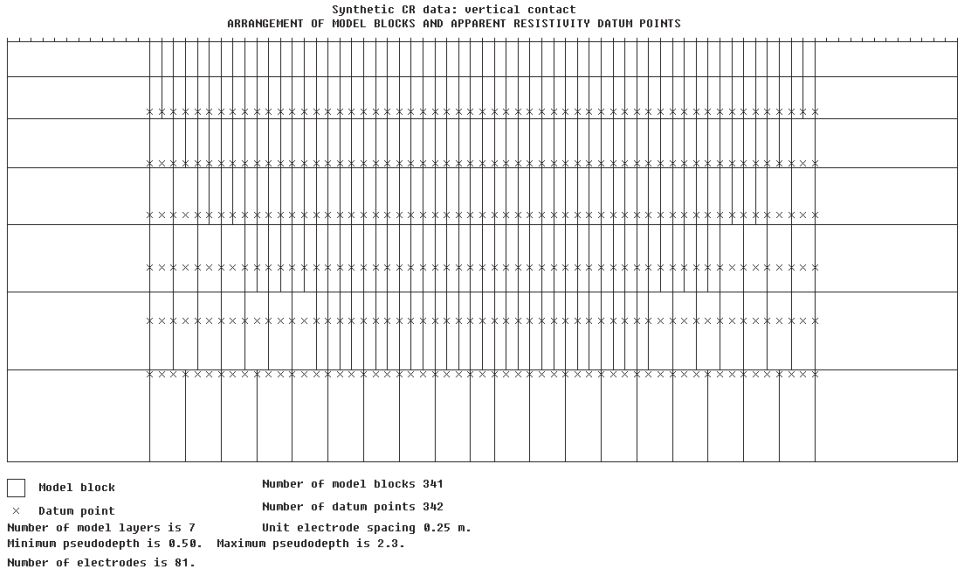

Figure 8.10: Example of model discretisation for the 2D inversion of towed-array CR data.

8.3.3 Examples

The use of 2D resistivity inversion for the interpretation of towed-array CR data will now be demonstrated using the same two examples as previously in the quasi-2D case, thus allowing comparison between the two approaches with regard to performance.

8.3.3.1 Synthetic data: shallow vertical contact

The first example is represented by a resistivity model identical to the one shown in Figure 8.6, i.e. a shallow vertical contact buried beneath a uniform,

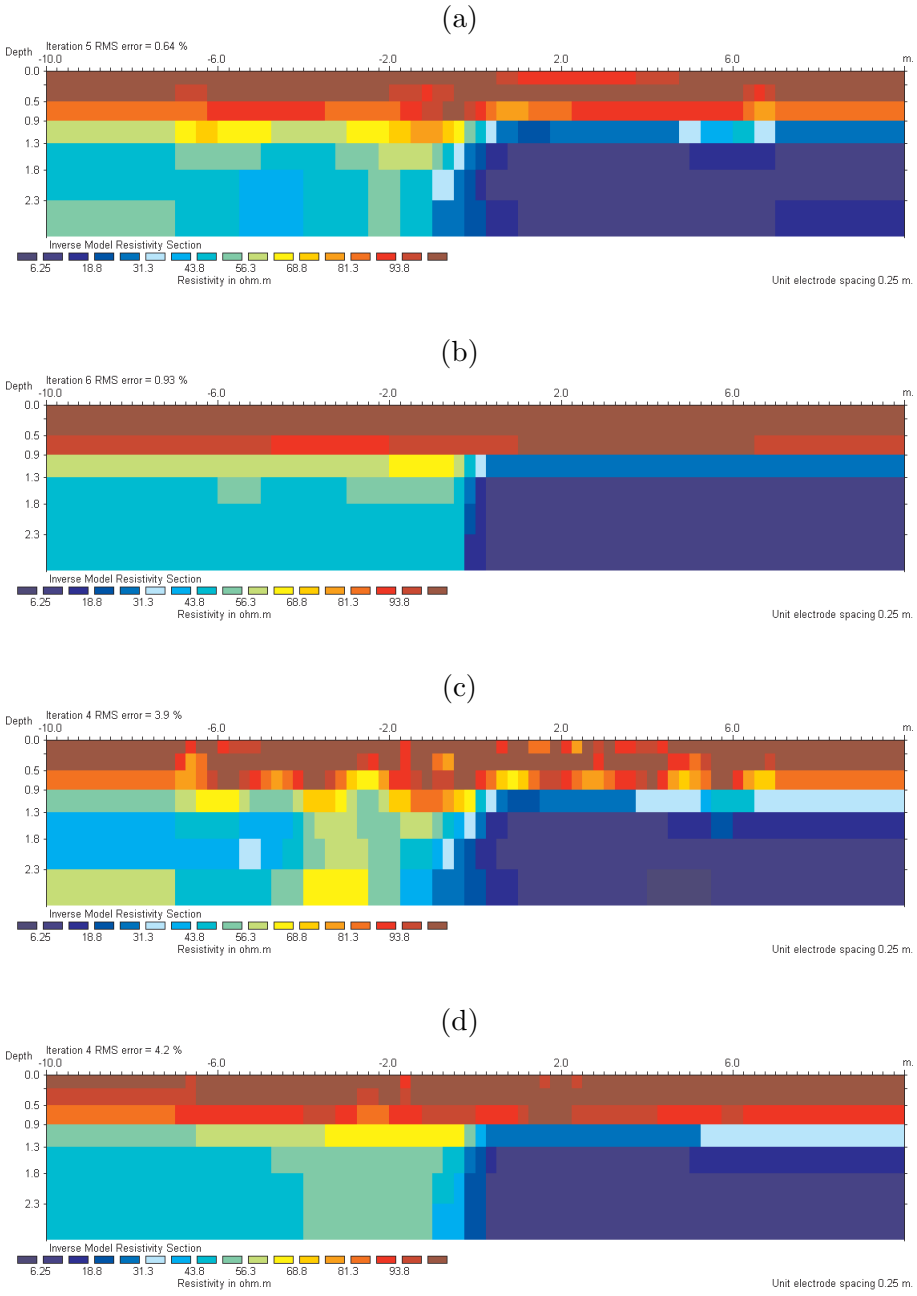

Figure 8.11: 2D inversion of synthetic towed-array CR data (CORIM™ geometry) for a shallow vertical contact. (a), (b) inverted model for noise-free data; (c), (d) inverted model for noisy data (5% Gaussian noise, same as in Figure 8.8); (a), (c) smoothness constraint; (b), (d) robust constraint.

Layer	Thickness [m]	Depth to bottom [m]
1	0.25	0.25
2	0.29	0.54
3	0.34	0.88
4	0.40	1.29
5	0.47	1.75
6	0.55	2.30
7	0.64	2.94

Table 8.3: Suitable layer parameters for inversion of CORIM™ data using RES2DINV.

	Model and inversion type	No. of iterations	RMS error [%]
(a)	Noise-free, smoothness-constrained	5	0.64
(b)	Noise-free, robust	6	0.93
(c)	5% Gaussian noise, smoothness-constrained	4	3.90
(d)	5% Gaussian noise, robust	4	4.20

Table 8.4: Number of iterations and RMS error values for the inversion of synthetic CORIM™ data over a shallow vertical contact.

moderately resistive surface layer. The same synthetic CORIM™ data that were used for the quasi-2D interpretation (cf. Section 8.2.4.1) were now presented to RES2DINV for a full 2D inversion.

As the apparent resistivity data had been calculated at intervals of 0.25 m, this distance was chosen as the fundamental electrode spacing in the RES2DINV model. Calculations had been performed for array positions over a distance of 20 m, so that a total number of 81 electrode positions were used in the model (Figure 8.10). The number of apparent resistivity datum points per CORIM™ channel was smaller (57) due to the loss of coverage at the model edges. The total number of datum points considered was 342. With regard to the vertical discretisation, the thickness of the top model layer was set to be the same as the fundamental electrode spacing, i.e. 0.25 m. Reflecting the general loss of resolution of the resistivity method with depth, it is reasonable to let the model layer thicknesses increase accordingly. The factor by which layer thicknesses are increased was set to 1.17, which resulted in a 7-layer model with a maximum depth extent of nearly 3.0 m (Table 8.3). In order to keep the number of model parameters smaller than the number of datum points, the discretisation was modified such that cells at the bottom and near the edges of the model had greater widths. The total number of model parameters was 341.

Analogous with the quasi-2D case, two different datasets were considered. One dataset consisted of noise-free apparent resistivities as obtained from the forward modelling, while a second dataset was contaminated by Gaussian noise with 5% amplitude. For each of the two datasets, two different inversion strategies were attempted. For the first approach, the conventional smoothness-constrained least-squares method (an l_2-norm optimisation) was used, while the second strategy involved the use of a robust inversion (an l_1-norm opti-

misation). The first option was expected to give a smoother result, while the second option was thought to be more suited to reconstructing the sharp boundary represented by the vertical contact.
The results of the inversion process are shown in Figure 8.11 using colour-coded model blocks. Figure 8.11a has the inverted model for the noise-free dataset using the smoothness-constrained method. The reconstruction of the general model properties, including absolute resistivities, is very accurate and the definition of the model geometry clearly better than in the quasi-2D approach (cf. Figure 8.7c). However, compared to the result of the robust inversion in 8.11b, the smoothness-constrained method has produced an inferior model. The robust inversion has recovered the boundaries of the model regions extremely well, including the extent of the surface layer and the vertical contact at $x = 0$ m. Due to the finite discretisation, the accuracy of the spatial reconstruction of boundaries is limited by the dimensions of the model cells.
Figure 8.11c shows the inverted model for the noisy dataset using a smoothness constraint. Compared to the noise-free case, the model is clearly less well defined and the fit between data and inverted model is worse in terms of the RMS error values (Table 8.4). In comparison with the quasi-2D case however, the advantages of the full 2D inversion are obvious (cf. Figure 8.8c). The individual regions of the model are much more coherent and the resulting model is much smoother. The result is even more convincing for the noisy dataset under a robust constraint (Figure 8.11c). In this case, the model properties (including sharp boundaries) have been recovered with high accuracy, while at the same time successfully suppressing much of the noise in the data (cf. Figure 8.7a).

8.3.3.2 Field data: river terraces at Chetwynd Barracks

The second example is the CORIM™ field dataset collected at Chetwynd Barracks (cf. Section 8.2.4.2). Again, the same data that were used in the quasi-2D case have been presented to RES2DINV for a full 2D inversion.
A fundamental electrode spacing of 0.25 m was chosen for lateral model discretisation. For a profile length of 163 m, a total number of 653 electrode postitions

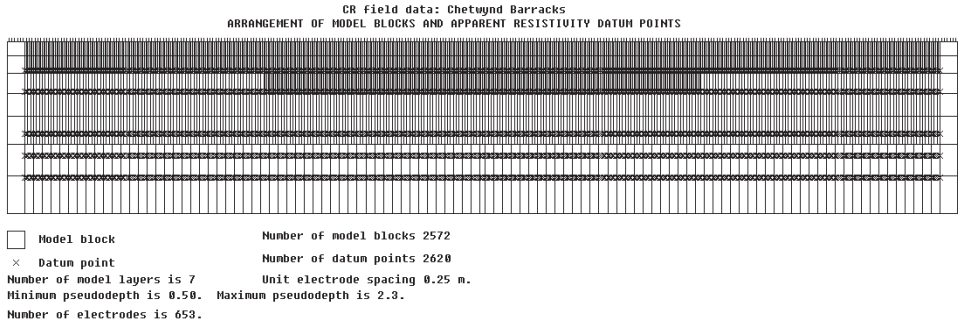

Figure 8.12: Example of model discretisation for the 2D inversion of CORIM™ field data, Chetwynd Barracks.

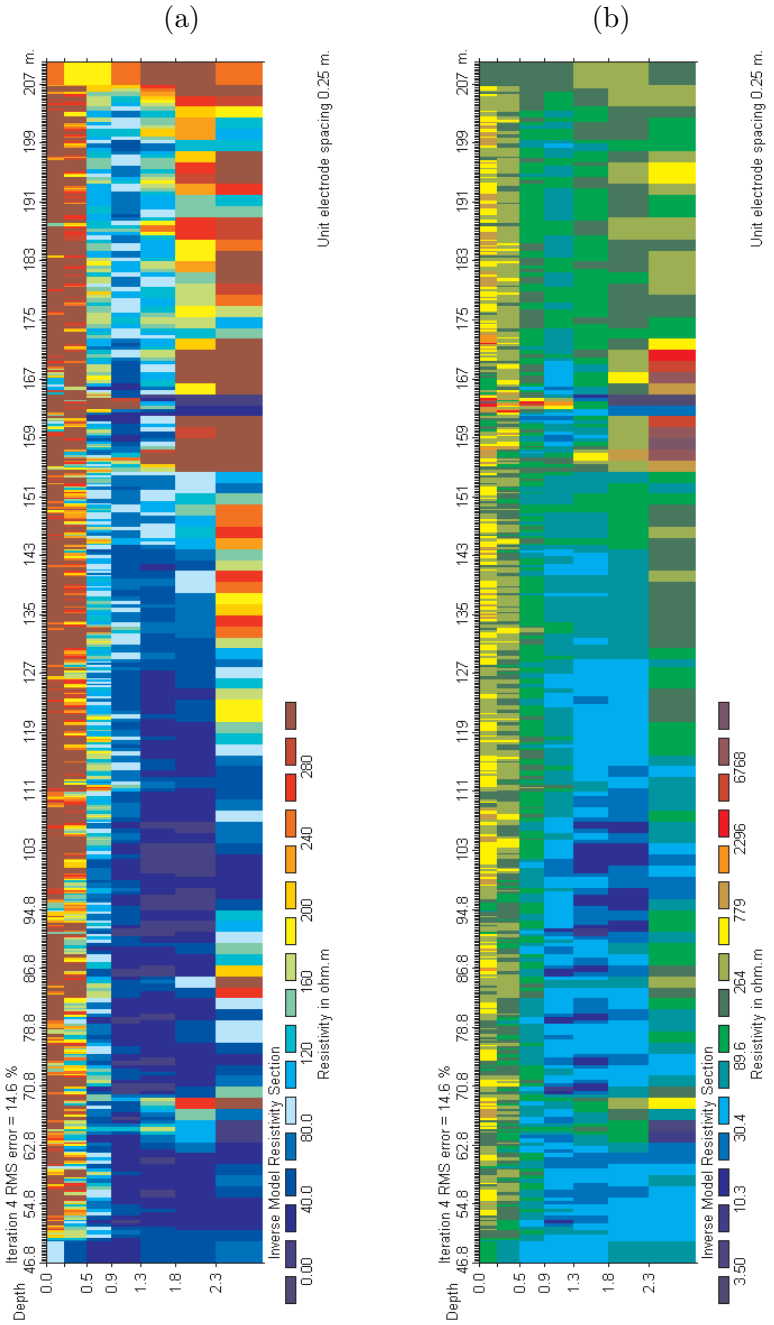

Figure 8.13: 2D inversion of CORIM™ field data, Chetwynd Barracks. (a) Inverted model (smoothness-constraint) colour-coded with the same colour scale as in the quasi-2D case; (b) inverted model (smoothness-constraint) using an optimised logarithmic colour scale.

were used in the model (Figure 8.12). The total number of apparent resistivity datum points was 2620. The same vertical discretisation that was employed for the synthetic data was also used for the field dataset, resulting in a 7-layer model with a total number of model parameters of 2572.
The dataset was inverted using a conventional smoothness constraint. The resulting resistivity model with colour-coded model cells is shown in Figure 8.13. Figure 8.13a represents the same colour scale that has been used in the quasi-2D case and for the 2D inversion of the synthetic data. The absolute resistivity values reconstructed from the apparent resistivity data are very similar between the 2D and quasi-2D models. However, the 2D inversion has resulted in a wider range of resistivities than the quasi-2D case, due to the presence of localised features with high resistivities. The same 2D-inverted model for the Chetwynd Barracks profile is therefore displayed with an optimised logarithmic colour scale in Figure 8.13b. Comparing Figure 8.13a with Figure 8.9c, it is evident that the 2D model confirms the basic properties of the model obtained with the quasi-2D approach. A resistive surface layer with similar properties ($> 100\,\Omega$m) is found in the 2D model also. Below 0.9 m, a conductive zone of 30–50 Ωm is observed, which appears to extend over the entire profile. The resistive zone at depth in the valley (right half of the profile) observed in the Zohdy model is also present here, but can be seen to recede further upslope towards the left of the profile. The anomalous zone around $x = 164\,$m is clearly visible in the 2D model also, but the vertical resolution of the dataset is too crude to allow for the buried target to be resolved in detail.

8.3.4 MCD: an alternative to iterative inversion

Two-dimensional inversion of large geoelectrical datasets using iterative linearised inversion is computationally expensive because partial derivatives (in the form of the Jacobian matrix) must be calculated and large linear systems of equations must be solved. The data volume acquired with computerised data acquisition systems or indeed mobile sensors such as towed CR arrays can be overwhelming and is likely to increase even more in the future, in accordance with the growing demand for higher resolution tomographic imagery. The interpretation of such datasets with conventional resistivity inversion may turn out to be inefficient, despite the availability of sufficiently powerful computational facilities.
Approximate one-pass 2D inversion procedures present an alternative to iterative linearised inversion, potentially speeding up the inversion by orders of magnitude relative to the iterative approach. One such algorithm, formulated as a multichannel deconvolution (MCD), has recently been suggested by Møller et al. (2001). Their procedure is based upon the equation for the electrical potential, linearised under the Born approximation, and makes use of the 2D form of the Fréchet derivatives evaluated for the homogeneous halfspace. The authors found that multichannel deconvolution is most suitable for the inversion of long profiles (several 100s of metres). Model estimates for profile lengths shorter than three times the longest electrode separation were found to require extra stabilisation in the lower part of the model. The application of the MCD

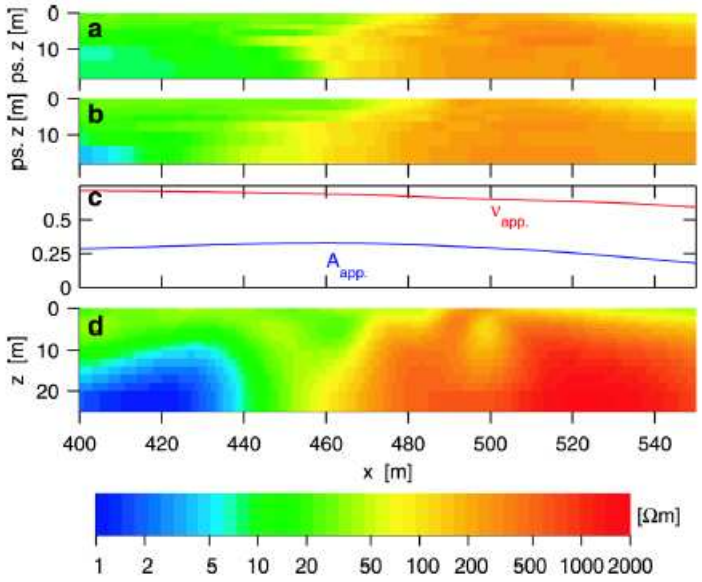

Figure 8.14: One-pass 2D inversion of PACES data by multichannel deconvolution (Møller et al., 2001). (a) Apparent resistivity pseudosection; (b) model response from the estimate in (d); (c) estimated shape parameter ν and logarithmic amplitude A from the data in (a); (d) model estimate.

algorithm to a PACES dataset (towed-array DC resistivity, Sørensen, 1996) is demonstrated in Figure 8.14. Although it would have been highly desirable to apply MCD to towed-array CR data, time restrictions and the fact that the algorithm by Møller et al. is not publicly available prevented any such testing as part of this thesis.

8.4 3D interpretation

The interpretational procedures described so far are suitable only for individual survey profiles (2D ERT). The acquisition and interpretation of *volumetric* data by towed array CR surveys (3D ERT) brings about further challenges which are discussed in this section. Complex subsurface structures can only be adequately represented by a 3D earth model. Conventional 3D DC resistivity surveys are typically conducted by using a regular grid of electrode positions (Loke and Barker, 1996a). An example of such a regular grid covered by parallel survey lines is shown in Figure 8.15. An optimal reconstruction of potentially complex 3D subsurface structures generally requires resistivity measurements with independent orientations of the four-point array (Chambers et al., 2002). In conventional DC resistivity surveys, data are therefore often acquired on orthogonal survey lines (Figure 8.15b) which are then interpreted jointly. For very large-scale tomographic surveys covering vast areas of ground, full spatial coverage with independent array orientations is extremely labour-intensive and time-consuming and data acquisition may have to be restricted to sequences of

parallel survey lines (Kuras et al., 2002), as demonstrated in Figure 8.15a. If the grid has different electrode spacings in the in-line and cross-line directions, the inclusion of individual cross-lines in the interpretation may be problematic due to the much larger number of 3D model cells required by typical interpretation schemes to accommodate such datasets. Despite this limitation, good results have been obtained by Kuras et al. (2002) using single-orientation data only, provided the subsurface resistivity distribution is not overly complex. For the purposes of this thesis, it will therefore be assumed, without loss of generality, that the use of single-orientation data obtained with towed CR arrays provides sufficient constraints to resolve relevant 3D structures.

8.4.1 3D iterative least-squares inversion

Automated 3D resistivity interpretation schemes have only recently begun to be routinely applied in environmental and engineering geophysical investigations. Early 3D algorithms (Park and Van, 1991; Shima, 1992; Sasaki, 1994) were mainly of academic interest, implemented on mainframe computers and thus inaccessible for wider audiences. In recent years, the arrival of powerful desktop computing made the development of PC-based inversion schemes possible, making 3D resistivity surveys and interpretation a viable option for a wide range of users.

Loke and Barker (1996a) have described a 3D smoothness-constrained least-squares inversion method (cf. Section 8.3.1 for the 2D case) which has proven to be robust and extremely popular amongst the geophysical community. In analogy to the 2D case, their 3D algorithm now solves the modified Gauss-Newton equation (8.6) for a 3D problem. This algorithm has been considered for the interpretation of 3D towed-array CR datasets for several reasons. Firstly, the algorithm is well-tested and converges rapidly even for larger datasets as encountered with high-density towed-array CR. Secondly, it is cell-based and assumes a regular grid of electrodes, so that the subsurface can be divided into a number of regularly-spaced model cells. The discretisation can vary in the x- and y-directions, so that survey lines can have different spacings to the in-line electrode spacing. Thirdly, it is widely available and can be readily applied to towed-array CR data, provided some basic rules regarding survey design are observed.

8.4.2 3D towed-array survey design and techniques

By the very nature of the towed-array CR technique, 3D data acquisition with towed CR arrays must necessarily be carried out along a sequence of linear profiles. Volumetric coverage may be obtained by conducting multi-offset measurements on parallel survey lines. For such datasets, the towed array is always orientated in a single direction and sampling intervals can be significantly different in in-line and cross-line directions (Figure 8.15c). Repeating the same survey in orthogonal direction may result in relatively large rectangular patches of ground between the survey lines which have no associated datum points (Figure 8.15d). Although improved geometric definition of complex targets may be

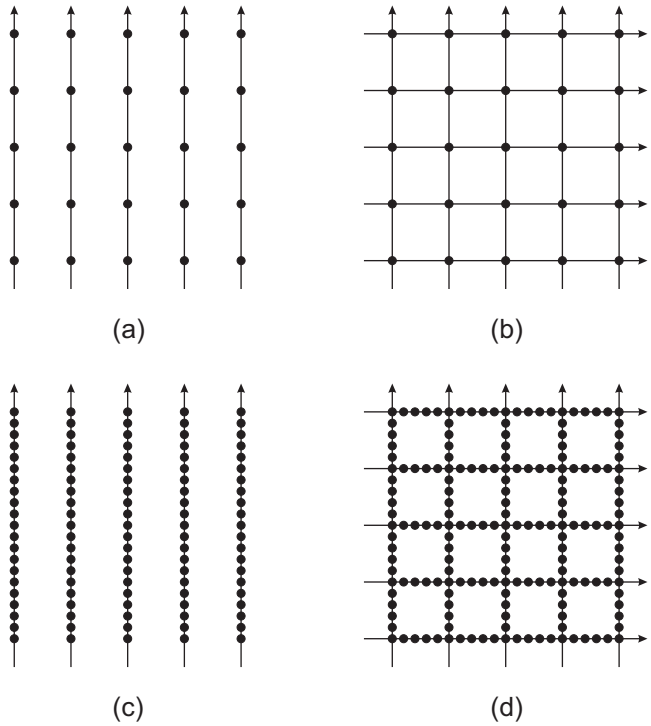

Figure 8.15: Example of parallel survey lines covering a regular grid of electrode/sampling positions. (a), (b) Sampling intervals equal or of the same order in both directions (typical for DC); (c), (d) Sampling intervals small in in-line direction, but larger line spacings (typical for CR); (a), (c) single-orientation survey; (b), (d) survey with two independent orientations in orthogonal directions

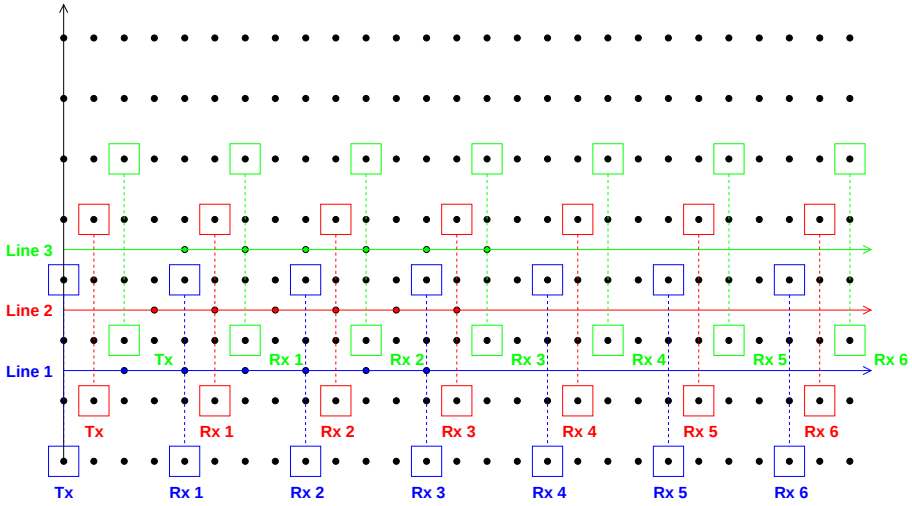

Figure 8.16: 3D towed-array CR survey on parallel lines representing a regular grid of electrode positions and sampling locations. Black dots = electrode positions; coloured dots = datum points

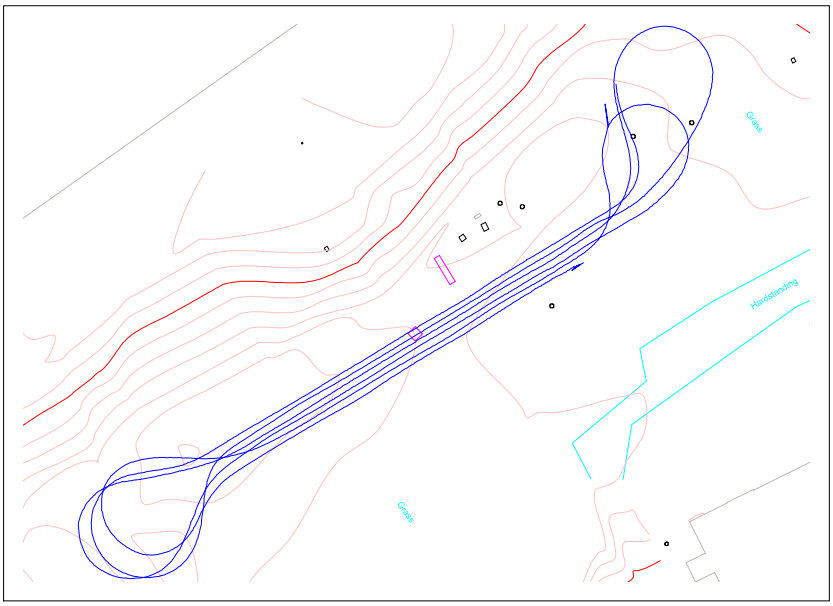

Figure 8.17: Continuous survey path for a bi-directional 3D towed-array CR survey using Real-Time Kinematic Differential GPS positioning.

achieved by collecting additional data with an independent orientation of the towed array, a 3D interpretation of complete datasets with regular meshes of model cells may be unrealistic due to the potentially large number of cells (and hence large number of model parameters) required compared to the smaller number of constraints imposed by the irregular coverage of the ground. With present computational capacity, such datasets would most likely still have to be degraded by downsampling onto a coarser regular grid.

The use of the equatorial array has further implications for the 3D interpretation of towed-array CR data. An application of RES3DINV with its concept of a regular 3D mesh to towed-array CR data implies that these have to be sampled in a manner that corresponds to data collected with a regular grid of conventional electrodes. Line spacings must be chosen such that electrode positions on adjacent survey lines are compatible with electrode positions in the 3D mesh. In order to avoid numerical resampling of the data, the simplest approach is to design the towed-array survey accordingly. Lateral coincidence of the sampling interval in profile direction can be ensured by starting the survey at a common baseline. For an equatorial array, coincidence in cross-profile direction can be achieved by choosing a line separation that has a relatively large common denominator with the dipole length of the equatorial array. A typical example is shown in Figure 8.16, where the line spacing is 1/3 of the dipole length of a CORIM™-type array, that is 0.5 m for 1.5 m dipoles.

The practical realisation of 3D ERT surveys with towed CR arrays is critically dependent on the capability to navigate the combination of towing vehicle and CR array over a sequence of survey lines with an accuracy of the order of centimetres. At the same time, the increased productivity of CR over conventional

DC resistivity due to higher efficiency of the dynamic measurement is a key advantage of the CR technique and should not be jeopardised by loss of time related to positioning and navigation. Experience with the CORIM™ and BGS CRI systems has shown that the most efficient method of acquiring data on parallel survey lines is by bi-directional surveying, where adjacent lines are covered in opposite directions and the vehicle is u-turned at the end of each line, thus following a continuous "snakepath" (Figure 8.17). Uni-directional surveying, where all survey lines are acquired in a single direction, is slower with long periods of system downtime due to lengthy repositioning. In an effort to increase spatial accuracy as well as survey speed, Real-Time Kinematic Differential GPS (DGPS/RTK) has been tested in conjunction with the BGS CRI system and used successfully for positioning and real-time navigation.

8.4.3 Forward modelling of 3D structures

Anticipation of the nature of the response from typical subsurface targets can help greatly with the design of geophysical surveys. With regard to the towed-array CR technique, such information is difficult to deduce from existing DC field data or modelling studies due to the unusual characteristics of the towed-array CR technique. With regard to geometry for example, the use of the equatorial dipole-dipole array is very uncommon in DC surveys, yet its properties are quite distinct from other, better known array types (cf. Section 7.1.3). The response of the equatorial array with respect to shallow 3D targets in particular is not well known.

A numerical forward modelling study has therefore been conducted to examine the response of typical towed CR arrays in the presence of simple subsurface structures with 3D geometry. The array geometry considered is that of the CORIM™ system, i.e. a 6-channel instrument with regular array spacings at 1 m intervals. One of the simplest geometric structures that is easy to model numerically is that of a unit cube with anomalous electrical properties (resistivity ρ_1) embedded in an otherwise homogeneous halfspace of resistivity ρ_0 (Figure 8.18). The unit cube has the dimensions $1\,\mathrm{m} \times 1\,\mathrm{m} \times 1\,\mathrm{m}$ and is buried at a depth of 1 m to its centre (0.5 m to its top). Using the 3D DC resistivity forward-modelling algorithm by Spitzer (1995, cf. Section 8.2.4.1), a towed-array survey was simulated by calculating the apparent resistivity observed at each of the six receiver channels on a sequence of parallel profiles in x-direction over this target. Current and potential dipoles were moved at constant separations along a sequence of regularly-spaced electrode positions, thus simulating towed-array data with a constant sampling interval. A sampling interval of 0.25 m in the x-direction was chosen. In the cross-profile direction (y), the discretisation was fine near the centre of the target, but coarser at greater distances away from the simulated survey line. This strategy allowed for high numerical accuracy while the number of model cells (and hence the computational expense) remained manageable. Multiple lines were simulated at a spacing of 0.5 m, with the centre line being centered above the target. Two different cases with reciprocal properties were considered for this study.

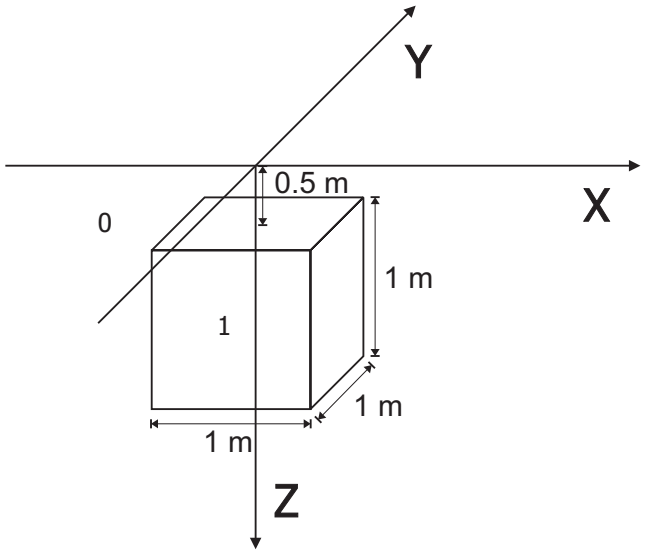

Figure 8.18: Model of a unit cube with resistivity ρ_1 embedded in a homogeneous halfspace of resistivity ρ_0.

Resistive cube. The first case comprised a resistive cube (100 Ωm) in a moderately resistive halfspace (50 Ωm). The calculated model response for receivers Rx 1–Rx 6 is shown in Figure 8.19 as a sequence of 3D surface plots. The result is symmetric about the xz- and yz-planes with respect to the centre of the target. At Rx 1, an anomaly with a single maximum at the centre is observed, with the response falling off monotonously in x and y-directions. For subsequent receivers, the anomaly splits up into two maxima on all the parallel profiles. The two maxima are moving further apart for longer array offsets (Rx 2–Rx 6). On the centre profile, the apparent resistivity level between these two maxima is always greater than the halfspace value, however on adjacent profiles it is much lower and may even fall *below* the halfspace value over the edges of the target. There, two minima can be observed along the respective profiles.

Conductive cube. In the second case a conductive cube (10Ωm) was considered, embedded in the same halfspace as before. The calculated model response for receivers Rx 1–Rx 6 is shown in Figure 8.20. The result is essentially inverse to that of the resistive cube but the same symmetries apply. At Rx 1, the anomaly is again defined by a single minimum at the centre. For the following receivers however, two minima occur which continue to move apart for increasing array offsets. On the centre profile, the response function between these minima is always less resistive than the halfspace, but on adjacent profiles it may well be more resistive. Over the edges of the target, two maxima are observed along the respective profiles.

This modelling study highlights a number of interesting aspects about the

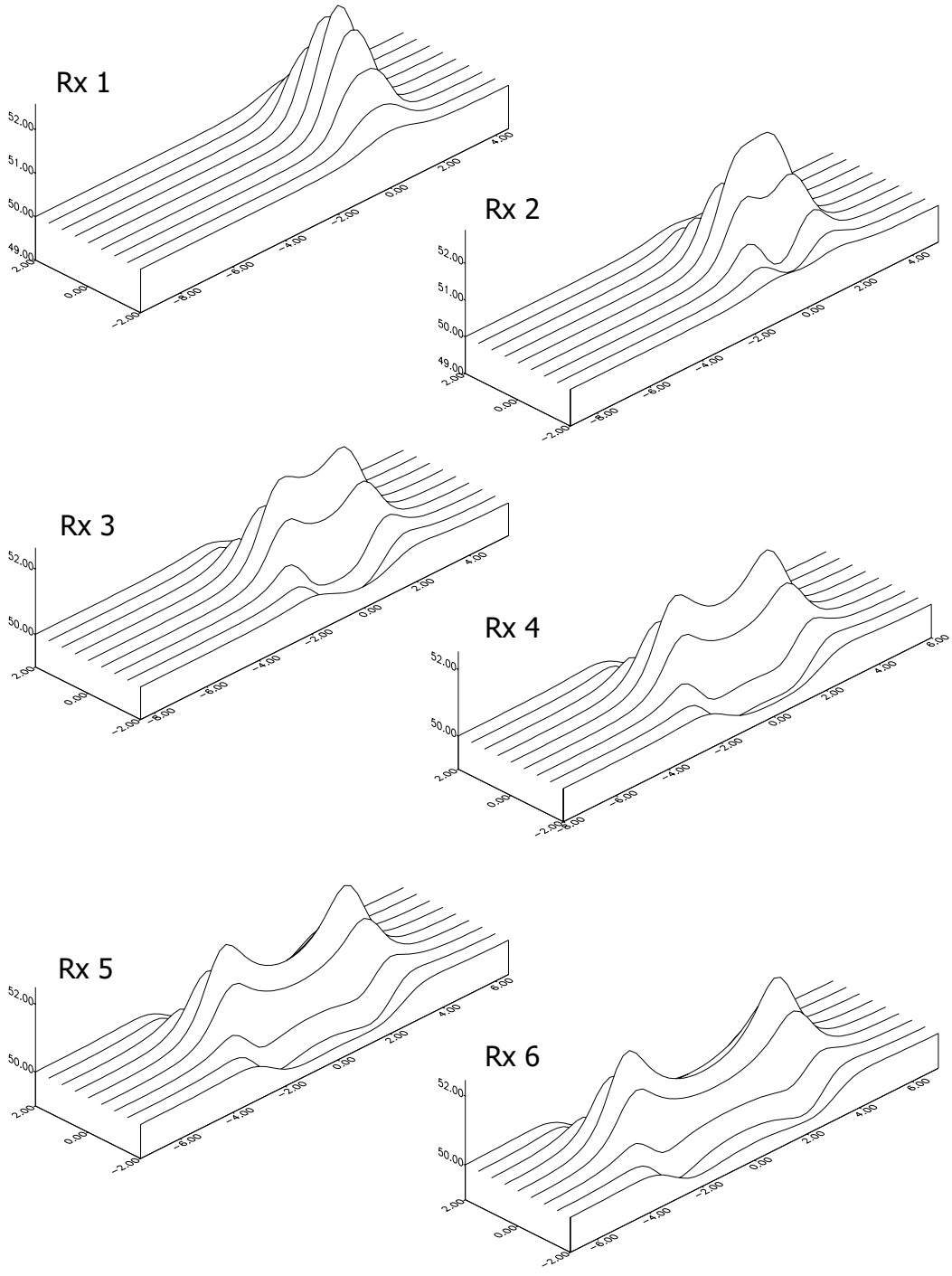

Figure 8.19: Model response from a resistive unit cube for a towed CR array with CORIM™ geometry.

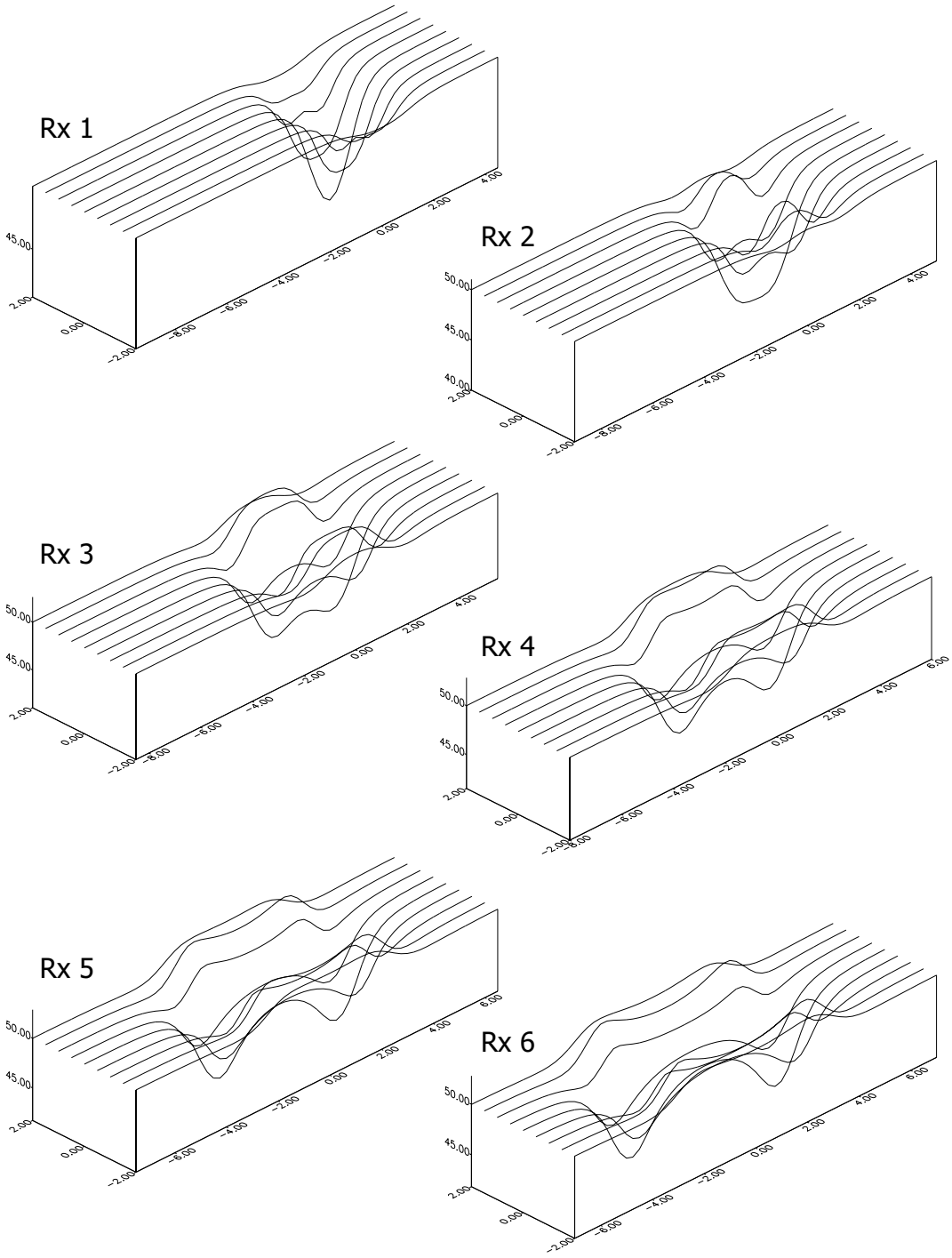

Figure 8.20: Model response from a conductive unit cube for a towed CR array with CORIM™ geometry.

response of towed CR arrays over simple 3D targets. The equatorial dipole-dipole array shows characteristic behaviour in the vicinity of localised buried features. The study has demonstrated that

1. over parts of a resistive cube, this array can be expected to produce an apparently conductive response and vice versa.

2. A single buried object is likely to be associated with *two* extrema on an apparent resistivity profile obtained with a towed CR array with equatorial geometry.

8.4.4 Examples

The use of 3D resistivity inversion for the interpretation of towed-array CR data will now be demonstrated by two examples. The first example is the synthetic dataset obtained from the forward modelling exercise described in the previous section. The second example is a field dataset over a simple buried structure.

8.4.4.1 Synthetic data: the unit cube

The synthetic datasets for the unit cube model were presented to RES3DINV for inversion. For the 3D mesh, a fundamental electrode spacing of 0.25 m in x-direction (in-line) and 0.5 m in y-direction (cross-line) was chosen in accordance with the calculated data. The datasets corresponded to measurements on a rectangular grid of 81×12 electrodes, as derived from 9 profiles over a length of 20 m with the cube at the centre of the grid. A total of 3078 datum points was included in each dataset. The vertical discretisation of the 3D model was chosen in analogy to the 2D case (Table 8.3). In the following, results are presented for the case of the resistive cube.

Resistive cube without noise. In the first instance, the resistive cube dataset was inverted without change, thus ignoring the effects of measurement noise. A smoothness constraint was applied and six iterations were carried out, after which the RMS error had been reduced to 0.07%. The resulting resistivity model is shown in Figures 8.21 (horizontal depth sections) and 8.22 (vertical cross-sections). The outline of the cube is indicated by a white rectangle in the relevant sections. A resistive anomaly is found, centred laterally on the 3D model (Figure 8.21) and reaching its highest values in the third model layer (0.54 m–0.88 m). Both the lateral and the vertical extent of the target have been reconstructed to a high accuracy, considering the smoothness constraint imposed on the inversion and the limited spatial resolution of the 3D resistivity model compared with the dimensions of the cube.

Resistive cube with Gaussian noise. For the second case, the same dataset was considered, however this time contaminated by Gaussian noise of 5% amplitude. All other parameters remained the same. The results of this inversion are shown in Figures 8.23 (horizontal depth sections) and 8.24 (vertical cross-sections). The inversion was stopped after two iterations, by which time

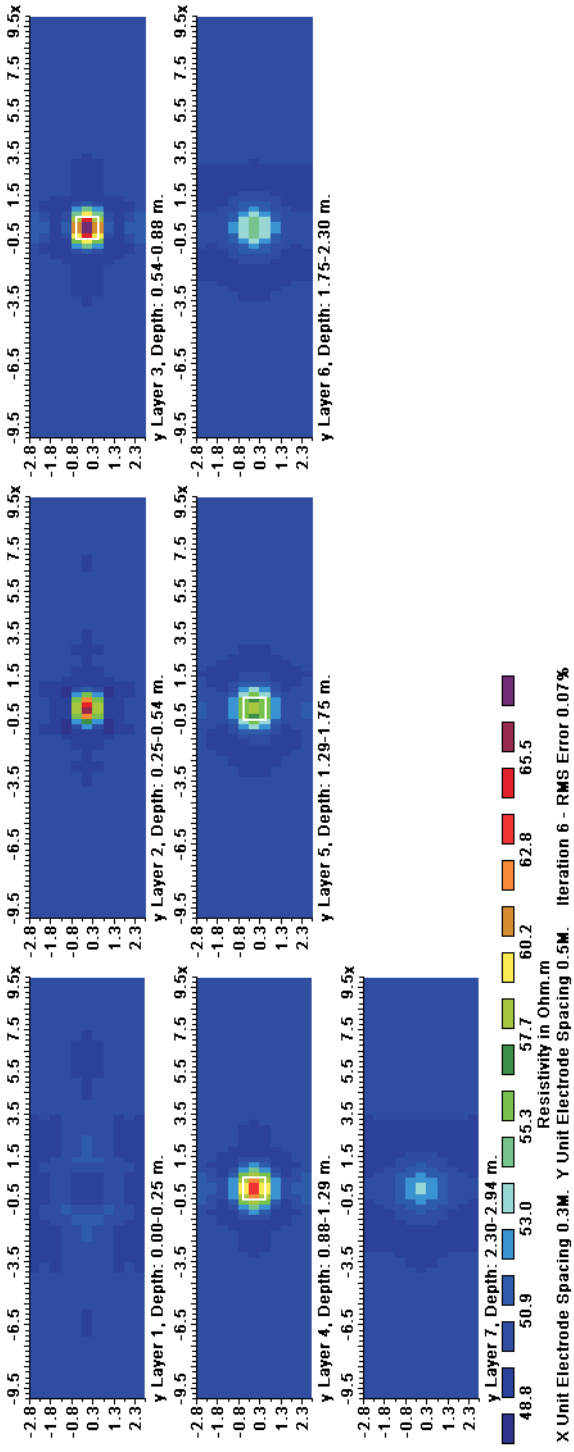

Figure 8.21: Horizontal depth sections of the 3D resistivity model for the resistive unit cube. The outline of the cube is shown as a white square.

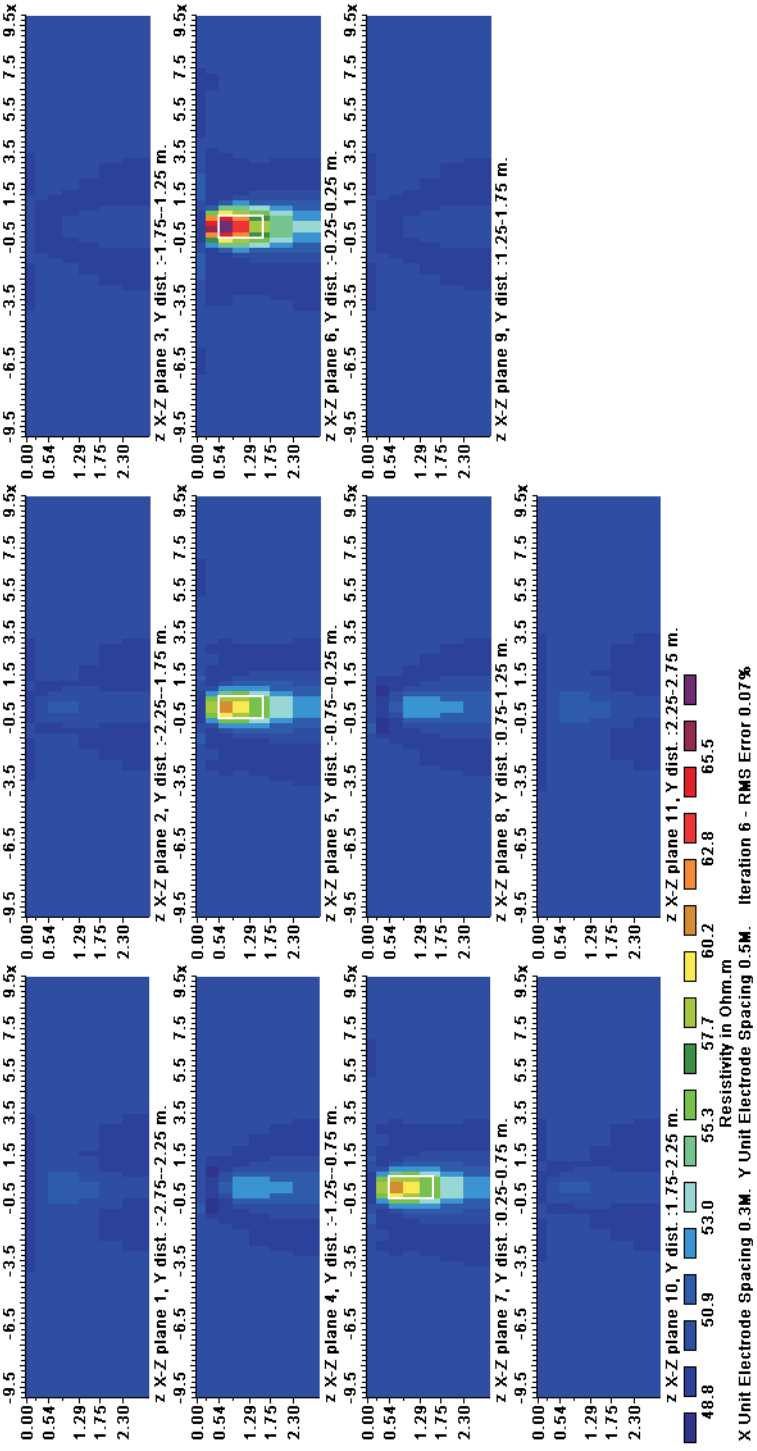

Figure 8.22: Vertical cross-sections of the 3D resistivity model for the resistive unit cube. The outline of the cube is shown as a white rectangle (2 × vertical exaggeration).

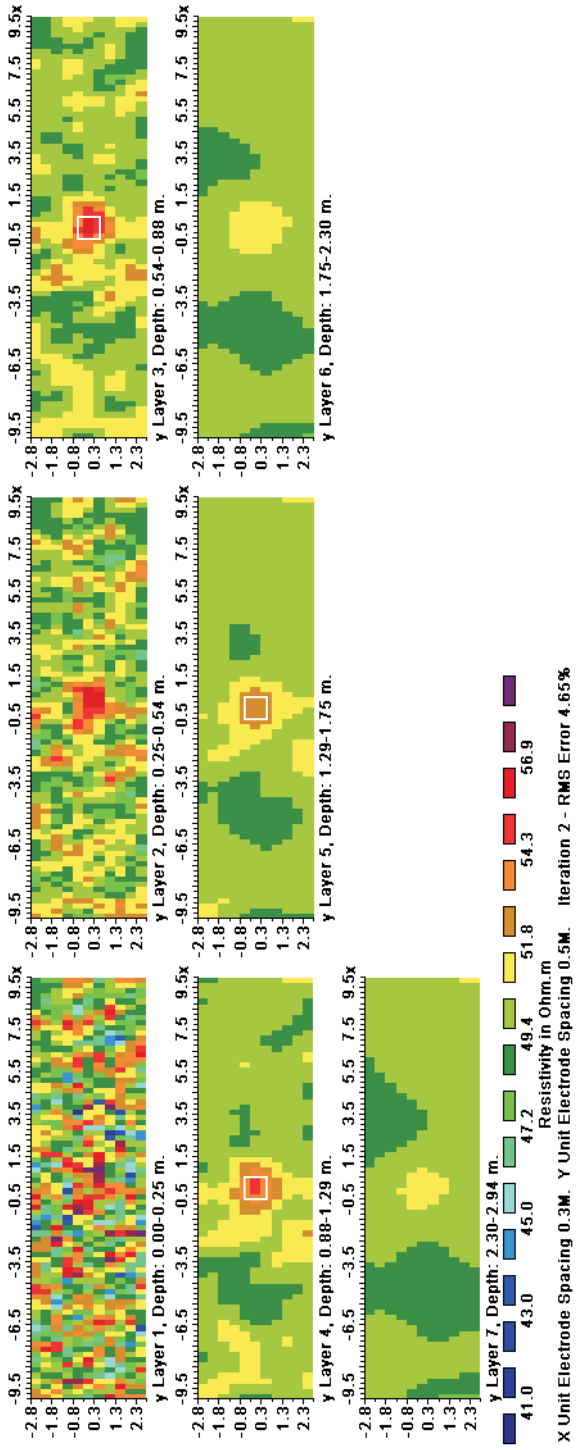

Figure 8.23: Horizontal depth sections of the 3D resistivity model for the resistive unit cube with 5% Gaussian noise. The outline of the cube is shown as a white square.

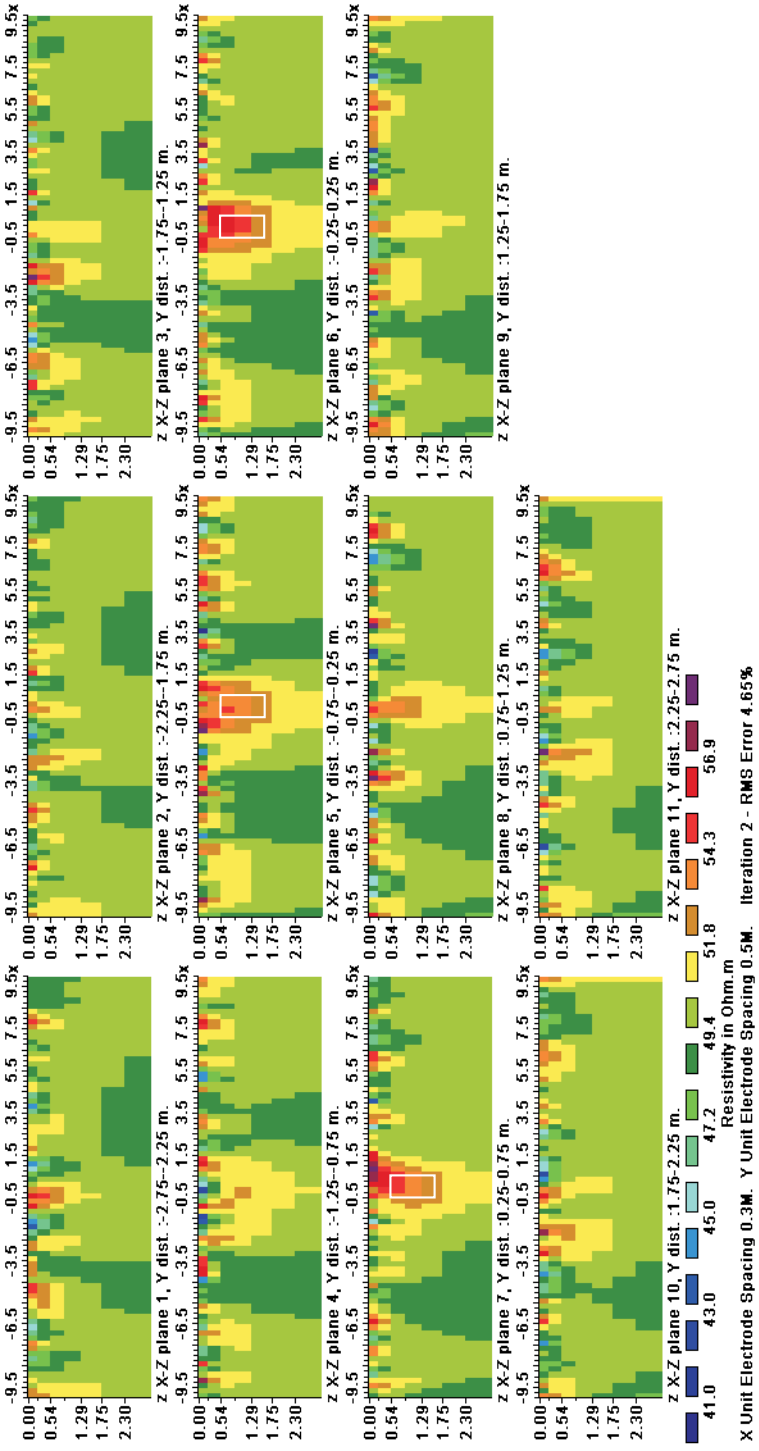

Figure 8.24: Vertical cross-sections of the 3D resistivity model for the resistive unit cube with 5% Gaussian noise. The outline of the cube is shown as a white rectangle (2 × vertical exaggeration).

the RMS error had been reduced to 4.56%. The range of resistivity values in the inverted model is now significantly higher and the model shows higher variance due to the added noise in the data, particularly in the upper model layers which are less affected by the inherent smoothing of the inversion procedure. Despite the noise content in the data, the target has still been reconstructed as a prominent resistive anomaly. The target geometry, particularly the lateral extent, is less well constrained than in the noise-free case, but the agreement between true and inverted model is still convincing. Again, the highest resistivity values are obtained for the third model layer.

The results for this synthetic example of a simple 3D target indicate that towed CR array can provide sufficient constraint for the detection and reconstruction of localised shallow structures with 3D geometry by tomographic methods. In this particular case, the exclusive use of CR data from a single array orientation has proven to be adequate for the satisfactory reconstruction of a unit cube.

8.4.4.2 Field data: the EIGG geophysical test site

The second example consists of a field dataset acquired with the CORIM™ system at the EIGG[2] test site at Southmeads Road, Leicester, UK. The site comprises a variety of buried environmental and engineering targets made of a range of different materials and installed under controlled conditions. Its purpose is to provide a facility for research and training for many aspects of shallow geophysical methods and surveys. The test site (Figure 8.25a) is described in detail by Hill (2000). It lies on the summit of a gentle hill-top and is characterised by a relatively uniform surface layer of clayey topsoil, which is approximately 0.3 m thick, grading down into Boulder Clay. The latter is uniform throughout the site, containing clasts set in a clay matrix. The unit is 16–18 m thick and underlain by Liassic clays and limestones. Conventional DC resistivity soundings have been used to determine the bulk resistivity of the Boulder Clay as approximately 23 Ωm. The water table is shallow, but the clay is of low permeability.
The target selected for the 3D towed-array CR survey is known as Area 8 and consists of small objects (metallic plates) embedded in a buried sand pit. Its constructional details are shown in Figure 8.25b. While the metallic plates are too small to have a significant effect on the resistivity measurement, the resistive sand provides good electrical contrast with the surrounding Boulder Clay and was therefore selected to act as the main target. The sand pit is 6 m long, 2 m wide and 1.7 m deep and is covered by 0.3 m of topsoil. Its long axis is aligned with the y-direction of the local coordinate system, which is approximately orientated south-north. The pit extends between $57\,\mathrm{m} \leq x \leq 59\,\mathrm{m}$ and $17\,\mathrm{m} \leq y \leq 23\,\mathrm{m}$ in local coordinates (cf. Figure 8.25b).
Eleven parallel profiles at a separation of 0.5 m were acquired over Area 8 using the CORIM™ system towed by a Land Rover (Figure 8.26). As the site conditions did not allow for the survey to be conducted in a bi-directional manner,

[2]Environmental and Industrial Geophysics Group of the Geological Society of London

(a)

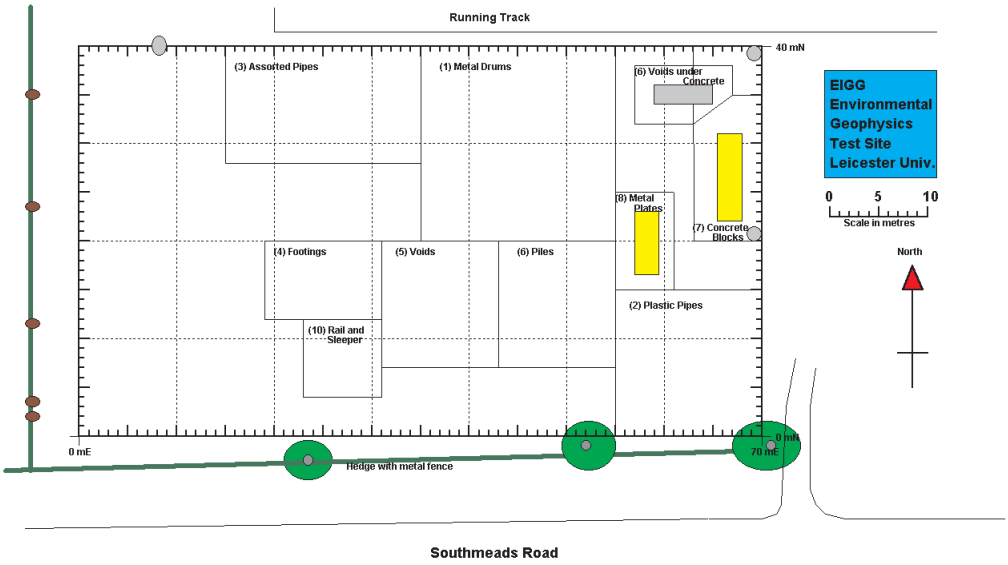

(b)

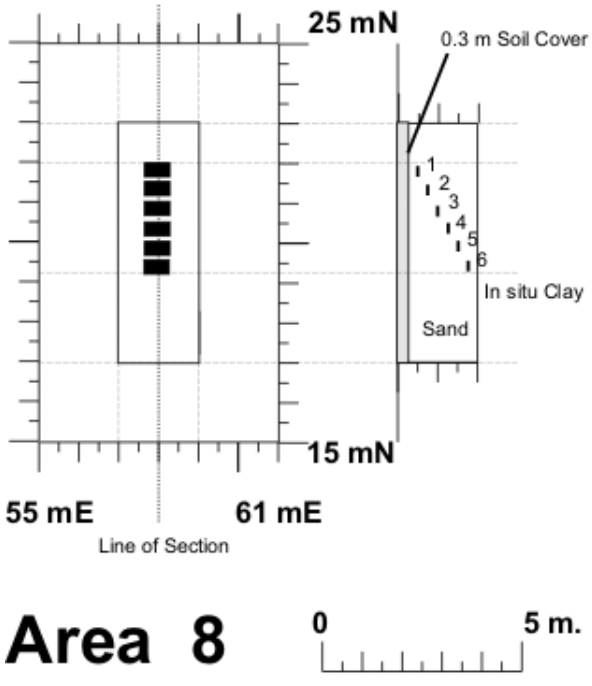

Figure 8.25: The EIGG geophysical test site at Southmeads Road, Leicester. (a) Site plan; (b) details of Area 8.

Figure 8.26: The CORIM™ system in field operation on the EIGG test site.

all profiles were acquired in positive y-direction (south-north). A sampling interval of 0.25 m along the survey line was chosen, resulting in a regular grid of electrode positions with 31×105 electrodes. An example of a recorded apparent resistivity profile, which demonstrates the high overall quality of the raw data, is shown in Figure 8.27. Data processing could therefore be kept to a minimum. Individual profiles were filtered with a predictor filter (cf. Section 7.3.1.2) to remove sporadic outliers and high wavenumber portions of the signal. All profiles were then collated into one single dataset and inverted with RES3DINV. The dataset comprised a total number of 5346 datum points. As before, the vertical discretisation of the 3D model was based on Table 8.3, leading to a 7-layer model. A smoothness constraint was imposed on the inversion. The inversion process was stopped after six iterations, by which time the RMS error had been reduced to 2.77%.

The resulting 3D resistivity model of Area 8 is shown in the form of horizontal depth sections in Figures 8.28 and 8.29, as vertical cross-sections in Figures 8.30–8.32 and as a 3D tomogram in Figure 8.33. Where applicable, the outline of the sand pit geometry is shown as a white rectangle. Similar to what was previously observed for the synthetic data, the surface layer is found to be predominantly resistive ($> 100\,\Omega$m), but generally of a high variability and little structure can be resolved in this layer (Figure 8.28). Layer 2 is still resistive ($> 50\,\Omega$m) and patchy, yet a coherent resistive feature associated with the top of the sand pit begins to appear in the centre of the section. From layer 3 onwards, the structure is fully resolved and sharply delimited against the conductive background (Figure 8.28 right and 8.29). The Boulder Clay surrounding the pit is found to be associated with resistivities of the expected order (20–30 Ωm). Particularly at medium and larger depths, the resistive structure is surrounded by a conductive halo ($20\,\Omega$m and below), possibly as a side-effect

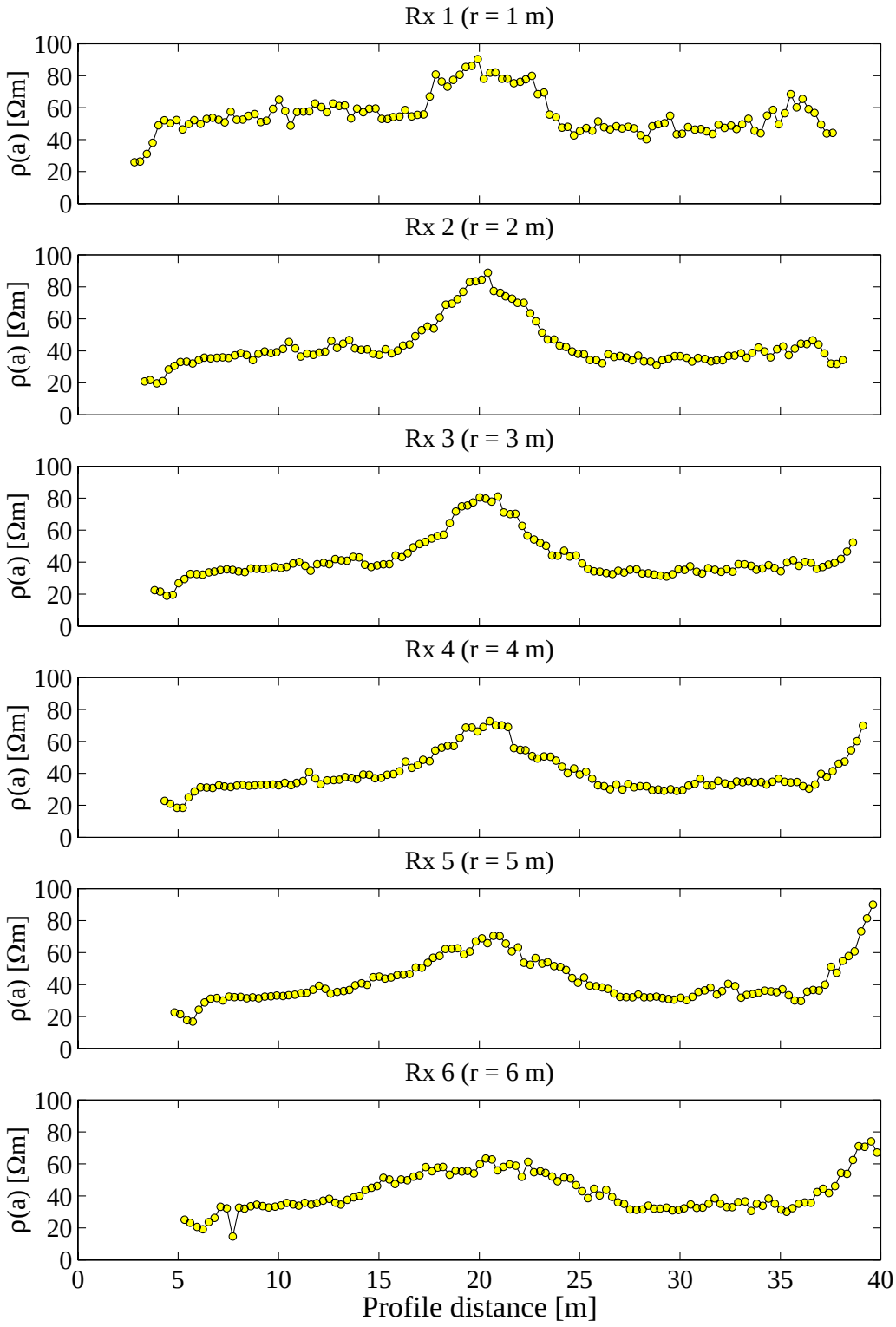

Figure 8.27: Example of an apparent resistivity profile recorded at Area 8 of the EIGG test site ($x = 58.5\,\mathrm{m}$).

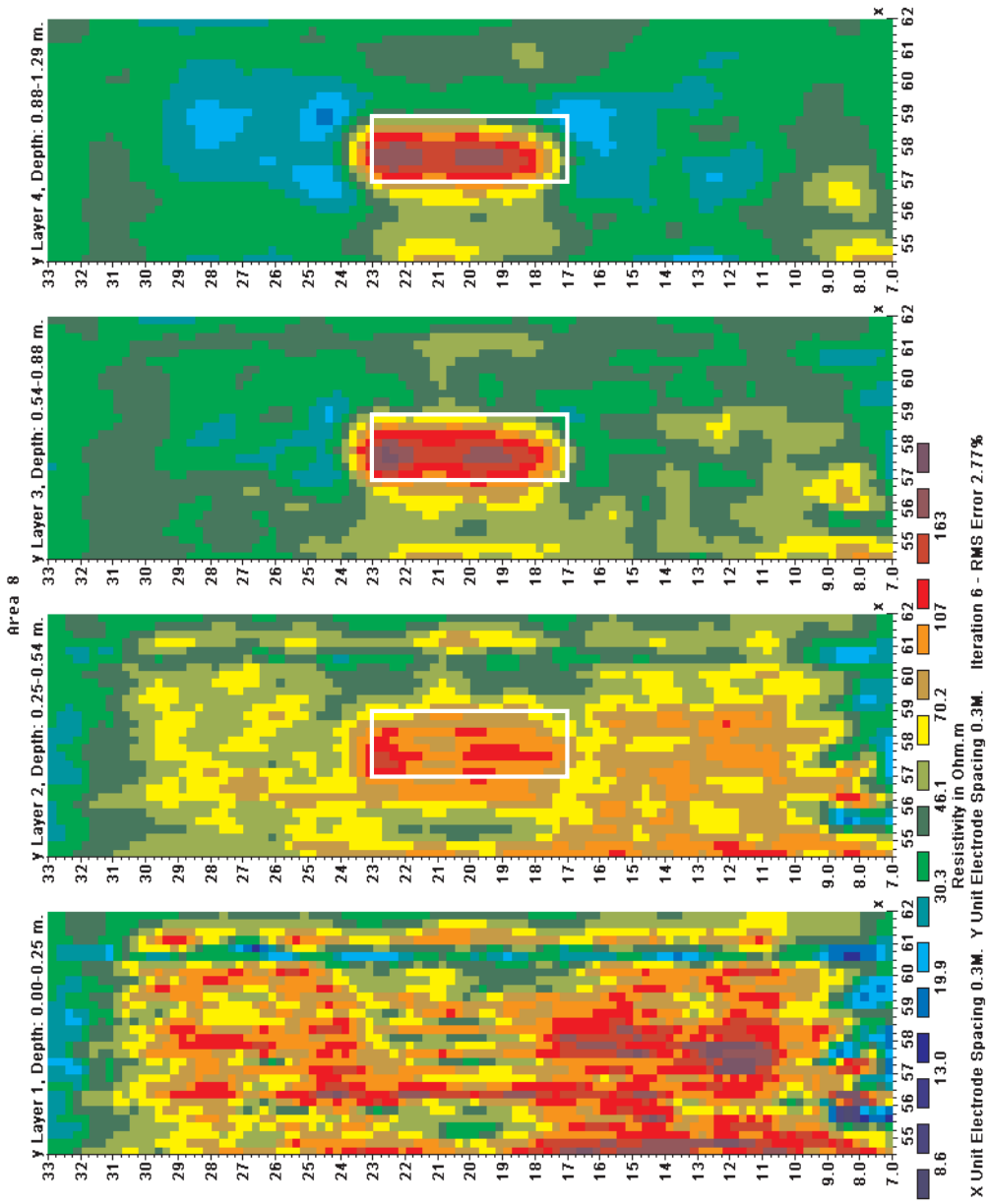

Figure 8.28: 3D resistivity model of Area 8 of the EIGG test site: horizontal depth sections, layers 1–4. The outline of the sand pit is shown as a white rectangle.

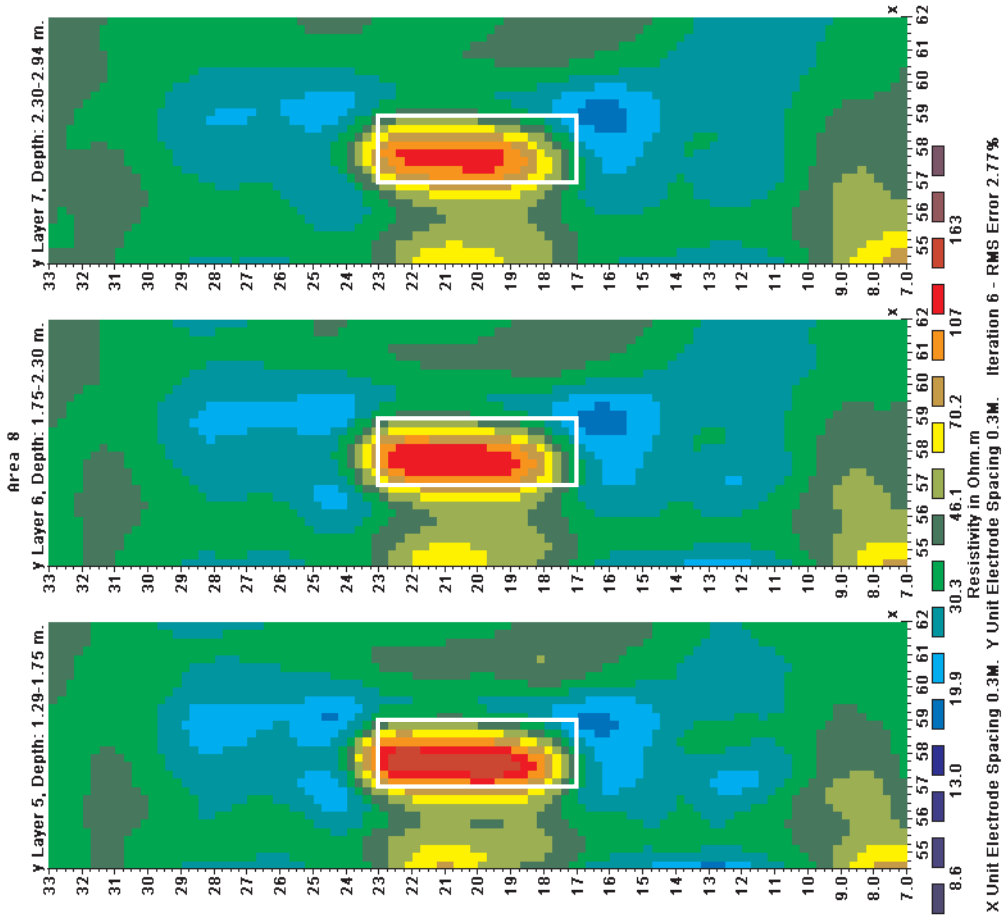

Figure 8.29: 3D resistivity model of Area 8 of the EIGG test site: horizontal depth sections, layers 5–7. The outline of the sand pit is shown as a white rectangle.

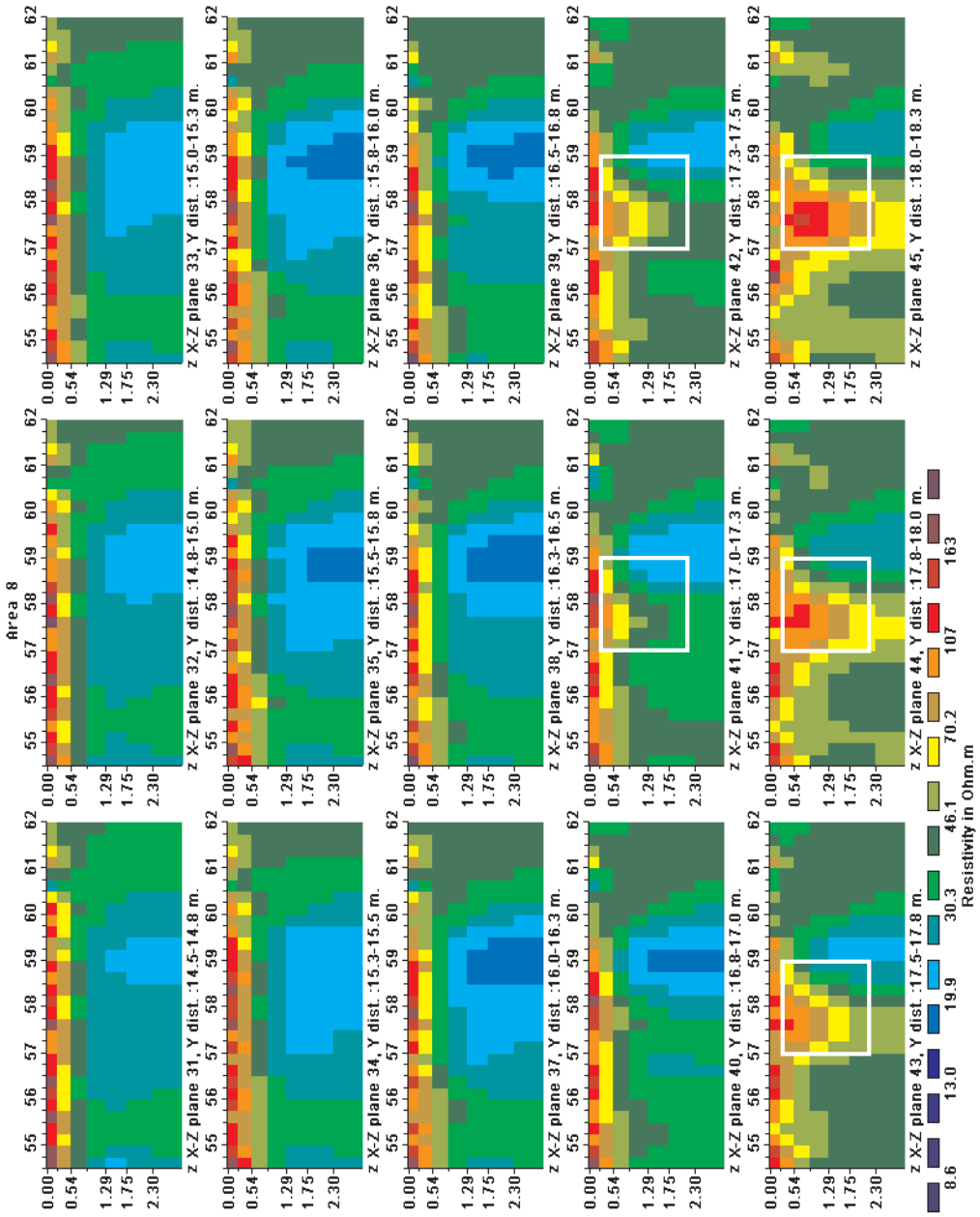

Figure 8.30: 3D resistivity model of Area 8 of the EIGG test site: vertical cross-sections ($y = 14.5\,\mathrm{m} \ldots 18.25\,\mathrm{m}$). The outline of the sand pit is shown as a white rectangle.

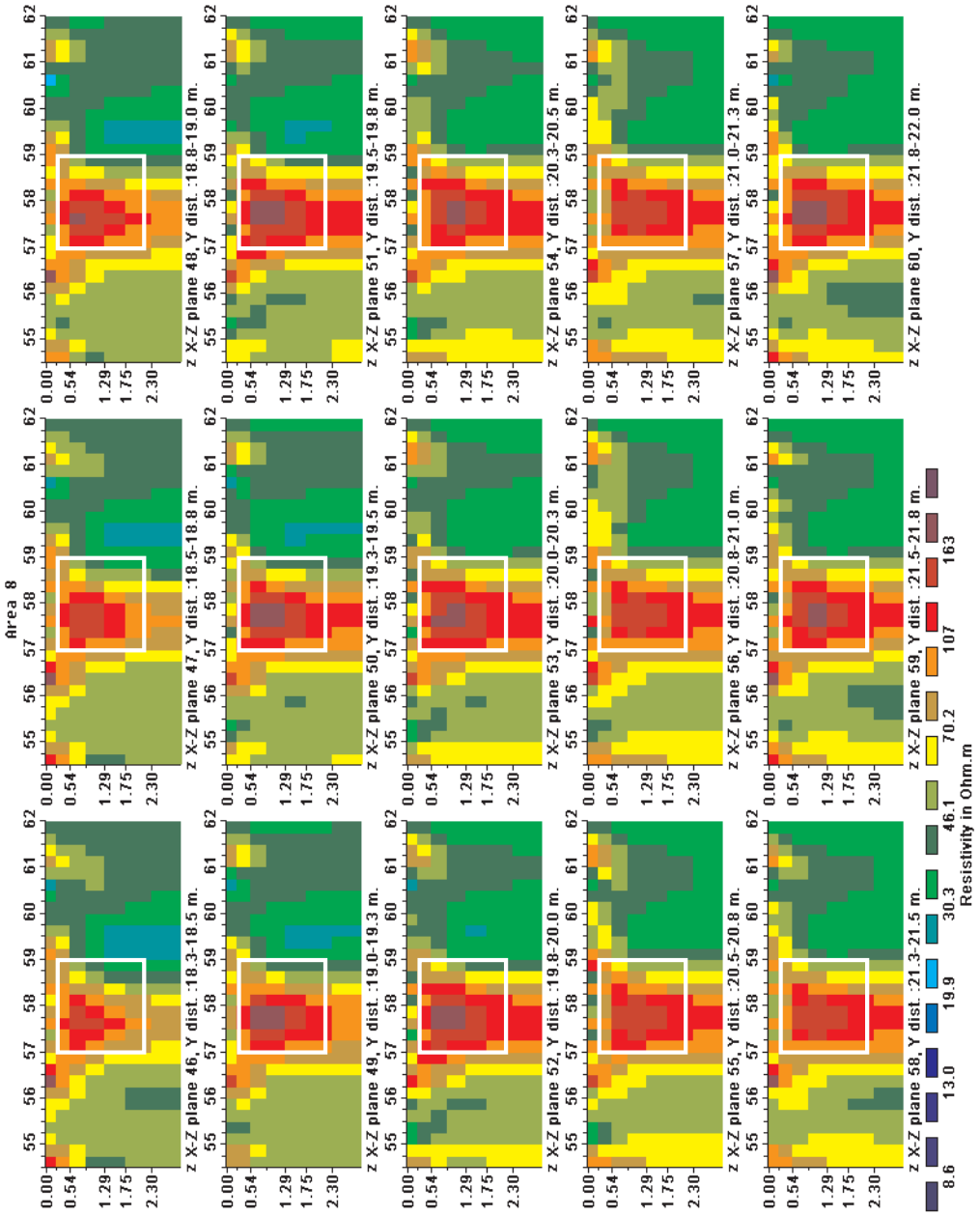

Figure 8.31: 3D resistivity model of Area 8 of the EIGG test site: vertical cross-sections ($y = 18.25\,\mathrm{m} \ldots 22.0\,\mathrm{m}$). The outline of the sand pit is shown as a white rectangle.

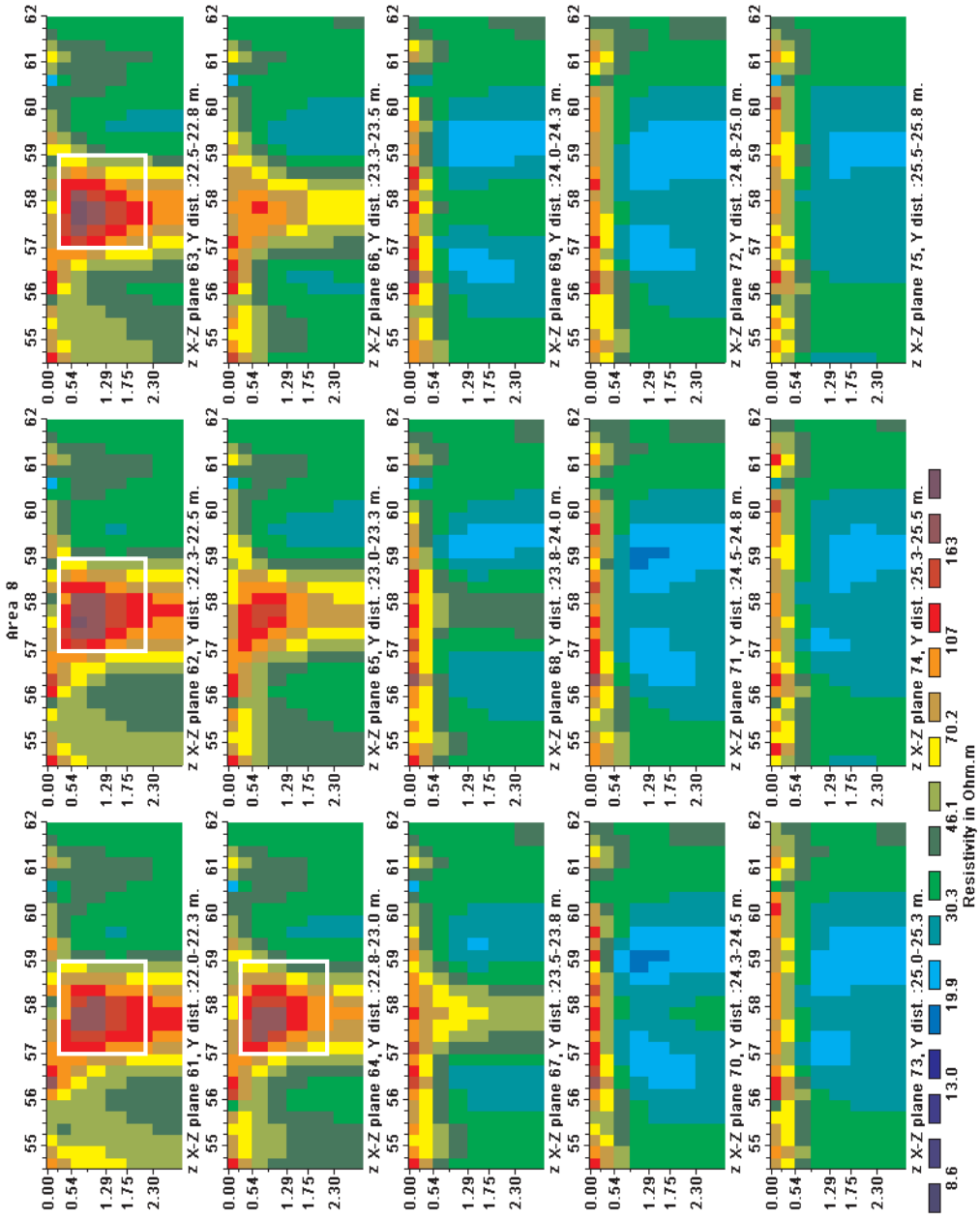

Figure 8.32: 3D resistivity model of Area 8 of the EIGG test site: vertical cross-sections ($y = 22.0\,\mathrm{m} \ldots 25.75\,\mathrm{m}$). The outline of the sand pit is shown as a white rectangle.

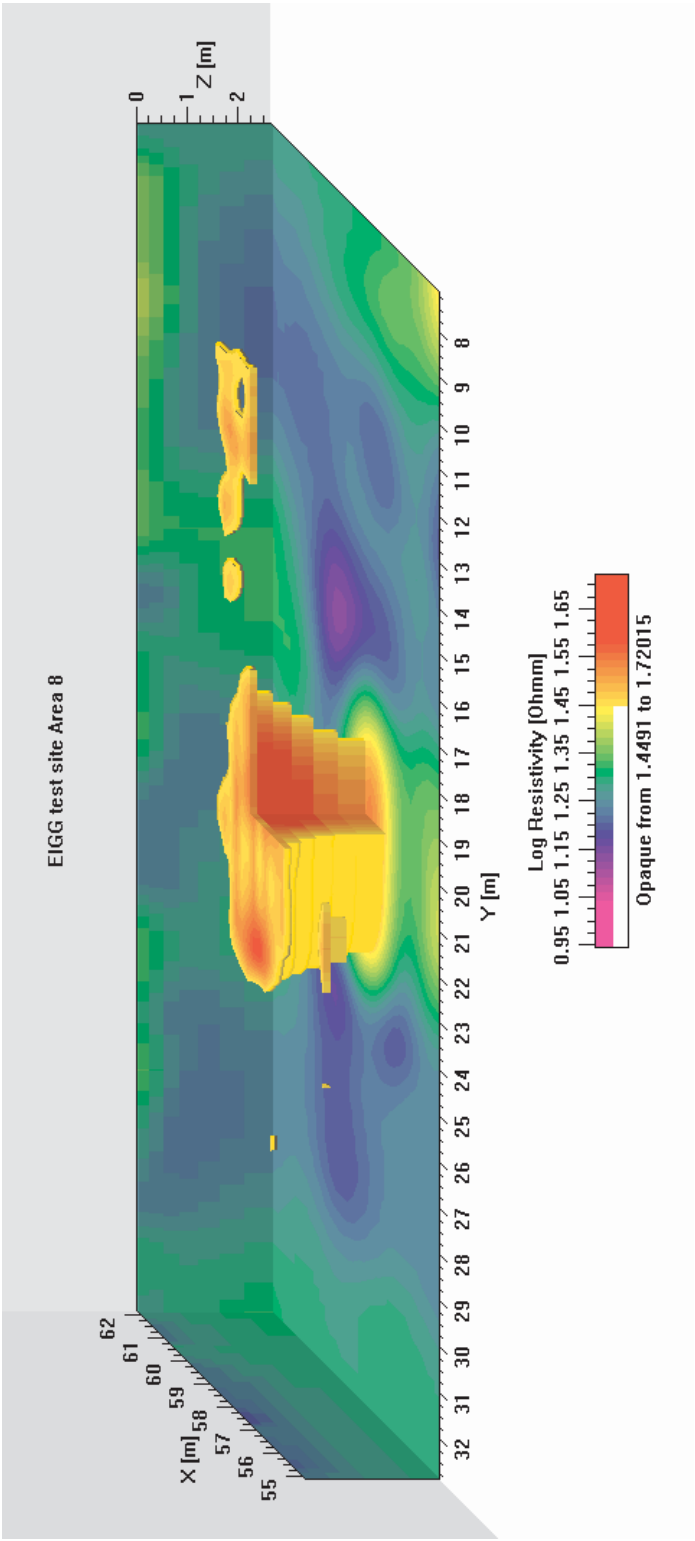

Figure 8.33: 3D tomogram of Area 8 of the EIGG test site, showing the resistivity iso-surface for $\rho = 28\,\Omega\mathrm{m}$. The opaque volume represents more resistive material.

of the Occam-type inversion method. Despite the smoothness constraint, the geometric definition of the target is remarkably precise, due largely to the high spatial resolution of the dataset and model. The only shortcoming of the inverted model is the lack of definition at depth. The bottom of the sand pit (2.0 m) is clearly not well resolved as the resistive feature is still prominent in the lowest model layer (2.30 m–2.94 m), masking the underlying Boulder Clay. The reason is that the longest array offset of the CORIM™ system (Rx 6) corresponds to a maximum effective depth of 2.33 m (cf. Table 7.1), which is unlikely to be sufficient to accurately resolve a horizontal boundary at 2.0 m depth.
The vertical cross-sections confirm the accurate spatial definition of the target. A sequence of cross-sections through the model in x-direction at 0.25 m intervals is shown in Figures 8.30–8.32. The resistive feature in the centre of the relevant sections matches the outline of the target (white rectangle), except for $23.0\,\text{m} \leq y \leq 23.5\,\text{m}$, where the extent of the target in y-direction has been slightly overestimated. It is also evident from Figure 8.31 that the bottom of the pit has not been resolved.
Finally, a 3D tomogram of the resistivity model of Area 8 shows a three-dimensional representation of the resistive sand pit as an opaque volume confined by the resistivity iso-surface at 28 Ωm. The view is towards east along the x-axis of the local coordinate system. For a better overview of the target, the more resistive layer of topsoil has been made transparent. A cutout in the front right corner of the resistive volume shows the structure of the resistivity distribution inside the target.

8.5 Discussion

In this chapter, the use of multi-offset towed-array CR data for tomographic resistivity imaging has been investigated. Results from synthetic modelling as well as field datasets indicate that such data are generally suitable for the application of conventional DC resistivity inversion schemes. In the light of the equivalence between resistivities derived by the DC and CR techniques, it is suggested that this methodology be termed "*capacitive resistivity imaging*".

Fixed-electrode versus towed-array acquisition. The fundamental difference between multi-offset data collected with a fixed electrode array on the one hand and a towed array on the other hand is the lack of spatial reference associated with the dynamic measurement, caused for example by variations in towing speed during fixed-rate acquisition. Such discrepancies may lead to a non-uniform distribution of datum points in the distance-pseudodepth plane. Data would then need to be resampled to be compatible with typical inversion schemes, which may introduce inaccuracies. The problem can be avoided by acquiring data at fixed distances (e.g. with an odometer) or at predefined positions on the ground (e.g. by means of GPS or similar positioning systems).
A second aspect that differs between the two acquisition techniques is that a regular grid of fixed electrodes can only accommodate a finite number of array

combinations, which is predetermined by the fundamental electrode spacing. In contrast, individual sensors on a towed array need not have any geometric relation to each other. Yet, with towed CR arrays it is more difficult to achieve similar depth coverage to that obtainable with conventional DC resistivity multi-offset measurements. This is due to the fact that in a dynamic measurement electrodes cannot be reused for different configurations as in a static measurement and hence the number of available array offsets is limited.

Quasi-2D interpretation. Quasi-2D techniques are applicable to multi-offset towed-array CR data. The simplest method is to collate the data as vertical electrical soundings, carry out a sequence of 1D inversions and interpret the results as a quasi-2D model ("CVES"). Such an approach is particularly useful if interpretation is to be carried out "on-the-fly", i.e. synchronously with data acquisition. Only one reading per dipole offset is required and simple inversion schemes such as the algorithm by Zohdy (1989) are sufficiently fast to instantly provide the user with a basic quasi-2D model. Experience with synthetic as well as field datasets shows that such models are indicative of major changes in the properties of the subsurface along the survey profile, but fail to accurately resolve complex structures as 2D and 3D effects remain unaccounted for. Other 1D inversion techniques such as a least-squares iterative approach are conceiveable in this context, but likely to be more time-consuming. Zohdy's method is straightforward and makes only minimal a-priori assumptions about the nature of the resistivity model. The number of model layers is always the same as the number of samples of the VES curve, i.e. the number of available depth levels in the multi-offset data. The Zohdy model is therefore a crude but genuine representation of the information contained in a single scan of towed-array CR data.

2D interpretation. If the subsurface is known to contain features with a more complex non-1D structure, a full 2D interpretation of multi-offset towed-array CR profile data is likely to be more accurate than the CVES-based approach. This is particularly so in the case of environmental and engineering site investigations where subsurface targets are expected to be localised and the electrical properties of the ground are likely to be discontinuous in both lateral and vertical directions. In those situations electrical current will flow in complex patterns that can no longer be modeled by a 1D earth. 2D interpretation techniques attempt to explain the measured data by means of 2D earth models, thus introducing lateral constraint into the model, however without taking potential 3D effects into account. The inversion of synthetic towed-array CR data for simple earth models (e.g. the vertical contact) has demonstrated the advantages of the 2D approach over CVES interpretation. Lateral variations and especially discontinuities are reconstructed much more accurately by the 2D inversion. As demonstrated in this chapter, noisy datasets are also dealt with better by 2D techniques since the entire dataset is considered as a whole. Individual 1D inversions are found to be much more susceptible to bias by measurement noise.

While these advantages have been known in the past for the case of DC resistivity, it is rarely ever recognised that perhaps the most critical factor for an accurate multi-dimensional interpretation is data density. The detectability of electrically anomalous zones in the subsurface by 2D resistivity inversion critically depends on the density of coverage with apparent resistivity data along the profile. In this aspect, towed-array CR is clearly superior to the DC technique because it enables efficient acquisition of high-density data, adding extra constraint to the interpretation of complex models of the subsurface compared to coarser DC datasets. Until recently however, 2D resistivity inversion algorithms were either not suitable for the interpretation of large-scale high-density datasets such as those produced by multi-offset towed-array CR or they were not widely available. The examples shown in this chapter demonstrate that this is no longer the case.

3D interpretation. The most accurate assessment of a highly complex subsurface by multi-offset resistivity measurements is only possible by a full 3D interpretation of the data. In the case of towed-array CR, this is highly unfamiliar terrain and there are no published examples in the open literature to date. It has been demonstrated in this chapter that some elementary rules must be observed in the design of 3D towed-array CR surveys to account for the characteristics of such datasets. Key parameters are the ratio between the dipole separations on the towed array and the sampling interval along the survey line and the ratio between the dipole length and the inter-line spacing if the equatorial geometry is used. It was shown that with a suitable survey geometry a standard commercial towed-array CR instrument can be used to acquire 3D datasets that can be interpreted by customary 3D resistivity inversion algorithms without modification.
A fundamental question regarding optimum 3D survey design with towed CR arrays is whether single-orientation data only can sufficiently constrain complex 3D targets in the shallow subsurface or whether data from two or more independent orientations are required. Tests with both synthetic and field datasets have demonstrated that single-orientation data acquired with a multi-offset equatorial array can be used to accurately reconstruct shallow targets with simple 3D geometry.

Chapter 9

Conclusions and further work

A unified approach to CR. Capacitive resistivity (CR) is a novel geophysical technique capable of complementing conventional DC resistivity in the built environment and other settings where galvanic contact cannot be achieved or results in poor data quality due to high contact resistances. Although the concept of using frequencies in the VLF range for measuring the resistivity of the subsurface under quasi-static conditions has been known for some time, previous research has approached the task from rather diverse angles (cf. Section 4.1). It has been shown in this thesis that these various endeavours can be unified by accepting that capacitive coupling between the sensors and the ground is the essential mechanism that unites all approaches. The emphasis on capacitive coupling makes this methodology distinct from other resistivity methods such as DC resistivity (galvanic coupling) or electromagnetic methods (inductive coupling). The term "capacitive resistivity" acknowledges this distinction and is therefore suggested as the most appropriate name for the technique.

Theoretical formulations of CR and their applicability. The work described in this thesis provides a systematic study of the physical principles of CR, their theoretical description and their practical implementation, thus delivering a full account of all relevant aspects of the technique. It was shown that a particular theoretical formulation of CR is inevitably linked with the type of capacitive sensor employed. The electrostatic formalism, which is based upon electrostatic theory and represents a generalisation of the concept of the DC four-point array, was found to be a suitable description of a capacitive measurement of resistivity under quasi-static conditions (cf. Section 4.6). For the electrostatic formalism to apply, sensors that can be approximated by point poles must be employed. It was shown by modelling of sensor capacitances that this can be accomplished by using plate-wire combinations (Section 5.4).
If conditions are such that the quasi-static approximation does not apply (high frequencies, low resistivities or large arrays), inductive effects become relevant so that coupling is no longer predominantly capacitive. Under such circumstances, only a full electromagnetic formulation provides an appropriate description of the quadrupole (cf. Section 4.7).

The complex transfer impedance under quasi-static conditions. A fundamental characteristic of CR is that the ground response in the form of the transfer impedance is a complex function, i.e. the observed potential may have a phase shift with respect to the injected current (Section 4.6.2.3). A non-zero CR phase observed under quasi-static conditions is entirely due to the capacitive nature of the coupling mechanism and a function of the geometry of the sensor array. Such phases are not caused by electromagnetic induction; neither are they a result of a subsurface material property (e.g. electrical polarisability). Hence CR phases are clearly distinct from phases observed by electromagnetic or induced polarisation/complex resistivity methods. A CR measurement as such cannot differentiate between the possible causes of a phase rotation. However, under quasi-static conditions and in the absence of polarisable media, the CR phase may be regarded as a diagnostic parameter in its own right.
Parametric studies based on a generalised frequency have shown that the transfer impedance is likely to be in-phase under typical conditions as the quadrature component is expected to be small (Section 4.6.4). However, for particularly conductive ground, at small array separations or for larger sensor elevations, a significant quadrature component may be observed, resulting in a phase rotation together with an increased magnitude compared to the DC case. Under such conditions the estimation of apparent resistivity using the magnitude of the transfer impedance is clearly flawed. Analysis of the phase-sensitive expression for apparent resistivity derived in this thesis has shown that it reduces to the classical DC formula for apparent resistivity, however as a function of the *in-phase* component of the transfer impedance instead of the magnitude (Section 4.6.5). In other words, under quasi-static conditions (i.e. the low induction number regime) apparent resistivity is proportional to the in-phase component of the CR response. Comparing this result to the well-known estimate of resistivity by the EM ground conductivity technique (Section 3.2), one may reach the conclusion that the two methodologies represent a fundamental "symmetry" of physics, whereby an *inductively* coupled measurement provides information about subsurface resistivity in the *quadrature* of the response function, while the equivalent information for a *capacitively* coupled measurement is contained in the *in-phase* component.

The optimal parameter range for quasi-static CR. A comprehensive parameter study for the CR response based on the electrostatic formalism has been undertaken in this thesis in order to investigate the applicability of the technique under typical conditions encountered in environmental and engineering site investigation surveys (Chapter 5). The results suggest that a realistic set of parameters does exist which facilitates a capacitive measurement of resistivity under quasi-static conditions at scales applicable to such surveys. A window of useable frequencies is defined by an upper frequency limit (25 kHz) associated with the low induction number condition and a lower frequency limit (1 kHz) to ensure a minimum current flow in the injection circuit. Geometric restrictions imposed on the CR technique comprise an upper limit for array separation to ensure low induction numbers and a maximum array elevation

beyond which adequate current injection cannot be guaranteed because of insufficient sensor capacitance. While the separation limit is critically dependent on the electrical properties of the ground (more resistive ground allows for greater separations), the elevation limit is purely a function of sensor design. For the plate-wire combination, critical capacitance levels are typically achieved at elevations below 10 mm (cf. Section 5.4.2.2).
The parameter study has revealed that the observation of significant CR phases is by no means improbable for the range of parameters typically associated with environmental and engineering site investigations. As an example, for an equatorial dipole-dipole array with a dipole separation of 2 m on very conductive ground ($\rho = 1\,\Omega$m), a typical phase rotation of $\phi \approx \pi/4$ may occur, i.e. in-phase and quadrature components may become comparable in size (cf. Figure 5.4). Under these circumstances, a phase-sensitive measurement is necessary since apparent resistivity would be overestimated if it were derived from the magnitude of the transfer impedance.

Properties of capacitive sensors. A further aspect of the parameter study was the investigation of the properties of capacitive sensors (Section 5.4). It was found that the theoretical concept of point poles postulated in the electrostatic formalism has a practical realisation in the plate-wire sensor. If this sensor type is designed such that the plate size is comparatively small against the dimensions of the dipole, then the influence of the wire segment on the total sensor capacitance is negligible and only the plate surface is relevant for the coupling and the measurement of the electric potential.
Capacitive measurements with line antennas cannot be adequately interpreted with the electrostatic formalism. To obtain a DC resistivity estimate from a line antenna measurement, an average contribution over the length of the antenna must be considered, hence the DC geometric factor is non-trivial in this case (cf. Section 4.5). The interpretation of line antenna datasets with standard DC interpretation schemes must be based on equivalent grounded dipoles (Section 4.5.3). This may not be straightforward, particularly if the separation between the two line antenna dipoles is small compared to their length.

Experimental validation of CR concepts. In this thesis, the fundamental concepts of CR have been validated experimentally in a series of elementary surveys. Firstly, the practical properties of real capacitive sensors were examined by measuring the effective sensor capacitance of a plate-wire combination directly in the field (Section 6.2.1). The results showed the reactive part of the impedance of the injection circuit to be dominant over ground resistance, i.e. the transmitter current is primarily a function of the sensor capacitance. It has also been shown that an effective sensor elevation can be deduced from the measured sensor capacitance using simple capacitance models. This elevation is theoretical since an ideal ground surface must be assumed; however, good correlation with practical elevations has been observed. This simple test can be regarded as further proof that the fundamental assumptions of the CR technique are consistent. Subsequently, wideband measurements of the electric field

were carried out to demonstrate that grounded and non-grounded dipoles are equivalent sensors for the electric field at the ground surface (Section 6.2.2).
The second part of the experimental programme was concerned with the spatial analysis of the complex transfer impedance in order to assess the applicability of the electrostatic formalism to practical CR measurements. A study of this kind was only possible after a prototype CR instrument had been developed that could accurately measure the fully complex transfer impedance. Both move-out and directional surveys were considered (Section 6.3). The results of the analysis showed a remarkable agreement between the observed data and the quasi-static model for all azimuths and for a wide range of array separations except at extremely short and very long offsets. At extremely short offsets, ρ_a was consistently overestimated due to the geometric distortion associated with the finite plate size. At long offsets, the onset of inductive effects was consistently observed in all datasets in the form of increasing magnitudes and a phase rotation away from zero phase. Consequently, apparent resistivities are also overestimated at long offsets. Comparative surveys using CR and conventional DC resistivity have shown a good level of agreement.

Dynamic measurements with towed CR arrays. It has been shown both conceptually and experimentally that reliable high-density dynamic measurements of the fully complex transfer impedance are possible with towed CR arrays. Spatial sampling may be "continuous" as CR arrays are not restricted to a finite set of electrode positions. Minimum sampling intervals for the CR technique were shown to be of the order of 1 cm (Section 7.1). The high frequency of operation allows for a stable measurement at realistic towing speeds, while towed DC techniques are limited to single-cycle estimates since they employ much lower frequencies. Due to its superior effective depth of investigation, the equatorial dipole-dipole array was found to be the most appropriate geometry for towed-array applications, particularly when space for manoeuvering is limited.
An evaluation of the operational characteristics of existing CR instruments as well as the newly developed BGS CRI system showed that all are capable of acquiring high-quality, highly repeatable data (Section 7.2). The commercial systems provide only magnitudes of the transfer impedance. Levels of towing-induced noise are generally low, provided that surface conditions are favourable. However, measurements with the BGS CRI system have shown that the same or indeed a superior level of quality and repeatability is possible for a dynamic measurement of the fully complex response. While all instruments performed well on soft ground, clear differences in performance were observed on hard, resistive surfaces such as roads and pavements, where the commercial systems were most affected by noise. The BGS CRI system, on the other hand, was found to be particularly well adapted to such environments, with the best-quality CRI data often being observed on roads. The information content of the CRI response was found to be significant at all scales. High repeatability at centimetre intervals is clearly a novelty for dynamically acquired near-surface resistivity data. The equivalence of towed-array CR measurements with con-

ventional DC traverses was verified experimentally, highlighting the amount of additional detail contained in CR data.
As with all geophysical techniques, CR data may be affected by noise. However, as a consequence of enhanced noise suppression by the signal detection technique, typical noise levels observed with the CRI system are likely to be far smaller than those observed in dynamic DC measurements (Section 7.3.1). Commercial CR systems were found to be more susceptible to noise, often expressed in characteristic outliers. While conventional filtering techniques are inappropriate for the suppression of such noise, predictive filtering was found to give useful results with typical towed-array CR data. The nature of the predictor filter allows for real-time data processing during acquisition. It was also demonstrated in this thesis that other geophysical processing techniques (e.g. micro-levelling) can be usefully applied to towed-array CR datasets (Section 7.3.2).

Electrical imaging with multi-offset towed-array CR. It has been demonstrated in this thesis that multi-offset towed-array CR data can be interpreted in a similar fashion to conventional multi-offset DC resistivity data (Chapter 8). The unprecedented data density provided by the CR technique allows for the creation of tomographic images at high resolutions. Capacitive resistivity imaging (CRI) is therefore potentially much better adapted to the complex structures encountered in environmental and engineering imaging applications than customary resistivity imaging with DC data.
It was shown that conventional DC interpretation techniques can be directly applied to towed-array CR data if some basic rules with regard to survey design are observed in order to account for fundamental differences between fixed-array and towed-array acquisition (Section 8.1). Data should be acquired at constant distance intervals (as opposed to constant time-frequency) and the array separations employed should form simple geometric relationships with each other and the sampling interval.

Interpretation schemes. A range of DC resistivity interpretation schemes were shown to be applicable to multi-offset towed-array CR data. Quasi-2D interpretation based on continuous vertical electrical soundings using a fast Zohdy-type inversion was shown to be a useful tool for "on-the-fly" interpretation during data acquisition (Section 8.2). However, while models derived from a quasi-2D interpretation are indicative of major changes in subsurface properties along the survey profile, they fail to accurately resolve complex 2D and 3D structures.
The advantages of a full 2D resistivity inversion over CVES interpretation were demonstrated by applying a modern, fully automated 2D resistivity inversion algorithm to both synthetic and real towed-array CR datasets (Section 8.3). Until recently, such algorithms were not suitable for the interpretation of large-scale high-density datasets. It has been shown that the reconstruction of lateral variations and discontinuities is much more accurate with a full 2D inversion, since the entire dataset is interpreted as a whole. Noisy datasets were also

found to be dealt with more favourably by 2D techniques.
Finally, the work has shown that multi-offset towed-array CR data can also be used for 3D imaging (Section 8.4). It was demonstrated that standard towed-array CR instruments can be employed to acquire 3D datasets which can be interpreted by automated 3D resistivity inversion algorithms without modification. With regard to optimum survey design, the question has arisen as to whether single-orientation data can sufficiently constrain complex 3D targets in the shallow subsurface or whether data from two independent orientations are required. Tests undertaken with both synthetic and field datasets have shown that satisfactory reconstruction of shallow targets with basic 3D geometry is possible with single-orientation data. It remains to be seen whether towed-array CR datasets are able to accurately resolve more complex targets such as those likely to be encountered in environmental and engineering site investigations.

Impact on environmental and engineering site investigations. The results of this research demonstrate that the CR technique is capable of extending the scope of conventional DC resistivity to environments where galvanic contact cannot be achieved or where high contact impedances result in poor data quality. As electrical imaging has become a well-established tool in environmental and engineering site investigations, it is thought that the option to conduct electrical resistivity tomography surveys in areas where DC measurements were previously difficult if not impossible may have a positive impact on such investigations. The main strengths of CR in this context are:

- Subsurface resistivity measurements are possible irrespective of surface materials and their electrical properties.
- Under quasi-static conditions, CR and DC data are equivalent and proven DC interpretation schemes may be applied to CR datasets.
- Towed-array data acquisition can provide high-resolution resistivity data at data densities which are otherwise impossible to achieve. Such data can contain relevant information down to the centimetre scale, thus potentially improving image resolution and hence target definition.

The two main weaknesses and limitations of CR are:

- The technique may not be suitable (or as applicable) on uneven terrain or rough surfaces.
- DC interpretation of CR data is limited to shallow depths since the condition of low induction numbers must be satisfied.

A potential application for an increased use of capacitive resistivity imaging in site investigations is the non-destructive testing of engineered structures such as roadbeds, bridges, foundations and similar installations. Tarmac roads and pavements have proven to be particularly favourable for towed-array CR surveys. When measuring the fully complex transfer impedance, CR phases may provide additional diagnostic information, for example by indicating the

breakdown of quasi-static conditions and onset of electromagnetic induction (e.g. detection of services, cf. Section 7.2.3.1). The detection of voids under tarmac/concrete is another application where phase information is expected to be beneficial.

Further work. The natural mode of operation for the CR technique is the low-induction number limit (cf. Section 4.6.2). Quasi-static conditions give rise to a very fortunate situation where the estimation of apparent resistivity can be restricted to the in-phase component of the transfer impedance. In this case, highly developed DC resistivity interpretation schemes are applicable to CR data. However, the examples shown in this work have demonstrated that the occurrence of significant CR phases is a reality, even under the quasi-static regime (Sections 6.3, 7.2.3.1). Further work is required to be able to interpret this additional source of information in more complex environments. So far, the theoretical description of the CR technique is restricted to a homogeneous halfspace in the quasi-static case (Section 4.6) and a 1D layered earth in the EM case (Section 4.7). The effects of 2D and 3D subsurface structures on the complex response cannot be comprehensively predicted at this stage. Development of suitable 2D and 3D modelling schemes or the adaptation of existing EM algorithms would therefore be highly desirable.
Further work is also required to accelerate and improve the interpretation of large multi-offset towed-array CR datasets. As indicated in Section 8.3.4, the application of fast one-pass inversion algorithms to such data may be advantageous compared with conventional 2D iterative least-squares inversion. It is suggested that such algorithms be tested and, if applicable, incorporated in the data acquisition software in order to facilitate preliminary interpretation of multi-offset towed-array CR data in the field.

Acknowledgements

This thesis could not have appeared in its present form without the kind assistance and generous support of numerous individuals and organisations.

I gratefully acknowledge the guidance and support of my supervisors, Dr Paul Nathanail (University of Nottingham) and Dr Richard Ogilvy (British Geological Survey) during the course of this work. I also wish to express my gratitude towards Dr Brian Atkin (UoN) for setting up this PhD project together with Richard and providing me with the opportunity to carry out this challenging research. My studies were generously supported by a Gas Technology Hub PhD studentship, jointly funded by the University of Nottingham and Advantica Technologies Ltd (formerly BG Technology). Additional resources were kindly provided by the British Geological Survey.
I am indebted to Dr David Beamish (BGS) for his continuing support and encouragement, sound scientific advice and many fruitful discussions. His shared enthusiasm for the rather unusual subject resulted in a most enjoyable collaboration and his careful review of the manuscript is gratefully acknowledged. The successful conclusion of this research would not have been possible without the contribution of Phil Meldrum (BGS), who developed the ingenious BGS prototype CRI system. Thanks are also due to Dr Jonathan Chambers (BGS) for proof-reading this thesis and to Dr Ian Lowndes (UoN) for acting as internal assessor and providing help and advice throughout the course of the research.
I also wish to express my thanks to Doug Groom and Chris Leech of Geometrics Inc./Geometrics UK for their support and provision of the OhmMapper™ system for testing; to Prof Dr Klaus Spitzer, TU Bergakademie Freiberg, Germany, for making his 3D forward modelling code available to me; to Dr Torleif Dahlin, Lund University, Sweden, Dr Panagiotis Tsourlos, Aristotle University of Thessaloniki, Greece, and Dr M. H. Loke, Universiti Sains Malaysia, for support and valuable discussions; to Dr Ian Hill, University of Leicester, for providing access to the EIGG test site at Southmeads Road, Leicester; to Capt. Pete Coe, 530 Specialist Team Royal Engineers (MAT), for arranging access to the training site at Chilwell Barracks, Nottingham; to Phil Reeve, East Midlands Development Agency, for arranging access to the Avenue Coking Works and to Frank Evans of BG Technology and Dr Andy Robinson of Komex Clarke Bond for arranging access to the BG site at Aylestone Road, Leicester. Many colleagues and friends have helped with the fieldwork, including Phil Meldrum, David Beamish, Jon Chambers, Richard Ogilvy, Kathryn Strange and Marcello Di Bonito. Their efforts are gratefully acknowledged.

Finally, my warmest thanks go to my parents, Werner and Elisabeth Kuras, and my sister Tina for all their love and continuing support throughout this endeavour.

Oliver Kuras
Nottingham, UK
December 2002

Bibliography

ABEM Instrument AB. WADI VLF: International Frequency List: ABEM printed matter no 93062, www.abem.se.

Acworth, R. I., and Griffiths, D. H., 1985, Simple data processing of tripotential apparent resistivity measurements as an aid to the interpretation of subsurface structure: Geophys. Prosp., **33**, 861–887.

Anon, 1988, Engineering Geophysics. Report of the Geological Society Engineering Group Working Party: Q. J. Eng. Geol., **21**, 207–271.

Anon, 1999, Code of practice for site investigations, BS 5930:1999: British Standards Institution, London.

Anon, 2000, Let's get geophysical: Ground Eng., **33**, no. 4, 26.

Anon, 2001, Code of practice for investigation of potentially contaminated sites, BS 10175:2001: British Standards Institution, London.

Barker, R. D., 1981, The offset system of electrical resistivity sounding and its use with a multicore cable: Geophys. Prosp., **29**, 128–143.

Barker, R. D., 1992, A simple algorithm for electrical imaging of the subsurface: First Break, **10**, no. 2, 53–62.

Barr, D., Bardos, R. P., Finnamore, J. R., and Nathanail, C. P., 2002, Nonbiological methods of investigation and characterisation of land contamination: Construction Industry Research and Information Association, London.

Baxter, L. K., 1997, Capacitive Sensors: Design and Applications: IEEE Press, New York.

Beck, M. S., Byars, M., Dyakowski, T., Waterfall, R., He, R., Wang, S. J., and Yang, W. Q., 1997, Principles and industrial applications of electrical capacitance tomography: Meas. Control, **30**, 197–200.

Benderitter, Y., Jolivet, A., Mounir, A., and Tabbagh, A., 1994, Application of the electrostatic quadripole to sounding in the hectometric depth range: J. Appl. Geophys., **31**, 1–6.

Bishop, I., Styles, P., Emsley, S. J., and Ferguson, N. S., 1997, The detection of cavities using the microgravity technique: case histories from mining

and karstic environments *in* McCann, D. M., Eddleston, M., Fenning, P. J., and Reeves, G. M., Eds., Modern Geophysics in Engineering Geology: The Geological Society, 153–166.

Börner, F. D., and Schön, J. H., 1991, A relation between the quadrature component of electrical conductivity and the surface area of sedimentary rocks: The Log Analyst, **32**, 612–613.

Börner, F., Gruhne, M., and Schön, J., 1993, Contamination indications derived from electrical properties in the low frequency range: Geophys. Prosp., **41**, 83–98.

Burns, R. A., Goriainov, N. N., Hunter, J. A., Judge, A. S., Skvortzov, A. G., Todd, B. J., and Timofeev, V. M., 1993, Co-operative Russian-Canadian geophysical investigations of permafrost on the Yamal Peninsula, Western Siberia: Proceedings of the 6th International Conference on Permafrost, Beijing, 66–71.

Cagniard, L., 1953, Basic theory of the magneto-telluric method of geophysical prospecting: Geophysics, **18**, no. 3, 605–635.

Carpenter, E. W., and Habberjam, G. M., 1956, A tripotential method of resistivity prospecting: Geophysics, **21**, no. 2, 455–469.

Carpenter, E. W., 1955, Some notes concerning the Wenner configuration: Geophys. Prosp., **3**, 388–402.

Chambers, J., Ogilvy, R., Meldrum, P., and Nissen, J., 1999, 3D resistivity imaging of buried oil- and tar-contaminated waste deposits: Eur. J. Env. Eng. Geophys., **4**, no. 1, 3–14.

Chambers, J. E., Ogilvy, R. D., Kuras, O., Cripps, J. C., and Meldrum, P. I., 2002, 3D electrical imaging of known targets at a controlled environmental test site: Environ. Geol., **41**, 690–704.

Charsley, T. J., Rathbone, P. A., and Lowe, D. J., Nottingham: a geological background for planning and development. Onshore Geology Series, WA/90/1: Technical report, British Geological Survey, 1990.

Claerbout, J. F., and Muir, F., 1973, Robust modeling with erratic data: Geophysics, **38**, no. 5, 826–844.

Coggon, J. H., 1971, Electromagnetic and electrical modeling by the finite element method: Geophysics, **36**, no. 1, 132–155.

Constable, S. C., Parker, R. L., and Constable, C. G., 1987, Occam's inversion: A practical algorithm for generating smooth models from electromagnetic sounding data: Geophysics, **52**, no. 3, 289–300.

Cottineau, L. M., Desmas, M., Lagabrielle, R., Leroux, V., Palma Lopes, S., and Sorin, J. L., 2000, Capacitive contact geoelectrical equipment development

for borehole environmental and engineering applications: Proceedings of the 6th meeting of the Environmental and Engineering Geophysical Society - European Section.

Cripps, J. C., McCann, D. M., Culshaw, M. G., and Bell, F. G., 1988, The Use of Geophysical Methods as an Aid to the Detection of Abandoned Shallow Mine Workings: Proceedings of the 2nd International Conference on Construction in Areas of Abandoned Mineworkings, Engineering Technics Press, 53–60.

Culshaw, M. G., McCann, D. M., and Donnelly, L. J., 2000, Impacts of abandoned mine workings on aspects of urban development: Trans. Instn. Min. Metall. (Sect. A: Min. technol.), **109**, no. 3, 132–138.

Dabas, M., Tabbagh, A., and Tabbagh, J., 1994, 3-D inversion in subsurface electrical surveying — I. Theory: Geophys. J. Int., **119**, 975–990.

Dahlin, T., and Bernstone, C., 1997, A roll-along technique for 3D resistivity data acquisition with multi-electrode arrays: Proceedings of the Symposium on the Application of Geophysics to Engineering and Environmental Problems (SAGEEP), Vol. 2, Reno, Nevada, EEGS, 927–935.

Dahlin, T., 1993, On the automation of 2D resistivity surveying for engineering and environmental applications: Ph.D. thesis, Lund University.

Dahlin, T., 1996, 2D resistivity surveying for environmental and engineering applications: First Break, **14**, no. 7, 275–283.

Das, U. C., and Ghosh, D. P., 1973, A study on the direct interpretation of dipole sounding resistivity measurements over layered earth: Geophys. Prosp., **21**, 379–400.

Das, U. C., and Parasnis, D. S., 1987, Resistivity and induced polarisation responses of arbitrarily shaped 3-d bodies in a two-layered earth: Geophys. Prosp., **35**, 98–109.

deGroot-Hedlin, C., and Constable, C., 1990, Occam's inversion to generate smooth, two-dimensional models from magnetotelluric data: Geophysics, **55**, no. 12, 1613–1624.

DETR. DETR Circular 2/2000 Contaminated Land: Implementation of Part IIA of the Environmental Protection Act 1990: Department of the Environment, Transport and the Regions, www.defra.gov.uk/environment/landliability/circ2-2000/index.htm, 2000.

Dey, A., and Morrison, H. F., 1979, Resistivity modelling for arbitrary shaped two-dimensional structures: Geophys. Prosp., **27**, 106–136.

Dobrin, M. B., and Savit, C. H., 1988, Introduction to Geophysical Prospecting: McGraw-Hill.

DoE. Environmental Protection Act 1990: Department of the Environment, Her Majesty's Stationery Office, www.hmso.gov.uk, 1990.

DoE. Environment Act 1995: Department of the Environment, Her Majesty's Stationery Office, www.hmso.gov.uk, 1995.

Douma, M., Timofeev, V. M., Rogozinski, A. W., and Hunter, J. A., 1994, A capacitive-coupled ground resistivity system for engineering and environmental applications: Results of two Canadian field tests: Expanded Abstracts of the 64th Annual Meeting of the Society of Exploration Geophysicists, 559–561.

Edwards, R. N., Lee, H., and Nabighian, M. N., 1978, On the theory of magnetometric resistivity (MMR) methods: Geophysics, **43**, no. 6, 1176–1203.

Edwards, R. N., 1974, The magnetometric resistivity method and its application to the mapping of a fault: Can. J. Earth Sci., **11**, 1136–1156.

Edwards, L. S., 1977, A modified pseudosection for resistivity and IP: Geophysics, **42**, no. 5, 1020–1036.

Ellis, R. G., and Oldenburg, D. W., 1994a, Applied geophysical inversion: Geophys. J. Int., **116**, 5–11.

——— 1994b, The pole pole 3-D dc-resistivity inverse problem - a conjugate-gradient approach: Geophys. J. Int., **119**, 187–194.

Environment Agency. Dealing with contaminated land in England: Progress in 2002 with implementing the Part IIA regime: www.environment-agency.gov.uk, 2002.

Everton, S., 1998, Under observation: Ground Eng., **31**, no. 5, 26–29.

Fuller, B. D., 1967, Two-dimensional frequency analysis and design of grid operators *in* Hansen, D. A., Heinrichs, W. E., Holmer, R. C., MacDougall, R. E., Rogers, G. R., Sumner, J. S., and Ward, S. H., Eds., Mining Geophysics: Volume II, Theory: Soc. Expl. Geoph.

Geselowitz, D. B., 1971, An application of electrocardiographic lead theory to impedance plethysmography: IEEE Trans. Biomed. Eng., **BME-18**, 39–41.

Ghosh, D. P., 1971a, The application of linear filter theory to the direct interpretation of geoelectrical resistivity sounding measurements: Geophys. Prosp., **19**, no. 2, 192–217.

——— 1971b, Inverse filter coefficients for the computation of apparent resistivity standard curves for a horizontally stratified earth: Geophys. Prosp., **19**, 769–775.

Grant, F. S., and West, G. F., 1965, Interpretation Theory in Applied Geophysics: McGraw-Hill, New York.

Grard, R., and Tabbagh, A., 1991, A mobile four-electrode array and its application to the electrical survey of planetary grounds at shallow depths: J. Geophys. Res., **96**, no. B3, 4117–4123.

Grard, R., 1990a, A quadrupolar array for measuring the complex permittivity of the ground: application to Earth prospection and planetary exploration: Meas. Sci. Technol., **1**, 295–301.

——— 1990b, A quadrupole system for measuring in situ the complex permittivity of materials: application to penetrators and landers for planetary exploration: Meas. Sci. Technol., **1**, 801–806.

Griffiths, D. H., and Barker, R. D., 1993, 2-dimensional resistivity imaging and modeling in areas of complex geology: J. Appl. Geophys., **29**, 211–226.

Griffiths, D. H., and Turnbull, J., 1985, A multi-electrode array for resistivity surveying: First Break, **3**, no. 7, 16–20.

Griffiths, D. H., Turnbull, J., and Olayinka, A. I., 1990, Two-dimensional resistivity mapping with a computer-controlled array: First Break, **8**, no. 4, 121–129.

Habberjam, G. M., 1979, Apparent resistivity observations and the use of square array techniques: Geoexploration Monographs, Series 1, No. 9. Gebrüder Borntraeger, Berlin, Stuttgart.

Healy, P. R., and Head, J. M., 1984, Construction over abandoned mine workings: Construction Industry Research and Information Association, London.

Hesse, A., Jolivet, A., and Tabbagh, A., 1986, New prospects in shallow depth electrical surveying for archaeological and pedological applications: Geophysics, **51**, no. 3, 585–594.

Hill, I. A. Environmental and Industrial Geophysics Group (EIGG) test sites: www.le.ac.uk/geology/iah/res/EIGG/eigghp.html, 2000.

Huang, H. P., and Fraser, D. C., 1999, Airborne resistivity data leveling: Geophysics, **64**, 378–385.

Isaksen, Ø., 1996, A review of reconstruction techniques for capacitance tomography: Meas. Sci. Technol., **7**, 325–337.

Jackson, J. D., 1975, Classical Electrodynamics: John Wiley & Sons, 2nd edition.

Keller, G. V., and Frischknecht, F. C., 1966, Electrical Methods in Geophysical Prospecting: Pergamon Press.

Keller, G. V., 1988, Rock and mineral properties *in* Nabighian, M. N., Ed., Electromagnetic Methods in Applied Geophysics — Volume 1, Theory: Soc. Expl. Geoph.

Keller, G. V., 1993, Electrical and electromagnetic methods in areas of complex geology: J. Appl. Geophys., **30**, no. 3, 161–173.

Kulessa, B., Jaekel, U., Bick, M., Hashagen, U., and Vereecken, H., 2000, Towards high-resolution imaging of subsurface pollution: an introduction to the Magneto-Electrical Resistivity Imaging Tool (MERIT): Proceedings of the Symposium on the Application of Geophysics to Environmental and Engineering Problems (SAGEEP), 925–934.

Kuras, O., Ogilvy, R. D., Chambers, J. E., Meldrum, P. I., and Lelliott, M., Determination of leachate distribution within the waste mass by 3D resistivity imaging, Pit 4, Calvert Landfill, Calvert, Buckinghamshire. Commissioned Report CR/02/117: British Geological Survey, 2002.

Lehmann, F., and Green, A. G., 1999, Semiautomated georadar data acquisition in three dimensions: Geophysics, **64**, 719–731.

Lesselier, D., and Habashy, T., 2000, Foreword: Inverse Problems, **16**, no. 5.

Li, Y. G., and Oldenburg, D. W., 1994, Inversion of 3-D dc resistivity data using an approximate inverse mapping: Geophys. J. Int., **116**, 527–537.

Lile, O. B., Morris, M., and Rønning, J. S., 1997, Estimating groundwater flow velocity from changes in contact resistance during a saltwater tracer experiment: J. Appl. Geophys., **38**, 105–114.

Lines, L. R., and Treitel, S., 1984, Tutorial: A review of least-squares inversion and its application to geophysical problems: Geophys. Prosp., **32**, 159–186.

Littlejohn, G. S., 1991, Inadequate site investigation: Ground Eng., **24**, 28–31.

Loke, M. H., and Barker, R. D., 1995, Least-squares deconvolution of apparent resistivity pseudosections: Geophysics, **60**, no. 6, 1682–1690.

Loke, M. H., and Barker, R. D., 1996a, Practical techniques for 3D resistivity surveys and data inversion: Geophys. Prosp., **44**, 499–523.

——— 1996b, Rapid least-squares inversion of apparent resistivity pseudosections by a quasi-Newton method: Geophys. Prosp., **44**, 131–152.

Loke, M. H., Electrical imaging surveys for environmental and engineering studies:, Unpublished report: www.geoelectrical.com, 1999.

McCann, D. M., Eddleston, M., Fenning, P. J., and Reeves, G. M., Eds., 1997, Modern Geophysics in Engineering Geology, Geological Society Engineering Geology Special Publication No. 12, The Geological Society, London.

McDowell, P. W., 2002, Geophysics in engineering investigations: Construction Industry Research and Information Association, London.

McNeill, J. D., Electromagnetic terrain conductivity measurement at low induction numbers: Technical note TN-6, Geonics Ltd., 1980.

Minty, B. R. S., 1991, Simple micro-levelling for aeromagnetic data: Explor. Geophys., **22**, 591–592.

Møller, I., Jacobsen, B. H., and Christensen, N. B., 2001, Rapid inversion of 2-d geoelectrical data by multichannel deconvolution: Geophysics, **66**, 800–808.

Mufti, I. R., 1978, A practical approach to finite-difference resistivity modeling: Geophysics, **43**, no. 5, 930–942.

Munkholm, M. S., Sørensen, K., and Jacobsen, B. H., 1995, Characterization and in-field suppression of noise in hydrogeophysics: Proceedings of the Symposium on the Application of Geophysics to Engineering and Environmental Problems (SAGEEP), 339–347.

Munkholm, M. S., 1996, Robust methods for transient electromagnetic and pulled array geoelectrical data processing: Ph.D. thesis, University of Aarhus.

Nathanail, C. P., 1999, Introduction to contaminated land management: Monitor Press, Sudbury.

Nathanail, C. P., 2001, Draft code consigned to dustbin: Ground Eng., **34**, no. 2, 7.

Ogilvy, R. D., Meldrum, P. I., and Chambers, J. E., 1999, Imaging of industrial waste deposits and buried quarry geometry by 3-D resistivity tomography: Eur. J. Env. Eng. Geophys., **3**, 103–114.

Ogilvy, R. D., Meldrum, P. I., Kuras, O., Beamish, D., and Chambers, J. E., 2001, Detection of abandoned mine-shafts by 3D resistivity tomography: a parametric modelling study: Proceedings of the 7th meeting of the Environmental and Engineering Geophysical Society - European Section, Birmingham, 166–167.

Ogilvy, R. D., Meldrum, P. I., Chambers, J. E., and Williams, G. M., 2002, The Use of 3D Electrical Resistivity Tomography to Characterise Waste and Leachate Distribution within a Closed Landfill, Thriplow, UK: J. Env. Eng. Geophys., **7**, no. 1, 11–18.

Olhoeft, G. R., 1980, Electrical properties of rocks *in* Touloukian, Y. S., Judd, W. R., and Roy, R. F., Eds., Physical properties of rocks and minerals: McGraw-Hill, 257–330.

Olhoeft, G. R., 1985a, Clay-organic reactions measured with complex resistivity: Geophysics, **50**, no. 2, 309.

——— 1985b, Low-frequency electrical properties: Geophysics, **50**, no. 12, 2492–2503.

O'Neill, D. J., 1975, Improved Linear Filter Coefficients for Application in Apparent Resistivity Computations: Bull. Aust. Soc. Explor. Geophys., **6**, no. 4, 104–109.

Oppenheim, A. V., and Schafer, R. W., 1999, Discrete-time signal processing: Prentice-Hall, 2nd edition.

Panissod, C., Dabas, M., Jolivet, A., and Tabbagh, A., 1997a, A novel mobile multipole system (MUCEP) for shallow (0-3 m) geoelectrical investigation: the 'Vol-de-canards' array: Geophys. Prosp., **45**, 983–1002.

——— 1997b, Electrostatic measurements in complex artificial (anthropogenic) grounds: Proceedings of the 3rd meeting of the Environmental and Engineering Geophysical Society - European Section, 163–166.

Panissod, C., Dabas, M., Hesse, A., Jolivet, A., Tabbagh, J., and Tabbagh, A., 1998, Recent developments in shallow-depth electrical and electrostatic prospecting using mobile arrays: Geophysics, **63**, no. 5, 1542–1550.

Parasnis, D. S., 1988, Reciprocity theorems in geoelectric and geoelectromagnetic work: Geoexploration, **25**, 177–198.

Parasnis, D. S., 1997, Principles of Applied Geophysics: Chapman & Hall, London, 5th edition.

Park, S. K., and Van, G. P., 1991, Inversion of pole-pole data for 3-D resistivity structures beneath arrays of electrodes: Geophysics, **56**, 951–960.

Pelton, W. H., Rijo, L., and Swift, C. M., 1978a, Inversion of two-dimensional resistivity and induced polarisation data: Geophysics, **43**, no. 4, 788–803.

——— 1978b, Mineral discrimination and removal of inductive coupling with multifrequency IP: Geophysics, **43**, no. 3, 588–609.

Perrier, F. E., Petiau, G., Clerc, G., Bogorodsky, V., Erkul, E., Jouniaux, L., Lesmes, D., Macnae, J., Meunier, J. M., Morgan, D., Nascimento, D., Oettinger, G., Schwarz, G., Toh, H., Valiant, M. J., Vozoff, K., and Yazici-Cakin, O., 1997, A one-year systematic study of electrodes for long period measurements of the electric field in geophysical environments: J. Geomagn. Geoelectr., **49**, 1677–1696.

Petrick, W. R., Sill, W. R., and Ward, S. H., 1981, Three-dimensional resistivity inversion using alpha centres: Geophysics, **46**, no. 8, 1148–1162.

POST, Contaminated Land:, Technical Report 15, Parliamentary Office of Science and Technology, 1993.

Reinecke, N., and Mewes, D., 1996, Recent developments and industrial/research applications of capacitance tomography: Meas. Sci. Technol., **7**, 233–246.

Reynolds, J. M., 1997, An Introduction to Applied and Environmental Geophysics: John Wiley & Sons.

Reynolds, J. M., 1998, The role of geophysics in the investigation of contaminated land: Proceedings of the Fifth International Conference, Re-Use of Contaminated Land and Landfills, 7-9 July 1998, Brunel University, London, Engineering Technics Press, 131–137.

Ringhandt, A., and Wagemann, H. G., 1993, An exact calculation of the 2-dimensional capacitance of a wire and a new approximation formula: IEEE Trans. Electron Devices, **40**, 1028–1032.

Roy, A., and Apparao, A., 1971, Depth of investigation in direct current methods: Geophysics, **36**, no. 5, 943–959.

Sakurai, T., and Tamaru, K., 1983, Simple formulas for two- and three-dimensional capacitances: IEEE Trans. Electron Devices, **30**, 183–185.

Sapozhnikov, B. G., Resistivity method without grounding: Unpublished report.

Sasaki, Y., 1994, 3-D resistivity inversion using the finite-element method: Geophysics, **59**, 1839–1848.

Sheriff, R. E., 1991, Encyclopedic Dictionary of Exploration Geophysics: Society of Exploration Geophysicists, Tulsa, 3rd edition.

Shima, H., Texier, B., Kobayashi, T., and Hasegawa, N., 1995, Fast imaging of shallow resistivity structures using a multichannel capacitive electrode system: 65th Annual Meeting of the Society of Exploration Geophysicists, Expanded Abstracts, 377–380.

Shima, H., Sakashita, S., and Kobayashi, T., 1996, Developments of non-contact data acquisition techniques in electrical and electromagnetic explorations: J. Appl. Geophys., **35**, 167–173.

Shima, H., 1992, 2-D and 3-D resistivity image reconstruction using crosshole data: Geophysics, **57**, 1270–1281.

Smith, N. C., and Vozoff, K., 1984, Two-dimensional dc resistivity inversion for dipole-dipole data: IEEE Trans. Geosci. Remote Sensing, **22**, 21–28.

Smythe, W. R., 1950, Static and Dynamic Electricity: McGraw-Hill, New York, 2nd edition.

Sommerfeld, A., 1909, Über die Ausbreitung der Wellen in der drahtlosen Telegraphie: Ann. Physik, **28**, 665.

Sommerfeld, A., 1926, Über die Ausbreitung der Wellen in der drahtlosen Telegraphie: Ann. Physik, **81**, no. 17, 1135–1153.

Sørensen, K., 1996, Pulled Array Continuous Electrical Profiling: First Break, **14**, no. 3, 85–90.

Soudain, M., 1998, Investigating changes: Ground Eng., **31**, no. 4, 16–17.

Spitzer, K., 1995, A 3-d finite-difference algorithm for dc resistivity modeling using conjugate-gradient methods: Geophys. J. Int., **123**, 903–914.

Spitzer, K., 1998, The three-dimensional DC sensitivity for surface and subsurface sources: Geophys. J. Int., **134**, 736–746.

Spitzer, K., 2001, Magnetotelluric static shift and direct current sensitivity: Geophys. J. Int., **144**, 289–299.

Storey, L. R. O., Aubry, M. P., and Meyer, P., 1969, A quadrupole probe for the study of ionospheric plasma resonances *in* Thomas, J. O., and Landmark, B. J., Eds., Plasma Waves in Space and Laboratory: Edinburgh University Press, 303–332.

Südekum, W., 2000, Mobile Elektrodengruppe zur oberflächennahen geoelektrischen Kartierung: Geologisches Jahrbuch, **E52**, 35–62.

Tabbagh, A., and Panissod, C., 2000, 1D complete calculation for electrostatic soundings interpretation: Geophys. Prosp., **48**, 511–520.

Tabbagh, A., Hesse, A., and Grard, R., 1993, Determination of electrical properties of the ground at shallow depth with an electrostatic quadrupole: field trials on archaeological sites: Geophys. Prosp., **41**, 579–597.

Telford, W. M., Geldart, L. P., and Sheriff, R. E., 1990, Applied Geophysics: Cambridge University Press, 2nd edition.

Tezkan, B., 1999, A review of environmental applications of quasi-stationary electromagnetic techniques: Surv. Geophys., **20**, 279–308.

Timofeev, V. M., Electric and electromagnetic profiling with ground capacitive line-antennas:, VSEGINGEO, Moscow, Russia. Translated by G. Rozenberg, edited by J. A. Hunter.

Timofeev, V. M., Rogozinski, A. W., Hunter, J. A., and Douma, M., 1994, A new ground resistivity method for engineering and environmental geophysics: Proceedings of the Symposium on the Application of Geophysics to Engineering and Environmental Problems (SAGEEP), 701–715.

Timofeev, V. M., 1973, Experience in the use of high frequency electrical geophysical methods in geotechnical and geocryological field studies: Proceedings of the 3rd International Conference on Permafrost, NAUKA, 238–247.

Timofeev, V. M., 1974, The employment of capacitively-coupled sensors in engineering and geological studies (in Russian): Ph.D. thesis, University of Moscow.

Timofeev, V. M., Some peculiarities of surface capacitive antennas used in electrical geophysical techniques:, Reference Information Issue 8/73, Gosstroi USSR, PNIIS, 1978.

Tripp, A. C., Hohmann, G. W., and Swift Jr., C. M., 1984, Two-dimensional resistivity inversion: Geophysics, **49**, 1708–1717.

Tsourlos, P., 1995, Modelling, interpretation and inversion of multielectrode resistivity survey data: Ph.D. thesis, University of York.

U.S. Environmental Protection Agency, Use of Airborne, Surface, and Borehole Geophysical Techniques at Contaminated Sites: A Reference Guide: Publ. No. EPA/625/R-92/007, 1993.

van Overmeeren, R. A., and Ritsema, I. L., 1988, Continuous vertical electrical sounding: First Break, **6**, no. 10, 313–324.

Vogelsang, D., 1995, Environmental Geophysics: Springer-Verlag, Berlin, New York.

Wait, J. R., and Gruszka, T. P., 1986, On electromagnetic coupling removal from induced polarization surveys: Geoexploration, **24**, 21–27.

Wait, J. R., 1955, Mutual electromagnetic coupling of loops over a homogeneous ground: Geophysics, **20**, 630–637.

Wait, J. R., 1969, Characteristics of antennas over lossy earth *in* Collin, R. E., and Zucker, F. J., Eds., Antenna Theory Part 2: McGraw-Hill.

Wait, J. R., 1982, Geo-Electromagnetism: Academic Press, New York.

Wait, J. R., 1995, Comments on: Benderitter et al., Application of the electrostatic quadripole to sounding in the hectometric depth range: J. Appl. Geophys., **34**, 79–80.

Walker, A. R., 2000, Multiplexed resistivity survey at the roman town of Wroxeter: Archaeol. Prosp., **7**, no. 2, 119–132.

Walter, M., 12. April 2001, Underground surveying goes overground: New Civil Engineer, pages 48–49.

Ward, S. H., and Hohmann, G. W., 1988, Electromagnetic theory for geophysical applications *in* Nabighian, M. N., Ed., Electromagnetic Methods in Applied Geophysics — Volume 1, Theory: Soc. Expl. Geoph.

Ward, S. H., 1967a, Electromagnetic Theory for Geophysical Applications *in* Hansen, D. A., Heinrichs, W. E., Holmer, R. C., MacDougall, R. E., Rogers, G. R., Sumner, J. S., and Ward, S. H., Eds., Mining Geophysics: Volume II, Theory: Soc. Expl. Geoph.

——— 1967b, The Electromagnetic Method *in* Hansen, D. A., Heinrichs, W. E., Holmer, R. C., MacDougall, R. E., Rogers, G. R., Sumner, J. S., and Ward, S. H., Eds., Mining Geophysics: Volume II, Theory: Soc. Expl. Geoph.

Ward, S. H., Ed., 1990, Geotechnical and Environmental Geophysics, Investigations in Geophysics, Soc. Expl. Geoph., Tulsa.

Wealthall, G. P., 1999, Local geology and hydrogeological properties of test site *in* Harrington, J. F., Ed., Fluid flow in fractures and faults: a feasibility study investigating the transport properties of the Mercia Mudstone Formation. Fluid Processes Series, Technical Report WE/97/13R: British Geological Survey.

West, J., 1997, Geophysical investigations: Ground Eng., **30**, no. 5, 33–34.

Yang, W. Q., and York, T. A., 1999, New ac-based capacitance tomography system: IEE Proc.-Sci. Meas. Technol., **146**, 47–53.

Yuan, C. P., and Trick, T. N., 1982, A simple formula for the estimation of the capacitance of two-dimensional interconnects in VLSI circuits: IEEE Electr. Dev. Lett., **3**, 391–393.

Zhang, J., Mackie, R. L., and Madden, T. R., 1995, 3-D resistivity forward modeling and inversion using conjugate gradients: Geophysics, **60**, 1313–1325.

Zohdy, A. A. R., 1989, A new method for the automatic interpretation of Schlumberger and Wenner sounding curves: Geophysics, **54**, no. 2, 245–253.

Zonge, K. L., and Hughes, L. J., 1986, Effect of electrode contact resistance on electric field measurements: Geophysics, **51**, no. 2, 463.

Appendix A

Fundamentals of electromagnetic theory

The nature of electromagnetic fields and their development in space and time is largely governed by the electrical properties of the surrounding media. The term "electromagnetic" includes both electric and magnetic fields; for simplicity, static fields of either kind will also be considered as electromagnetic in the following. Geomaterials such as rocks, soils, manmade ground and building materials represent media of both conductive and dielectric character. In order to study the general response of such media to electromagnetic fields, a complete electromagnetic formulation has to be considered from the outset. This section summarises essential chapters from Ward and Hohmann (1988), Jackson (1975) and Ward (1967a) using the rationalised MKSA unit system.

A.1 Maxwell's equations

The fundamental mathematical model of electromagnetic theory is represented by Maxwell's equations which relate the electromagnetic field to its sources. The vectors that constitute the electromagnetic field are the electric field intensity $\mathbf{E}$, the magnetic induction $\mathbf{B}$, the dielectric displacement $\mathbf{D}$ and the magnetic field intensity $\mathbf{H}$. The sources are the spatial distributions of electric charge density η and of electric current density $\mathbf{j}$. In the space-time domain Maxwell's equations are typically described as

$$\nabla \cdot \mathbf{D} = \eta \tag{A.1}$$

$$\nabla \times \mathbf{H} = \mathbf{j} + \frac{\partial \mathbf{D}}{\partial t} \tag{A.2}$$

$$\nabla \times \mathbf{E} = -\frac{\partial \mathbf{B}}{\partial t} \tag{A.3}$$

$$\nabla \cdot \mathbf{B} = 0. \tag{A.4}$$

Equation A.1 is also known as Faraday's Law, (A.2) as Ampère's Law and (A.4) as Coulomb's Law. From a combination of these axiomatic equations one obtains the equation of continuity which identifies the time-varying charge

distributions as the sources of electric current:

$$\frac{\partial \eta}{\partial t} + \nabla \cdot \mathbf{j} = 0. \tag{A.5}$$

A.2 Constitutive relations

Equations A.1–A.4 are uncoupled differential equations for **D**, **H**, **E**, **B** and **j**. The system becomes linearly coupled through the constitutive relations

$$\mathbf{D} = \varepsilon \mathbf{E} \tag{A.6}$$
$$\mathbf{B} = \mu \mathbf{H} \tag{A.7}$$
$$\mathbf{j} = \sigma \mathbf{E} \tag{A.8}$$

where in the general case dielectric permittivity ε and electrical conductivity σ are complex frequency-dependent functions

$$\varepsilon(\omega) = \varepsilon'(\omega) + i\varepsilon''(\omega) \tag{A.9}$$
$$\sigma(\omega) = \sigma'(\omega) + i\sigma''(\omega) \tag{A.10}$$

however the magnetic permeability μ can usually be assumed real and independent of frequency. (A.8) is commonly known as Ohm's Law. Resistivity ρ is defined as the inverse of conductivity by

$$\varrho = \frac{1}{\sigma} \tag{A.11}$$

and it is mostly a matter of convenience which of the two is chosen. Resistivity is more closely associated with galvanic techniques while conductivity is used in the context of induction-based techniques. Relative dielectric permittivity is defined by

$$\varepsilon_r = \frac{\varepsilon}{\varepsilon_0} \tag{A.12}$$

as a dimensionless number where $\varepsilon_0 = 8.854 \cdot 10^{-12}$Fd/m is the permittivity of free space. The real part of ε_r is referred to as the dielectric constant of a material. In analogous fashion relative magnetic permeability is defined as

$$\mu_r = \frac{\mu}{\mu_0} \tag{A.13}$$

where $\mu_0 = 4\pi \cdot 10^{-7}$H/m is the magnetic permeability of free space.
Nonlinear behaviour of geomaterials is usually a second order effect and will be neglected for the purposes of this work. For anisotropic media the scalar quantities may be replaced by their tensorial equivalents so that relations similar to (A.6)–(A.8) apply to field components.

A.3 Wave equations and the wavenumber

Maxwell's equations (A.2) and (A.3) may now be coupled by substituting (A.6)–(A.8) and keeping in mind that $\nabla \cdot \mathbf{E} = 0$ and $\nabla \cdot \mathbf{H} = 0$ in homogeneous regions. This yields the wave equations in $\mathbf{E}$ and $\mathbf{H}$

$$\nabla^2 \mathbf{E} - \mu\varepsilon \frac{\partial^2 \mathbf{E}}{\partial t^2} - \mu\sigma \frac{\partial \mathbf{E}}{\partial t} = 0 \tag{A.14}$$

$$\nabla^2 \mathbf{H} - \mu\varepsilon \frac{\partial^2 \mathbf{H}}{\partial t^2} - \mu\sigma \frac{\partial \mathbf{H}}{\partial t} = 0. \tag{A.15}$$

For our purposes it is more revealing to consider these relations in the space-frequency domain, that is after the application of a one-dimensional Fourier transform

$$\mathbf{F}(\mathbf{r}, t) \longrightarrow \tilde{\mathbf{F}}(\mathbf{r}, \omega) \tag{A.16}$$

with the Fourier transform pair

$$\tilde{\mathbf{F}}(\mathbf{r}, \omega) = \int_{-\infty}^{\infty} \mathbf{F}(\mathbf{r}, t) e^{-i\omega t} dt \tag{A.17}$$

$$\mathbf{F}(\mathbf{r}, t) = \frac{1}{2\pi} \int_{-\infty}^{\infty} \tilde{\mathbf{F}}(\mathbf{r}, \omega) e^{i\omega t} d\omega \tag{A.18}$$

which yields a set of Helmholtz equations in $\mathbf{E}$ and $\mathbf{H}$

$$\nabla^2 \mathbf{E} + k^2 \mathbf{E} = 0 \tag{A.19}$$

$$\nabla^2 \mathbf{H} + k^2 \mathbf{H} = 0. \tag{A.20}$$

with

$$k^2 = \mu\varepsilon\omega^2 - i\mu\sigma\omega \tag{A.21}$$

where k is the complex wave number which Keller (1988) identifies as the one term into which all rock properties and frequency group and which characterises the interaction of the electromagnetic field with the medium.

A.4 Diffusion or propagation?

The nature of that interaction in the application of electromagnetic methods is dictated by the behaviour of the wave number with change in frequency. This becomes clearer when we consider that the term $\mu\varepsilon\omega^2$ in (A.21) will be associated with displacement currents while $\mu\sigma\omega$ represents conduction currents. At frequencies less than 10^5Hz we usually have $\mu\varepsilon\omega^2 \ll \mu\sigma\omega$ for geomaterials so that the wave number becomes

$$k = (-i\mu\sigma\omega)^{1/2} \tag{A.22}$$

and the Helmholtz equations turn into diffusion equations. Diffusion describes the attenuation of fields in the conductive medium under absorption of energy

and conversion into ohmic heat. All low-frequency EM techniques are based on the diffusive regime.
For higher frequencies $\mu\varepsilon\omega^2$ and $\mu\sigma\omega$ are of the same order which is the regime of attenuated wave propagation. This is applicable to high-frequency techniques such as Ground Penetrating Radar.

A.5 Plane wave propagation

In order to understand the properties of a conductive halfspace model, it useful to study the propagation of plane electromagnetic waves under vertical incidence at the surface. When such a wave travels vertically downwards its amplitude is subject to attenuation due to electromagnetic diffusion. This effect can be quantified by the so-called electromagnetic skin depth, a scale length characteristic to the electrical properties of the halfspace. The skin depth is given by

$$\delta = \sqrt{\frac{2}{\omega\mu_0\sigma}}. \tag{A.23}$$

It equates to the distance at which the amplitude of the plane wave has been attenuated to $1/e$ of its amplitude at the surface.

A.6 Complex electrical properties

Electrical properties may be described in several different notations.

σ, ε real. If conductivity and permittivity are both assumed real then in the space-frequency domain Ampère's law (A.2) together with the constitutive equations (A.6) and (A.8) transforms into

$$\nabla \times \mathbf{H} = \mathbf{j} + i\omega\mathbf{D} = (\sigma_R + i\omega\varepsilon_R)\mathbf{E}. \tag{A.24}$$

It is evident that the total current density $\nabla \times \mathbf{H}$ consists of a component which is in-phase and one that is in quadrature with the electric field. Independent of notation, σ_R is always associated with conduction currents while ε_R is associated with displacement currents.

σ complex. For a complex conductivity σ (A.24) can be generalised using (A.10):

$$\nabla \times \mathbf{H} = \sigma\mathbf{E} = (\sigma' + i\sigma'')\mathbf{E} \tag{A.25}$$

where

$$\sigma' = \sigma_R \quad \text{and} \quad \sigma'' = \omega\varepsilon_R. \tag{A.26}$$

Ohmic conductivity σ_R is now the in-phase component of complex conductivity while dielectric permittivity ε_R has been absorbed by its quadrature component.

ε complex. For a complex permittivity ε (A.24) can be generalised using (A.9):

$$\nabla \times \mathbf{H} = i\omega\varepsilon\mathbf{E} = i\omega(\varepsilon' + i\varepsilon'')\mathbf{E} \tag{A.27}$$

where

$$\varepsilon' = \varepsilon_R \quad \text{and} \quad \varepsilon'' = -\frac{\sigma_R}{\omega}. \tag{A.28}$$

Dielectric permittivity is now the in-phase component of complex permittivity while ohmic conductivity has been absorbed by its quadrature component.

σ, ε complex. If both σ and ε are assumed complex then both include conductive and permittive properties:

$$\nabla \times \mathbf{H} = ((\sigma' + i\sigma'') + i\omega(\varepsilon' + i\varepsilon''))\mathbf{E}. \tag{A.29}$$

Appendix B

Electrical Capacitance Tomography

Capacitive sensor technology is routinely employed for a variety of non-geophysical applications. This section provides a brief introduction to a well-established technique known as Electrical Capacitance Tomography (ECT) which has found many technical applications. Its methodology bears a number of similarities with capacitive resistivity.

B.1 Applications of ECT in Industrial Process Tomography

The tomographic imaging method is now an accepted standard in many areas such as medicine, materials science or process engineering and a whole range of techniques has been developed to image the interior physical properties of solid, liquid or gaseous materials of artificial or biological origin. Tomographic techniques offer a method for obtaining an image indirectly, e.g. through solid-walled vessels or opaque materials. Industrial Process Tomography (IPT) in particular is a fast-growing field which aims to directly analyse the internal characteristics of process plants in order to improve the design and operation of industrial equipment. It typically deals with substances such as aggressive and fast-moving fluids, gases and solids and multi-phase mixtures. Robust non-invasive sensors are required as measuring instruments for such applications. Electrical Capacitance Tomography (ECT) is one of the wide range of tomographic techniques available. A recent introduction to ECT is given in Beck et al. (1997).

B.2 Basic principle

ECT systems typically operate under the assumption of a 2D geometry, i.e. the material properties to be imaged are assumed to vary across the cross-sectional area of, for example, a section of pipeline. The cross-section to be imaged is then surrounded by a set of capacitive electrodes formed from simple metal

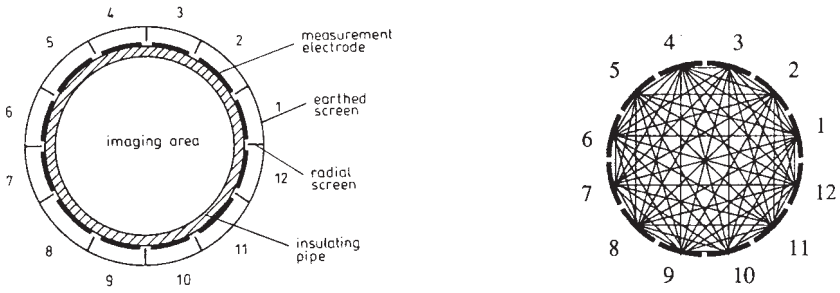

Figure B.1: The principle of ECT sensors. Left: cross-sectional view of typical ECT sensor with 12 measurement electrodes (Yang and York, 1999). Right: possible electrode combinations with a 12-electrode ECT sensor (Beck et al., 1997).

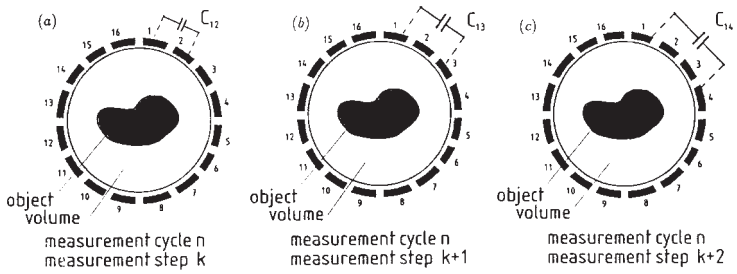

Figure B.2: Schematic representation of the sequential sampling of ECT electrodes (Reinecke and Mewes, 1996).

plates (Figure B.1). These can be mounted either inside or outside the vessel depending on the wall material. For insulating wall materials such as plastic, the electrodes are often mounted on the outside surface and the measurement is entirely non-invasive. The basic idea is to measure the changes in capacitance between all possible combinations of electrodes which occur when material with different electrical properties is introduced into the sensor area (Figure B.2). From these changes in capacitance, an image based on the variation of the permittivity within the cross-section can be obtained.

B.3 Image reconstruction

ECT images are currently still of relatively low resolution, with square 32×32 pixel grids being typical of current systems. The values of the individual pixels must be calculated from the set of capacitance measurements in a process similar to that of a resistivity inversion. Linear back-projection algorithms are among the simplest and fastest methods currently in use. However, model-based reconstruction techniques as known in resistivity inversion are found to produce more accurate results (Isaksen, 1996).

B.4 Applications

A classical application of ECT is the imaging of cross-sections of conveyor pipes, e.g. to identify different flow classes or distinguish different phases in multi-phase flow. For example, discrimination of gas and oil phases in the two-phase flow from oil wells has been successfully achieved with ECT. Combustion imaging is another popular application of ECT where information about the state of flames or explosions, unburnt fuels and exhaust residues can be gathered.